Theoretical Study of Ion Toroidal Rotation in the Presence of Lower Hybrid Current Drive in a Tokamak

by

Jungpyo Lee

Submitted to the Department of Nuclear Science and Engineering
in partial fulfillment of the requirements for the degree of
Doctor of Philosophy in Nuclear Science and Engineering
at the
MASSACHUSETTS INSTITUTE OF TECHNOLOGY
June 2013

Author .....
Department of Nuclear Science and Engineering
May 13, 2013

Certified by .....
Prof. Felix I. Parra
Assistant Professor of Nuclear Science and Engineering
Thesis Supervisor

Certified by .....
Dr. Paul T. Bonoli
Senior Research Scientist
Thesis Reader

Certified by .....
Dr. Peter J. Catto
Senior Research Scientist
Thesis Reader

Accepted by .....
Prof. Mujid S. Kazimi
TEPCO Professor of Nuclear Science and Engineering
Chair, Department Committee on Graduate Students

Theoretical Study of Ion Toroidal Rotation in the Presence of Lower Hybrid Current Drive in a Tokamak

by

Jungpyo Lee

Submitted to the Department of Nuclear Science and Engineering
on May 13, 2013, in partial fulfillment of the
requirements for the degree of
Doctor of Philosophy in Nuclear Science and Engineering

Abstract

In this thesis, the effect of the lower hybrid current drive on ion toroidal rotation in a tokamak is investigated theoretically. Lower hybrid frequency waves are utilized to drive non-inductive current for steady state tokamaks and ion toroidal rotation is used to control disruptions and improve confinement. It has been observed in many tokamaks that lower hybrid waves can change the ion toroidal rotation. These measurements indicate that it may be possible to control rotation with lower hybrid waves, but to do it, it is necessary to understand the mechanisms underlying the rotation change. The toroidal angular momentum injected by the lower hybrid waves initiates acceleration in the the counter-current direction. The parallel and perpendicular components of the toroidal angular momentum are transferred from the waves to ions through electrons via two different channels, and the ions obtain the full toroidal angular momentum injected by the lower hybrid waves after several ion collision times. The momentum transferred to the ions is transported out by turbulent radial transport. The radial transport of toroidal angular momentum is evaluated using gyrokinetics corrected to the higher order in poloidal rhostar. The higher order corrections lead to momentum redistribution even in the absence of rotation, which is called intrinsic momentum transport. The intrinsic momentum transport due to diamagnetic effects is an important piece of the radial momentum transport. The change in the steady state rotation due to lower hybrid waves is estimated theoretically by evaluating the momentum source, the momentum pinch and diffusion, and the intrinsic momentum transport. The effect of the current profile on the intrinsic momentum transport, which is modified by the lower hybrid wave, may explain the reversal of the rotation change from counter-current direction to co-current direction observed in low plasma current discharges in Alcator C-Mod.

Thesis Supervisor: Prof. Felix I. Parra
Title: Assistant Professor of Nuclear Science and Engineering

Acknowledgments

There are many people who have offered their support and wisdom in helping me complete this thesis, and I would like to mention a few of them below.

First and foremost, I would like to thank my supervisor, Prof. Felix Parra. Most of the work presented here would have been impossible without his guidance. He has provided me with innumerable great ideas and taught me how to break through any given problem, based on his incomparably deep and broad understanding on plasma physics. Additionally, he has supported me with warm friendship, and for that I am deeply grateful.

I would also like to thank Dr. Paul Bonoli who has had faith in my potential from the beginning of my Ph.D program and encouraged me to build my theoretical logic. He taught me a lot of about RF wave theory, and also gave me enormous practical support as my advisor. I sincerely thank the other committee members, Dr. Peter Catto and Prof. Ron Parker. They motivated me to have an interest in this thesis topics, and their questions and suggestions helped me to progress in this research and improve the presentation of this thesis.

I would like to highlight the theory group involved in this research at MIT plasma science and fusion center. Dr. John Wright helped me to solve the theoretical and numerical problems in the RF wave part of this thesis, and Dr. Michael Barnes and Dr. Darin Ernst gave me invaluable scientific advice on the matter of plasma turbulence. Without their assistance, I would have much trouble finishing this thesis. I would like to acknowledge their contributions.

The experimental group at Alcator C-mod has also supported this work by providing measured data for the comparison with theory. I would especially like to thank the members of the X-ray spectroscopy group and lower hybrid wave group: Dr. Yuri Podpaly, Dr. John Rice, Dr. Matt Reinke, Chi Gao, Dr. Syuin'ichi Shiraiwa, Dr. Orso Meneghini, and Dr. Greg Wallace.

Of course my friends gave me much emotional support. The graduate students in this plasma center enabled me to have an enjoyable life at MIT. I am grateful to friends in my first-year class of 2008, Bob, Dan, Geoff, Mike Churchill and Mike Garrett; and to Korean graduate students, Seung-Gyou baek, Jinseok Ko, and Choongki Sung. I have also enjoyed being with my friends in the MIT swim club and the Korean language class. I would like

to express my deepest gratitude to old friends, Jung-Rok, Wonjung, and Sanha.

This work was financially supported by a Samsung Scholarship, and by a Fusion Energy Sciences program and a RF Scientific Discovery through Advanced Computing program under U. S. Department of Energy contracts. Many numerical simulations were carried out using computer resources on NERSC, PPPL, and MIT PSFC.

Finally, I am also indebted to my parents Jong-soo and Young-sook, and my sister Se-mi. They were supportive of me despite the distance.

Contents

Nomenclature

Miscellaneous

$\langle \ldots \rangle$	Gyroaverage holding $\mathbf{R}$, $\mathcal{E}$, μ and t fixed.
$\langle \ldots \rangle_s$	Flux surface average.
$\langle \ldots \rangle_b$	Bounce average.

Greek letters

α in Chapter 2 and 3	Phase of gyromotion.
α in Chapter 4	Coordinate perpendicular to the magnetic field, satisfying $\mathbf{B} = \nabla\alpha \times \nabla\psi$
ψ	Poloidal magnetic flux, radial coordinate.
ψ_0	Poloidal magnetic flux at the last closed flux surface
θ	Poloidal angle
φ, $\hat{\varphi}$	Toroidal angle and unit vector in the toroidal direction.
ϵ	Inverse aspect ratio r/R.
ρ_e, ρ_i	Electron and ion Larmor radii, $m_e c v_e/eB$ and $m_i c v_i/Z_i eB$.
$\rho_{\star,e}$	Small ratios of electron Larmor radii over the radial scale length, ρ_e/a.
$\rho_\star$	Small ratios of ion Larmor radii over the radial scale length, ρ_i/a.
$\rho_{\star,\theta}$	Small ratios of poloidal ion Larmor radii over the radial scale length (Poloidal rhostar), $(B/B_\theta)\rho_i/a$.
Ω_e, Ω_i	Electron and ion gyrofrequencies, $eB/m_e c$ and $Z_i eB/m_i c$.
ν_{ii}, ν_{ie}, ν_{ee}, ν_{ei}	Ion-ion, ion-electron, electron-electron and electron-ion Braginskii collision frequencies.
ϕ	Electrostatic potential.
ϕ_0^{bg}	Lowest order long wavelength background electrostatic potential.

ϕ_1^{tb}	Short wavelength turbulent electrostatic potential, $O(\rho_\star(T_e/e))$.
ϕ_2^{tb}	Higher order turbulent electrostatic potential, $O((B/B_\theta)\rho_\star\phi_1^{tb})$.
$\langle\phi\rangle$	Electrostatic potential averaged over a gyromotion.
μ	Gyrokinetic magnetic moment defined to be an adiabatic invariant to higher order, $v_\perp^2/2B$
Π	Radial transport of toroidal angular momentum.
Π_1, Π_2	Turbulent radial fluxes of toroidal angular momentum to lowest order and to higher order in $(B/B_\theta)\rho_\star$.
Π_{int}	Intrinsic radial transport of toroidal angular momentum.
ω	Frequency of the lower hybrid wave.
ω_{LH}	Lower hybrid resonant frequency.
Ω_φ	Toroidal angular frequency.
$\Omega_{\varphi,E}$, $\Omega_{\varphi,d}$	Toroidal angular frequencies for E×B flow and diamagnetic flow.
χ_φ	Ion toroidal momentum diffusivity.
$\chi_{\varphi,E}$, $\chi_{\varphi,d}$	Ion toroidal momentum diffusivities for E×B flow and diamagnetic flow.
χ_i	Ion heat diffusivity.

Roman letters

a	Minor radius in a tokamak.
A	Area of the flux surface, $V'(\psi_0/a)$.
$\mathbf{B}$, B, $\hat{\mathbf{b}}$	Magnetic field, magnetic field magnitude, and unit vector parallel to the magnetic field.
B_θ	Magnitude of the poloidal component of the magnetic field.
B_φ	Magnitude of the toroidal component of the magnetic field.
c	Speed of light.
$D_{gB,s}$	Gyro-Bohm diffusion coefficient for a species, s
e	Electron charge magnitude.
$\mathcal{E}$	Kinetic energy of the particle $v^2/2$.
$\mathbf{E}$	Electric field.
f_e	Electron distribution function, dependent on $\mathbf{r}$, $\mathcal{E}$, μ and α.

$f_{0,e}$, $f_{i,e}$	Lowest order electron and ion distribution function, usually dependent on gyrokinetic variables $\mathbf{R}$, $\mathcal{E}$, μ
f_i	Ion distribution function, usually dependent on the gyrokinetic variables $\mathbf{R}$, $\mathcal{E}$ and μ.
$f_{0,e}^{bg}$,$f_{0,i}^{bg}$	Lowest order electron and ion background distribution functions, assumed to be non-fluctuating.
$f_{1,e}^{bg}$,$f_{1,i}^{bg}$	Higher order electron and ion background distribution functions, $O\left((B/B_\theta)\rho_{\star,e}f_{M,e}\right)$ and $O\left((B/B_\theta)\rho_\star f_{M,i}\right)$
$f_{1,e}^{tb}$, $f_{1,i}^{tb}$	Short wavelength turbulent electron and ion distribution functions, $O(\rho_\star f_{M,e})$ and $O(\rho_\star f_{M,i})$.
$f_{2,e}^{tb}$, $f_{2,i}^{tb}$	Higher order turbulent electron and ion distribution functions, $O((B/B_\theta)\rho_\star f_{1,e}^{tb})$ and $O((B/B_\theta)\rho_\star f_{1,i}^{tb})$.
$f_{1,e}^{LH}$	Perturbed background electron distribution function due to lower hybrid waves.
$\widetilde{f_{1,e}^{LH}}$	Gyrophase dependent piece of $f_{1,e}^{LH}$.
$\langle f_{1,e}^{LH} \rangle$	Gyrophase independent piece of $f_{1,e}^{LH}$.
$f_{M,e}$, $f_{M,i}$	Electron and ion Maxwellian distribution functions.
$F_{0,e}$, $F_{0,i}$	Lowest order electron and ion distribution functions at the outer-midplane.
I	Function RB_φ; it only depends on ψ to lowest order.
$\mathbf{J}$	Current density.
$k_\parallel$, $k_\perp$	Wavenumbers parallel and perpendicular to the magnetic field.
L	Characteristic length in the problem.
m, n	Poloidal and toroidal mode number of a wave.
m_e, m_i	Electron and ion masses.
n_e, n_i	Electron and ion densities.
$n_\parallel$, n_φ	Parallel and toroidal refractive index of a wave.
p_e, p_i	Electron and ion pressures.
P_φ	Ion toroidal momentum pinch coefficient.
$P_{\varphi,E}$, $P_{\varphi,d}$	Ion toroidal momentum pinch coefficients for E×B flow and diamagnetic flow.

q	Safety factor.
$\hat{s}$	Magnetic shear, $(r/q)(\partial q/\partial r)$.
$\mathbf{r}$	Position of the particle.
r	Radial coordinate, $(\psi/\psi_0)a$
R	The distance between the axis of symmetry and the position of the particle, also used as major radius in a tokamak.
$\mathbf{R}$	Position of the gyrocenter.
T_e, T_i	Electron and ion temperatures.
T_φ	External torque due to lower hybrid waves in the toroidal direction.
$T_\varphi^{\parallel}$	Parallel component of the toroidal direction external torque.
$\Delta T_\varphi^{\perp} + \Delta T_\varphi^{\alpha}$	Perpendicular component of the toroidal direction external torque.
u	Magnitude of relativistic velocity
$u_\parallel$, $u_\perp$	Relativistic velocity component parallel and perpendicular to the magnetic field.
ϑ	Pitch angle in the relativistic velocity space, $\tan^{-1}(u_\perp/u_\parallel)$.
$\mathbf{v}$	Velocity of the particle.
$v_\parallel$, $v_\perp$	Velocity component parallel and perpendicular to the magnetic field.
v_{te}, v_{ti}	Electron and ion thermal velocities, $\sqrt{2T_e/m}$ and $\sqrt{2T_i/M}$.
$\mathbf{v}_E^{tb}$	Gyrokinetic E×B drift due to short wavelength turbulent potential.
$\mathbf{v}_M$	∇B and curvature drift.
$\mathbf{v}_C$	Drift due to the Coriolis force.
V'	Flux surface volume element $\partial V/\partial\psi$.
$\mathbf{V_e}$, $\mathbf{V_i}$	Electron and ion average velocities.
V_φ	Ion toroidal average velocity.
x, y	Coordinate perpendicular to the magnetic field.
$\hat{\mathbf{x}}, \hat{\mathbf{y}}$	Unit vectors perpendicular to the magnetic field.
z	Coordinate parallel to the magnetic field.
$\hat{\mathbf{z}}$	Unit vector parallel to the magnetic field, $\hat{\mathbf{b}}$.
Z_i	Ion charge number.

Chapter 1

Introduction

Controlled nuclear fusion will be one of the most important milestones in human progress. The most promising way to achieve nuclear fusion is to use magnetic confinement. The tokamak is the best candidate among the nuclear fusion reactor concepts based on magnetic confinement.

However, the tokamak has also several limitations. One is steady state operation which is difficult to achieve because of the need to drive a substantial toroidal current in the plasma [1, 2, 3]. Unexpected disruptions due to magnetohydrodynamic (MHD) instabilities are also a problem [4, 5]. Another problem is the reduced confinement due to turbulence [6]. To solve these critical problems, radio frequency waves (specifically lower hybrid waves) are utilized to drive toroidal current [7, 8], and ion rotation can be used to control disruptions [9, 10] and improve confinement [11, 12, 13]. This thesis investigates the relation between the two solutions: how the lower hybrid waves affect the ion rotation.

Tokamaks have a strong toroidal magnetic field ($\sim$ 10 Tesla), and a poloidal magnetic field ($\lesssim$ 1 Tesla) generated by either inductive currents due to the central solenoid or radio frequency current drive. Both magnetic fields are necessary to ensure confinement of single particles. The lower hybrid waves are injected from a phased waveguide array or launcher with toroidal wave momentum that drives non-inductive currents to replace the inductive currents. In addition to the original purpose, current drive, it has been observed in many tokamaks that lower hybrid waves can change the ion toroidal rotation [14]. These measurements indicate that it may be possible to control rotation with lower hybrid waves, but to do it, it is necessary to understand the mechanisms underlying the rotation change.

In this thesis, the rotation change due to lower hybrid waves is studied. I show that the momentum input from lower hybrid waves needs to be taken into account. I also demonstrate that the momentum redistribution due to turbulence is important to explain the observations.

The rest of the chapter is organized as follows. In Sec. 1.1, I will review the theory of lower hybrid waves and its use for current drive in experiments. In Sec. 1.2, the current understanding of turbulence in a tokamak is explained, and the interactive relation between the rotation and the turbulence is briefly discussed. In Sec. 1.3, the experimental observations of toroidal rotation changes due to lower hybrid wave injection are given as a motivation for this study.

1.1 Lower hybrid waves in tokamaks

The frequency of the lower hybrid wave (ω = O(1) GHz) is selected to be above the lower hybrid resonance frequency (i.e. $\omega \gtrsim 2\omega_{LH}$) to drive current instead of heating, and to avoid significant parametric decay of the wave due to nonlinear coupling with ion sound quasi modes and ion cyclotron quasi modes [15, 16]. Here, the lower hybrid resonance frequency is $\omega_{LH}^2 \simeq \frac{\omega_{pi}^2}{1+\omega_{pe}^2/\Omega_e^2}$, where ω_{pe}, ω_{pi} and Ω_e are the electron and ion plasma frequency and the electron gyrofrequency, respectively. The lower hybrid wave propagation in a tokamak is described by the slow wave branch of the electrostatic plasma dispersion relation [17, 18, 19],

$$D(\omega) = Sk_\perp^2 + Pk_\parallel^2 = 0, \tag{1.1}$$

where $S \simeq 1 + \omega_{pe}^2/\Omega_e^2 - \omega_{pi}^2/\omega^2 \sim O(1)$ and $P \simeq -\omega_{pe}^2/\omega^2 \gtrsim O(100)$ are the components of the dielectric tensors in this range of frequency, and $k_\perp$ and $k_\parallel$ are the wavevectors perpendicular and parallel to the static magnetic field, respectively. Consequently, the slow wave has a perpendicular wavelength (O(1) mm) much shorter than the parallel wavelength (O(10) mm) (the slow wave is called "slow" due to the low perpendicular phase velocity). The direction of the wave energy flux is determined by the group velocity, given by

$$\frac{V_{gr\parallel}}{V_{gr\perp}} = \frac{\partial D(\omega)/\partial k_\parallel}{\partial D(\omega)/\partial k_\perp} = \frac{Pk_\parallel}{Sk_\perp} = -\frac{k_\perp}{k_\parallel} \gtrsim O(10), \tag{1.2}$$

where $V_{gr\perp}$ and $V_{gr\parallel}$ are the perpendicular and parallel group velocity of the lower hybrid waves, respectively. The fact that the parallel group velocity is larger than the perpendicular group velocity results in propagation that follows the magnetic field line and takes several toroidal circulations to penetrate radially (see Fig. 1-1). The waves propagate until they are damped by significant electron Landau damping [20]. The propagation of the lower hybrid waves will be explained more quantitatively in Sec. 2.2.1

The electron Landau damping transfers the wave energy and momentum to electrons when the parallel phase velocity of the wave is the same as the electron parallel velocity [7, 21]. Because most of the electron distribution function is Maxwell-Boltzmann, waves with a lower parallel phase velocity interact with a larger population of electrons and Landau damp faster. Consequently, to have strong damping in the core, the lower hybrid wave must have a parallel wavevector that is sufficiently small to penetrate into the core without strong damping at the edge but large enough to have strong damping when it reaches to the core. The parallel wave vector is proportional to the parallel refractive index of the wave ($n_\parallel = \frac{k_\parallel c}{\omega}$), where c is the speed of light. The parallel refractive index is determined by the toroidal refractive index (n_φ), fixed by the launcher due to the toroidal axisymmetry, and the poloidal refractive index (n_θ), which changes due to the plasma dispersion. The toroidal refractive index of the wave is given by the asymmetric antenna spectrum at the lower hybrid wave launcher.

Additionally, to ensure accessibility, the toroidal refractive index should be larger than a critical value at which the slow wave mode converts to the fast wave mode [22]. As a result, in many experiments, the toroidal refractive index is carefully chosen (e.g. $n_\varphi \sim -2$ in Alcator C-Mod), and the wave energy and momentum are transferred to the non-thermal fast electrons ($v_\parallel \sim 2.5v_{te} - 10v_{te}$). Here, the negative sign of the toroidal refractive index implies a counter-current direction wavevector, and $v_\parallel$ and v_{te} are the parallel electron velocity and electron thermal velocity, respectively.

Because the wave momentum is transferred to electrons, additional current is driven by lower hybrid waves. The wave momentum given by the toroidal refractive index at the launcher is in the counter-current direction (i.e. $n_\varphi < 0$) to push electrons in the counter-current direction and increase the current. Strong diffusion in velocity space in the parallel direction occurs due to the resonant momentum transfer, and it is balanced by the electron pitch angle scattering and the electron-ion friction. As a result, a long or plateau tail is

generated along the parallel velocity in the steady state distribution function (see Fig. 5 in [7]).

The driven current can be evaluated using Maxwell's equations to calculate the electric fields and a Fokker-Planck equation to calculate the electron distribution function by balancing collisions and the velocity quasilinear diffusion due to the lower hybrid waves. The detailed evaluation of the wave electric field and the electron distribution function will be explained in Sec. 2.2.1 and Sec. 2.2.2. For a given lower hybrid wave power, a higher current drive efficiency results in more driven current. The simplest estimation of the driven current is given by the increased electron velocity due to the energy transfer from the lower hybrid ($\Delta v_{\parallel} \sim \frac{P_{LH}}{(n_e m_e v_{\parallel})\Delta \mathrm{Vol}}\Delta t$) in an electron collision time ($\Delta t \sim \nu_e^{-1}$), resulting in the current drive efficiency, $\frac{I_{LH}}{P_{LH}} \sim \frac{e n_e \Delta v_{\parallel} \Delta \mathrm{A}}{P_{LH}} \sim \frac{1}{2\pi R}\frac{e}{m_e v_{\parallel} \nu_e} \propto \frac{v_{\parallel}^2}{n_e R}$. Here, P_{LH} is the lower hybrid wave power, I_{LH} is the lower hybrid wave driven current, R is the major radius of a tokamak, n_e, m_e, and e are the electron density, mass, and charge, and ΔVol and ΔA are the volume and the area where the energy is transferred, respectively. The dependence of the electron collision frequency ν_e on the density and the parallel velocity is used (i.e. $\nu_e \propto n_e v_{\parallel}^{-3}$).

Considering that the wave energy transfers to electrons due to Landau damping when the electron parallel velocity is the same as the parallel phase velocity of the wave, the current drive efficiency is decreased for a large parallel refractive index (i.e. $\frac{I_{LH}}{P_{LH}} \propto \frac{1}{n_e n_{\parallel}^2 R}$). This implies another constraint on the selection of the toroidal refractive index at the launcher. Note that the efficiency also decreases for larger tokamaks with a higher density. An elaborate analytical calculation of current drive efficiency can be done using Langevin equations [7], but more accurate values of efficiency can only be obtained numerically using a two dimensional collision operator in velocity space as is done in Sec. 2.2.2. Many of the observations (e.g. motional Stark effect diagnostics and hard X-ray diagnostics) in lower hybrid current drive experiments are well-reproduced by theory and simulation [23, 24, 25].

The current drive efficiency for momentum transfer by electron Landau damping is approximately 4/3 times larger than the efficiency for cyclotron damping (see Fig. 9 in [7]). The cyclotron damping current drive is caused by an increased collision time due to increased perpendicular energy. The current drive efficiency of electron cyclotron current drive is smaller than that of lower hybrid wave current because the latter accelerates electrons directly in the parallel direction [7]. It is a significant advantage of the lower hybrid waves for current drive.

Another advantage of the lower hybrid wave is the availability of off-axis current drive which is beneficial to control the safety factor profile. The radial location of the current drive is determined by the location of the wave damping, which can be controlled using the toroidal refractive index at the launcher. Although the radial location of the electron cyclotron damping is controllable by tuning the wave frequency to take advantage of the inhomogeneity of the magnetic field, the off-axis damping of electron cyclotron waves results in a significant increase in the number of trapped electrons, which cannot drive current. As a result, the current drive efficiency of electron cyclotron off-axis current drive is reduced substantially.

A significant problem has been found recently for lower hybrid current drive at reactor-relevant densities. Recently, for high plasma densities and diverted plasmas (e.g. line averaged density $> 10^{20}\mathrm{m}^{-3}$ in Alcator C-Mod), it has been observed that penetration of LH waves into the plasma core becomes problematic (e.g. Alcator C-Mod [26], FTU [27] and JET [28]). This density limit for the wave propagation is still not well understood, but modifiying the edge electron temperature [27] and changing the poloidal location of the lower hybrid wave launcher have been proposed as solutions to overcome the density limit.

In this thesis, I investigate only how the lower hybrid waves affect the ion toroidal rotation when the wave couples well and penetrates into the core. Because the injected wave momentum is transferred to ions when electrons reach steady state, the lower hybrid waves accelerate ions as well as electrons.

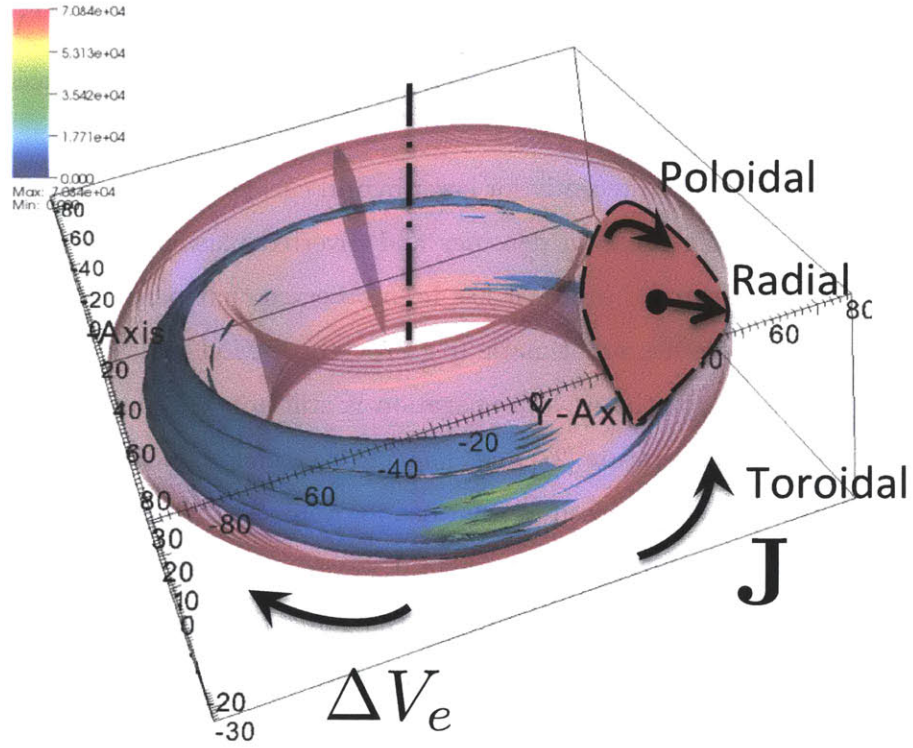

Figure 1-1: Simulated lower hybrid wave propagation in a tokamak. A tokamak is a donut shaped volume of plasma confined by toroidal and poloidal magnetic fields. It is axisymmetric. In the two-dimensional cross section (in dashed lines), the poloidal direction ($\hat{\theta}$) and the radial direction ($\hat{\psi}$) are shown. The resonance cone of lower hybrid waves is indicated by the color contours that give the electric field strength. The electric fields were calculated with TORLH [24] and CQL3D [29]. The wave momentum is transferred to push electrons (ΔV_e) in the counter-current direction (towards $-\mathbf{J}$) for current drive.

1.2 Turbulence and ion toroidal rotation

The plasma confinement in a tokamak is limited by the radial transport of particles and energy. Due to the toroidal geometry, there is inherent collisional transport of particles and energy, called neoclassical transport. Neoclassical theory considers Coulomb collisions between particles and finite width particle orbits in tokamak geometry [30, 31]. However, the measured size of the transport in many tokamaks is of gyro-Bohm size which is much larger than the neoclassical transport. It is believed that the gyro-Bohm scale transport is due to micro-turbulence [32, 33]. The gyro-Bohm diffusion coefficient for a species is defined by

$$D_{gB,s} = \frac{\rho_s}{L_\psi}\rho_s v_{ts} = \frac{\rho_s}{L_\psi}\frac{cT_s}{Z_s eB}, \tag{1.3}$$

where L_ψ is the radial scale length of the tokamak, B is the magnetic field strength, and ρ_s, v_{ts}, $Z_s e$ and T_s are the gyro-radius, the thermal velocity, the charge and the temperature of the species, respectively.

Micro-turbulence in a tokamak is caused by drift-wave instabilities driven by temperature and density gradients [34, 35]. A small initial electromagnetic perturbation is amplified by the instability, but it becomes self-regulated and the amplified perturbation is saturated in a short time by nonlinear coupling with other spectral modes, causing turbulence. During the coupling process, the energy injected into the long wavelength modes by the instability cascades to small wavelengths where the energy is dissipated [36, 37]. As a result of the nonlinear saturation, the size, the wavelength and the frequency of the fluctuating turbulence are determined. The typical size of the fluctuations is around 1% of the non-fluctuating background quantity. The nonlinear beating between two small fluctuating quantities results in the gyro-Bohm scale transport. For example, the radial E×B drift due to the fluctuating electrostatic potential beats with the temperature fluctuations to give non-zero radial transport of energy. The transport time and length scales are much longer than the turbulent fluctuation time period and wavelength, respectively.

In a low β tokamak (e.g. Alcator C-Mod), the turbulence that contributes most to the transport is electrostatic, driven by modes such as the ion temperature gradient driven mode (ITG) [38, 39] and the trapped electron mode (TEM) [40, 41]. For this reason, I only consider electrostatic turbulence modes. Here, β is the ratio of plasma pressure

to magnetic field pressure. Turbulence driven by ITG and TEM modes has relatively long radial correlation length, extending several ion Larmor radii (3-10ρ_i). Generally, turbulence with large radial correlation lengths contributes more to the radial transport than small scale turbulence. Based on this consideration, I do not treat small electron scale turbulence driven by the electron temperature gradient (ETG) [42, 43] in this thesis. ETG driven turbulence may be important for electron energy transport, but it is unlikely to produce much momentum transport, the main focus of this thesis, because ETG only drives electron transport and electrons do not carry much directed momentum compared to ions. The evaluation of the small wavelength turbulence is challenging in terms of computational resources and time. Also, I neglect electromagnetic modes which are important only in high β tokamaks (e.g. $\beta \gtrsim 1\%$) where the parallel Alfven wave dynamics may be more important than the ion sound wave dynamics [44, 45].

There has been remarkable progress in the understanding of ITG turbulence using linear [46, 47, 48] and nonlinear analysis [49, 50, 51, 52, 53]. From linear analysis, the ballooning structure in the parallel direction for a given perpendicular wavelength is obtained [46]. Streamers with long radial wavelengths have the largest growth [48]. In the nonlinear analysis, zonal modes obtain energy from the other linearly growing modes. Because zonal modes have negligible parallel variation, they are not Landau damped, and they can grow fast via nonlinear coupling with other modes. These zonal modes have short radial wavelengths and no poloidal variation, resulting in strongly sheared poloidal and toroidal E×B flow (zonal flow) [54, 55]. Zonal flow plays a role in the regulation of linearly growing modes because its velocity shear contributes to the turbulence decorrelation [56, 57, 58, 59]. The turbulence reaches a statistical equilibrium state in which zonal modes and other spectral modes interact nonlinearly exchanging energy. The resulting drift wave turbulence can be described by gyrokinetics [60, 61] and the equilibrium state can be obtained using nonlinear gyrokinetic codes [45, 52, 62].

The toroidal ion rotation considered in this thesis is also known to be important for turbulence [11, 12]. The perpendicular flow shear suppresses the linear instabilities, while a sufficiently large parallel flow shear can destabilize a parallel velocity gradient mode (PVG) [11, 63]. In experiments, flow shear can suppress turbulence and generate transport barriers [6, 13].

The turbulence determines the toroidal rotation profile because it causes radial transport

of toroidal angular momentum [64], which will be studied in Chapter 4. The self-consistent radial electric field for low flow (much slower than the ion thermal speed) is obtained by evaluating the radial transport of toroidal angular momentum using higher order gyrokinetics. Figure 1-2 shows the relations between turbulence and the ion toroidal rotation in the presence of the lower hybrid waves. In this thesis, I will evaluate each effect of lower hybrid waves on the toroidal rotation separately, because the effects can be described in separate time scales, as will be explained in Sec. 3.5.2 and Sec. 5.3.3. However, to predict the effect of the lower hybrid waves on the rotation in a given scenario, all the effects in the diagram need to be evaluated self-consistently.

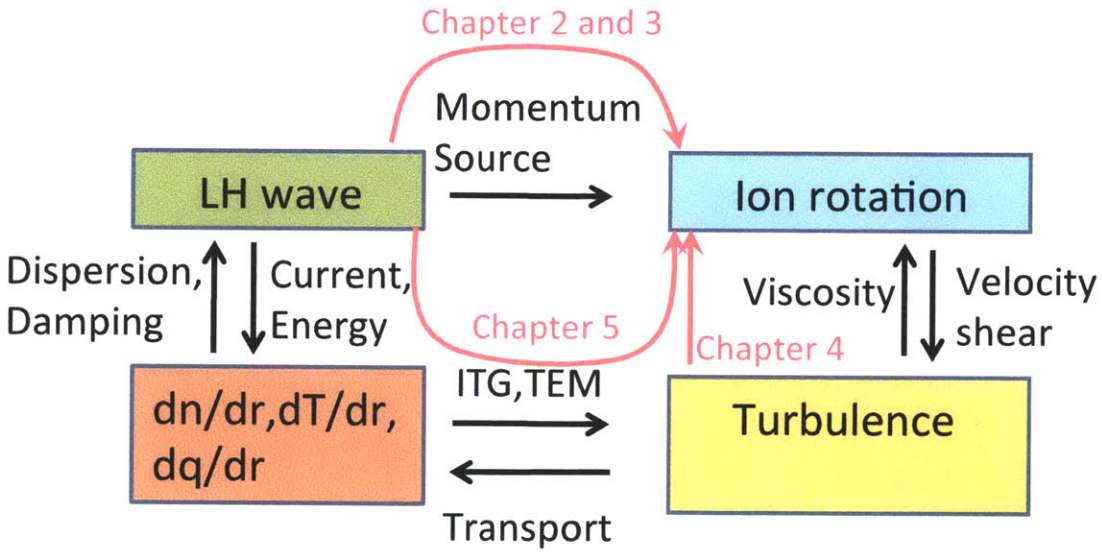

Figure 1-2: A diagram of the relations between lower hybrid waves, background plasma, turbulence, and ion toroidal rotation. The lower hybrid waves give momentum but also change the density, temperature, and safety factor profiles. The changed plasma profiles can modify the turbulence, and the turbulent radial transport of particles and temperature can change the plasma density and temperature profiles, modifying the lower hybrid wave propagation and damping. The turbulent transport of momentum can change the ion rotation profiles, and at the same time the new rotation profile can modify the turbulence through its velocity shear.

1.3 Measurements of rotation changes due to lower hybrid waves

Significant toroidal rotation changes due to the injection of LH waves have been observed in many tokamaks. In Alcator C-Mod, the toroidal rotation of the main ions is estimated by the Doppler shift of the line emission from impurities using a high resolution imaging X-ray crystal spectrometer. It is assumed that the rotation is the same for both the main ions and the impurities in the core [14].

For a discharge with high plasma current ($I_p \gtrsim 500kA$), the ion toroidal rotation in the core is accelerated in the counter-current direction right after the lower hybrid wave injection, and the acceleration is slowed down and almost saturated in $O(100)$ msec. After the lower hybrid wave is turned off, the ion rotation approximately returns to the state prior to the lower hybrid wave injection (see the red curve in Fig. 1-3). The change in the steady state rotation after the wave injection is in the counter-current direction, which is same direction as the wave momentum, and the size of the change is well correlated with the size of the internal inductance drop, which is a measure of the size of the lower hybrid wave power absorption off-axis (see Fig. 3 in [14]).

For a discharge with low plasma current ($I_p \lesssim 500kA$), the change in the steady state rotation after the wave injection is in the co-current direction, which is opposite to the wave momentum input [65, 66]. As shown in the blue curve in Fig. 1-3, the initial acceleration after lower hybrid injection is in the counter-current direction, but it changes direction to co-current at about 150 msec after the wave injection. Eventually, the rotation change is saturated in another several hundred milliseconds, and it is in the co-current direction.

This reversal of the rotation change due to lower hybrid waves shows strong correlation with the total plasma current (or the safety factor at the edge) and a relatively weaker correlation with the plasma density in Alcator C-Mod [66]. According to [66], a high safety factor at the edge and low plasma density are likely to give a co-current direction change. In other tokamaks (Tore Supra, JET, JT60U, and EAST), only co-current rotation changes due to the lower hybrid injection are found [66]. Although there is little data to verify the correlations, the co-current direction change in other tokamaks is consistent with the correlations in Alcator C-Mod, because it occurs when the plasma density is much below the density in Alcator C-Mod.

To explain the experimental observations of ion toroidal rotation change, the lower hybrid wave momentum source is evaluated in Chapter 2, the mechanisms to transfer momentum from the waves to ions are investigated in Chapter 3, and the radial turbulent transport of momentum is studied in Chapter 4. Theoretical estimates of the effect of lower hybrid waves on the change of the steady state rotation are compared with the measurements in Chapter 5. I selected two Alcator C-Mod discharges shown in Fig. 1-3, and I used the experimental parameters of these two discharges to evaluate the wave momentum input and the turbulent momentum flux. I will distinguish the two discharges by calling one of them "the high plasma current case" ($I_p = 700kA$) and the other "the low plasma current case" ($I_p = 350kA$) in this thesis.

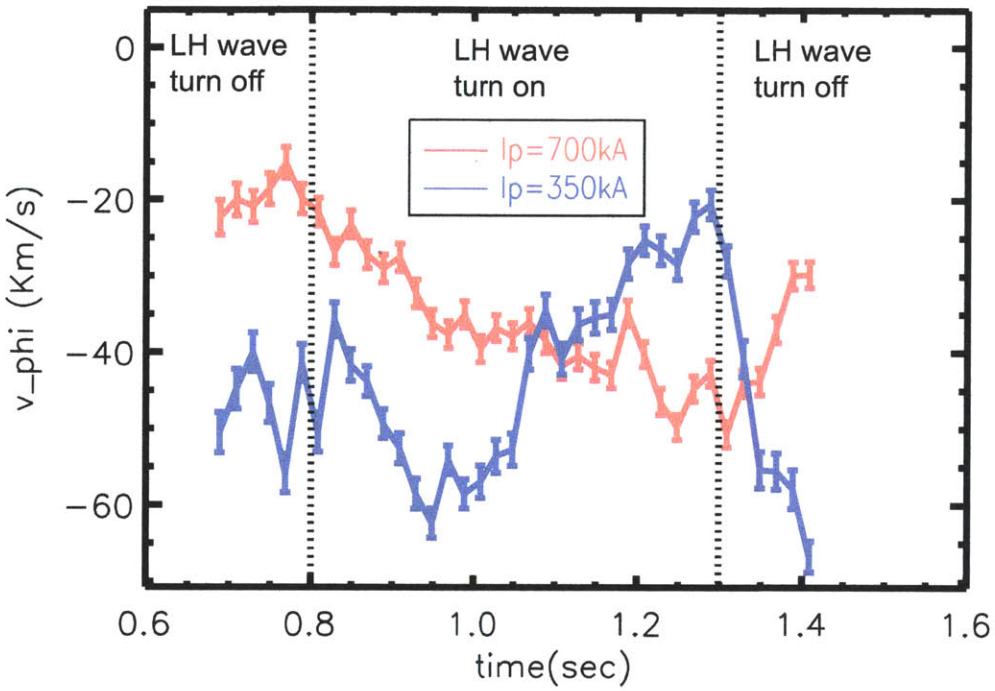

Figure 1-3: Time history of the ion toroidal rotation at the magnetic axis for two Alcator C-Mod discharges. Co-current direction rotation is positive in this graph, and counter-current direction is negative. The red curve is for the high plasma current case ($I_p = 700kA$) and the blue curve is for the low plasma current case ($I_p = 350kA$).

Chapter 2

Lower hybrid wave propagation and damping

The propagation path of lower hybrid waves in a tokamak is primarily determined by the wave dispersion due to the plasma, and the propagation length is determined by the wave damping due to the energy transfer to electrons. Lower hybrid waves transfer their energy and momentum by electron Landau damping (ELD) [20] that occurs when the phase velocity of the waves is same as the electron parallel velocity. To find the effect of the lower hybrid waves on the ion torodal rotation, it is necessary to evaluate the toroidal momentum transfer from the waves to electrons. In existing tokamaks, the resonant interaction between the waves and electrons is well described by quasilinear diffusion in velocity space.

In this chapter, I investigate the validity of the widely used Kennel-Engelmann (K-E) quasilinear diffusion operator [21] that assumes a constant magnetic field along the electron orbit. To understand the impact of generalizing this assumption to a tokamak where the magnitude of the magnetic field varies on a flux surface, I introduce a broad bandwidth wave spectrum which has been used in the past to validate the fast decorrelation process between resonances. Some acceptable errors are identified for the use of the K-E quasilinear diffusion operator [67].

Using the K-E quasilinear operator, the energy and parallel momentum transfer are evaluated in a full wave simulation with the self-consistent wave electric field and the self-consistent electron distribution function modification due to lower hybrid waves.

The rest of the chapter is organized as follows. In Sec. 2.1, the quasilinear diffusion

coefficient is evaluated including the broad-band wave effect. In Sec. 2.2, I explain the way to evaluate the energy transfer by iterating a full wave simulation code and a relativistic bounce averaged Fokker-Planck code together for self-consistency. In Sec. 2.3, I suggest two equivalent methods to find the parallel momentum transfer. Finally, an example of the evaluation of the energy and momentum transfer is given in the discussion in Sec. 2.4.

2.1 Validity of quasilinear velocity diffusion

The Kennel-Engelmann quasilinear diffusion operator is derived from kinetic theory with the zero-order particle trajectory having a constant velocity along the magnetic field [21]. The Kennel-Engelmann operator is widely used to evaluate electron Landau damping. Since the first experimental evidence of Landau damping [68], many researchers have investigated the validity of the quasilinear diffusion operator experimentally [69, 70, 71, 72] and theoretically [73, 74, 75, 76, 77, 78]. Recently, the statistical analysis of wave-particle interactions using a finite number of particles was introduced to describe more realistic diffusion coefficients including mode coupling of different waves and nonlinear effects [79, 80, 81].

The coefficient for the one-dimensional quasilinear diffusion operator that models electron Landau damping can be simply given by

$$D_k = \left\langle \frac{\Delta v \Delta v}{2\Delta t} \right\rangle_t = \frac{\pi e^2 E_k^2}{2m_e^2} \delta(kv - \omega), \tag{2.1}$$

where v, m_e, e are the velocity, mass, and charge of an electron, respectively, ω is the wave frequency, k is the wave vector, E_k is the intensity of the wave, $\langle ... \rangle_t$ is the time average and δ is the Dirac-delta function. The original quasilinear diffusion coefficient in Eq. (2.1) was obtained under the assumption of constant zero order velocity.

However, if the perturbation of the velocity due to the wave is considered, a resonant particle in a wave spectral mode is trapped in a potential well rather than diffused in phase space [73]. The trapping width in velocity space is $\Delta v_{trap} = \sqrt{\frac{eE_k}{m_e k}}$ (see Fig. 2 in [73]).

Diffusion in velocity space requires decorrelation between the phase of the wave and the perturbation of the particle velocity. For collisionless particles, multiple spectral modes of the wave can give sufficient decorrelation. The spectral interval in k-space within the wave packet (dk) determines the interval of resonances in velocity space ($\Delta v_{dk} = \omega/k - \omega/(k +$

$dk) \simeq (\omega/k)(dk/k))$. If the spacing of the resonances is smaller than the trapping width in velocity space, the resonances overlap and the particle can be diffused. This is the first condition for validity of the quasilinear diffusion coefficient [74],

$$\Delta v_{dk} < \Delta v_{trap} \tag{2.2}$$

This condition determines a lower limit of the electric field intensity in a given spectrum for quasilinear diffusion, which corresponds to the Chirikov threshold in the standard mapping for random kicks [74, 76, 82] (see Fig. 2 in [76] and Fig. 9 in [82]). This condition was also investigated in several experiments [71, 72].

The typical electric field intensity of lower hybrid waves in front of the launcher (about $10 - 100\,[\mathrm{kV/m}]$) satisfies the quasilinear diffusion condition. It is far beyond the Chirikov threshold [74] given in Eq. (2.2), but it is still below the nonlinear limit. The nonlinearity of the diffusion due to the strong electric field was studied theoretically [75, 77, 78, 83], and it was also investigated in an experiment [70], in which the saturation of wave growth was measured. I can assume that the lower hybrid waves in a tokamak are in the quasilinear regime due to their moderate electric field intensity.

To find additional errors due to the toroidal geometry, I consider the effect of the variation of the parallel velocity on the perturbed orbit integration carried out in the kinetic theory with a broad-band wave. That is, in a tokamak which has a helical static magnetic field that varies in magnitude with major radius, the electron velocity parallel to the magnetic field changes to conserve the magnetic moment. I reconsider the quasilinear theory in a tokamak with velocity perturbation, not only from the electric field but also from the extra force, $-\mu\nabla B_0$, where μ is the magnetic moment and ∇B_0 is the gradient of the static magnetic field [17, 84, 85]. In this section, I demonstrate that the broad-band spectrum of the wave makes the quasilinear theory valid even for tokamak geometry by proper decorrelation processes.

The modified diffusion operator taking into account the velocity perturbation in a tokamak was given by T.H. Stix in [17] in the form of a phase integral. He also demonstrated that in the presence of an effective collision frequency the phase integral recovers a similar result to the original Kennel-Engelmann quasilinear diffusion coefficient in [21]. However, for a high phase velocity wave such as lower hybrid wave in a high temperature tokamak,

the electron collision frequency is about 10^5 [s^{-1}], which is much smaller than the electron bounce frequency, about 10^7 [s^{-1}]. Thus, collisions are not intense enough to satisfy the decorrelation condition for quasilinear diffusion. In this case, a plausible decorrelation mechanism in a tokamak is the interaction between multiple spectral modes of the electric field with similar magnitudes, which I call the broad-band wave effect.

I have concluded that the bounce averaged diffusion operator in (2.24) is equal to the standard bounce averaged quasi-linear diffusion coefficient in (2.11) within acceptable errors [67]. There is an error due to the imperfect decorrelation of the phase in the current orbit period with the previous orbit history [76, 82]. I found that there is another error due to the correlation between the different resonances in an orbit period, and it is found to be small after averaging. Considering the enormous resources and effort required to calculate all phase integrals for the exact diffusion coefficient, the errors considered in this section are likely to be sufficiently small so as to justify use of the standard bounce averaged quasi-linear diffusion coefficient which is currently used in many numerical codes.

The analysis of the broad-band effect is carried out in the following subsections. In subsection 2.1.1, the physical mechanism of the broad-band spectrum giving the decorrelation between temporal periodic kicks is explained. In subsection 2.1.2, the typical bounce-averaged quasilinear diffusion operator with constant zero order velocity is reviewed, and in subsection 2.1.3 the perturbed velocity due to the tokamak geometry is considered to correct the bounce-averaged quasilinear diffusion operator, and the decorrelation due to the broad-band wave is applied to the correction to find the errors made by assuming the Kennel-Engelmann quasilinear diffusion operator.

2.1.1 Broad-band wave effect

In this subsection, the broad-band wave effect on quasilinear diffusion is explained with a simple picture. When the electron Larmor radius is much smaller than the perpendicular wavelength, the quasilinear diffusion is associated almost entirely with the parallel wavenumber, which is obtained by a combination of toroidal and poloidal spectral modes. The interval between the parallel spectral modes of a wave ($dk_\parallel$) is determined by the periodicity in the toroidal direction ($2\pi R$) and the poloidal direction (about $2\pi r$), where R and r are the major and minor radii of the tokamak, respectively.

When a large enough number of spectral modes exists, the acceleration of a resonant electron can be described as a linear summation of the modes as represented in Eq. (2.3),

$$\lim_{s\to\infty}\sum_{j=-s}^{j=s}\int_0^t dt'\, e^{i(\omega-(k_\parallel+jdk_\parallel)v_\parallel)t'} = \lim_{s\to\infty}\sum_{j=-s}^{j=s} N\int_0^{t_p} dt'\, e^{-ijdk_\parallel v_\parallel t'}, \tag{2.3}$$

where the resonance condition $\omega - k_\parallel v_\parallel = 0$ is used. Here, $v_\parallel$ is the parallel velocity, $k_\parallel$ is the central parallel wave vector in the wave packet, and $dk_\parallel$ is the interval between two contiguous parallel wavevectors. A time period is defined as $t_p = \frac{2\pi}{dk_\parallel v_\parallel}$, and $N = t/t_p$ is the number of t_p in the interval t. There are $2s+1$ number of wavevectors, from $(k_\parallel - sdk_\parallel)$ to $(k_\parallel + sdk_\parallel)$, in the bandwidth of the wave, and the broad-band assumption means a large number of wavevectors with similar intensity.

In a typical resonance model used for quasilinear diffusion, only the spectral modes with phase velocity exactly equal to the electron parallel velocity contribute to the integral, whereas the contribution of other modes is temporally averaged out. It can be interpreted as a spectral Dirac delta function for many spectral modes. That is, Eq. (2.3) becomes

$$\lim_{s\to\infty}\sum_{j=-s}^{j=s} N\int_0^{t_p} dt'\, e^{-ijdk_\parallel v_\parallel t'} = \sum_{j=-\infty}^{j=\infty} Nt_p\delta_{j0}, \tag{2.4}$$

where δ_{ij} stands for the Kronecker delta. This corresponds to the resonance by fast decorrelation with an unperturbed velocity.

Alternatively, if the spectral mode summation is done before the time integral, it results in temporal periodic kicks due to the phase mixing between the different spectral modes described in Eq. (2.5), that is, Eq. (2.3) for many spectral modes becomes

$$\begin{aligned}
&\int_0^t dt' \lim_{s\to\infty}\sum_{j=-s}^{j=s} e^{-ijdk_\parallel v_\parallel t'} = \int_0^t dt' \lim_{s\to\infty}\frac{e^{isdk_\parallel v_\parallel t'} - e^{-isdk_\parallel v_\parallel t'}}{e^{idk_\parallel v_\parallel t'} - 1} \\
= &\int_0^t dt' \lim_{s\to\infty}\frac{\sin((2s+1)(dk_\parallel v_\parallel t'/2))}{\sin(dk_\parallel v_\parallel t'/2)} = \int_0^t dt' \sum_{n=-\infty}^{\infty} 2\pi\delta\left(dk_\parallel v_\parallel t' + 2\pi n\right) \\
= &\int_0^t dt' \sum_{n=-\infty}^{\infty} t_p\delta\left(t' - nt_p\right) = Nt_p,
\end{aligned} \tag{2.5}$$

where $\delta(t)$ is the Dirac delta function and $\lim_{s\to\infty}\frac{\sin((2s+1)(x/2)}{2\pi\sin(x/2)} = \sum_j \delta(x+2\pi j)$ is used. These two pictures of a spectral delta function in Eq. (2.4) and a temporal delta function in

Eq. (2.5) are equivalent and integrate to the same value. Fig. 2-1 shows the equivalence of these two pictures by phase diagrams. The summation along the time coordinate (vertical) gives a spectral delta function, and the summation along the spectral coordinate (horizontal) gives a temporal delta function. The final result is the same independent of the integral that is taken first.

Using the temporal kick interpretation of the broad-band wave has several significant benefits for the validation of the quasilinear diffusion. First, the velocity does not need to be updated during the very short kicks provided that the electric field is not too strong. Also, for a broad-band wave, the unperturbed velocity need not decorrelate fast during the whole time period, because the velocity evolution becomes diffusive due to overlap between the different resonant modes in the broad band spectrum, if the electric field intensity is beyond the Chirikov threshold [74].

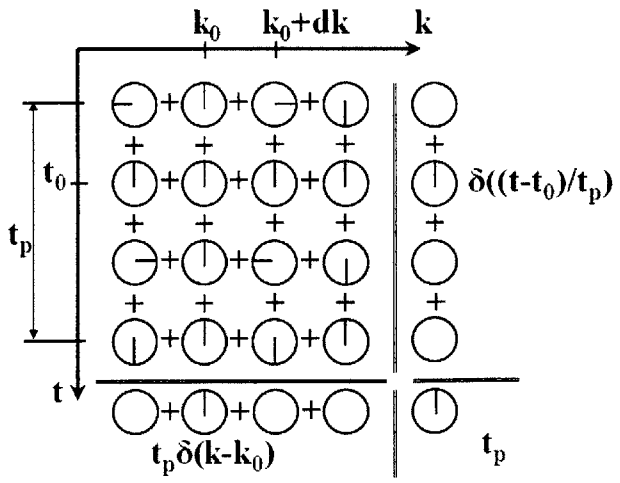

Figure 2-1: A diagram in time-spectral space showing the equivalence of the diffusion by a single spectral mode with a temporally constant kick, and by a broad-band spectral model with temporal periodic kicks. The bars in the circles indicate the phase direction of the acceleration terms in Eq. (2.3), and t_p is the time period of the kicks in Eq. (2.5). The circle outside the double lines is the result of summing a sinusoidal function having the phases in a row or a column inside the double lines. Notice the total acceleration by the summation in time and spectral space is the same, even though the representations of the delta functions are different. No bar in the circle stands for the summation over the sinusoidal functions being equal to zero.

2.1.2 Bounce averaged quasilinear diffusion in a tokamak

The Fokker-Planck equation for a given species is

$$\frac{\partial f_s}{\partial t} + \mathbf{v} \cdot \nabla f_s + \frac{Z_s e}{m_s} \left(\mathbf{E} + \frac{\mathbf{v} \times \mathbf{B}}{c} \right) \cdot \nabla_v f_s = C(f_s), \tag{2.6}$$

where $f_s(\mathbf{r}, \mathbf{v}, t)$ is the distribution function, $Z_s e$ and m_s are the charge and mass of the species, and $\mathbf{E}$ and $\mathbf{B}$ are the electric and magnetic field, respectively. Here C is the Fokker-Planck collision operator. For magnetized plasmas with a strong static magnetic field, the lowest order distribution function does not depend on the gyrophase angle because of the fast gyration. For the lower hybrid wave that has a resonant interaction with electrons, the Fokker-Planck equation for electrons to lowest order is

$$\frac{\partial f_{0,e}}{\partial t} + v_{\parallel} \hat{\mathbf{b}} \cdot \nabla f_{0,e} = \langle C(f_{0,e}) \rangle + \langle Q(f_{0,e}) \rangle, \tag{2.7}$$

where $f_{0,e}(\mathcal{E}, \mu, \psi, \theta, t)$ is the lowest order electron distribution function in terms of the kinetic energy $\mathcal{E} = \frac{v^2}{2}$ and the magnetic moment $\mu = \frac{v_\perp^2}{2B}$, $v_\perp$ is the perpendicular velocity and B is the magnitude of the magnetic field. The magnetic drift for electrons is small, so it is neglected in Eq. (2.7). Here, $\langle ... \rangle = \int_0^{2\pi} d\alpha / 2\pi (...)$ is the gyroaverage, α is the gyrophase, $\hat{\mathbf{b}}$ is the unit vector for the magnetic field, θ is the poloidal angle, and ψ is the poloidal magnetic flux and works as radial coordinate in tokamaks. In Eq. (2.7), a toroidal average is used to eliminate the toroidal dependence of $f_{0,e}$. The effect of the lower hybrid wave on the background electrons is expressed by the quasilinear operator, $Q(f_s) = -\frac{Z_s e}{m_s} \left\langle \nabla_v \cdot \left[\left(\mathbf{E} + \frac{\mathbf{v} \times \mathbf{B}}{c} \right) f_s \right] \right\rangle_W$, where $\langle ... \rangle_W$ indicates the average over a number of wave periods in time and space (see Appendix A for the derivation of $Q(f_{0,e})$). The standard K-E quasilinear diffusion operator is derived in Appendix A, but the bounce averaged quasilinear diffusion operator is described in this subsection for the tokamak geometry.

The static magnetic field (the equilibrium magnetic field) in a tokamak is defined as $\mathbf{B} = I \nabla \varphi + \nabla \varphi \times \nabla \psi$, where φ is the toroidal angle, $\hat{\varphi}$ is the unit vector in the toroidal direction, R is the major radius and $\nabla \varphi = \hat{\varphi} / R$. The toroidal magnetic field $B_\varphi = I/R$ is determined by a function $I(\psi)$ that is only a function of the poloidal magnetic flux to the lowest order.

Taking the bounce average of Eq. (2.7) eliminates the parallel streaming term on the

left hand side, resulting in

$$\frac{\partial f_{0,e}}{\partial t} = \frac{1}{\tau_b}\oint \frac{d\ell}{v_\parallel}[\langle C(f_{0,e})\rangle + \langle Q(f_{0,e})\rangle] = \langle\langle C(f_{0,e})\rangle\rangle_b + \langle\langle Q(f_{0,e})\rangle\rangle_b. \tag{2.8}$$

Here, $\langle ...\rangle_b = \frac{1}{\tau_b}\oint \frac{d\ell(...)}{v_\parallel(\mathcal{E},\mu,\ell)}$ is the bounce average along the orbit distance ℓ, and $\tau_b(\mathcal{E},\mu) = \oint \frac{d\ell}{v_\parallel(\mathcal{E},\mu,\ell)}$ is the bounce time. Here, $f_{0,e}$ does not depend on θ to lowest order because we assume that $v_\parallel \hat{\mathbf{b}}\cdot\nabla f_{0,e}$ is much larger than $\langle C(f_{0,e})\rangle$ and $\langle Q(f_{0,e})\rangle$. Since the bounce averaged integral $\oint \frac{d\ell}{v_\parallel}$ can be also described in terms of poloidal angle as $\oint \frac{d\theta}{v_\parallel \hat{\mathbf{b}}\cdot\nabla\theta}$, the bounce averaged quasilinear operator [17, 86] is

$$\begin{aligned}\langle\langle Q(f_{0,e})\rangle\rangle_b &= \left[\frac{\partial}{\partial\mathcal{E}}\left(\langle\mathcal{D}_{\mathcal{E},\mathcal{E}}\rangle_b\frac{\partial f_{0,e}}{\partial\mathcal{E}} + \langle\mathcal{D}_{\mathcal{E},\mu}\rangle_b\frac{\partial f_{0,e}}{\partial\mu}\right)\right. \\ &\left. + \frac{\partial}{\partial\mu}\left(\langle\mathcal{D}_{\mu,\mathcal{E}}\rangle_b\frac{\partial f_{0,e}}{\partial\mathcal{E}} + \langle\mathcal{D}_{\mu,\mu}\rangle_b\frac{\partial f_{0,e}}{\partial\mu}\right)\right].\end{aligned} \tag{2.9}$$

Using the poloidal mode number m, the toroidal mode number n, and the frequency ω of the wave, the parallel component of the wave electric field is $E_\parallel = \sum_{(m,n)} E_\parallel^{(m,n)} e^{i(m\theta+n\varphi-\omega t)}$. The phase of the oscillation along the static magnetic field is approximately obtained by $m\theta + n\varphi \simeq (m+qn)\theta + n\varphi_0$ where q is the safety factor, and φ_0 is the toroidal position of the magnetic field at a poloidal angle. For simplicity, I use the phase $(m+qn)\theta + n\varphi_0$ in this section, which corresponds to the phase using straight line coordinates with $\frac{\mathbf{B}\cdot\nabla\varphi}{\mathbf{B}\cdot\nabla\theta} = q$. Then, the averaged diffusion coefficient for the case of electron Landau damping is

$$\begin{aligned}\langle\mathcal{D}_{\mathcal{E},\mathcal{E}}\rangle_b &= \frac{e^2}{2m_e^2}\frac{1}{2\pi}\frac{1}{\tau_b}\int_0^{2\pi} d\varphi_0 \oint \frac{d\theta}{v_\parallel\hat{\mathbf{b}}\cdot\nabla\theta}\mathrm{Re}\left[\left\langle \mathbf{v}\cdot\mathbf{E}^*(\mathbf{r})\int_{-\infty}^{t} dt' e^{i\omega(t-t')}\mathbf{v}'\cdot\mathbf{E}(\mathbf{r}')\right\rangle\right] \\ &\simeq \frac{e^2}{2m_e^2}\frac{1}{\tau_b}\mathrm{Re}\left[\sum_{(n_1,m_1),(n_2,m_2)}\frac{1}{2\pi}\int_0^{2\pi} d\varphi_0 e^{i(n_2-n_1)\varphi_0}\right. \\ &\times \oint \frac{d\theta}{v_\parallel\hat{\mathbf{b}}\cdot\nabla\theta} e^{i((m_2+qn_2)-(m_1+qn_1))\theta}\left(v_\parallel J_0\left(\frac{k_{1\perp}v_\perp}{\Omega_e}\right)E_\parallel^{m_1,n_1}\right)^* \\ &\left.\times \int_{-\infty}^{t} dt' e^{i((m_2+qn_2)(\theta'-\theta)-\omega(t'-t))}\left(v'_\parallel J_0\left(\frac{k_{2\perp}v'_\perp}{\Omega_e}\right)E_\parallel^{m_2,n_2}\right)\right],\end{aligned} \tag{2.10}$$

where $(t',\mathbf{r}',\mathbf{v}')$ is a point of phase space along the particle trajectory, whose end point corresponds to $(t,\mathbf{r},\mathbf{v})$. Here, $\mathcal{D}_{\mathcal{E},\mathcal{E}}$ is averaged over the toroidal angle φ_0, and J_0 is the zero order Bessel function of the first kind with argument $k_\perp v_\perp/\Omega_e$, with perpendicular wave vector $k_\perp$, perpendicular velocity $v_\perp$ and electron gyrofrequency Ω_e. Expressions similar to

Eq. (2.10) are found for $\langle \mathcal{D}_{\mathcal{E},\mu} \rangle_b$, $\langle \mathcal{D}_{\mu,\mathcal{E}} \rangle_b$ and $\langle \mathcal{D}_{\mu,\mu} \rangle_b$ in [86].

If a particle is assumed to move with constant parallel velocity (unperturbed velocity), the resonance condition is obtained by $\int_{-\infty}^{t} e^{i((m_2+qn_2)(\theta'-\theta)-\omega(t'-t))}dt' = \pi\delta(k_\parallel v_\parallel - \omega)$. Using no coupling between the different toroidal modes, $\int_0^{2\pi} d\varphi_0 e^{i(n_2-n_1)\varphi_0} = 2\pi\delta_{0,n_2-n_1}$, then the quasilinear diffusion coefficient [86] can be summarized as

$$\begin{aligned} \langle \mathcal{D}_{\mathcal{E},\mathcal{E}} \rangle_b &= \frac{\pi e^2}{2m_e^2}\frac{1}{\tau_b} Re\Big[\sum_{n_1=n_2} \sum_{(m_1,m_2)} \oint \frac{d\ell}{v_\parallel} W(\mathcal{E},\mu,\ell)\delta(\omega - k_\parallel v_\parallel(\ell)) \Big] \\ &= \frac{\pi e^2}{2m_e^2}\frac{1}{\tau_b} Re\Big[\sum_{n_1=n_2} \sum_{(m_1,m_2)} \sum_{resonance} \frac{W(\mathcal{E},\mu,\ell_r)}{|v_\parallel^2(\ell_r)\kappa'(\ell_r))|} \Big], \end{aligned} \tag{2.11}$$

where $\kappa' = \frac{\partial\kappa(\ell)}{\partial\ell}$, $\kappa(\ell) = \frac{\omega - k_\parallel(\ell)v_\parallel}{v_\parallel}$, and the resonance occurs at $\ell = \ell_r$. Here, electric fields at the resonances are included in

$$W(\mathcal{E},\mu,\ell) = e^{i((m_2+qn_2)-(m_1+qn_1))\theta} \left(v_\parallel J_0 \left(\frac{k_{1\perp}v_\perp}{\Omega_e} \right) E_\parallel^{m_1,n_1} \right)^* \left(v_\parallel J_0 \left(\frac{k_{2\perp}v_\perp}{\Omega_e} \right) E_\parallel^{m_2,n_2} \right). \tag{2.12}$$

Eq. (2.11) counts all resonances for both passing and trapped particles except the resonances at the tips of banana orbit that are not important for Landau damping due to almost zero parallel velocity. The parallel wave vector is given by

$$k_\parallel^{m_2,n_2}(\ell) = m_2(\hat{\mathbf{b}}\cdot\nabla\theta) + n_2(\hat{\mathbf{b}}\cdot\nabla\varphi). \tag{2.13}$$

At the resonance, $k_\parallel^{m_2,n_2}(\ell_r) = \frac{\omega}{v_\parallel}$. In Sec. 2.1.3, the standard quasilinear diffusion coefficient in Eq. (2.11) is modified to allow the parallel velocity to change along the particle orbit.

2.1.3 Modified diffusion in phase space with a broad-band wave

To take into consideration the parallel velocity perturbation, I need to reconsider the evaluation of the phase integral in Eq. (2.10). The bounce averaged quasilinear diffusion coefficient in Eq. (2.10) is rewritten as

$$\langle \mathcal{D}_{\mathcal{E},\mathcal{E}} \rangle_b = \frac{e^2}{2m_e^2} \langle I(\mathcal{E},\mu,\ell) \rangle_b = \frac{e^2}{2m_e^2} \frac{1}{\tau_b} \int_0^L \frac{d\ell}{v_\parallel(\ell)} I(\mathcal{E},\mu,\ell), \tag{2.14}$$

where L is a distance for a poloidal bounce orbit. Here, I follow the notation in [17]. The function $I(\mathcal{E},\mu,\ell)$ that includes the phase history in a broad-band wave is

$$\begin{aligned} I(\mathcal{E},\mu,\ell) &= \sum_n \int_0^\infty d\tau \sum_{m=-s}^{m=s} W(\mathcal{E},\mu,\ell(\tau)) e^{i\int_0^\tau d\tau'(\omega-(k_\parallel+mdk_\parallel)v_\parallel)} \\ &= -\sum_n \int_\ell^{\ell(\tau=\infty)} \frac{d\ell'}{v_\parallel} \sum_{m=-s}^{m=s} W(\mathcal{E},\mu,\ell') e^{-i\chi(\ell,\ell')} e^{imdk_\parallel(\ell'-\ell)}, \end{aligned} \tag{2.15}$$

where $\frac{d\ell'}{d\tau} = -v_\parallel$. The range of the double integral in Eq. (2.14) in terms of ℓ for the bounce averaging and ℓ' for the phase memory is depicted in Fig. 18-1 in [17]. In this section, I assume broad-band spectra only in the poloidal modes, resulting in $2s+1$ spectral modes in the range $-s \le m \le s$ in Eq. (2.15) and $dk_\parallel = \hat{\mathbf{b}} \cdot \nabla\theta$ in Eq. (2.13). Other possibilities, such as the wave having broad-band spectra in toroidal mode number, are explained in [67]. Note that I have used the approximation of $\int_\ell^{\ell'} d\ell'' dk_\parallel(\ell'') \simeq dk_\parallel(\ell'-\ell)$ in Eq. (2.15) to simplify the derivation. It is trivial to use the more accurate expression with the integral $\int_\ell^{\ell'} d\ell'' dk_\parallel(\ell'')$ once the derivation is done. The phase in Eq. (2.15) is

$$\chi(\ell,\ell') = \int_\ell^{\ell'} \frac{d\ell''}{v_\parallel(\ell'')} [\omega - k_\parallel(\ell'') v_\parallel(\ell'')]. \tag{2.16}$$

Because the phase around the resonance location contributes significantly to the diffusion coefficient, the phase is expanded in terms of ℓ' around the resonance at $\ell' = \ell_r$ by a Taylor series up to the second order. The first order term in the series vanishes (i.e. $\frac{\partial\chi}{\partial\ell'}|_{\ell'=\ell_r} = \kappa(\ell_r) = \frac{\omega - k_\parallel(\ell_r)v_\parallel(\ell_r)}{v_\parallel(\ell_r)} = 0$), giving

$$e^{i\chi(\ell,\ell')} \simeq \sum_r e^{i\chi(\ell,\ell_r)} e^{-i\frac{\kappa'}{2}(\ell'-\ell_r)^2}, \tag{2.17}$$

where r is the index for all possible resonances.

Eq. (2.15) can be divided into a summation of integrals in which each integral is only over one period,

$$I(\mathcal{E},\mu,\ell) = -\sum_n \Big\{ \int_\ell^{\ell-L} d\ell' \sum_{r_{T1}} I_{n,1}(\ell,\ell',\ell_{r_{T1}}) + \int_{\ell-L}^{\ell-2L} d\ell' \sum_{r_{T2}} I_{n,2}(\ell,\ell',\ell_{r_{T2}}) + ... \Big\}, \tag{2.18}$$

where r_{Ti} is used to label the resonances only in the i^{th} period, $\ell - iL < \ell' \leq \ell - (i-1)L$. The integrand in the i^{th} period of Eq. (2.18) is approximately

$$I_{n,i} \simeq \frac{1}{v_\parallel(\ell_{r_{Ti}})} e^{-i\chi(\ell,\ell_{r_{Ti}})} \langle W(\mathcal{E},\mu,\ell_{r_{Ti}})\rangle_m e^{-i\frac{\kappa'}{2}(\ell'-\ell_{r_{Ti}})^2} \times \frac{\sin[(s+1/2)dk_\parallel(\ell'-\ell)]}{\sin[dk_\parallel/2(\ell'-\ell)]}, \tag{2.19}$$

where the phase is expanded around each resonance using Eq. (2.17), and $\langle W(\mathcal{E},\mu,\ell_{r_{Ti}}))\rangle_m$ is averaged over the poloidal modes at the resonance.

To obtain Eq. (2.19), the variation in $v_\parallel(\ell)$ is assumed to be usually much smaller than the variance in $e^{-i\chi(\ell,\ell')}$ around the resonance. This assumption implies that the change of $v_\parallel(\ell)$ by the external force, $-\mu\nabla B_0$, is not explicitly shown in the integral. The summation in the poloidal modes gives the sinusoidal term in Eq. (2.19) which plays the role of periodic kicks for large s (because $\lim_{s\to\infty} \frac{\sin((2s+1)(x/2)}{2\pi\sin(x/2)} = \sum_j \delta(x+2\pi j)$).

The integrand $I_{n,i}$ in Eq (2.19) with many poloidal modes (large s) is approximately

$$I_{n,i} \simeq \sum_j \frac{2\pi}{v_\parallel(\ell_{r_{Ti}})} e^{-i\chi(\ell,\ell_{r_{Ti}})} \langle W(\mathcal{E},\mu,\ell_{r_{Ti}})\rangle_m e^{-i\frac{\kappa'}{2}(\ell'-\ell_{r_{Ti}})^2} \times \delta(\ell'-\ell+L_{\rm k}j), \tag{2.20}$$

where $L_{\rm k} = 2\pi/dk_\parallel$ is the distance between the periodic kicks due to the broad-band wave.

If the spectrum is broad-band in both poloidal and toroidal mode number, which results in $L_{\rm k} > L$, the kick due to the resonance r_{Ti} cannot happen in every poloidal orbit. In this case, the condition for the non-zero value of the periodic Dirac-delta function in Eq. (2.20), $\ell' - \ell + L_{\rm k}j = 0$, will not generally coincide with the conditions for the resonance, $\ell' = \ell_{r_{Ti}}$ and $\ell = \ell_{r_{Ti}} + (i-1)L$. Thus, the consecutive resonances at the same poloidal location are

separated by a long distance which is the least common multiple of $L_{\rm k}$ and L, resulting in a negligible correlation between the resonances if this long distance is comparable to or longer than the collisional mean-free path. The decorrelation between resonances in the different orbit periods makes the contribution of the phase memory from the previous orbits small, resulting in

$$I(\mathcal{E},\mu,\ell) \simeq -\int_{\ell}^{\ell-L} d\ell' \sum_{n}\sum_{r_{T1}} I_{n,1}. \tag{2.21}$$

Taking the bounce average of $I(\mathcal{E},\mu,\ell)$ in Eq. (2.14) using Eq. (2.21), the diffusion coefficient is approximately the same as the original one with unperturbed velocity in Eq. (2.11) (see Appendix C for the derivation)

However, for the wave whose spectrum is broad-band only in poloidal mode number, both $L_{\rm k}$ and L are the length of a poloidal orbit. If $L_{\rm k}$ is the same as L, the resonances at the same poloidal location happen in every poloidal orbit. In this case, the periodic Dirac-delta function in Eq. (2.20) for every $i^{\rm th}$ period is the same due to the same periodicity, giving the relation of the integrands between two consecutive periods

$$I_{n,i+1} \simeq e^{-i\chi_0} I_{n,i}, \tag{2.22}$$

where $\chi_0 = \chi(\ell_{r_{Ti}}, \ell_{r_{Ti}} - L)$ is the constant phase change between the two periods. Here, $\langle W(\mathcal{E},\mu,\ell')\rangle_m$ and $v_{\parallel}(\ell')$ are assumed to be periodic and the resonances in different periods happen in the same poloidal locations. Using Eq. (2.22), the summation of the integral $I(\mathcal{E},\mu,\ell)$ in Eq. (2.18) is

$$I(\mathcal{E},\mu,\ell) \simeq -\frac{1}{1-e^{-i\chi_0}} \sum_{n} \left\{ \int_{\ell}^{\ell-L} d\ell' \sum_{r_{T1}} I_{n,1} \right\}. \tag{2.23}$$

It is possible to neglect the factor $1/(1-e^{-i\chi_0})$ in Eq. (2.23) if the particles decorrelate after a few kicks due to the broad-band effect. However, it is known that the decorrelation due to broad-band waves is not perfect [76, 82]. For the electric field range of our interest, the actual diffusion coefficient of a single particle is generally more or less 10 percent larger than the quasilinear diffusion coefficient from mode coupling. The reason is the correlation between the current velocity change and that of he two prior periods.

Another possible error comes from the correlation between the different resonances in a

period. Taking the bounce average of $I(\mathcal{E},\mu,\ell)$ in Eq. (2.14) results in

$$\langle I(\mathcal{E},\mu,\ell)\rangle_b = \frac{1}{\tau_b}\sum_n \left\{ \sum_{r_1=r_2} \frac{\pi\langle W(\mathcal{E},\mu,\ell_{r_2})\rangle_m}{|v_\parallel^2(\ell_{r_2})\kappa'(\ell_{r_2})|}(2s+1) + \sum_{r_1\neq r_2} H_n(\ell_{r_1},\ell_{r_2}) \right\}, \qquad (2.24)$$

where ℓ_{r_1} and ℓ_{r_2} are the resonance positions in the ℓ and ℓ' integral paths respectively, and $H_n(\ell_{r_1},\ell_{r_2})$ is the additional contribution to the diffusion coefficient from phase correlation between different resonances in a period, as derived in Appendix C.

For example, consider a passing particle that has an outer mid-plane parallel velocity $v_{\parallel 0} = 1.12\times 10^8 m/s$ and perpendicular velocity $v_{\perp 0} = 10^8 m/s$ on the $q = 2.001$ flux surface in a tokamak with major radius $R = 0.6$ and minor radius $r = 0.2$, and a wave with a peak poloidal wavenumber of $m_0 = 30$ in a broad-band and ten toroidal wave modes in a narrow-band $n = 26 - 35$. In this case, the second term in Eq. (2.24) is 7.7% of the first term. Even for trapped electrons, the real part of $H_n(\ell_{r_1},\ell_{r_2})$ still averages to a small value. Consequently, I conclude that the phase integral of the diffusion coefficient due to a broad-band wave in Eq. (2.24) reduces to the original value Eq. (2.11), because $(2s+1)$ times the average value of $\langle W(\mathcal{E},\mu,\ell_{r_2})\rangle_m$ gives the original summation over the poloidal mode number m.

The factor, $(2s+1)$ in Eq. (2.24) which is the number of poloidal modes, can be understood as "a kick on a kick" (or "the square of the Dirac delta function"), where the first kick represents the resonance for electron Landau damping in the phase integral, and the second kick corresponds to the periodic random kick due to the broad-band wave. The diffusion coefficient in Eq. (2.24) is approximately the same as the original one with unperturbed velocity in Eq. (2.11). One can think of the two different derivations of the quasilinear diffusion coefficient as being the two different representations shown in Fig. 2-1. I will use the Kennel-Engelmann quasilinear diffusion coefficient to describe the damping of the lower hybrid wave energy in Sec. 2.2, because the waves have a broad-band spectrum that gives the sufficient decorrelation for quasilinear diffusion.

2.2 Wave power transfer to electrons

The propagation path of the lower hybrid waves has been evaluated by geometric optics because the wavelength of the wave over most of the tokamak radius is small enough to satisfy the assumption of the Wentzel-Kramers-Brillouin (WKB) expansions [18, 29]. The ray-tracing technique is based on geometric optics and gives the spatial change of the wave vector of the ray that is defined as the vector normal to the constant phase surface of the wave. The group velocity and the phase velocity of the ray are determined by the local dispersion relation of the wave and a fixed wave frequency. The simplified dispersion relation for an electrostatic slow mode is given in Eq. (1.1).

However, in the case of a lower hybrid wave that is weakly damped and reflects from the low density cutoff boundary at the plasma edge, the wavelength is comparable to the characteristic scale length of the plasma parameters, and the WKB expansion is not applicable (see Fig. 2-2). To describe the diffraction and focusing of the wave in the caustic, full wave solvers in the lower hybrid frequency range have been used [24, 25, 87, 88]. I have compared a full wave code (TORLH) [24] with a ray-tracying code (GENRAY) [29]. Their results agree well for the strongly damped waves (i.e. a single-pass damping), but non-negligible differences are found for weakly damped waves (i.e. multi-pass damping). In this chapter, the full-wave code TORLH is described extensively because I need it to model the lower hybrid waves in the discharges of interest shown in Fig. 1-3. The waves are weakly damped in this case.

The full wave solver (TORLH) is based on a full wave solver for electromagnetic waves in the ion cyclotron frequency range (TORIC) [89] that solve Maxwell's equations with self-consistent plasma currents. The constitutive relations between the non-local plasma current and the electric fields are given kinetically using the zero-order particle trajectory. The ion cyclotron wave solver TORIC retains the thermal wave modes for small wavelength (e.g. ion Bernstein mode and ion cyclotron mode) [90] by using a finite Larmor radius (FLR) expansion of the conductivity operator, retaining up to the second order in the ion Larmor radius ρ_i relative to the perpendicular wavelength $\lambda_\perp$ [91]. However, for the frequency of the lower hybrid wave in most experiments, $\omega > 2\omega_{LH}$, the ion plasma wave branch associated with the hot plasma correction is inaccessible. Hence, the slow wave mode and the fast wave mode given by cold plasma dispersion are sufficient to describe the typical

propagation of the lower hybrid wave [19]. Accordingly, for TORLH, only zeroth order FLR terms are retained for ions. The power absorption due to the transit time magnetic pumping (TTMP) associated with the terms ($\sim (k_\perp \rho_e)^2$) is very weak in TORLH, although it is retained along with the cross-term between TTMP and electron Landau damping.

The lower hybrid wave injected from the launcher propagates only as the slow wave mode before mode converting to the fast wave mode. The slow wave is electrostatic, and it is damped by electron Landau damping that causes velocity space diffusion of the non-thermal fast electrons. The non-Maxwellian electron distribution function evolves consistently with a balance between the energy transfer from the wave and the electron collisions, resulting in a plateau in the distribution function with a much lower gradient than the gradient of the Maxwellian in the parallel velocity direction.

The evolution of the distribution function is calculated with a bounced averaged Fokker-Planck code (CQL3D) that solves Eq. (2.8). In the Fokker-Planck equation, the quasilinear diffusion coefficient is proportional to the wave energy density (or the square of the electric field magnitude) as shown in the previous section. Conversely, the modified distribution function also affects the electric field magnitude by changing the degree of damping through the imaginary part of the susceptibility in Maxwell equations. In steady state, the distribution function and the electric field are self-consistent, if the solutions from the electromagnetic field solver (TORLH) and the Fokker-Planck equation (CQL3D) have been iterated to convergence.

The propagation path of the wave determined by the real part of the susceptibility is not significantly modified by the non-Maxwellian distribution function obtained in this iteration process. Because only a small fraction of the electron density ($\lesssim 1\%$) in the high parallel velocity tail is resonant with the high phase velocity wave via electron Landau damping, the small deviation from the Maxwellian distribution does not contribute significantly to the dispersion of the wave. Thus, in TORLH, the real part of the susceptibility is approximated by the real part of the plasma dispersion function, that is obtained using a Maxwellian distribution function.

2.2.1 Maxwell equation solver

The full wave solver, TORLH, is written in MPI-Fortran90, and it uses a combined finite element method (FEM) and spectral decomposition to solve Maxwell's equations in a Galerkin weak variational form [92],

$$\int dr^3 \mathbf{F}^* \cdot \left[\nabla \times \nabla \times \mathbf{E} - \frac{\omega^2}{c^2} \left\{ \mathbf{E} + \frac{4\pi i}{\omega} (\mathbf{J}^p + \mathbf{J}^A) \right\} \right] = 0, \tag{2.25}$$

where $\mathbf{J}^A$ is the applied antenna current and $\mathbf{F}$ is an arbitrary vector function satisfying the same boundary condition as the electric field. Here, $\mathbf{J}^p$ is the plasma current generated by the electric field. Because the toroidal spectral mode of the wave is conserved, the electric field is solved in terms of the poloidal mode m and the radial coordinate ψ. While the toroidal modes are decoupled each due to the toroidal axis-symmetry, the poloidal modes are coupled because of the dependence of the static magnetic field on the poloidal angle. The constitutive relation between the plasma current and the electric field for each poloidal mode at a radius ψ is

$$\mathbf{J}^p_m(\psi) = -\frac{i\omega}{4\pi} \overleftrightarrow{\chi} (k^m_\parallel, \psi) \cdot \mathbf{E}_m(\psi) \tag{2.26}$$

where $\overleftrightarrow{\chi}$ $(k^m_\parallel, \psi)$ is the susceptibility tensor, and it is approximated using the dielectric tensor $\overleftrightarrow{\epsilon}$ from the cold plasma dispersion,

$$\overleftrightarrow{\epsilon} \cdot \mathbf{E}_m = \left(\overleftrightarrow{I} + \overleftrightarrow{\chi} \right) \cdot \mathbf{E}_m \simeq \mathcal{L}(E_{m+}) \hat{\mathbf{e}}_+ + \mathcal{R}(E_{m-}) \hat{\mathbf{e}}_- + \mathcal{P}(E_{m\parallel}) \hat{\mathbf{b}} \tag{2.27}$$

where $E_{m\pm} = \frac{E_{mx} \pm i E_{my}}{2}$, $\hat{\mathbf{e}}_\pm = \frac{\hat{\mathbf{x}} \pm i\hat{\mathbf{y}}}{2}$, and x and y are the orthogonal coordinates in the plane perpendicular to the magnetic field. Here, Stix notation [17] is used. For instance, the operator $\mathcal{P}(E_\parallel)$ is

$$\mathcal{P}(E_\parallel) = E_\parallel - \sum_s \frac{\omega^2_{ps}}{\omega^2} \int_0^\infty dv_\perp 2\pi v_\perp \int_{-\infty}^\infty \frac{dv_\parallel}{n_e v_{te}} v_\parallel \frac{\partial f_e}{\partial v_\parallel} \left(i\omega \int_{-\infty}^t dt' e^{i(k_\parallel v_\parallel - \omega)t'} E_\parallel \right), \tag{2.28}$$

where the zero order particle trajectory is considered, and the perpendicular motion is ignored in the zero-order Larmor radius expansion. For the real part of the susceptibility,

a Maxwellian distribution function is assumed, resulting in

$$Re\{\mathcal{P}(E_\parallel)\} \simeq E_\parallel \left[1 - \sum_s \frac{\omega_{ps}^2}{\omega^2}\left(\frac{\omega}{k_\parallel v_{ts}}\right)^2 Z'\left(\frac{\omega}{k_\parallel v_{ts}}\right)\right] \tag{2.29}$$

$$\simeq -\frac{\omega_{pe}^2}{\omega^2} E_\parallel \qquad \text{for the lower hybrid frequency range,} \tag{2.30}$$

where ω_{ps} is the plasma frequency of the species s.

The damping of the electric field by electron Landau damping is evaluated using the imaginary part of a component of the susceptibility in Eq. (2.27), $Im\{\chi_{\parallel\parallel\parallel}\} = Im\{\hat{\mathbf{b}} \cdot \overleftrightarrow{\chi} \cdot \hat{\mathbf{b}}\} = \frac{1}{E_\parallel} Re\{\mathcal{P}(E_\parallel)\}$. Because the wave is resonant with fast electrons having parallel velocities of about 10% of the speed of light, it is necessary to include the relativistic corrections in the velocity space integration for $Im\{\chi_{\parallel\parallel\parallel}\}$. Then, the imaginary part of the susceptibility is defined by [92, 93]

$$Im\{\chi_{\parallel\parallel\parallel}\} = -2\pi^2 \frac{1}{n_e v_{te}} \left(\frac{\omega_{pe}}{k_\parallel}\right)^2 \int_0^\infty du_\perp u_\perp J_0^2 \left(\frac{k_\perp v_\perp}{\Omega_{r,e}}\right) \frac{1}{\frac{\partial v_\parallel}{\partial u_\parallel}} \frac{\partial f_{0,e}}{\partial u_\parallel}\bigg|_{v_\parallel = \omega/k_\parallel}, \tag{2.31}$$

where $\Omega_{r,e} = \Omega_e/\gamma$ is the relativistic electron gyrofrequency, $\mathbf{u} = \gamma \mathbf{v}$ and u are the relativistic velocity and its magnitude, respectively, $\mathcal{E} = \gamma c^2$ is the relativistic energy and $\gamma = (1 + (u/c)^2)^{1/2} = (1 - (v/c)^2)^{-1/2}$. Here, the distribution function $f_{0,e}$ is non-Maxwellian, and it is obtained from the bounce averaged Fokker-Planck equation in (2.8).

To find the electric field in Eq. (2.25) in TORLH, the electric field and the test function are radially discretized by finite elements using the cubic Hermite polynomial basis. For a fixed toroidal spectral mode, it results in a block tri-diagonal matrix system due to the adjacent radial mesh interactions of the basis. The master matrix in the system has a radial dimension of n_1 block rows, and each row has three massive blocks, $\overleftrightarrow{L}_i$ $\overleftrightarrow{D}_i$ and $\overleftrightarrow{R}_i$ (Here, the matrices $\overleftrightarrow{L}_i$ and $\overleftrightarrow{R}_i$ are different from the operators $\mathcal{L}$ and $\mathcal{R}$ in (2.27)). Each block is a dense matrix whose size is $n_2 \times n_2$ due to the poloidal spectral mode coupling. Here, n_2 is equal to six times the poloidal spectral mode number, where the factor of six is due to the three components of the electric field and their radial derivatives. The radial derivatives are explicitly calculated to satisfy the continuity of the radial derivative across the elements by using the cubic Hermite polynomial basis. Then, the matrix equation for each radial

element is

$$\overleftrightarrow{L}_i \cdot \mathbf{x}_{i-1} + \overleftrightarrow{D}_i \cdot \mathbf{x}_i + \overleftrightarrow{R}_i \cdot \mathbf{x}_{i+1} = \mathbf{y}_i \quad \text{for i=1,...}n_1, \tag{2.32}$$

where $\mathbf{x}_i$ and $\mathbf{y}_i$ are complex vectors whose size is n_2, and $\mathbf{y}_i$ is given by the boundary conditions at the wall, the antenna, and the magnetic axis of a tokamak. Then, the total master matrix size is $(n_1 n_2) \times (n_1 n_2)$. Typical values of n_1 and n_2 are about 1000 and 6000, respectively, to resolve a lower hybrid wave with a small perpendicular wavevector $\lambda_\perp \simeq 1\text{mm}$.

I developed a three-dimensional (3-D) processor configuration for a parallel solver to solve this massive block-tridiagonal matrix system [94]. Previously, the solver employed a parallel matrix computation algorithm using LU decomposition (ScaLAPACK) for each block operation in a two-dimensional (2-D) processor grid, while keeping the serial Thomas algorithm as a tri-diagonal matrix solver. The purpose of the added parallelization dimension is to retard the saturation of scaling with processor number due to communication overhead and inefficient cache use. As the most suitable algorithm, I implemented the combined method of "Partitioned Thomas method" and "Cyclic Odd-Even Reduction" in TORLH. The 3-D parallel solver using thousands of processors shows more than 5 times improved computational speed with the optimized 3-D grid compared to the 2-D parallel solver for the same problem size.

Once the electric field is obtained for every poloidal mode and radius, the flux surface averaged energy transfer is evaluated. The power absorption in a flux surface from the LH wave [17, 92, 93] is defined as

$$\begin{aligned} P_{abs}(\psi) &\equiv \left\langle \frac{1}{2} \sum_n \sum_m \sum_{m'} Re\left\{ e^{i(m'-m)\theta} \mathbf{J}^{m',n*} \cdot \mathbf{E}^{m,n} \right\} \right\rangle_s \\ &\simeq \frac{1}{\tau_s} \frac{\omega}{8\pi} \sum_n \sum_m \sum_{m'} \oint \frac{d\ell}{B} Re\left\{ e^{i(m'-m)\theta} E_\parallel^{m',n*} E_\parallel^{m,n} \right\} Im\{\chi_{\parallel\parallel}\}. \end{aligned} \tag{2.33}$$

The radial profile for power absorption that will be shown later in Fig. 2-4 (b) is obtained from Eq. (2.33) based on the electric field in Fig. 2-2.

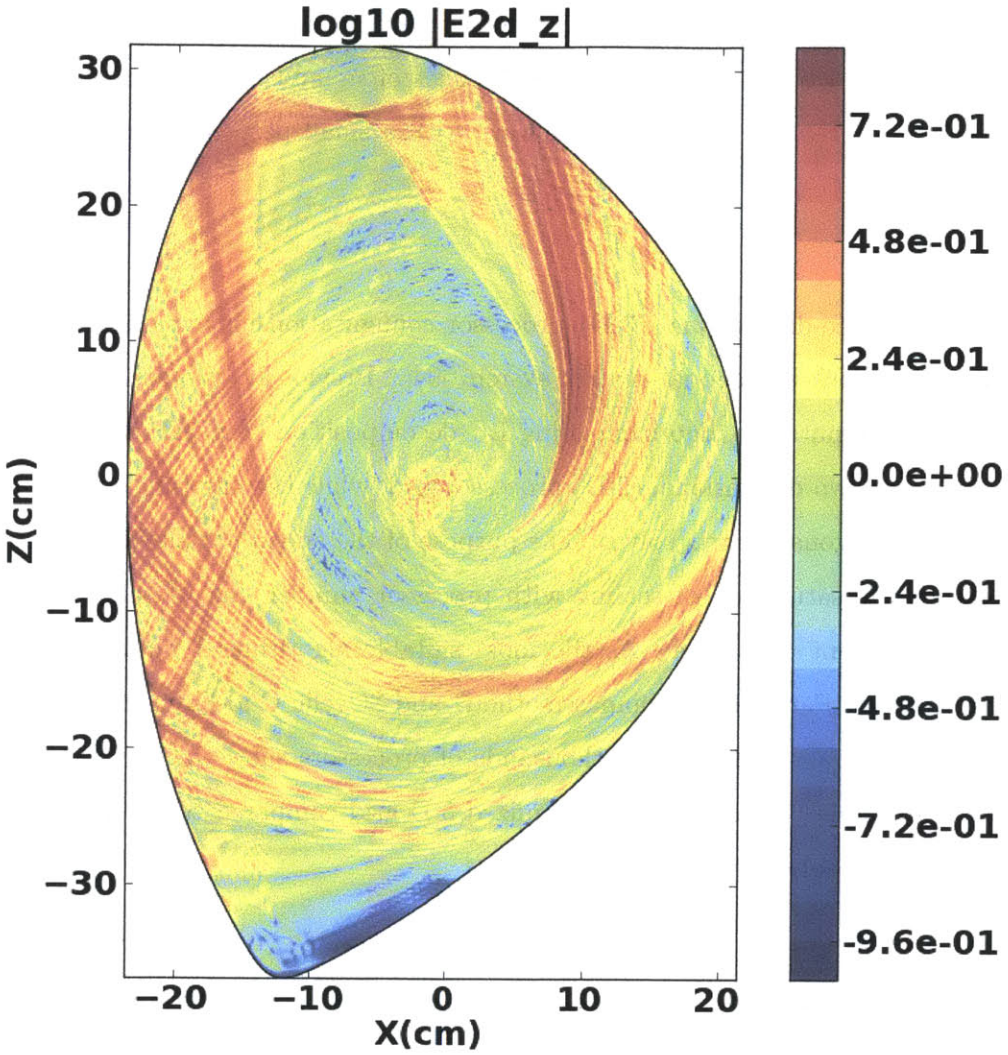

Figure 2-2: The poloidal cross section of the parallel electric field intensity obtained with TORLH for the high current case in Alcator C-Mod shown in Fig. 1-3. $B_\varphi = 5.3T$, $I_p = 700kA$, $T_e(\psi/\psi_0 = 0) = 3.5keV$, $n_e(\psi/\psi_0 = 0) = 1.2 \times 10^{20}$, $n_\parallel = -1.6$ and $P_{abs} = 0.8MW$.

2.2.2 Evolution of non-Maxwellian distribution function

The non-Maxwellian distribution function is evolved through a balance between collisions and the quasilinear diffusion in velocity space due to the lower hybrid waves, using the bounce averaged Fokker-Planck code (CQL3D) [29]. CQL3D is a finite difference time advance code with two relativistic velocity variables (a magnitude u and a pitch angle $\vartheta = \tan^{-1}(\frac{u_\perp}{u_\parallel})$) and a radial variable (ψ), where $u_\perp$ and $u_\parallel$ are the relativistic velocities perpendicular and parallel to the static magnetic field, respectively. It describes the distribution function for a species in terms of the variables at the outer-midplane $F_{0,s}(u_0, \vartheta_0(\vartheta,\theta), \psi, t) = f_{0,s}(u, \vartheta, \theta, \psi, t)$. The magnitude u is conserved but the pitch angle varies along the orbit keeping the relativistic magnetic moment constant, $\frac{u_\perp^2}{2B} = \frac{u_{\perp 0}^2}{2B_0}$ (i.e. $\frac{\sin\vartheta^2}{B} = \frac{\sin\vartheta_0{}^2}{B_0}$). Here, the subscript 0 for the velocity and the magnetic field denotes the values at the outer midplane of the tokamak.

The collision term and quasilinear diffusion term in the electron Fokker-Planck equation can be expressed as the divergence of the flux in 2-D relativistic velocity space (u and ϑ) [95, 85],

$$\begin{aligned}\langle C(f_{0,e})\rangle + \langle Q(f_{0,e})\rangle &= -\nabla\cdot\Gamma = \frac{1}{u^2}\frac{\partial}{\partial u}\left\{\mathsf{A} + \mathsf{B}\frac{\partial}{\partial u} + \mathsf{C}\frac{\partial}{\partial \vartheta}\right\} f_{0,e} \\ &\quad + \frac{1}{u^2\sin\vartheta}\frac{\partial}{\partial\vartheta}\left\{\mathsf{D} + \mathsf{E}\frac{\partial}{\partial u} + \mathsf{F}\frac{\partial}{\partial\vartheta}\right\} f_{0,e}. \end{aligned} \tag{2.34}$$

Using Eq. (2.34), the bounce averaged equation equivalent to Eq. (2.8) in terms of the relativistic velocity is

$$\begin{aligned}\frac{d(\lambda F_{0,e})}{dt} &= -\nabla\cdot\Gamma_0 = \frac{1}{u_0^2}\frac{\partial}{\partial u_0}\left[\left\{\mathsf{A}_0 + \mathsf{B}_0\frac{\partial}{\partial u_0} + \mathsf{C}_0\frac{\partial}{\partial\vartheta_0}\right\} F_{0,e}\right] \\ &\quad + \frac{1}{u_0^2\sin\vartheta_0}\frac{\partial}{\partial\vartheta_0}\left[\left\{\mathsf{D}_0 + \mathsf{E}_0\frac{\partial}{\partial u_0} + \mathsf{F}_0\frac{\partial}{\partial\vartheta_0}\right\} F_{0,e}\right], \end{aligned} \tag{2.35}$$

where $\lambda = v_{\parallel 0}\tau_b$, and the properties of the bounce average in Appendix B are used. The coefficients are composed of the collisional contribution and quasilinear diffusion contribution (e.g. $\mathsf{B}_0 = \mathsf{B}_{0C} + \mathsf{B}_{0ql}$). For the mildly relativistic Fokker-Planck collision operator, the coefficients for A_{0C},..., F_{0C} are given in [96, 95]. For electron Landau damping, the quasilinear diffusion coefficient in the energy direction taking relativistic effects into account [92]

is

$$\begin{aligned}
\mathsf{B}_{0ql} &= \lambda \langle \mathsf{B} \rangle_b = \frac{e^2}{2m_e^2} v_{\|0} \mathrm{Re} \sum_{m_1} \sum_{m_2} \oint \frac{d\theta}{v_\| \hat{\mathbf{b}} \cdot \nabla \theta} e^{i(m_2 - m_1)\theta} \frac{u_\|^4}{\gamma^2 (\omega/k_\|^{m_1})(\omega/k_\|^{m_2})} \\
&\times \left(J_0 \left(\frac{k_{1\perp} v_\perp}{\Omega_e} \right) E_\|^{m_1} \right)^* \left(J_0 \left(\frac{k_{2\perp} v_\perp}{\Omega_e} \right) E_\|^{m_2} \right) \delta(\omega - k_\| v_\|). \qquad (2.36)
\end{aligned}$$

The resonance condition is applied to the non-relativistic parallel velocity even for the realistic velocity space diffusion (compare the above with Eq. (2.11) and (2.12)). The dominant parallel direction diffusion results in non-zero values for C_{0ql}, E_{0ql} and F_{0ql} that are given by their relations with B_{0ql} in the Appendix D.

Once the steady state non-Maxwellian distribution function is achieved in sub-milliseconds by the balance between collisions and the quasilinear diffusion in Eq. (2.35), the flux surface averaged value of the energy transferred from the wave to electrons is evaluated in CQL3D as

$$\begin{aligned}
P_{abs}(\psi) &= \left\langle \int d^3u (\gamma - 1) m_e c^2 Q(f_{0,e}) \right\rangle_s = \frac{1}{B_0 \tau_s} \int d^3u_0 \lambda \left\langle (\gamma - 1) m_e c^2 Q(f_{0,e}) \right\rangle_b \\
&= -\frac{m_e c^2}{B_0 \tau_s} \int d^3u_0 \frac{\partial \gamma}{\partial u} \mathsf{B}_{0ql} \frac{\partial F_{0,e}}{\partial u_0}, \qquad (2.37)
\end{aligned}$$

where Eq. (B.6) and integration by parts are used. Here $\frac{\partial \gamma}{\partial u} = \frac{u}{\gamma c^2}$. For the high plasma current case given in Fig. 1-3, the radial profile of power absorption obtained using Eq. (2.37) is shown in Fig. 2-4 (b).

2.2.3 Self-consistent full wave simulation

Self-consistency between the electric field and the electron distribution function is obtained by iterating the two codes TORLH and CQL3D. The following nonlinear equations summarize the iteration,

$$\begin{aligned} \mathbf{E}^n(\psi) &= \mathrm{S}_{\mathrm{TORLH}}\left(\chi(F^n(\psi,u,\vartheta))\right) \\ F^{n+1}(\psi,u,\vartheta) &= \mathrm{S}_{\mathrm{CQL3D}}\left(D_{ql}(\mathbf{E}^n(\psi))\right), \end{aligned} \tag{2.38}$$

where $\mathrm{S}_{\mathrm{TORLH}}$ and $\mathrm{S}_{\mathrm{CQL3D}}$ represent the operations performed by TORLH that solves Eq. (2.25), and by CQL3D that solves Eq. (2.35). The nonlinear operator $\mathrm{S}_{\mathrm{TORLH}}$ applied on the electron distribution function gives the electric field, and the nonlinear operator $\mathrm{S}_{\mathrm{CQL3D}}$ applied on the electric field results in the steady state bounce averaged electron distribution. The superscripts in the electric field and distribution function indicate the iteration number.

Fig 2-3 gives a typical iteration between TORLH and CQL3D. To explain the observed convergence of the iteration, I use a simplified model based on the relation between the Poynting energy flux and the power absorption in Eq. (2.39) to evaluate the electric field energy density, $\frac{1}{16\pi}\left[\mathbf{E}^* \cdot \frac{\partial(\omega \overleftrightarrow{\epsilon})}{\partial\omega} \cdot \mathbf{E}\right]$. For simplicity, I only consider the parallel electric field and a distribution function that only depends on the parallel velocity, and I ignore the poloidal dependence,

$$V_{g\psi}\frac{\partial \epsilon_{\parallel\parallel}(E_\parallel^2)^n(\psi)}{\partial\psi} = -P_{abs} = -\frac{\omega}{8\pi}(E_\parallel^2)^n Im\left\{\chi(F^n(\psi,v_\parallel))\right\}, \tag{2.39}$$

$$F^{n+1}(\psi,v_\parallel) = C_F \exp\left(-\frac{1}{v_{te}^2}\int_{-\infty}^{v_\parallel} dv_\parallel \frac{v_\parallel}{1+(v_\parallel^3/v_{te}^3)D_{ql}((E_\parallel^2)^n)/(\nu_{ee}v_{te}^2(2+Z))}\right), \tag{2.40}$$

where $V_{g\psi}$ is the group velocity of the wave packet in the radial direction, and $\epsilon_{\parallel\parallel}$ is the parallel diagonal component of the dielectric tensor $\overleftrightarrow{\epsilon}$. The steady state distribution in (2.40) is obtained from the balance between the 1-D model collision operator $C_e = \nu_{ee}v_{te}^2(2+Z_i)\frac{\partial}{\partial v_\parallel}\left(\frac{v_{te}^3}{v_\parallel^3}\frac{\partial}{\partial v_\parallel} + \frac{v_{te}}{v_\parallel^3}\right)$, and the 1-D quasilinear diffusion coefficient in the parallel direction $Q = \frac{\partial}{\partial v_\parallel}D_{ql}\frac{\partial}{\partial v_\parallel}$ [7]. Here, C_F is the integration constant needed to satisfy the electron density conservation, $n_e = \int_{-\infty}^{\infty} dv_\parallel F$. By neglecting the contribution from the perpendicular electric field on the left hand side of Eq. (2.39), one misses an important factor in the energy density. Also, the oversimplified 1-D model collision operator for the pitch angle scattering underestimates the LH wave current drive efficiency by about a factor

of two [97] and does not conserve momentum. However, I assume that these assumptions will not affect significantly this convergence analysis.

In the radial region of interest, where there is strong damping, I assume that the wavevectors of the waves do not change radially, and the parallel electric field intensity is non-zero only in the range of wavevector $k_{\parallel 2} < k_{\parallel} < k_{\parallel 1}$, where $\Delta k_{\parallel} = k_{\parallel 1} - k_{\parallel 2} \ll k_{\parallel 1}$. Also, the electric field is assumed to result in a constant quasilinear diffusion coefficient,

$$D_{ql} \simeq \left(\frac{eE_{\parallel}}{m_e}\right)^2 \frac{1}{k_{\parallel 1}} \Pi\left(\frac{\omega}{k_{\parallel 1}}, \frac{\omega}{k_{\parallel 2}}\right), \tag{2.41}$$

where $E_{\parallel}^2 = \sum_m \sum_n (E_{\parallel}^{m,n})^2$ for all m and n in the parallel spectral range and $\Pi(v_a, v_b)$ is an approximation of the Dirac delta function given by a rectangular function with the height of $\frac{1}{v_b - v_a}$ in the range of $v_a < v < v_b$.

Using the quasilinear diffusion coefficient in Eq. (2.40), the susceptibility in Eq. (2.31) is approximated by

$$\begin{aligned} Im\{\chi\} &= \frac{2\pi\omega_{pe}^2}{n_e\omega} Im\left\{\int_{-\infty}^{\infty} dv_{\parallel} \frac{v_{\parallel}}{\omega - k_{\parallel} v_{\parallel}} \frac{\partial F(v_{\parallel})}{\partial v_{\parallel}}\right\} \\ &\simeq \frac{2\pi^2\omega_{pe}^2}{n_e v_{te}^2 \omega} \int_{-\infty}^{\infty} dv_{\parallel} \frac{1}{k_{\parallel 1}} \frac{\Pi\left(\frac{\omega}{k_{\parallel 1}}, \frac{\omega}{k_{\parallel 2}}\right) v_{\parallel}^2 F(v_{\parallel})}{1 + (v_{\parallel}^3/v_{te}^3) D_{ql}/(\nu_{ee} v_{te}^2 (2+Z))} \end{aligned} \tag{2.42}$$

$$\simeq \begin{cases} \alpha_1 \dfrac{2\pi^2\omega_{pe}^2}{n_e v_{te}^2 \omega k_{\parallel 1}} \left(\dfrac{\omega}{k_{\parallel 1}}\right)^2 F\left(\dfrac{\omega}{k_{\parallel 1}}\right) & \text{for } \dfrac{(E_{\parallel}^2)^n}{\alpha_2} \ll 1 \\ \dfrac{2\pi^2\omega_{pe}^2 \nu_{ee} v_{te}^3 (2+Z)}{n_e \omega} \left(\dfrac{m_e}{eE_{\parallel}}\right)^2 \ln\left(\dfrac{k_{\parallel 1}}{k_{\parallel 2}}\right) F\left(\dfrac{\omega}{k_{\parallel 1}}\right) & \text{for } \dfrac{(E_{\parallel}^2)^n}{\alpha_2} \gg 1 \end{cases}, \tag{2.43}$$

where the different solutions in Eq. (2.43) are obtained in two different limits. The two limits are characterized by the relative size of the two terms of the denominator in Eq. (2.42), and they are determined by $\frac{(E_{\parallel}^2)^n}{\alpha_2} = \left(\frac{\omega}{k_{\parallel 1} v_{te}}\right)^3 \frac{D_{ql}}{\nu_{ee} v_{te}^2 (2+Z)}$ being smaller or larger than 1. Here, $\alpha_2 \simeq \nu_{ee} v_{te}^5 (2+Z) \Delta k_{\parallel} \left(\frac{k_{\parallel 1}}{\omega}\right)^2 \left(\frac{m_e}{e}\right)^2$, where I use the quasilinear diffusion coefficient in Eq. (2.41).

For $\frac{(E_{\parallel}^2)^n}{\alpha_2} \ll 1$, the electron distribution is almost Maxwellian with a weak plateau. In this case, to calculate $Im\{\chi\}$, $F(v_{\parallel} = \omega/k_{\parallel 2}) \ll F(v_{\parallel} = \omega/k_{\parallel 1})$ is used, making $\alpha_1 = \frac{(\sqrt{\pi}/4)(\mathrm{erf}(v_2) - \mathrm{erf}(v_1)) - (v_2 e^{-v_2^2} - v_1 e^{-v_1^2})/2}{v_2 - v_1} \frac{1}{v_1^2 e^{-v_1^2}}$, where $\mathrm{erf}(v) = \frac{1}{\sqrt{\pi}} \int_0^v dx e^{-x^2}$, $v_1 = \frac{\omega}{k_{\parallel 1} v_{te}}$ and $v_2 = \frac{\omega}{k_{\parallel 2} v_{te}}$. On the other hand, for $\frac{(E_{\parallel}^2)^n}{\alpha_2} \gg 1$, a strong plateau is established by strong velocity diffusion. In this case, $F(v_{\parallel} = \omega/k_{\parallel 2}) \simeq F(v_{\parallel} = \omega/k_{\parallel 1})$ is used. For both the weak

and the strong plateau, $F(v_\parallel = \omega/k_{\parallel 1}) \simeq C_F \exp(-(\omega/(k_{\parallel 1} v_{te}))^2)$.

Substituting Eq. (2.43) into Eq. (2.39) for the next iteration, I obtain the spatial damping of the wave energy when the wave propagates into the core plasma (in the negative ψ direction),

$$\frac{\partial (E_\parallel^2)^{n+1}}{\partial(-\psi/\psi_0)} \simeq \begin{cases} -\alpha_1 C_E (E_\parallel^2)^{n+1} & \text{for } \dfrac{(E_\parallel^2)^n}{\alpha_2} \ll 1 \\ -\alpha_2 C_E \dfrac{(E_\parallel^2)^{n+1}}{(E_\parallel^2)^n} & \text{for } \dfrac{(E_\parallel^2)^n}{\alpha_2} \gg 1 \end{cases}, \tag{2.44}$$

where $C_E \simeq \frac{C_F}{n_e v_{te}} \frac{\pi \psi_0 \omega_{pe}^2}{4 V_{g\psi} v_{te} \epsilon_{\parallel\parallel} k_{\parallel 1}} \left(\frac{\omega}{k_{\parallel 1}}\right)^2 e^{-\left(\frac{\omega}{k_{\parallel 1} v_{te}}\right)^2}$. Here, ψ_0 is the poloidal flux at the last flux surface used to normalize ψ. For the weak plateau case, α_1 is determined by the exponential decay of the distribution function within the range $\frac{\omega}{k_{\parallel 1}} < v_\parallel < \frac{\omega}{k_{\parallel 2}}$ in velocity space. If $F(v_\parallel = \omega/k_{\parallel 2}) \ll F(v_\parallel = \omega/k_{\parallel 1})$, α_1 is less than 0.5. In the equation for the weak plateau (i.e. for $\frac{(E_\parallel^2)^n}{\alpha_2} \ll 1$), the spatial decay rate of the energy density is determined by $\alpha_1 C_E$ ($\alpha_1 C_E > 1$ for strong damping and $\alpha_1 C_E < 1$ for weak damping).

The different steps in the iteration to find the self-consistent solution in Fig. 2-3 for the high current case can be interpreted as several transitions between the weak plateau regime (i.e. $(E_\parallel^2)^n/\alpha_2 \ll 1$) and the strong plateau regime (i.e. $(E_\parallel^2)^n/\alpha_2 \gg 1$). In the initial iteration, the distribution function is assumed to be Maxwellian, so the electric field solution is in the weak plateau regime. The right hand side of Eq. (2.44) shows that the electric field in the current iteration ($(E_\parallel^2)^{n+1}$) has little relation with the previous iteration ($(E_\parallel^2)^n$) if the electric field is in the weak plateau regime. However, after the strong plateau is established, the wave damping is amplified for a weaker electric field because the electric field of the previous iteration is in the denominator in Eq. (2.44). If I assume that the waves propagate only inward, they have a weaker electric field at the inner radii than at outer radii due to damping. As a result, the power absorption is stronger at inner radii than outer radii (see the change of the blue lines from iteration 1 to iteration 2 for inner radii $\psi/\psi_0 < 0.4$ and outer radii $\psi/\psi_0 > 0.4$ in Fig. 2-3).

The damped electric field gives rise to stronger damping, resulting in a peak in the damping profile (see the peak of blue lines at $\psi/\psi_0 \simeq 0.3$ in iteration 3 of Fig 2-3), until the damping is so strong that it weakens the electric field inducing the weak plateau. Then, it becomes under-damped due to the small α_1 for the weak plateau. The difference between

under-damping and over-damping is large, when the broadening of the wave spectrum is large because α_1 is smaller for larger Δk. In Fig. 2-3, the power absorption changes significantly over iterations around $\psi/\psi_0 = 0.2$, because the spectral broadening at that radius is the biggest as shown in the plot of effective refractive index in Fig. 2-4 (c). Eventually, the difference between the under-damping and over-damping disappears and the self-consistent power absorption profile is obtained (see the iteration 12 in Fig. 2-3). However, the convergence in the last iterations is slow.

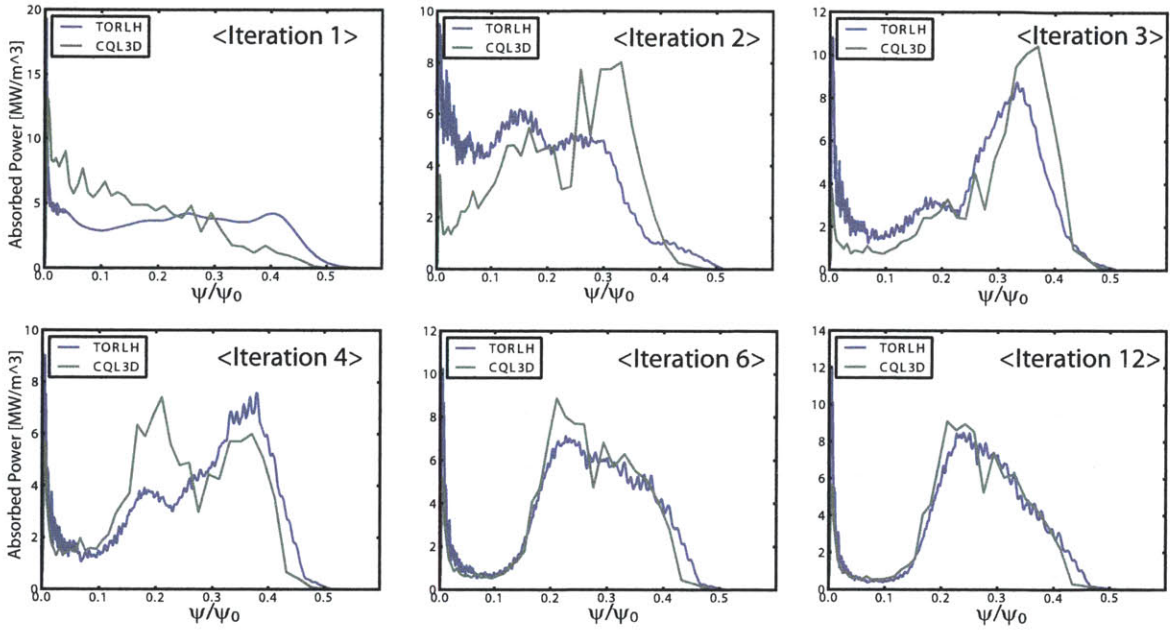

Figure 2-3: The convergence process of the power absorption profile by iterating TORLH and CQL3D for the high current case shown in Fig. 2-2.

2.3 Parallel momentum transfer to electrons

When the lower hybrid waves are damped by electron Landau damping, the wave transfers its toroidal angular momentum to electrons. The toroidal angular momentum is composed of the toroidal projections of the parallel angular momentum and the perpendicular angular momentum. The parallel momentum can be evaluated using the gyro-averaged Kennel-Engelmann quasilinear diffusion coefficient explained in Sec. 2.1. In this section, I suggest two equivalent methods to evaluate the parallel momentum source term: one is to use the wave dielectric constant in the full-wave code to solve Maxwell equations and the other is to use the modified bounce averaged constant in the Fokker-plank equation. The two methods result in the same value of the momentum source separately if a converged solution is given by the coupled nonlinear process explained in Sec. 2.2.3. The perpendicular component of the momentum will be calculated and explained in Sec. 3.2.

2.3.1 Evaluation of the parallel momentum transfer using the full wave code

To evaluate the flux surface averaged parallel momentum source, I have introduced a new variable η in (2.45) which is defined in a similar manner as the susceptibility χ used for the bounce averaged power absorption (2.33). The toroidal projection of the parallel angular momentum transfer (torque) by lower hybrid waves is,

$$\begin{aligned} T_\varphi^{\parallel}(\psi) &= \left\langle \int d^3u (m_e R u_\varphi) \frac{\partial}{\partial u_\parallel} \left(\langle D_{ql} \rangle \frac{\partial f_{0,e}}{\partial u_\parallel} \right) \right\rangle_s \\ &= \left\langle \int du^3 (-m_e R \hat{\mathbf{b}} \cdot \hat{\varphi}) \langle D_{ql} \rangle \frac{\partial f_{0,e}}{\partial u_\parallel} \right\rangle_s \\ &\simeq \frac{1}{\tau_s} \sum_n \sum_m \sum_{m'} \oint \frac{d\ell}{B} Re \left\{ e^{(m'-m)\theta} E_\parallel^{m',n*} E_\parallel^{m,n} \right\} Im\{\eta\}., \end{aligned} \tag{2.45}$$

where $\langle D_{ql} \rangle$ is the gyroaveraged quasilinear diffusion coefficient for electron Landau damping. Comparing this momentum transfer to the energy transfer in $P_{abs} = \langle \int du^3 \gamma m_e c^2 Q(f_{0,e}) \rangle_s \simeq \left\langle \int du^3 (-m_e u_\parallel / \gamma) \langle D_{ql} \rangle \frac{\partial f_{0,e}}{\partial u_\parallel} \right\rangle_s$, we can see that there is a difference of a factor $u_\parallel/\gamma$ in the velocity space integration. Using the properties of the Dirac-delta function in the quasilinear diffusion coefficient for the electron Landau damping, the non-relativistic parallel velocity $v_\parallel = u_\parallel/\gamma$ is not a variable but a constant $\omega/k_\parallel$ in the velocity space integration. Then, a

simple relation between η and χ in (2.33) is obtained,

$$Im\{\eta\} = \frac{k_\parallel}{\omega} R(\hat{\mathbf{b}}\cdot\hat{\varphi}) Im\{\chi_{\parallel\parallel}\} = \frac{n_\parallel}{c} R\cos\Theta Im\{\chi_{\parallel\parallel}\}, \tag{2.46}$$

where $n_\parallel$ is the parallel refractive index and Θ is the angle between toroidal direction and the magnetic field vector. For the high current case in Fig. 1-3, the toroidal projection of the parallel angular momentum transfer is evaluated using Eq. (2.45), and its radial profile is shown in Fig. 2-4 (a).

2.3.2 Evaluation of the parallel momentum transfer using the Fokker-Planck code

The evaluation of the flux surface averaged parallel angular momentum transfer using the bounced-averaged operator is more complicated than calculating the power absorption, because the parallel angular momentum of a particle changes along the particle orbit in the inhomogeneous magnetic field. Consequently, the bounce averaged parallel torque density cannot be evaluated using the previous bounce averaged coefficients in Eq. (2.35). For example, the coefficients E_{0ql} and F_{0ql} in Appendix D should be modified, because the differential operator $\frac{\partial}{\partial\vartheta_0}$ does not commute with the parallel momentum that depends on ϑ_0. In CQL3D, I have defined new bounce averaged coefficients for the parallel momentum transfer, using integration by parts to remove the non-commuting operator.

Using the gyro-averaged quasilinear term $\langle Q(f_{0,e})\rangle$ in Eq. (2.34), the toroidal projection of the parallel momentum transfer is

$$\begin{aligned}\left\langle \int d^3u (m_e u_\varphi R)\langle Q(f_{0,e})\rangle \right\rangle_s &= \left\langle (\hat{\mathbf{b}}\cdot\hat{\varphi}) \int du d\vartheta (u^2\sin\vartheta)(m_e u_\parallel R)\left[\frac{1}{u^2}\frac{\partial}{\partial u}\left[\left\{\mathsf{B}\frac{\partial}{\partial u}+\mathsf{C}\frac{\partial}{\partial\vartheta}\right\} f_{0,e}\right]\right.\right. \\ &\left.\left. +\frac{1}{u^2\sin\vartheta}\left[\frac{\partial}{\partial\vartheta}\left\{\mathsf{E}\frac{\partial}{\partial u}+\mathsf{F}\frac{\partial}{\partial\vartheta}\right\} f_{0,e}\right]\right]\right\rangle_s = -\left\langle (\hat{\mathbf{b}}\cdot\hat{\varphi}) \int d^3u \left[\frac{1}{u^2}(m_e\cos\vartheta R)\right.\right. \\ &\left.\left. \times\left\{\mathsf{B}\frac{\partial}{\partial u}+\mathsf{C}\frac{\partial}{\partial\vartheta}\right\} f_{0,e} + \frac{1}{u^2\sin\vartheta}\frac{\partial}{\partial\vartheta}\left[(m_e u\cos\vartheta R)\left\{\mathsf{E}\frac{\partial}{\partial u}+\mathsf{F}\frac{\partial}{\partial\vartheta}\right\} f_{0,e}\right]\right]\right\rangle_s \end{aligned} \tag{2.47}$$

To perform the velocity space integration in the flux surface averaged expression in Eq. (2.47), I used the property in Eq. (B.6), similar to what was done in going from Eq. (2.34)

to Eq. (2.35),

$$\int d^3u_0\lambda\left\langle (m_e u_\varphi R)Q(f_e)\right\rangle_b = -\int d^3u_0\lambda\Big\langle (\hat{\mathbf{b}}\cdot\hat{\varphi})\Big[\tfrac{1}{u^2}(m_e\cos\vartheta R)\left\{\mathsf{B}\tfrac{\partial}{\partial u}+\mathsf{C}\tfrac{\partial}{\partial\vartheta}\right\}f_{0,e}$$
$$+\tfrac{1}{u^2\sin\vartheta}\tfrac{\partial}{\partial\vartheta}\left[(m_e u\cos\vartheta R)\left\{\mathsf{E}\tfrac{\partial}{\partial u}+\mathsf{F}\tfrac{\partial}{\partial\vartheta}\right\}f_{0,e}\right]\Big]\Big\rangle_b = \int du_0 d\vartheta_0(-m_e\sin\vartheta_0)$$
$$\times\left[\left\{\mathsf{B}_{0M}\tfrac{\partial}{\partial u_0}+\mathsf{C}_{0M}\tfrac{\partial}{\partial\vartheta_0}\right\}f_{0,e}+\left\{\mathsf{E}_{0M}\tfrac{\partial}{\partial u_0}+\mathsf{F}_{0M}\tfrac{\partial}{\partial\vartheta_0}\right\}F\right]. \tag{2.48}$$

The new coefficients for the momentum change calculation are defined as,

$$\mathsf{B}_{0M} = \lambda\left\langle(\hat{\mathbf{b}}\cdot\hat{\varphi}\cos\vartheta R)\mathsf{B}\right\rangle_b \tag{2.49}$$
$$\mathsf{E}_{0M} = -\lambda\left\langle(\hat{\mathbf{b}}\cdot\hat{\varphi}uR)\mathsf{E}\right\rangle_b \tag{2.50}$$
$$= \lambda\left\langle\left(\hat{\mathbf{b}}\cdot\hat{\varphi}\frac{\sin^2\vartheta}{\cos\vartheta}R\right)\mathsf{B}\right\rangle_b, \tag{2.51}$$

and the relation $\mathsf{C}_{0M}/\mathsf{B}_{0M} = \mathsf{F}_{0M}/\mathsf{E}_{0M} = \mathsf{C}_{0ql}/\mathsf{B}_{0ql}$ in Appendix D holds. The corrections to the coefficients B_{0M} and E_{0M} for the evaluation of the parallel momentum are odd around the pitch angle $\vartheta_0 = \pi/2$. Conservation of the magnetic moment (i.e. $\frac{\partial\vartheta_0}{\partial\vartheta} = \frac{\cos\vartheta}{\sin\vartheta}\frac{\sin\vartheta_0}{\cos\vartheta_0}$) is used in Eq. (2.51). Then, the angular momentum transfer can be simplified as

$$T_\varphi^{\parallel}(\psi) = \int d^3u_0\lambda\left\langle(m_e u_\varphi R)\langle Q(f_{0,e})\rangle\right\rangle_b$$
$$= \int du_0 d\vartheta_0(-m_e\sin\vartheta_0)\left(\mathsf{B}_{0M}+\mathsf{E}_{0M}\right)\left\{\frac{\partial}{\partial u_0}-\frac{\sin\vartheta_0}{v_0\cos\vartheta_0}\frac{\partial}{\partial\vartheta_0}\right\}F_{0,e}, \tag{2.52}$$

where the new coefficients B_{0M} and E_{0M} are evaluated in CQL3D using the electric field calculated by TORLH. Eq. (2.52) is verified by comparing the radial profile of the parallel momentum transfer with that evaluated in TORLH using Eq. (2.45) as shown in Fig. 2-4 (a).

2.4 Discussion

The self-consistent distribution function and electric fields are obtained by nonlinear iterations between the wave code TORLH (Maxwell equation solver) [92] and the relativistic 3-D bounce averaged Fokker-Planck code CQL3D [29]. Before using the quasilinear diffusion coefficient in the codes, I considered the limitation of the quasilinear diffusion model,

and I concluded that the quasilinear approximation is acceptable for the realistic condition of a broad-band wave in Sec. 2.1. Using the distribution function and electric fields, the toroidal projection of the parallel momentum transfer is evaluated by two equivalent methods in TORLH and CQL3D. The momentum source evaluation is important to determine the effect on ion toroidal rotation of the LH wave injection, as will be discussed in the next chapter.

As an example, the energy and momentum transfer are calculated in TORLH and CQL3D for the high current case in Alcator C-Mod. The curves in Fig. 2-4 (b) show good agreement between the power absorption profiles evaluated by TORLH using Eq. (2.33) and by CQL3D using Eq. (2.37), respectively, indicating self-consistency between the two codes. The parameters for the simulation are $B_\varphi = 5.3T$, $I_p = 700kA$, $T_e(0) = 3.5keV$, $n_e(0) = 1.2 \times 10^{20}$, and $n_\parallel = -1.6$ with Alcator C-Mod lower single null magnetic field equilibrium. The relatively low parallel refractive index of the antenna results in multi-pass propagation of the wave fronts until the parallel index is up-shifted enough ($n_\parallel \simeq -3$) by the variation in the poloidal mode number to have strong Landau damping in a population of tail electrons. The multiple peaks in the radial profile of power absorption are associated with multi-pass damping. The toroidal projection of the parallel momentum transfer is evaluated by TORLH using Eq. (2.45) and by CQL3D using Eq. (2.52) as shown in Fig. 2-4 (a).

The size of the wave parallel momentum density is the parallel refractive index times the energy density [98]. Using this fact, I can define the effective flux surface averaged parallel refractive index as the ratio of momentum transfer to energy transfer in Fig. 2-4 (c). This is an additional advantage of the evaluation of the momentum transfer in the full-wave code, because the parallel refractive index is not given explicitly in the full wave code unlike in the ray-tracing code. The magnitude of parallel refractive index is important to quantify, as it determines the broadening and the upshift of the wave spectrum, which are important to explain the power absorption and the current drive of lower hybrid waves.

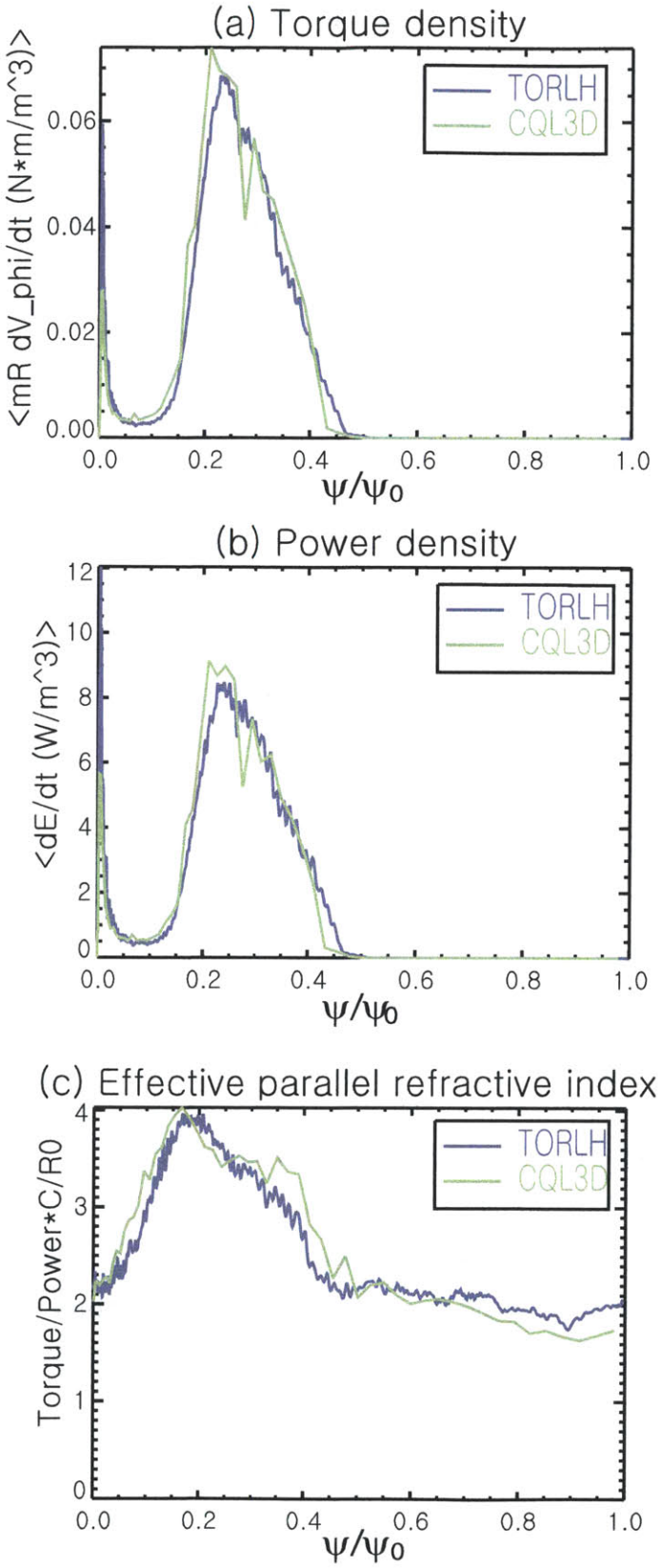

Figure 2-4: Comparison of radial profile of (a) torque density, (b) power density, and (c) the effective parallel refractive index of the wave, obtained by two codes, a full-wave Maxwell equation solver (TORLH) and a Fokker-Planck code (CQL3D).

Chapter 3

Momentum transfer from lower hybrid waves to ions

The toroidal momentum transfer between the lower hybrid (LH) waves and electrons by Landau resonance is widely accepted. However, the main mechanism of the momentum transfer from electrons to ions was not clear. In this chapter, I describe two different channels for the transfer of perpendicular and parallel momentum from the waves to ions through electrons. Both channels are important for toroidal momentum transfer of lower hybrid waves because the size of the projections in the toroidal direction of the parallel and perpendicular momentum are comparable. These two channels usually contribute in opposite directions to the ion toroidal momentum and have different time scales.

The channel for the parallel momentum transfer has been considered in previous work [99, 100, 101]. The parallel momentum is transferred from waves to electrons when the energy is transferred due to the resonance of the wave with the parallel motion of electrons, as shown in Sec. 2.3. The collisions between electrons and ions transfer the parallel momentum from electrons to ions. However, the channel for perpendicular momentum transfer was not self-evident. It was first found in [102]. If the perpendicular momentum transfer via electron Landau damping is ignored, the transfer of toroidal angular momentum to the plasma will be larger than the injected toroidal angular momentum, as previous work found incorrectly [99, 100, 101]. A proper quasilinear treatment that takes the electron gyromotion into account proves that both perpendicular and parallel momentum are transferred to the electrons. As a result, the total toroidal angular momentum of the wave at the launcher

is transferred to the electrons.

The perpendicular momentum is transferred to ions through an outward radial electron drift. Typically, this outward drift is about 100 times larger than the inward radial drift of the trapped electrons proposed to explain the ion toroidal rotation change in the counter-current direction due to the lower hybrid waves [103, 104, 105]. Ions follow the electron radial drift with the same speed to satisfy ambipolarity, but there are several transient phenomena before reaching this condition. Transiently, the radial electric field is changed due to charge separation, and it affects both toroidal and poloidal rotation. After an ion-ion collision time, the poloidal rotation decays, the radial electric field is determined only by the toroidal rotation, and the ambipolarity condition is satisfied.

The rest of this chapter is organized as follows. In Sec. 3.1, I investigate the change of the lower hybrid wave momentum as the waves propagates into a tokamak. In Sec. 3.2, I show that one needs to include the flux in the gyrophase angle direction in the quasilinear diffusion operator to evaluate the perpendicular momentum transfer. In Sec. 3.3, the outward radial electron drift due to the perpendicular momentum transfer is investigated and it is compared with two other radial drifts due to the parallel momentum transfer proposed by previous work. In Sec. 3.4, the momentum transfer from electrons to ions is investigated. The evolution of the ambipolar ion radial drift that appears due to the perpendicular momentum transfer is explained. In Sec. 3.5, the various time scales of the momentum transfer are reviewed and the theoretical estimate of the rotation change is compared with experimental results.

3.1 Momentum of lower hybrid waves

The wave momentum density is defined as $\mathbf{k}/\omega$ times the energy density, where $\mathbf{k}$ is the wave vector and ω is the wave frequency [98]. When lower hybrid waves have non-resonant interactions with the particles over a long propagation distance, the wave energy density does not change but the poloidal wave vector changes due to the dispersion relation of the lower hybrid wave, and consequently the poloidal wave momentum varies. On the other hand, when the wave has resonant interactions with the particles over a short propagation distance, the wave energy density is reduced and the wave vector remains unchanged.

Figure 3-1 shows the typical behavior of a LH wave in an inhomogeneous tokamak. As

the wave propagates from the low field side launcher, it develops a very high poloidal wave vector (about 10 times larger than the toroidal wave vector) due to the plasma dispersion relation in Eq. (1.1) [106]. The large poloidal wave vector contributes to the parallel wave number $k_{||}$ as much as the toroidal wave vector does, even overcoming the small ratio of the poloidal magnetic field over the toroidal magnetic field, $\frac{B_\theta}{B_\varphi} \sim 0.1$ ($k_{||} = \frac{B_\varphi}{B} k_\varphi + \frac{B_\theta}{B} k_\theta$ in a circular tokamak, where B_φ, B_θ, B are toroidal, poloidal, and total magnetic field, and k_φ, k_θ are toroidal and poloidal wave numbers, respectively). That results in the parallel refractive index $n_{||} \equiv \frac{k_{||} c}{\omega} \sim -3$ of the damped wave, significantly larger than the toroidal index $n_\varphi \equiv \frac{k_\varphi c}{\omega} \sim -1.6$ at the launcher, as shown in Fig. 3-1 (the negative sign means that the wave propagates in the counter-current direction of the tokamak). The electron Landau damping of the wave becomes stronger where the phase velocity of the wave becomes lower (in other words, where the refractive index becomes higher), since a lower phase velocity resonates with more electrons.

As shown in Fig. 3-1, until the wave reaches the region where the parallel phase velocity of the wave is sufficiently reduced by the poloidal mode coupling (e.g. $n_{||} \sim -3$) to interact with less energetic electrons, the resonant interaction is negligible. Nevertheless, the poloidal momentum of the wave changes due to the inhomogeneity of the magnetic field and the plasma density and temperature. There is a significant gain of poloidal wave momentum according to the change of the poloidal mode number.

In the eikonal limit, the poloidal mode number of the LH wave ($m \simeq k_\theta r$ in a circular tokamak) is determined by the poloidal variation of the dispersion relation, D in Eq. (1.1), along a ray path [106],

$$\frac{dm}{dt} = \frac{\partial D(\omega, m, n_e, T_e, B_\varphi)}{\partial \theta} \Big/ \frac{\partial D(\omega, m, n_e, T_e, B_\varphi)}{\partial \omega}. \tag{3.1}$$

The increase in m can be as large as nq at the resonance position. Here, $n \simeq k_\varphi R$ and $q \simeq \frac{r}{R} \frac{B_\varphi}{B_\theta}$ are the toroidal mode number and the safety factor, respectively.

The origin of the increased poloidal momentum is the external force required to keep the density n_e, the temperatures T_e and T_i, and the static magnetic field B_φ constant in time in the dispersion relation. These parameters are assumed to be fixed in the dispersion relation because the transport and the resistive time scale are much longer than the propagation time of the wave. The wave exerts a non-resonant force that can affect the evolution of the

background profile. The non-resonant interaction can be studied as a combination of the Reynolds stress and the Lorentz force in both fluid models [107, 108] and kinetic models [109, 110, 111, 112], and it has no effect on the toroidal flow [112, 113]. In general, this non-resonant force is smaller than the resonant one by a factor of $v_g/(\gamma^{LH}L) < 1$, where L is the characteristic length of variation of the background, v_g is the group velocity of the wave, and γ^{LH} is the wave damping rate at the resonance region. However, the accumulated momentum transfer by the non-resonant force along the ray path is not negligible. The wave gains poloidal momentum slowly from the plasma in the non-resonant region, and then transfers it back to the plasma over a short distance where it resonates. Consequently, the lower hybrid wave has redistributed the poloidal momentum of the plasma in a tokamak. The effect that this has on the poloidal rotation is small due to the strong poloidal collisional damping in a tokamak [114].

On the other hand, the toroidal mode number does not change due to the toroidal symmetry of a tokamak, and the original amount of wave toroidal angular momentum is fully transferred to the plasma in the resonance region (see the constancy of the green line in Fig. 3-1).

When the wave energy is transferred to the plasma due to a resonance, the corresponding wave momentum is also transferred to the plasma. This relation has been verified by evaluating the Lorentz force in fluid models [107, 115] and kinetic models [116, 117, 118]. However, the toroidal momentum transfer by resonance has been calculated incorrectly for the LH wave [99, 100, 101] resulting in an incorrect radial electric field. These calculations have ignored an important contribution to the Kennel-Engelmann quasilinear diffusion coefficient. The Kennel-Engelmann quasilinear diffusion coefficient [21] describes the resonant interaction of the plasma with the wave. The gyroaverage of this quasilinear operator is used to model the diffusion of the distribution function in velocity space. However, since some components of the momentum, such as the toroidal direction, depend on the gyrophase, the diffusion in gyrophase must be taken into account for momentum transfer calculations, and the gyroaveraged quasilinear operator is not sufficient to explain the total toroidal momentum transfer. I reexamine the amount of momentum transfer from LH wave to the plasma by resonant interaction in the next section. The new contribution to momentum transfer that I find is important because the poloidal wave number is large in the resonance region, giving $k_\parallel > k_\varphi$ as discussed above. Using the gyroaveraged quasilinear operator only

transfers the parallel wave momentum, leading to an incorrect evaluation of the toroidal angular momentum transferred by the wave.

3.2 Perpendicular momentum transfer to electrons

In this section, I study the quasilinear diffusion in velocity space including the gyrophase. From the quasilinear diffusion operator derived in Appendix A, the momentum deposited by the wave is evaluated by applying the resonance condition. This proof can be applied to any type of resonance (cyclotron or Landau damping) and any direction of momentum. For convenience and without loss of generality, I discuss toroidal angular momentum which has both perpendicular and parallel components. Let z be the direction parallel to the static magnetic field (i.e. $\hat{\mathbf{z}} = \hat{\mathbf{b}}$), and x, y the orthogonal coordinates (see Figure 3-2 (a)). Then, using the gyrophase angle α, the velocity is $\mathbf{v} = v_\perp \cos\alpha\hat{\mathbf{x}} + v_\perp \sin\alpha\hat{\mathbf{y}} + v_\parallel\hat{\mathbf{z}} = v_\perp\hat{\boldsymbol{\rho}} + v_\parallel\hat{\mathbf{z}}$, and its toroidal component is $v_\varphi = v_\perp \cos\alpha(\hat{\mathbf{x}}\cdot\hat{\boldsymbol{\varphi}}) + v_\perp \sin\alpha(\hat{\mathbf{y}}\cdot\hat{\boldsymbol{\varphi}}) + v_\parallel(\hat{\mathbf{z}}\cdot\hat{\boldsymbol{\varphi}})$, where $\hat{\boldsymbol{\rho}} = \mathbf{v}_\perp/v_\perp$ and $\hat{\boldsymbol{\varphi}}$ is the unit vector in the toroidal direction. The wavenumber vector is defined as $\mathbf{k} = k_\perp\cos\beta\hat{\mathbf{x}} + k_\perp\sin\beta\hat{\mathbf{y}} + k_\parallel\hat{\mathbf{z}} = k_\perp\cos(\alpha-\beta)\hat{\boldsymbol{\rho}} - k_\perp\sin(\alpha-\beta)\hat{\boldsymbol{\alpha}} + k_\parallel\hat{\mathbf{z}}$, and the electric field is $\mathbf{E} = E_x\hat{\mathbf{x}} + E_y\hat{\mathbf{y}} + E_\parallel\hat{\mathbf{z}} = E_\perp\hat{\boldsymbol{\rho}} + E_\alpha\hat{\boldsymbol{\alpha}} + E_\parallel\hat{\mathbf{z}}$, where $\hat{\boldsymbol{\alpha}} = \hat{\mathbf{z}}\times\hat{\boldsymbol{\rho}}$ is the unit vector perpendicular to both $\mathbf{v}_\perp$ and the magnetic field. Here, $E_\perp = E_x\cos\alpha + E_y\sin\alpha = (E_+ + E_-)\cos(\alpha-\beta) - i(E_+ - E_-)\sin(\alpha-\beta)$, and $E_\alpha = -E_x\sin\alpha + E_y\cos\alpha = -i(E_+ - E_-)\cos(\alpha-\beta) - (E_+ + E_-)\sin(\alpha-\beta)$, where $E_\pm = \frac{1}{2}(E_x \pm iE_y)e^{\mp i\beta}$.

Using the velocity space flux in the perpendicular velocity direction ($\Gamma_\perp$) in Eq. (A.4), the flux in the gyrophase direction (Γ_α) in Eq. (A.5), and the flux in the parallel direction ($\Gamma_\parallel$) in Eq. (A.6), the quasilinear diffusion operator for species s is defined as,

$$Q(f_s) \equiv \frac{Z_s e}{m_s}\left[\frac{1}{v_\perp}\frac{\partial}{\partial v_\perp}(v_\perp\Gamma_\perp) + \frac{1}{v_\perp}\frac{\partial\Gamma_\alpha}{\partial\alpha} + \frac{\partial\Gamma_\parallel}{\partial v_\parallel}\right]. \tag{3.2}$$

For the energy transfer, the contribution of the flux in the gyrophase direction vanishes due to the integral over α, as shown in Eq. (A.9). However, the gyroaveraged quasilinear operator used for the energy transfer is not sufficient to calculate the toroidal momentum transfer, which has gyrophase dependent components. The total toroidal angular momen-

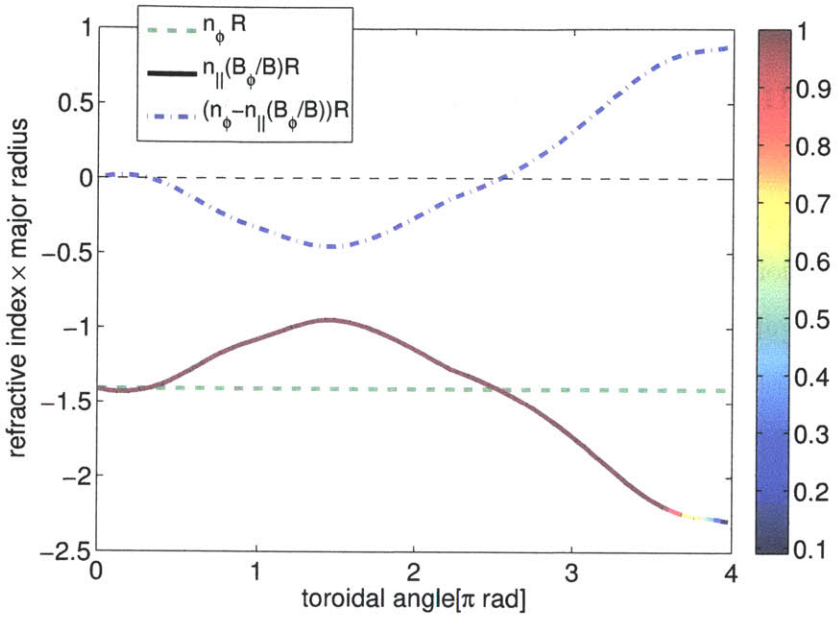

Figure 3-1: Evolution of the toroidal angular momentum of a LH wave in terms of the propagation toroidal angle from the launcher. The solid line is the toroidal projection of the parallel refractive index multiplied by the major radius ($n_{\|}(B_{\varphi}/B)R$), which is an important parameter for Landau damping. The color of the solid line is the normalized Poynting flux of a ray. The power of the LH wave is absorbed by electron Landau damping beyond toroidal angle 3.5π, where the color of the solid line changes from red to blue. In this power absorption region, $n_{\|}(B_{\varphi}/B)R$ is around -2.3, much higher than original toroidal refractive index multiplied by the major radius ($n_{\varphi}R \simeq -1.4$). This graph corresponds to one of the LH wave rays for the high current case ($I_p = 700kA$) in Alcator C-Mod with $B_{\varphi} = 5.3T$, major radius $R_0 = 0.67m$, minor radius $a = 0.22m$, core electron temperature $T_e = 3.5KeV$, core electron density $n_e = 1.2 \times 10^{20}m^{-3}$, initial $n_{\|} = -1.6$ and $P_{abs} = 0.8MW$. These profiles are calculated using the ray tracing technique in Genray-CQL3D [29]. Ray tracing can be problematic at the reflection point (toroidal angle=2.2π) where the characteristic length of the change of the plasma parameters is shorter than the wavelength. However, the upshift in $n_{\|}$ for strong damping (as shown beyond toroidal angle 3.5π) is widely seen in both ray tracing codes [106] and full wave codes [24, 25] for typical LH wave experimental parameters.

tum deposited by the wave on the electrons (torque) is

$$T_\varphi = 2\pi \int_{-\infty}^{\infty} dv_\parallel \int_0^{\infty} dv_\perp v_\perp \langle m_e R v_\varphi Q(f_e) \rangle \equiv T_\varphi^{\parallel} + \Delta T_\varphi^{\perp} + \Delta T_\varphi^{\alpha}, \tag{3.3}$$

where

$$T_\varphi^{\parallel} = eR \int_{-\infty}^{\infty} dv_\parallel \int_0^{\infty} dv_\perp v_\perp \int_0^{2\pi} d\alpha (\hat{\mathbf{z}} \cdot \hat{\boldsymbol{\varphi}}) \Gamma_\parallel \tag{3.4}$$

is the component of momentum transfer that one obtains when using the gyroaveraged quasilinear operator, whereas

$$\Delta T_\varphi^{\perp} = -eR \int_{-\infty}^{\infty} dv_\parallel \int_0^{\infty} dv_\perp v_\perp \int_0^{2\pi} d\alpha (-\cos\alpha (\hat{\mathbf{x}} \cdot \hat{\boldsymbol{\varphi}}) - \sin\alpha (\hat{\mathbf{y}} \cdot \hat{\boldsymbol{\varphi}})) \Gamma_\perp , \tag{3.5}$$

$$\Delta T_\varphi^{\alpha} = -eR \int_{-\infty}^{\infty} dv_\parallel \int_0^{\infty} dv_\perp v_\perp \int_0^{2\pi} d\alpha (\sin\alpha (\hat{\mathbf{x}} \cdot \hat{\boldsymbol{\varphi}}) - \cos\alpha (\hat{\mathbf{y}} \cdot \hat{\boldsymbol{\varphi}})) \Gamma_\alpha \tag{3.6}$$

are the contributions that appear when the complete dependence on the gyrophase is retained.

Using the perturbed distribution function and the expansion in Bessel functions described in Appendix A, the toroidal momentum transfer term in the parallel direction, $T_\varphi^{\parallel}$, becomes

$$\begin{aligned} T_\varphi^{\parallel} &= -\frac{\pi e^2 R}{m_e} \sum_{\mathbf{k}} \int_{-\infty}^{\infty} dv_\parallel \int_0^{\infty} dv_\perp 2\pi v_\perp \sum_n \delta(\omega - k_\parallel v_\parallel - n\Omega)(\hat{\mathbf{z}} \cdot \hat{\boldsymbol{\varphi}}) \\ &\times \frac{k_\parallel v_\perp^2}{\omega} |\chi_{\mathbf{k},n}|^2 L(f_{0,e}) = \sum_{\mathbf{k}} \left\{ \frac{k_\parallel}{\omega} P_{abs,\mathbf{k}} R(\hat{\mathbf{z}} \cdot \hat{\boldsymbol{\varphi}}) \right\} \\ &= \sum_{\mathbf{k}} \left\{ \frac{n_\parallel}{c} P_{abs,\mathbf{k}} R(\hat{\mathbf{z}} \cdot \hat{\boldsymbol{\varphi}}) \right\}, \end{aligned} \tag{3.7}$$

where $\chi_{\mathbf{k},n} = E_{\mathbf{k},\parallel} J_n \frac{v_\parallel}{v_\perp} + E_{\mathbf{k},+} J_{n-1} + E_{\mathbf{k},-} J_{n+1}$ is the effective electric field, $P_{abs,\mathbf{k}}$ is the wave power absorption in Eq. (A.11) and $J_n(\lambda)$ are the Bessel functions of the first kind with integer order n. The operator $L(f_0) = \left(1 - \frac{k_\parallel v_\parallel}{\omega}\right) \frac{1}{v_\perp} \frac{\partial f_0}{\partial v_\perp} + \frac{k_\parallel v_\perp}{\omega} \frac{1}{v_\perp} \frac{\partial f_0}{\partial v_\parallel}$ is introduced in [17, 21]. See Appendix E for the detailed derivation of Eq. (3.7). The piece of the momentum transfer $T_\varphi^{\parallel}$ is directly related to the gyroaveraged quasilinear diffusion operator used to calculate the power absorption (compare Eq. (3.7) with Eq. (A.11)). The direction of diffusion is determined by the characteristics of the operator $L(f_0)$ (i.e. the tangents to

the contours $v_\perp^2 + \left(v_\parallel - \frac{\omega}{k_\parallel}\right)^2$ =constant), and the magnitude of the diffusion is determined by the projection of the distribution function gradient onto these characteristics [17, 21] (see Figure 3-3).

In particular, for electron Landau damping of the LH wave (i.e. $\omega = k_\parallel v_\parallel$), this piece of the toroidal momentum transfer can be simplified to the following equation within a small error of $O\left(\left(\frac{k_\perp v_\perp}{\Omega_e}\right)^2 \frac{\Omega_e}{\omega}\right)$:

$$\begin{aligned} T^{\parallel}_{\varphi,ELD} &\simeq -\frac{\pi e^2 R}{m_e} \sum_{\mathbf{k}} \int_{-\infty}^{\infty} dv_\parallel \int_0^{\infty} dv_\perp 2\pi v_\perp \delta(\omega - k_\parallel v_\parallel) |E_{\mathbf{k},\parallel}|^2 \frac{\partial f_{e0}}{\partial v_\parallel} J_0^2(\lambda)(\hat{\mathbf{z}} \cdot \hat{\boldsymbol{\varphi}}) \\ &= \int_{-\infty}^{\infty} dv_\parallel \int_0^{\infty} dv_\perp 2\pi v_\perp m_e R v_\varphi \frac{\partial}{\partial v_\parallel} \left(\langle \overline{D_{ql}^{ELD}} \rangle \frac{\partial f_{e0}}{\partial v_\parallel} \right), \end{aligned} \tag{3.8}$$

where the gyroaveraged quasilinear diffusion coefficient for electron Landau damping is $\langle \overline{D_{ql}^{ELD}} \rangle = \frac{\pi e^2}{m_e^2} \sum_{\mathbf{k}} \delta(\omega - k_\parallel v_\parallel) |E_{\mathbf{k},\parallel}|^2 J_0^2(\lambda)$ and it is the same as the coefficient given in Eq. (2.1). The factor of two difference between the above diffusion coefficient and Eq. (2.1) arises because the summation in k-space picks up contributions from $Re(\omega_k)$ and $Re(\omega_{-k})$. For Landau damping, the quasilinear diffusion happens only in the parallel direction (see Figure 3-3).

Equation (3.8) exemplifies the problems that appear if the gyroaveraged quasilinear diffusion operator is employed to evaluate toroidal angular momentum transfer. Using the typical gyroaveraged quasilinear diffusion coefficient, one can only evaluate the parallel momentum transfer $T_\varphi^{\parallel}$ instead of the full momentum transfer T_φ. For the rest of the toroidal momentum transfer, I need the quasilinear diffusion operator before the gyrophase averaging,

$$\begin{aligned} \Delta T_\varphi^{\perp} + \Delta T_\varphi^{\alpha} &= -eR \sum_{\mathbf{k}} \int_{-\infty}^{\infty} dv_\parallel \int_0^{\infty} dv_\perp 2\pi v_\perp \int_0^{2\pi} \frac{d\alpha}{2\pi} \Bigg[E^*_{\mathbf{k},\parallel} \frac{k_\perp v_\parallel}{\omega} \\ &\times (\cos\beta(\hat{\mathbf{x}} \cdot \hat{\boldsymbol{\varphi}}) + \sin\beta(\hat{\mathbf{y}} \cdot \hat{\boldsymbol{\varphi}})) + \left(1 - \frac{k_\parallel v_\parallel}{\omega}\right)(E^*_{\mathbf{k},x} \hat{\mathbf{x}} \cdot \hat{\boldsymbol{\varphi}} + E^*_{\mathbf{k},y} \hat{\mathbf{y}} \cdot \hat{\boldsymbol{\varphi}}) \\ &+ i\left(\frac{k_\perp v_\perp}{\omega}\right)(E^*_{\mathbf{k},+} - E^*_{\mathbf{k},-})(\sin\alpha(\hat{\mathbf{x}} \cdot \hat{\boldsymbol{\varphi}}) - \cos\alpha(\hat{\mathbf{y}} \cdot \hat{\boldsymbol{\varphi}})) \Bigg] f_{\mathbf{k}}. \end{aligned} \tag{3.9}$$

Using Appendix E, I can simplify this equation to

$$\Delta T_{\varphi}^{\perp} + \Delta T_{\varphi}^{\alpha} = -\frac{\pi e^2 R}{m_e} \sum_{\mathbf{k}} \int_{-\infty}^{\infty} dv_{\parallel} \int_{0}^{\infty} dv_{\perp} 2\pi v_{\perp}$$
$$\times \sum_n \delta(\omega - k_{\parallel} v_{\parallel} - n\Omega)(\cos\beta(\hat{\mathbf{x}} \cdot \hat{\boldsymbol{\varphi}}) + \sin\beta(\hat{\mathbf{y}} \cdot \hat{\boldsymbol{\varphi}})) \frac{k_{\perp} v_{\perp}^2}{\omega} |\chi_{\mathbf{k},n}|^2 L(f_{0,e})$$
$$= \sum_{\mathbf{k}} \left(\frac{\mathbf{k}_{\perp} \cdot \hat{\boldsymbol{\varphi}}}{\omega} P_{abs,\mathbf{k}} R \right) = \sum_{\mathbf{k}} \left\{ \frac{n_{\perp}}{c} P_{abs,\mathbf{k}} R(\cos\beta(\hat{\mathbf{x}} \cdot \hat{\boldsymbol{\varphi}}) + \sin\beta(\hat{\mathbf{y}} \cdot \hat{\boldsymbol{\varphi}})) \right\}. \quad (3.10)$$

However, the perpendicular momentum transfer, $\Delta T_{\varphi}^{\perp} + \Delta T_{\varphi}^{\alpha}$, cannot change the gyroaveraged distribution function as shown in Fig. 3-3. As a result, it cannot drive a parallel current, while a perpendicular energy transfer (e.g. in the electron cyclotron current drive (ECCD) [7]) can drive parallel current through collisions because it can change the gyroaveraged distribution function in the perpendicular direction.

In conclusion, for any resonance (e.g. cyclotron, Landau damping), the total toroidal angular momentum transfer according to Eq. (3.7) and Eq. (3.10) is

$$T_{\varphi} = T_{\varphi}^{\parallel} + \Delta T_{\varphi}^{\perp} + \Delta T_{\varphi}^{\alpha} = \sum_{\mathbf{k}} \left(\frac{\mathbf{k} \cdot \hat{\boldsymbol{\varphi}}}{\omega} P_{abs,\mathbf{k}} R \right), \quad (3.11)$$

as expected [98, 107, 115, 116, 117, 118]. The toroidal angular momentum absorbed in the plasma is equal to the launched momentum only when both the parallel and the perpendicular momentum are taken into account correctly, as shown in Fig. 3-2 (b).

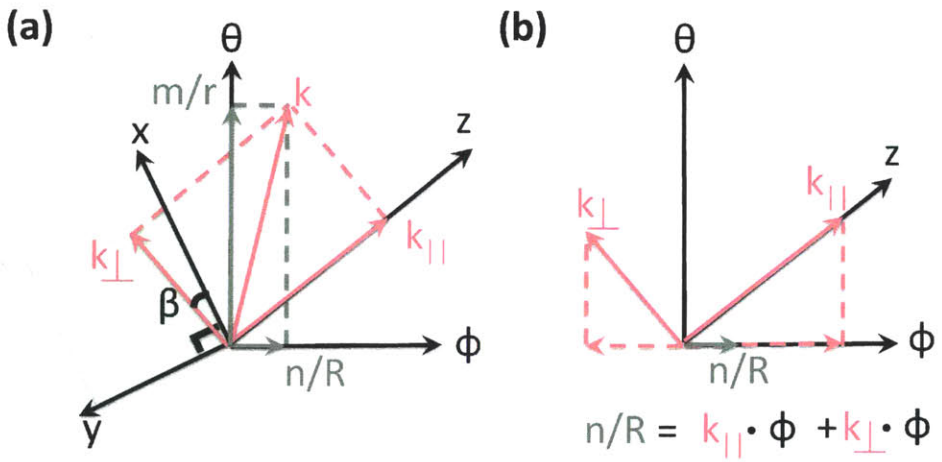

Figure 3-2: (a) Sketch of a wave vector $\mathbf{k} = (m/r)\hat{\boldsymbol{\theta}} + (n/R)\hat{\boldsymbol{\varphi}} = \mathbf{k}_\perp + \mathbf{k}_\parallel$ in a parallel (z)-perpendicular (x, y) coordinate system and in a toroidal (φ)-poloidal (θ) coordinate system. Here, n and m are the toroidal and poloidal wave number, respectively, and the radial wave vector is not represented, because it cannot contribute to the toroidal momentum. For the LH wave, the component $k_\parallel$ has a bigger toroidal projection than the initial toroidal component n/R at the launcher due to poloidal coupling. (b) Sketch of the toroidal momentum conservation. The sum of the toroidal projection of $k_\parallel$ and $k_\perp$ is equal to the launched toroidal wave vector n/R.

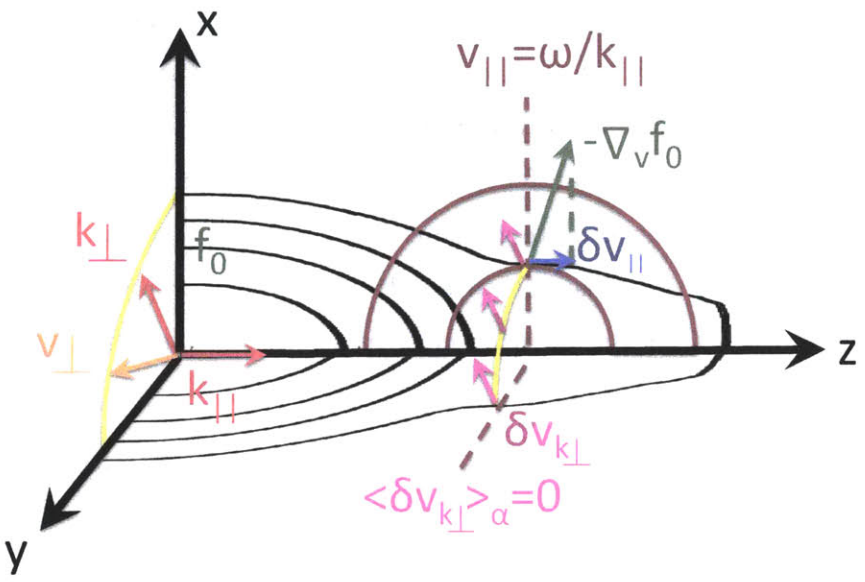

Figure 3-3: Sketch of the quasilinear diffusion direction and magnitude in $v_\parallel - v_\perp$ space (i.e. a parallel (z)-perpendicular (x, y) coordinate system). The black contours in the $x-z$ plane and the $y-z$ plane are the contours of the gyroaveraged distribution function and the brown contours are the characteristics of the operator $L(f_0)$. The diffusion direction is tangential to the characteristics, $v_\perp^2 + \left(v_\parallel - \frac{\omega}{k_\parallel}\right)^2$ =constant. For Landau damping, the intensity of the diffusion is determined by the projection of $\nabla_v f_0$ onto the characteristics of the operator $L(f_0) = 0$ at $v_\parallel = \omega/k_\parallel$. The diffusion in velocity space results in an average increase of the parallel velocity, $\delta v_\parallel$. The perpendicular momentum transfer $\delta v_{k_\perp}$ has the direction of $\mathbf{k}_\perp$, but its effect on the distribution function vanishes due to the fast gyromotion (the averaged perpendicular acceleration represented by the pink arrows in the yellow circle in the x-y plane vanishes).

3.3 Electron radial drift due to waves

In this section, I investigate different types of electron radial drifts that can be induced by the resonant momentum transfer from the LH wave. These electron radial drifts will be related to the momentum transfer mechanisms from electrons to ions in the next section. The dominant radial electron drift comes from toroidal momentum transfer in the perpendicular plane (Sec. 3.3.1). The Lorentz force in the toroidal direction due to the radial drift is comparable ($O(100\%)$) to the LH wave momentum source, giving a sizeable radial drift (O(1mm/sec)) that has an outward direction in tokamaks. Other radial drifts induced by the wave parallel momentum transfer are relatively small. The passing electron radial drift caused by the resonance gives a Lorentz force which is $O(10\%)$ of the LH wave momentum (Sec. 3.3.2), and the Ware-like LH wave induced pinch by trapped electrons [103] is associated with only $O(1\%)$ of the LH wave momentum transfer (Sec. 3.3.3).

3.3.1 Outward electron radial drift due to perpendicular wave momentum

The quasilinear term due to the LH wave in the Fokker-Plank equation gives rise to a correction to the electron distribution function, $f_e^{LH} = f_e' - f_e$, where f_e' and f_e are the electron distribution function with and without the LH wave respectively. For convenience, I write f_e^{LH} as a function of kinetic energy $\mathcal{E} = \frac{1}{2}v^2$, magnetic moment $\mu = \frac{v_\perp^2}{2B}$, and the gyrophase angle α. Note that the electron distribution function $f_{0,e}$ in Chapter 2 is gyroaveraged, but the gyrophase dependence is included in this chapter to consider the perpendicular momentum transfer. The equation for f_e^{LH} in these variables is

$$\frac{\partial f_e^{LH}}{\partial t} - \frac{e}{m_e}(v_\parallel \hat{\mathbf{b}} + \mathbf{v_d}) \cdot \nabla\phi \frac{\partial f_e^{LH}}{\partial \mathcal{E}} + v_\parallel \hat{\mathbf{b}} \cdot \nabla f_e^{LH} + \mathbf{v_d} \cdot \nabla f_e^{LH} + \Omega_e \frac{\partial f_e^{LH}}{\partial \alpha}$$
$$= C_e(f_e^{LH}) + Q(f_e'), \tag{3.12}$$

where ϕ is the background potential, $C_e(f_e)$ is the linearized collision operator to the order of interest (i.e. $C_e(f_e^{LH}) = C_{ee}(f_e^{LH}, f_e) + C_{ee}(f_e, f_e^{LH}) + \sum_i C_{ei}(f_e^{LH}, f_i)$), and $\mathbf{v_d}$ is the ∇B and curvature drift. In Eq. (3.12) I only consider the long wavelength and slowly evolving piece of the distribution function because the quasilinear term affects mainly the background distribution function. The size of the first term is small after the plateau is established in the

electron distribution function due to the balance between quasilinear diffusion and collisions as explained in Chapter 2. The temporal changes are eventually determined by the gyro-Bohm transport time scale, $\partial/\partial t \sim D_{gB,i}/a^2 \sim \rho_\star^2 v_{ti}/a \sim \sqrt{m_i/m_e}\rho_{\star,e}^2 v_{te}/a$, making it much smaller than other terms in (3.12). Here, $D_{gB,i}$ is the gyro-Bohm diffusion coefficient for ions defined in Eq. (1.3), a is the minor radius, v_{ti} and v_{te} are the ion and electron thermal velocity, respectively, and $\rho_\star = \rho_i/a \ll 1$, $\rho_{\star,e} = \rho_e/a \sim \sqrt{m_e/m_i}\rho_\star$ are the small ratios of ion and electron Larmor radius over the radial scale length, respectively. The third term in Eq. (3.12) is of order $v_{te}f_e^{LH}/(qR)$, where q is the safety factor and R is the major radius. The second and fourth terms in Eq. (3.12) are smaller than the third term by $(B/B_\theta)\rho_{\star,e}$. The gyromotion term $\Omega_e \frac{\partial f_e^{LH}}{\partial \alpha}$ is much larger than any of the other terms (i.e. $v_\parallel \nabla_\parallel f_e^{LH} / \left(\Omega_e \frac{\partial f_e^{LH}}{\partial \alpha}\right) \sim a\rho_{\star,e}/(qR) \ll 1$ and $C(f_e^{LH}) / \left(\Omega_e \frac{\partial f_e^{LH}}{\partial \alpha}\right) \sim \nu_e/\Omega_e \ll 1$). Then the lowest order equation is trivial, $\Omega_e \frac{\partial f_{0,e}^{LH}}{\partial \alpha} = 0$ (i.e. $f_{0,e}^{LH} = \langle f_e^{LH} \rangle$), and the next order equation is

$$v_\parallel \nabla_\parallel f_{0,e}^{LH} + \Omega_e \frac{\partial f_{1,e}^{LH}}{\partial \alpha} = C_e(f_{0,e}^{LH}) + Q(f_e'). \tag{3.13}$$

Here, I have neglected the time derivative term, the perpendicular drift term, and the term due to the background potential. The gyrophase independent part can be obtained by taking the gyroaverage of Eq. (3.13),

$$v_\parallel \nabla_\parallel f_{0,e}^{LH} = C_e(f_{0,e}^{LH}) + \langle Q(f_e') \rangle, \tag{3.14}$$

where $C_e(f_{0,e}^{LH}) = \langle C_e(f_{0,e}^{LH}) \rangle$ is used for the gyrophase independent distribution function. The above equation gives the steady state solution to Eq. (2.7). The quasilinear term balances with the collision operator and the parallel streaming term. The gyrophase dependent part, $\widetilde{f_{1,e}^{LH}} = f_{1,e}^{LH} - \langle f_{1,e}^{LH} \rangle$, is obtained from the gyrophase dependent contribution to Eq. (3.13), giving

$$\begin{aligned} \Omega_e \frac{\partial \widetilde{f_{1,e}^{LH}}}{\partial \alpha} &= Q(f_e') - \langle Q(f_e') \rangle \\ &= -\frac{e}{m_e}\left[\frac{1}{v_\perp}\frac{\partial}{\partial v_\perp} v_\perp (\Gamma_\perp - \langle \Gamma_\perp \rangle) + \frac{1}{v_\perp}\frac{\partial \Gamma_\alpha}{\partial \alpha} + \frac{\partial}{\partial v_\parallel}(\Gamma_\parallel - \langle \Gamma_\parallel \rangle)\right]. \end{aligned} \tag{3.15}$$

Its solution is

$$\begin{aligned}\widetilde{f_{1,e}^{LH}} &= -\frac{e}{m_e\Omega_e}\int d\alpha\left[\frac{1}{v_\perp}\frac{\partial}{\partial v_\perp}v_\perp(\Gamma_\perp-\langle\Gamma_\perp\rangle)+\frac{1}{v_\perp}\frac{\partial\Gamma_\alpha}{\partial\alpha}+\frac{\partial}{\partial v_\parallel}(\Gamma_\parallel-\langle\Gamma_\parallel\rangle)\right] \\ &\sim \frac{\Delta T_\varphi^\perp+\Delta T_\varphi^\alpha}{n_e m_e v_{te}R\Omega_e}f_{Me}. \end{aligned} \tag{3.16}$$

Thus, the collisional toroidal friction due to the gyrophase dependent piece of the distribution function is much smaller than the corresponding RF force,

$$\int dv^3(m_eRv_\varphi)C(\widetilde{f_{1,e}^{LH}}) \sim \left(\frac{\nu_e}{\Omega_e}\right)\left(\Delta T_\varphi^\perp+\Delta T_\varphi^\alpha\right), \tag{3.17}$$

and most of the perpendicular momentum transfer is balanced by the Lorentz force $\int dv^3(m_eRv_\varphi)\Omega_e\frac{\partial\widetilde{f_{1,e}^{LH}}}{\partial\alpha}$ from Eq. (3.15).

The radial particle flux can be obtained from

$$\langle\boldsymbol{\Gamma}_\mathbf{e}\cdot\nabla\psi\rangle_s \simeq \left\langle\int dv^3 f_{0,e}^{LH}\mathbf{v_d}\cdot\nabla\psi\right\rangle_s+\left\langle\int dv^3\widetilde{f_{1,e}^{LH}}v_\perp\hat{\boldsymbol{\rho}}\cdot\nabla\psi\right\rangle_s, \tag{3.18}$$

where $\boldsymbol{\Gamma}_\mathbf{e}$ is the electron particle flux due to the correction f_e^{LH}. From the steady state Fokker-Planck equation given in Eq. (3.13), taking the moment $(m_ev_\varphi R)$ and a flux-surface average of the resulting moment equation, I can relate the radial pinch $\langle\boldsymbol{\Gamma}_\mathbf{e}\cdot\nabla\psi\rangle_s$ to the correction f_e^{LH} by

$$\begin{aligned}\frac{e}{c}\langle\boldsymbol{\Gamma}_\mathbf{e}\cdot\nabla\psi\rangle_s &\simeq \left\langle\frac{n_\varphi-n_\parallel(\hat{\mathbf{z}}\cdot\hat{\boldsymbol{\varphi}})}{c}RP_{abs}\right\rangle_s \\ &+ \left\langle(\hat{\mathbf{z}}\cdot\hat{\boldsymbol{\varphi}})R\int d^3v m_e v_\parallel\left[C(f_{0,e}^{LH})+\langle Q(f_e')\rangle\right]\right\rangle_s. \end{aligned} \tag{3.19}$$

To obtain Eq. (3.19), I use the fact that the first and second term on the left hand side of Eq. (3.13) give the first and second term on the right hand side of Eq. (3.18), respectively. The right hand side of Eq. (3.19) is obtained by decomposing the right hand side of Eq. (3.13) into the gyrophase dependent and gyrophase independent pieces,

$$C_e(f_e^{LH})+Q(f_e') \simeq \left[Q(f_e')-\langle Q(f_e')\rangle\right]+\left[C_e(f_{0,e}^{LH})+\langle Q(f_e')\rangle\right]. \tag{3.20}$$

The second term on the right hand side of Eq. (3.19) is the parallel force balance obtained

from the second term on the right hand side of Eq. (3.20), which will be discussed in the next subsection. The first term on the right hand side of Eq. (3.19) is the toroidal projection of the perpendicular wave momentum transfer, $\left(\Delta T_{\varphi}^{\perp} + \Delta T_{\varphi}^{\alpha}\right)$, which comes from the first term on the right hand side of Eq. (3.20). In Eq. (3.20) I have already neglected the perpendicular collisional friction (see Eq. (3.17)).

Collisions transfer most of the parallel wave momentum to the ions, but the rest of the toroidal angular momentum (e.g. $n_{\varphi}R - n_{\|}(B_{\varphi}/B)R \simeq 0.9$ in Fig. 3-1) remains and it has the opposite toroidal direction to the original toroidal angular wave momentum, giving an electron outward pinch that is opposite to the inward pinch predicted in previous work [14, 103, 105]. Physically, the outward radial pinch comes from the effect of the perpendicular wave momentum transfer $\Delta T_{\varphi}^{\perp} + \Delta T_{\varphi}^{\alpha}$ on the gyromotion (see Fig. 3-4 (a)). This electron pinch is still very small compared to the Ware pinch [119]. For example, if $1MW$ of LH wave power is locally absorbed in a volume of 0.1 m^3 where the plasma density is $10^{20}\mathrm{m}^{-3}$, the poloidal magnetic field is $B_{\theta} = 0.5T$, and the refractive index is $n_{\varphi} - n_{\|}(B_{\varphi}/B) = 1$, then the electron outward radial pinch is about 4 mm/s which is a hundred times smaller than the Ware pinch for a DC toroidal electric field of 0.2 V/m.

The new outward radial particle pinch in this section does not cause a significant radial transport of the toroidal angular momentum because it is typically smaller than the turbulent particle pinch. Instead, the outward radial electron pinch only transfers the toroidal momentum from the electrons to the ions because the ions follow the radial motion of the electrons due to the ambipolarity condition, as will be discussed in Sec. 3.4.

3.3.2 Passing electron radial drift due to parallel wave momentum

To solve for the gyrophase independent perturbation $\left\langle f_e^{LH} \right\rangle$ due to the LH wave in Eq. (3.14), I use a subsidiary expansion of $f_{0,e}^{LH} = f_{0,e}^{LH,0} + f_{0,e}^{LH,1} + ...$, in the small ratio of the collision frequency over the transit frequency in the banana regime. The lowest order equation is $\nabla_{\|} f_{0,e}^{LH,0} = 0$, implying that $f_{0,e}^{LH,0}$ is a flux function. The next order equation is

$$v_{\|}\nabla_{\|} f_{0,e}^{LH,1} = C_e(f_{0,e}^{LH,0}) + \left\langle Q(f_e') \right\rangle . \tag{3.21}$$

Taking a bounce average of (3.21), the left hand side of (3.21) vanishes,

$$\left\langle C_e(f_{0,e}^{LH,0}) + \langle Q(f_e') \rangle \right\rangle_b = 0. \tag{3.22}$$

Again, the above equation gives the steady state solution to Eq. (2.8). According to Eq. (B.3), for passing particles this equation is equivalent to

$$\left\langle \frac{B}{v_\parallel} \left(C_e(f_{0,e}^{LH,0}) + \langle Q(f_e') \rangle \right) \right\rangle_s = 0. \tag{3.23}$$

In general, the solution $f_{0,e}^{LH,0}$ to equation (3.23) does not make the second term on the right hand side of Eq. (3.19) vanish, giving a non-zero radial drift due to the passing electrons. This imbalance comes from the variation of $v_\parallel$, B and R along the orbit, which is of the order of the local aspect ratio, $O(r/R)$. Here, r is the radius of a flux surface from the magnetic axis. For the electrons resonant with the LH wave, the effect of the change of $v_\parallel$ along the orbit is negligible because most resonant electrons have much larger parallel velocity than perpendicular velocity (i.e. small magnetic moment, $\mu \simeq 0$) due to the high phase velocity of the wave in the parallel direction. The non-vanishing contribution to the radial pinch is due to the competition between the localized wave power absorption within a flux surface and the collisions that occur over the whole flux surface.

Physically, this pinch can be explained by how the passing orbit of a single electron is changed by the resonance. The canonical angular momentum of the electron $\psi^* = \psi + I v_\parallel/\Omega_e$ determines the radial deviation of the electron orbit from the flux surface ψ due to the curvature and ∇B drifts. Here $I = RB_\varphi$ is a flux function to lowest order. After the resonance with the negative $k_\parallel$ of the LH wave, the absolute value of the negative velocity of the resonant electrons is increased by $|\Delta v_\parallel|$ due to the absorbed wave power. Accordingly, the change of the canonical momentum is $\Delta\psi^* = I\Delta v_\parallel/\Omega_e < 0$, where the gyrofrequency Ω_e is evaluated at the resonance point within the flux surface. Assuming the low frequency collisions cause the resonant electron to lose its momentum only after many transits, I can use the temporally averaged radial location to describe its radial motion. The increase in

the bounce averaged radial position of the particle is

$$\Delta \langle \psi \rangle_b = \langle \psi_2 \rangle_b - \langle \psi_1 \rangle_b = \Delta\psi^* - \left\{ \left\langle \left(\frac{I v_\parallel}{\Omega_e} \right)_2 \right\rangle_b - \left\langle \left(\frac{I v_\parallel}{\Omega_e} \right)_1 \right\rangle_b \right\} \tag{3.24}$$

$$= \frac{I \Delta v_\parallel}{\Omega_e} - \frac{m_e c I}{e} \left(\frac{\oint_2 dl/B}{\tau_{b2}} - \frac{\oint_1 dl/B}{\tau_{b1}} \right) \tag{3.25}$$

$$\simeq I \Delta v_\parallel \left(\frac{1}{\Omega_e} - \frac{1}{\Omega_{e0}} \right). \tag{3.26}$$

Here, the values with the subscripts 1 and 2 are before and after the resonance, respectively, and τ_b is the bounce time. From Eq. (3.24) to Eq. (3.25), Eq. (B.3) is used. From Eq. (3.25) to Eq. (3.26), I neglect the radial displacement due to the poloidal variation of the parallel velocity because of the small magnetic moment ($\mu \simeq 0$). The average of $v_\parallel/B$ in Eq. (3.24) and Eq. (3.25) is approximated by the value of $v_\parallel/B$ obtained using the magnetic field at the magnetic axis. This approximation can be justified by a small inverse aspect ratio expansion. The frequency Ω_{e0} is the gyrofrequency at the magnetic axis. Equation (3.26) means that the temporally averaged particle radial flux due to the resonance is negative for a low field side resonance (inward radial pinch) and positive for a high field side resonance (outward radial pinch), as shown in Fig. 3-4 (b). The increase in the curvature drift due to the increase in the parallel velocity after the resonance results in the different passing orbits depending on the resonance location on the flux surface. This radial drift is included in the second term on the right hand side of Eq. (3.19) as the competition between the localized wave power absorption within a flux surface and the collisions that occur over the whole flux surface. For a typical small inverse aspect ratio tokamak, this imbalance is small, about 10% (O(r/R)) of the total momentum transfer.

3.3.3 Trapped electron radial drift due to parallel wave momentum

For trapped electrons, since odd functions in $v_\parallel$ vanish under the bounce average according to Eq. (B.4), Eq. (3.22) becomes

$$\left\langle C_e(f_{0,e}^{LH,0}) \right\rangle_b = - \left\langle \langle Q^{even}(f_e') \rangle \right\rangle_b . \tag{3.27}$$

The trapped particle contribution to the distribution function $f_{0,e}^{LH}$ is an even function of $v_{\|}$ because the bounce averaged quasilinear term is even. Two trapped electrons at the outer-midplane that have opposite parallel velocities have the same electron Landau damping resonance at the same point in their banana orbits due to the small electron banana width (see Fig. 3-4 (c)). The non-zero $f_{0,e}^{LH}$ due to the LH wave can be understood as follows: a trapped electron is accelerated only when it resonates with the wave, that is, when its velocity is the same as the wave phase velocity, and this acceleration continues every transit until it collides. As a result, it has an open trajectory that moves inward every bounce. There is no net gain of toroidal angular momentum for the trapped electron because $f_{0,e}^{LH}$ is an even function, but there is a gain of canonical angular momentum that leads to a Ware-like LH induced pinch. This pinch is the contribution of the trapped electrons to the second term on the right hand side of Eq. (3.19). The LH wave trapped electron pinch is tiny, because the power absorption by trapped electron is less than 1% of total wave power due to the small size of the population of trapped electrons resonant with the LH wave phase velocity ($\omega/k_{\|} \sim 3v_{th} - 10v_{th}$) . It results in a very small contribution to the radial pinch (approximately less than 0.1mm/s).

The mechanism behind the radial pinch by trapped electrons is similar to the mechanism of the outward radial pinch due to the gyromotion described in section 3.3.1. Instead of considering the effect of the acceleration on the gyromotion, one needs to consider its effect on the banana orbit (compare Fig. 3-4 (a) and Fig. 3-4 (c)).

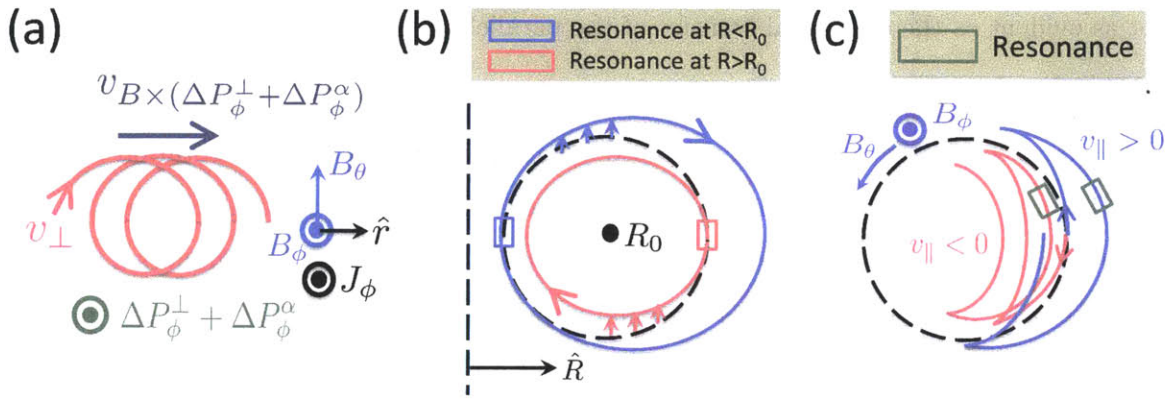

Figure 3-4: (a) Sketch of the outward radial drift during the gyromotion due to the perpendicular momentum transfer, $\left(\Delta T_\varphi^\perp + \Delta T_\varphi^\alpha\right)$. The direction of the toroidal component of the perpendicular force is the same as the direction of the plasma current J_φ. (b) Sketch of the poloidal cross section of the trajectories for two passing electrons that receive wave parallel momentum at the inner-midplane (blue) and the outer-midplane (red), respectively. The dashed black line is the transit orbit before the resonances. Due to the increased curvature drift (upward direction) after the resonance, the passing electron orbits are different depending on the resonance location. The temporally averaged radial flux is outward for a resonance at $R < R_0$ and inward for a resonance at $R > R_0$. (c) Sketch of the poloidal cross section of the trajectories for trapped electrons that receive wave parallel momentum. The dashed black line is a flux surface. For both signs of $v_\parallel$ at the outer-midplane on the flux surface, the orbits move inward and increase their width with every bounce.

3.4 Momentum transfer from electrons to ions

Once the toroidal momentum of the LH wave is transferred to the electrons by resonance, most of the parallel momentum is transferred to the ions by electron-ion collisions, but the perpendicular momentum is balanced not by collisions but by the Lorentz force due to the outward electron radial drift as shown in Sec. 3.3. In this section, I describe how the perpendicular momentum is transferred from electrons to ions because the mechanism is not as evident as the collisional transfer of the parallel momentum.

The electron radial drifts due to LH waves cause charge separation. The radial non-ambipolar electron pinch has been proposed as an explanation for the ion rotation induced by LH waves in references [14, 103, 105]. These references argued that the counter-current direction momentum transfer from the LH wave to the trapped electrons induces a radially inward pinch, and it results in an additional inward radial electric field to ensure ambipolarity. The excess radial electric field is presumed to lead to ion toroidal rotation in the counter-current direction due to the radial force balance for ions [103, 104],

$$\Delta E_r + \frac{1}{c}\left(B_\varphi \Delta V_\theta - B_\theta \Delta V_\varphi\right) \simeq 0, \tag{3.28}$$

where ΔE_r, ΔV_θ, and ΔV_φ are the change in the radial electric field, the ion poloidal velocity, and the ion toroidal velocity due to the lower hybrid wave injection, respectively. The change in the ion radial pressure is neglected.

However, this argument based on the excess radial electric field given in [103, 104] is misleading and does not describe the main mechanism behind the change in the ion torodial rotation due to lower hybrid waves. This argument ignores many important aspects of the problems. First, the outward electron radial drift due to the perpendicular force is much larger than the inward trapped electron pinch as shown in Sec. 3.3. Second, the excess radial electric field due to the non-ambipolar radial drift cannot determine the toroidal rotation directly, because the excess electric field changes its value to satisfy Eq. (3.28) as the poloidal rotation decays in an ion-ion collision time while ΔV_φ remains constant [55, 120, 121], finally giving

$$\Delta E_r' \simeq \frac{1}{c} B_\theta \Delta V_\varphi. \tag{3.29}$$

Here, $\Delta E_r'$ is the change in the radial electric field after the poloidal rotation decays, giving $\Delta E_r' \neq \Delta E_r$. Last but not least, the toroidal rotation is controlled primarily by turbulent radial transport of torodial angular momentum [64].

The temporal evolution of the radial electric field due to the non-ambipolar radial drift affects both poloidal and toroidal rotation in times shorter than the ion-ion collision time. The poloidal and toroidal rotation are affected by different viscosities in a tokamak. After the poloidal flow decays due to strong collisional viscosity in an ion-ion collision time scale [55, 120, 121], the ambipolarity condition is satisfied and the excess electric field due to the non-ambipolar radial drift changes to satisfy Eq. (3.29). Finally, the toroidal rotation obtained by balancing the external torque and the turbulent radial momentum transport in Eq. (3.33) can be used to calculate the radial electric field using radial force balance and neoclassical theory.

Until the ions follow electrons with same speed to satisfy ambipolarity, the temporal evolution of the radial electric field follows the sequence below:

First, in a very short time period longer than an ion gyration period and electron bounce time, but shorter than electron collision time ($L_\parallel/v_{te} \sim \Omega_e^{-1} < t \ll \nu_e^{-1}$, e.g. 10^{-9} sec $< t \ll 10^{-6}$ sec for Alcator C-Mod), the depletion of electrons due to the electron radial drift changes the electrostatic potential $\phi(\psi)$, which varies only radially if a poloidally uniform radial drift is assumed. In the time scale of the electron bounce period, the poloidally uniform potential couples with the spectral modes having finite poloidal mode number through the curvature and ∇B radial drifts. These modes with non-zero poloidal mode number due to the electron bounce motion are similar to the geodesic acoustic modes (GAM) due to the ion bounce motion [122, 123]. However, in this case, the ion motion only contributes through the classical polarization due to the ion gyration, because the time scale is too short to affect the ion bounce motion. The modes with non-zero poloidal mode number are strongly damped due to electron Landau damping, and only the mode of the potential with zero poloidal mode number remains.

Second, after an electron collision time and an ion bounce time but before an ion collisional time ($\nu_e^{-1} \sim L_\parallel/v_{ti} < t \ll \nu_{ii}^{-1}$, e.g. 10^{-6} sec $< t \ll 10^{-4}$sec for Alcator C-Mod), the electron collisions result in the decay of the electron poloidal flow that occurs due to the potential $\phi(\psi)$. Ions start to shield the potential by neoclassical polarization due to ion bounce motion which is much stronger than the shielding by the classical polarization [54].

Lastly, after ion-ion collision time ($\nu_{ii}^{-1} < t$, e.g. 10^{-4} sec $< t$ for Alcator C-Mod), the ion poloidal rotation decays due to the strong ion collisional viscosity and only the ion toroidal flow remains [55]. In this time scale, the electron polarization due to the radial electric field is negligible compared to the ion polarization, because they have the same polarization mechanisms but the electron Larmor radius is much smaller than the ion Larmor radius. Then, the quasineutrality condition obtained by including the ion polarization is equivalent to the ion toroidal force balance in Eq. (3.33) without the radial current. Thus, ambipolarity is satisfied and the radial electric field is self-consistently determined by Eq. (3.33) for the evolution of the toroidal angular momentum.

After ambipolarity is satisfied, the ion radial drifts, which have the same speed as the electron radial drifts, generate a Lorentz force in the toroidal direction. The size of the toroidal angular momentum transfer due to the Lorentz force is the same as the momentum transfer due to the electron radial drift in Eq. (3.19). Because the electron radial pinch is dominantly driven by the perpendicular momentum piece of the lower hybrid waves, the Lorentz force caused by the ion radial drifts acting on the ion toroidal motion is the main transfer mechanism of perpendicular wave momentum to ions.

3.5 Review of momentum transfer

In Sec. 3.1, 3.2, 3.3 and 3.4, I proved that the toroidal angular momentum of the lower hybrid wave at the launcher is fully transferred to the ions. This transfer occurs after electron-ion collisions transfer the parallel momentum, and after the radial electric field due to the electron non-ambipolar radial flux settles into steady state in an ion-ion collision time. In this section, the different time scales are summarized, and the momentum transfer in each channel is compared with measurements. In addition, I derive an ion momentum transport equation that also proves that the full toroidal momentum is transferred from lower hybrid waves to ions.

3.5.1 Ion momentum equation

The Fokker-Planck equation for electrons with a quasilinear diffusion term due to the lower hybrid waves is,

$$\frac{\partial f_e}{\partial t} + \mathbf{v}\cdot\nabla f_e + \left(\frac{e}{m_e}\nabla\phi - \Omega_e \mathbf{v}\times\hat{\mathbf{b}}\right)\cdot\nabla_v f_e = C_{ee}(f_e) + C_{ei}(f_e, f_i) + Q(f_e), \quad (3.30)$$

and the Fokker-Planck equation for ions is

$$\frac{\partial f_i}{\partial t} + \mathbf{v}\cdot\nabla f_i + \left(-\frac{Z_i e}{m_i}\nabla\phi + \Omega_i \mathbf{v}\times\hat{\mathbf{b}}\right)\cdot\nabla_v f_i \;=\; C_{ii}\{f_i\} + C_{ie}\{f_i, f_e\}. \quad (3.31)$$

Here, f_e and f_i are the distribution functions of electrons and ions, respectively, Ω_e and Ω_i are the gyrofrequency of electrons and ions, respectively, and ϕ is the electrostatic potential. On the right hand side, C_{ee}, C_{ei}, C_{ii}, and C_{ie} are the collision operators for electron-electron, electron-ion, ion-ion, and ion-electron collisions, respectively, and Q is the quasilinear diffusion operator due to the lower hybrid wave described in Appendix A.

The momentum equations for electrons and ions are obtained by taking the moments $m_e\mathbf{v}$ of Eq. (3.30) and $m_i\mathbf{v}$ of (3.31). Summing the two species momentum equations, the total momentum change in the two species due to the electric field and collisions vanishes since the collision operators conserve momentum and the electric field terms cancel out due to quasineutrality. The change of the ion rotation is determined by the total momentum conservation equation,

$$\frac{\partial(n_i m_i \mathbf{V_i})}{\partial t} = -\nabla\cdot\left[\overleftrightarrow{p_i} + p_{e\perp}(\overleftrightarrow{I} - \hat{\mathbf{b}}\hat{\mathbf{b}}) + p_{e\parallel}\hat{\mathbf{b}}\hat{\mathbf{b}}\right] + \frac{1}{c}\mathbf{J}\times\mathbf{B} + \int d^3v m_e \mathbf{v} Q(f_e), \quad (3.32)$$

where $\mathbf{V_i}$ is the ion fluid velocity, $\overleftrightarrow{I}$ is the identity tensor, $\overleftrightarrow{p_i}$ is the ion pressure tensor, $p_{e\perp}$ and $p_{e\parallel}$ are the electron perpendicular and parallel pressure, respectively, and $\mathbf{J}$ is the current density. Here, the small electron inertial term and the small electron viscosity terms are neglected. Multiplying the toroidal component of Eq. (3.32) by major radius and flux surface averaging result in the equation,

$$\frac{\partial}{\partial t}\langle n_i m_i R V_\varphi\rangle_s = -\frac{1}{V'}\frac{\partial}{\partial\psi}(V'\Pi) + \frac{1}{c}\langle\mathbf{J}\cdot\nabla\psi\rangle_s + \left\langle\int d^3v m_e R v_\varphi Q(f_e)\right\rangle_s, \quad (3.33)$$

where $V' = \int d\theta d\varphi (\mathbf{B}\cdot\nabla\theta)^{-1}$ is the flux surface volume and $\Pi = m_i\left\langle\int d^3v f_i R(\mathbf{v}\cdot\hat{\varphi})(\mathbf{v}\cdot\nabla\psi)\right\rangle_s$

is the radial transport of ion toroidal angular momentum. Here, I have used $\mathbf{B} = I\nabla\varphi + \nabla\varphi \times \nabla\psi$ and the property of the flux surface average $\langle \nabla \cdot X \rangle_s = \frac{1}{V'} \frac{\partial \langle V' X \cdot \nabla\psi \rangle_s}{\partial \psi}$. The radial current in the second term on the right hand side vanishes due to quasineutrality, so the change of ion toroidal angular momentum is determined by two remaining terms on the right hand side, the radial momentum transport and the original toroidal momentum transfer from the lower hybrid waves to electrons. Equation (3.33) gives the evolution of the toroidal rotation on the transport time scale (> 10 msec) during which the ambipolarity condition is satisfied. The transient momentum transfer between electrons and ions due to the electron radial drifts and collisions cannot explain the ion rotation change on this time scale.

3.5.2 Different time scales

Two channels of momentum transfer from the waves to the ions via electrons are described in Fig. 3-5, and each transfer mechanism has a different characteristic time scale. The lower hybrid waves are injected with a frequency of several GHz ($\sim \omega_{LH}$), which is between the electron gyrofrequency (Ω_e) and the ion gyrofrequency (Ω_i). The plasma current oscillating with the lower hybrid wave frequency disperses the wave. After the wave path is determined, electrons receive toroidal momentum by Landau resonance. After an electron collision time, the electron distribution function almost reaches steady state (electron plateau build-up time $\tau^{LH \to e} \lesssim$ O(1) msec), and the amount of momentum transfer from the wave to the electrons in each flux surface is determined.

After electrons reach steady state, the parallel momentum is transferred to ions by electron-ion collisions in a time scale $\tau_{\|}^{e \to i}$ that is determined by the inverse of the electron-ion collision frequency ν_{ei}^{-1}. The perpendicular momentum is transferred to ions in $\tau_{\perp}^{e \to i}$ in which ions follow the electron outward radial drift for ambipolarity. The ambipolarity is established by modifiying the radial electric field first through the neoclassical polarization in an ion transit time scale $L_{\|}/v_{ti}$, and later via collisional decay of the poloidal rotation in an ion-ion collision time ν_{ii}^{-1} [55].

The initial direction of toroidal momentum that the ions gain from the LH wave is determined by the transfer mechanism having the shorter time scale among $\tau_{\|}^{e \to i}$ and $\tau_{\perp}^{e \to i}$. The comparison between these time scales determines the initial direction because the

toroidal projection of the parallel and perpendicular momentum transfers typically have opposite sign, as shown in Fig. 3-4 (b).

However, as soon as both parallel and perpendicular momentum are transferred to the ions, the ion momentum change achieves the original size and direction of the launched LH wave toroidal angular momentum input. Then, in the ion transport time scale τ_{φ}^{turb} (O(1 msec)-O(100 msec)), due to the turbulent radial transport of ion toroidal angular momentum (turbulent viscosity), the momentum is radially transferred out as will be discussed in the next chapter. Eventually, the change of ion toroidal rotation by LH wave is saturated and the system (a tokamak) can reach steady state: the momentum input from the LH wave balances the outflow of toroidal angular momentum due to the ion momentum turbulent transport.

Because the momentum transport time scale is more or less of the order of the time resolution for the measurements of ion rotation in a tokamak $\tau_{\varphi,resol}^{measure}$ = O(10 msec), the very initial change in the measured rotation after the lower hybrid wave injection may be affected by both the radial transport due to turbulence as well as the momentum source from the lower hybrid wave. Also, it is difficult to differentiate each momentum transfer mechanism in Fig. 3-5 with measurements because they occur in times shorter than the resolution time. To explain the saturation of the measured rotation in $\tau_{\varphi,sat}^{measure}$ = O(100 msec), the turbulent radial transport of toroidal angular momentum must be balanced with the momentum source on the right hand side of Eq. (3.33)

(a)

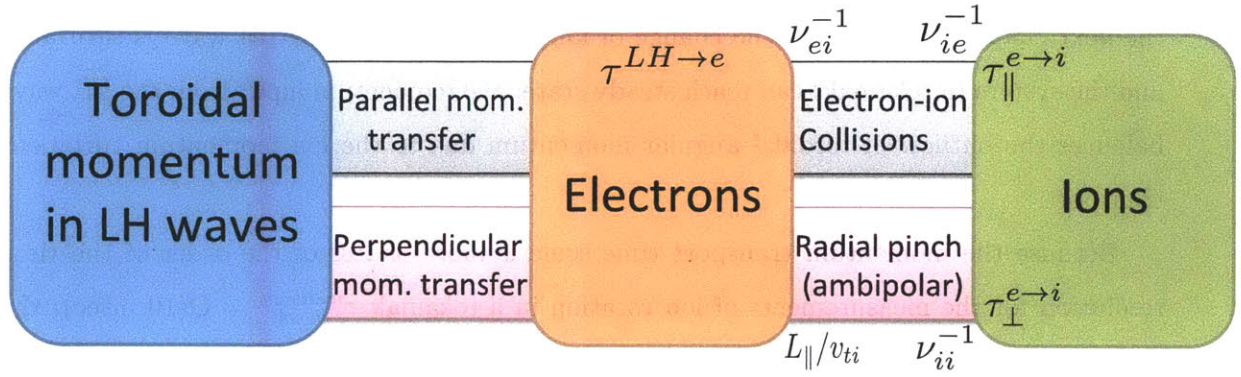

(b)

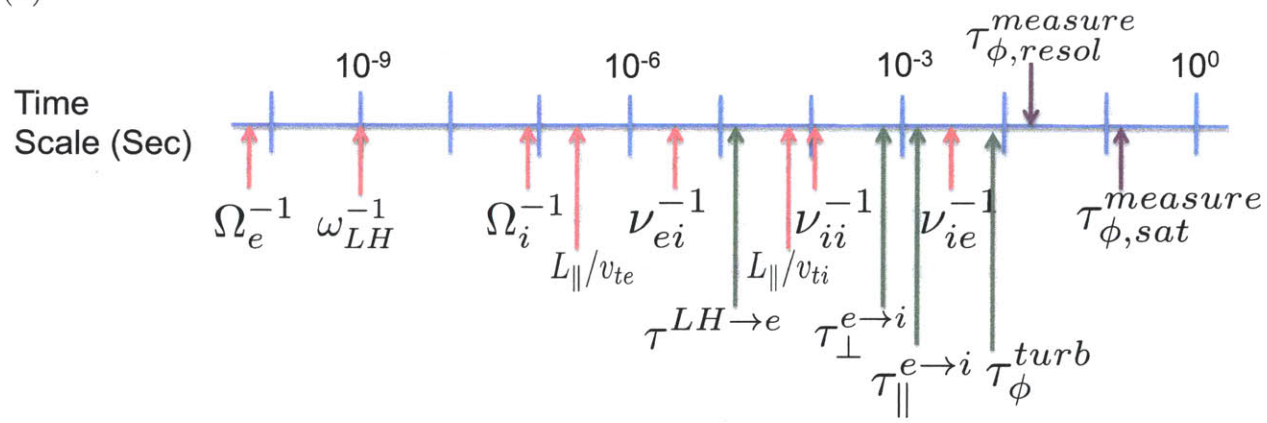

Figure 3-5: (a) A diagram of the toroidal momentum transfer mechanisms from lower hybrid waves to ions through electrons. The upper channel is for the parallel momentum transfer and the lower channel is for the perpendicular momentum transfer. The symbols in the channels are the time scale of each transfer mechanism. (b) Time scales related to the momentum transfer in a time line.

3.5.3 Comparison of the momentum source with the measured rotation change

In this section, I compare the initial change of the measured toroidal rotation after the lower hybrid injection with the simulation results for the parallel and perpendicular momentum transferred to ions.

The parallel momentum contribution to the toroidal momentum transfer, $T_\varphi^{\parallel}$ in Eq. (3.4), was evaluated using coupled simulations of TORLH and CQL3D. The result is shown in Fig. 2-4 (a). Because the toroidal mode number of the lower hybrid wave is conserved in a tokamak, the radial profile of the toroidal momentum transfer is the same as the radial profile of the energy transfer in Fig. 2-4 (b) multiplied by $n_\varphi R/c$, where n_φ is the toroidal refractive index. Consequently, the radial profile of the perpendicular momentum contribution to the toroidal momentum transfer, $\Delta T_\varphi^{\perp} + \Delta T_\varphi^{\alpha}$ in Eq. (3.10), is evaluated by subtracting the parallel momentum contribution in Fig. 2-4 (a) from the the radial profile of the toroidal momentum transfer based on the curve in Fig. 2-4 (b).

Figure 3-6 shows the initial change in the measured toroidal rotation for the high current case given in Fig. 2-4. The yellow dashed curve shows the time-averaged acceleration of the rotation after 20 msec (from t=0.79 sec to t=0.81 sec). The time interval that I use is limited by the resolution of the X-ray diagnostics in Alcator C-Mod. The lower hybrid waves transfer their momentum constantly from t=0.80 sec to t=1.30 sec. The calculated torque is the summation of the blue solid curve ($T_\varphi^{\parallel}$) and the red solid curve ($\Delta T_\varphi^{\perp} + \Delta T_\varphi^{\alpha}$).

The discrepancy between the simulated torque and the measured rotation change is probably due to the experimental errors and significant turbulent momentum transport. Considering the large experimental noise in the rotation measurement, the uncertainty is probably larger than the error bars indicate. Also, the transport time scale τ_φ^{turb} is likely to be less than 10 msec. For this reason, the radial transport of momentum (e.g. diffusion or pinch) is probably important for this rotation making it difficult to quantify the relation of the momentum source with the measurement.

The green dashed curve in Fig. 3-6 shows the time-averaged acceleration of the rotation after 40 msec (from t=0.79 sec to t=0.83 sec). In this longer time interval, the momentum pinch is evidently shown by comparing the green dashed curve with the yellow dashed curve. Although the radial profiles of the acceleration are deviated from the radial profiles of the

momentum transfer due to the radial transport of momentum, the size of the time-averaged acceleration is comparable to the total toroidal momentum transfer.

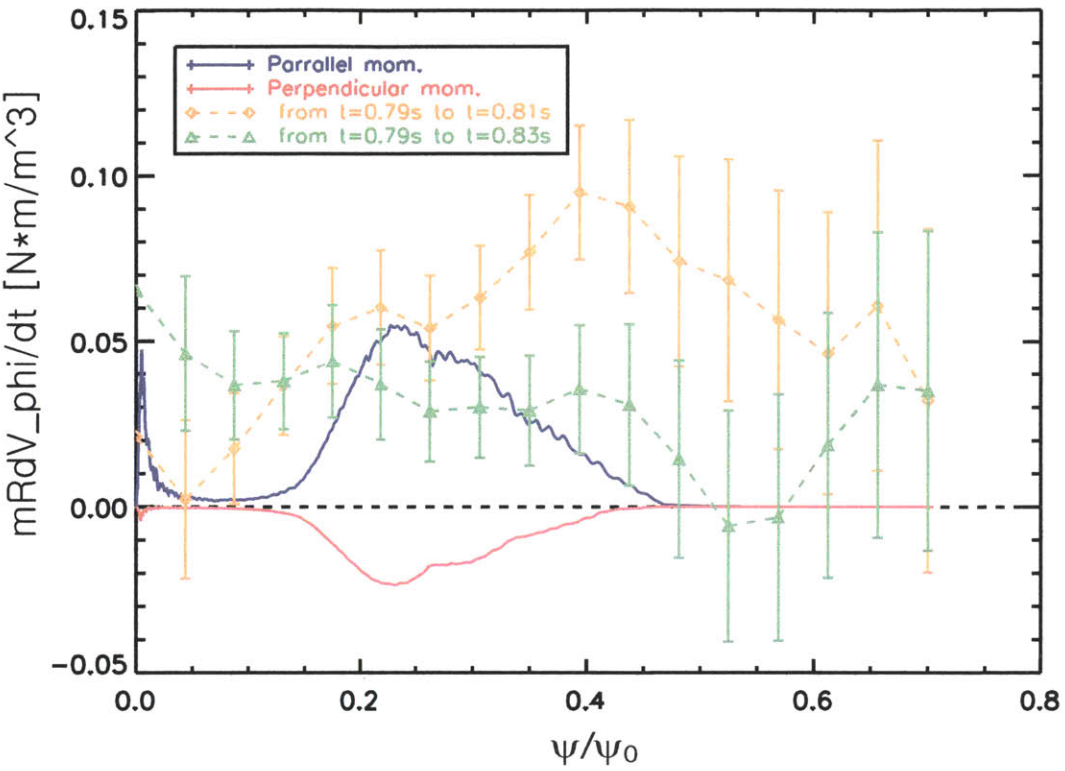

Figure 3-6: Comparison of radial profiles of the measured ion toroidal angular rotation change with the simulation results for the toroidal angular momentum torque from lower hybrid waves. The parallel momentum transfer contribution to the torque (blue solid), $T_\varphi^{\parallel}$ in Eq. (3.4), and the perpendicular momentum transfer contribution to the torque (red solid), $\Delta T_\varphi^{\perp} + \Delta T_\varphi^{\alpha}$ in Eq. (3.10), are shown. In the graphs, positive means counter-current direction. Two experimental curves (yellow dashed and green dashed) show the acceleration of the rotation averaged over time intervals of 20 msec and 40 msec, respectively. The lower hybrid wave injection starts at t=0.80 sec and the constant momentum transfer from the wave to the plasma continues until t=1.30 sec.

Chapter 4

Turbulent momentum transport

The radial transport of ion toroidal angular momentum redistributes the momentum injected by lower hybrid waves. The time scale of the momentum transport measured in tokamaks is of the order of the gyro-Bohm diffusion scale, and the transport is expected to be dominated by drift-wave microturbulence. The turbulence is well described by gyrokinetics [60, 61, 64].

The ion toroidal rotation observed in tokamaks without external momentum source or with a sufficiently small momentum source (e.g. lower hybrid waves in Alcator C-Mod) is much smaller than the ion thermal velocity, resulting in a low Mach number ($\mathrm{Ma} \equiv V_\varphi / v_{ti} \sim 0.1 - 0.2$) [124]. For low flow plasmas, the momentum transport can be decomposed into three terms: diffusion, advection and intrinsic momentum transport. The radial profile of toroidal rotation is determined by balancing all the components of the momentum transport with the momentum source (e.g. the source evaluated in Chapter 3). In this chapter, I investigate the radial transport of momentum by turbulence using low flow gyrokinetics. The effect of the lower hybrid wave on the momentum transport will be treated in Chapter 5.

Among the many possible effects that cause momentum transport, this chapter focuses on the intrinsic momentum transport due to diamagnetic flows. In Sec. 4.1, gyrokinetics is introduced and the symmetry of the lowest order gyrokinetic equations that results in no net momentum transport is explained. In Sec. 4.2, I list and explain the several mechanisms that break the symmetry and cause momentum transport. I focus on the contribution of the diamagnetic flow to symmetry breaking. In Sec. 4.3, I narrow the scope of the investigation

to a new mechanism of intrinsic momentum transport due to different momentum pinches for the diamagnetic flow and the E×B flow. The intrinsic momentum transport is numerically evaluated using gyrokinetic equations that are higher order in poloidal rhostar. In Sec. 4.4, the impact of the intrinsic momentum transport on the rotation profile is discussed.

4.1 Gyrokinetics and symmetry

In this section, I explain how to evaluate the radial momentum transport by drift-wave turbulence using gyrokinetics. Gyrokinetics is a kinetic description of electromagnetic (or electrostatic) turbulence that averages the gyromotion while keeping finite Larmor radius effect [61]. The frequency of the drift-wave microturbulence is much smaller than the gyrofrequency, permitting the separation of the gyromotion from the parallel streaming and the perpendicular drift motion. Then, particle motion can be described by the position of the gyration center, and only two velocity space variables (for example, the kinetic energy $\mathcal{E} = v^2/2$ and magnetic moment $\mu = v_\perp^2/2B$). Here, $v_\perp = \sqrt{v^2 - v_\parallel^2}$ and $v_\parallel$ are the velocities perpendicular and parallel to the static magnetic field, $\mathbf{B}$, respectively, and B is the magnitude of the static magnetic field. Gyrokinetics also assumes $\rho_i/l_\perp \sim 1$ and $l_\perp/l_\parallel \sim \rho_i/a \equiv \rho_\star \ll 1$. Here, $l_\parallel$ and $l_\perp$ are the turbulence length scales parallel and perpendicular to a static magnetic field, respectively, a is the minor radius and ρ_i is the ion Larmor radius. For simplicity, I will only use gyrokinetic equations for electrostatic turbulence which is the most relevant in low β tokamaks (e.g. Alcator C-Mod).

The radial flux of ion toroidal angular momentum in Eq. (3.33) is dominantly due to the fluctuating radial E×B drift carrying the toroidal angular momentum, and it can be evaluated using

$$\Pi \simeq \Pi^{tb} = \left\langle m_i \int d^3v f_i^{tb} (\mathbf{v} \cdot \hat{\varphi} R)(\mathbf{v}_E^{tb} \cdot \nabla\psi) \right\rangle_s , \tag{4.1}$$

where m_i is the ion mass, R is the major radius, $\mathbf{v}_E^{tb} \cdot \nabla\psi$ is the radial drift due to the electrostatic turbulence and f_i^{tb} is the turbulent piece of the ion distribution function. The fluctuating radial drift and distribution function are given by the gyrokinetic equations.

The radial momentum transport can be expanded in the small parameters $\rho_\star$ and $(B/B_\theta)\rho_\star$, i.e. $\Pi^{tb} = \Pi_1 + \Pi_2 + ...$ Here, B_θ is the magnitude of the poloidal magnetic

field. The lowest order radial flux (Π_1) corresponds to the size of the gyro-Bohm diffusion of thermal velocity, $\Pi_1 \sim D_{gB,i}\frac{n_i m_i v_{ti} R}{a} = \rho_\star^2 n_i m_i v_{ti}^2 R$, where I have used the gyro-Bohm diffusion coefficient in Eq. (1.3) and the minor radius (a) as the radial scale length of a tokamak. The lowest order gyrokinetic equations described in this section can be used to evaluate the gyro-Bohm scale transport of particles and energy, but the lowest order radial flux of momentum (Π_1) can only be calculated if the plasma flow is sonic, otherwise $\Pi_1 = 0$ as I will prove. The higher order radial flux ($\Pi_2 \sim (B/B_\theta)\rho_\star \Pi_1$) is given by higher order gyrokinetics described in section 4.2.1. The lowest order gyrokinetic equation for species s without any background flow is

$$\frac{\partial f_{1,s}^{tb}}{\partial t} + \left(v_\parallel \hat{\mathbf{b}} + \mathbf{v}_{M,s} - \frac{c}{B}\nabla\langle\phi_1^{tb}\rangle \times \hat{\mathbf{b}}\right)\cdot\nabla f_{1,s}^{tb}$$
$$= \frac{c}{B}\nabla\langle\phi_1^{tb}\rangle \times \hat{\mathbf{b}}\cdot\nabla f_{0,s}^{bg} + \frac{Z_s e}{m_s}[v_\parallel \hat{\mathbf{b}} + \mathbf{v}_{M,s}]\cdot\nabla\langle\phi_1^{tb}\rangle\frac{\partial f_{0,s}^{bg}}{\partial \mathcal{E}} + \langle C(f_s)\rangle, \tag{4.2}$$

where $\hat{\mathbf{b}}$ is the unit vector parallel to the magnetic field, c is the speed of the light, C is the ion collision operator and $\mathbf{v}_{M,s} = (\mu/\Omega_s)\hat{\mathbf{b}} \times \nabla B + ((v_\parallel)^2/\Omega_s)\hat{\mathbf{b}} \times (\hat{\mathbf{b}}\cdot\nabla\mathbf{b})$ is the ∇B and curvature drift. Here, m_s is the mass and $Z_s e$ is the charge of the species, $\Omega_s = Z_s eB/m_s$ is the gyrofrequency, and $\langle ... \rangle$ is the average over the gyromotion. The distribution function of a species is assumed to have a non-fluctuating background piece f_s^{bg} and a fluctuating piece due to turbulence f_s^{tb} (i.e. $f_s = f_s^{bg} + f_s^{tb}$). For the gyrokinetic equation in Eq. (4.2), the distribution function is approximately $f_s \simeq f_{0,s}^{bg} + f_{1,s}^{tb}$ to lowest order in $\rho_\star$. The subscript denotes the order in $\rho_\star$. The background piece is $f_{0,s}^{bg} = f_{M,s}$, where $f_{M,s}$ is the lowest order distribution function, which is a Maxwellian. The size of the fluctuating piece is much smaller than the background piece, $f_{1,s}^{tb} \sim \rho_\star f_{M,s}$. Also, ϕ_1^{tb} is the short wavelength turbulent potential whose size is $O(\rho_\star(T_e/e))$, where T_e is the electron temperature.

The gyrokinetic equation can be derived for every species and they are coupled by imposing the quasineutrality condition,

$$\sum_s Z_s e\left\{\int d^3v \left(f_{1,s}^{tb} - \frac{Z_s e(\phi_1^{tb} - \langle\phi_1^{tb}\rangle)}{T_s} f_{M,s}\right)\right\} = 0, \tag{4.3}$$

where the second term in the parentheses on the left hand side is the polarization density due to the gyromotion.

Because the turbulence parallel length scales are much larger than the perpendicular

length scales ($l_\perp/l_\parallel \sim \rho_\star$), it is convenient to use the coordinates ψ and α to solve Eq. (4.2). The coordinates ψ and α are perpendicular to the magnetic field. Here, α is not the gyro phase as in Chapter 2 and 3, but it is

$$\alpha = \varphi - I(\psi) \int_0^\theta d\theta' \frac{1}{\mathbf{B}\cdot\nabla\theta'} \frac{1}{R^2(\psi,\theta')}, \tag{4.4}$$

where $\mathbf{B} = I\nabla\varphi + \nabla\varphi \times \nabla\psi$, $I = B_\varphi R$ and B_φ is the toroidal magnetic field. The static magnetic field satisfies $\mathbf{B} = \nabla\alpha \times \nabla\psi$. Using the poloidal angle (θ) as the coordinate that follows the magnetic field, the slow variation in the parallel coordinate (θ) and the fast variation in the perpendicular coordinates (ψ and α) of the turbulence are well described by solutions of the form

$$f_s^{tb}(\psi,\alpha,\theta;\mathcal{E},\mu,\sigma;t) = \sum_{k_\psi,k_\alpha} \hat{f_s^{tb}}(k_\psi,k_\alpha,\theta;\mathcal{E},\mu,\sigma;t) e^{i(k_\psi\psi + k_\alpha\alpha)}, \tag{4.5}$$

$$\phi_1^{tb}(\psi,\alpha,\theta;t) = \sum_{k_\psi,k_\alpha} \hat{\phi}_1^{tb}(k_\psi,k_\alpha,\theta;t) e^{i(k_\psi\psi + k_\alpha\alpha)}, \tag{4.6}$$

where k_ψ and k_α are the wavevectors in ψ and α coordinates by the Fourier decomposition, respectively, and σ is the sign of the parallel velocity ($v_\parallel = \sigma\sqrt{2(\mathcal{E}-\mu B)}$). The form in Eq. (4.5) and (4.6) is clearly an eikonal approximation with a phase factor e^{iS} in which

$$S \equiv k_\psi\psi + k_\alpha\alpha. \tag{4.7}$$

The parallel variation of turbulence in Eq. (4.2) is represented by the poloidal angle dependence (i.e. $\hat{\mathbf{b}}\cdot\nabla = \hat{\mathbf{b}}\cdot\nabla\theta(\partial/\partial\theta)$).

For a poloidally up-down symmetric tokamak, the lowest order gyrokinetic equations of Eq. (4.2) and (4.3) satisfy the symmetry [125, 126]

$$\hat{f_{1,s}^{tb}}(\theta, v_\parallel, k_\psi) = -\hat{f_{1,s}^{tb}}(-\theta, -v_\parallel, -k_\psi), \tag{4.8}$$

$$\hat{\phi}_1^{tb}(\theta, k_\psi) = -\hat{\phi}_1^{tb}(-\theta, -k_\psi), \tag{4.9}$$

because the operators in the gyrokinetic equation have the following symmetry properties: $\left(v_\parallel\partial/\partial\theta\right)(\theta, v_\parallel) = \left(v_\parallel\partial/\partial\theta\right)(-\theta, -v_\parallel)$, $(\mathbf{v}_{M,s}\cdot\nabla S)(\theta, k_\psi) = (\mathbf{v}_{M,s}\cdot\nabla S)(-\theta, -k_\psi)$ and $\left(\nabla S'\times\hat{\mathbf{b}}\cdot\nabla S''\right)(k'_\psi, k''_\psi) = -\left(\nabla S'\times\hat{\mathbf{b}}\cdot\nabla S''\right)(-k'_\psi, -k''_\psi)$, where the three wave coupling

is satisfied by $k_\psi = k_\psi{}' + k_\psi''$ and $k_\alpha = k_\alpha{}' + k_\alpha''$.

To see the effect of this symmetry on the momentum transport, the turbulent radial flux of toroidal angular momentum in Eq. (4.1) is written as an integral and a summation,

$$\Pi^{tb} \equiv \sum_{k_\psi} \int_{-\infty}^{\infty} d\theta dv_\parallel \pi^{tb}(\theta, v_\parallel, k_\psi), \tag{4.10}$$

where $\pi^{tb} = \frac{2\pi m_i B}{\mathbf{B}\cdot\nabla\theta} \int_0^\infty d\mu \left\langle f_i^{tb}(\mathbf{v}\cdot\hat{\varphi}R)(\mathbf{v}_E^{tb}\cdot\nabla\psi)\right\rangle$. The integrand π^{tb} is also expanded in $\rho_\star$ and $(B/B_\theta)\rho_\star$, as Π^{tb} (i.e. $\pi = \pi_1 + \pi_2 + ...$). Accordingly, $\Pi_1 = \sum_{k_\psi} \int_{-\infty}^{\infty} d\theta dv_\parallel \pi_1$ is the lowest order radial flux and $\Pi_2 = \sum_{k_\psi} \int_{-\infty}^{\infty} d\theta dv_\parallel \pi_2$ is the higher order flux in poloidal rhostar $\rho_{\star,p} \equiv \frac{B}{B_\theta}\rho_\star$.

Because there are contributions of parallel and perpendicular momentum to the toroidal angular momentum, the radial flux of the toroidal angular momentum can be also decomposed into $\Pi^{tb} = \Pi_\parallel + \Pi_\perp$. The parallel contribution to Π^{tb} in Eq. (4.1) is

$$\Pi_\parallel = \left\langle \frac{m_i c I}{B^2}(\nabla\phi\times\hat{\mathbf{b}})\cdot\nabla\psi \int d^3v f_i^{tb} v_\parallel \right\rangle_s, \tag{4.11}$$

and it dominates over the perpendicular contribution $\Pi_\perp$. The perpendicular contribution is due to the gyro-phase dependent piece of the distribution function,

$$\Pi_\perp = \left\langle \frac{m_i c}{B^2}(\nabla\phi\times\hat{\mathbf{b}})\cdot\nabla\psi \int d^3v f_i^{tb}(\mathbf{v}\times\hat{\mathbf{b}})\cdot\nabla\psi \right\rangle_s \sim \frac{B_\theta}{B}\Pi_\parallel, \tag{4.12}$$

where $\hat{\varphi}R = \frac{I}{B}\hat{\mathbf{b}} - \frac{1}{B}\hat{\mathbf{b}}\times\nabla\psi$ is used.

From the symmetry properties in Eq. (4.8) and Eq. (4.9), the momentum transport is antisymmetric under the inversion of the poloidal angle, the parallel velocity, and the radial wave vector,

$$\pi_1(\theta, v_\parallel, k_\psi) = -\pi_1(-\theta, -v_\parallel, -k_\psi), \tag{4.13}$$

where $\pi_1 = \pi_{\parallel,1} + \pi_{\perp,1}$ has the parallel momentum contribution $\pi_{\parallel,1} \propto \sum_{k_\alpha} Re[ik_\alpha \hat{f_{1,i}^{tb}} \langle\hat{\phi_1^{tb}}\rangle^* v_\parallel]$ and the perpendicular momentum contribution $\pi_{\perp,1} \propto \sum_{k_\alpha} Re[ik_\alpha \hat{f_{1,i}^{tb}} \langle\hat{\phi_1^{tb}}\rangle^* (i(k_\psi|\nabla\psi|^2 + k_\alpha \nabla\psi\cdot\nabla\alpha)v_\perp^2)]$. As a result, the total sum of turbulent momentum transport vanishes (i.e. $\Pi_1 = 0$) due to the symmetry property of the gyrokinetic solutions unless there is symmetry breaking mechanism.

In Fig. 4-1, I give a physical picture of the reason for the vanishing momentum transport. The turbulent fluctuations in the parallel velocity are odd around the outer midplane, resulting in no net momentum transport when they are carried by the radial E×B flow due to the fluctuating potential. However, if there are mechanisms that break the symmetry, non-zero momentum transport occurs and toroidal angular momentum is redistributed in a tokamak. For example, the diamagnetic effect shown in Fig. 4-2 results in symmetry breaking of higher order gyrokinetics, as will be explained in the next section (i.e. $\Pi_2 \neq 0$).

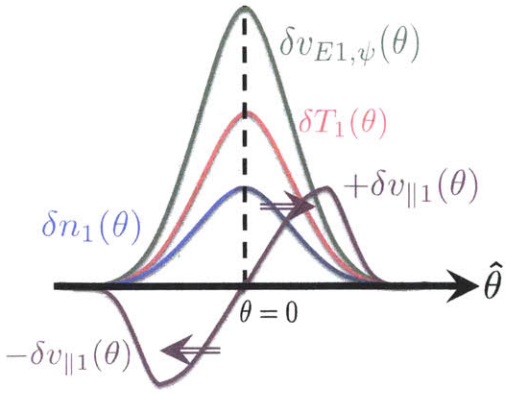

Figure 4-1: Sketch of the ion temperature gradient driven turbulence showing ballooning structure along the parallel coordinate (θ). The radial component of the fluctuating E×B drift $\delta v_{E1,\psi} = \mathbf{v}_E^{tb} \cdot \nabla\psi$, the fluctuating density δn_1 and the fluctuating temperature δT_1 have a peaked amplitude at the outer-midplane ($\theta = 0$). The high pressure at $\theta = 0$ pushes ions to each side, resulting in the antisymmetry of the fluctuating velocity $\delta v_{\|}$ with respect to $\theta = 0$ and no net radial transport of parallel angular momentum.

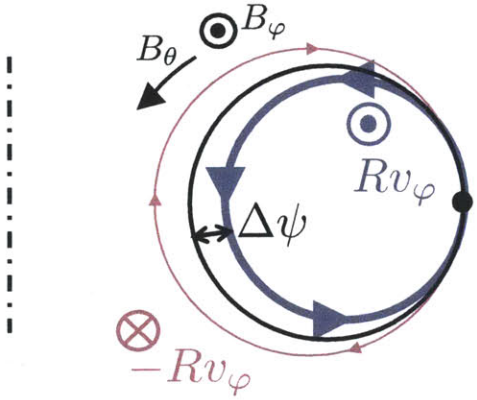

Figure 4-2: Sketch of the origin of the diamagnetic particle flow. The poloidal cross section of a flux surface is represented by the black solid circle. The particles with positive parallel velocity drift radially inward (blue circle), while the particles with the negative parallel velocity drift radially outward (red circle). Because the plasma at inner radii is denser and hotter than the plasma at outer radii, the total parallel flux at the outer mid plane is positive and the ion diamagnetic flow is $V_{\|,d} \sim \Delta\psi \frac{\partial \ln p_i}{\partial \psi} v_{ti} \sim \rho_\star \frac{B}{B_\theta} v_{ti}$.

4.2 Symmetry breaking mechanisms

There are several effects that break the symmetry of the lowest order gyrokinetic equations described in the previous section. Each symmetry breaking mechanism has a certain regime in the parameter space where it is more important than other mechanisms. Hence one can self-consistently evaluate each mechanism separately in its corresponding regime.

The symmetry in θ is broken in up-down asymmetric tokamaks [127]. However, it is unclear how significant the effect of up-down asymmetry is. The change in the measured ion rotation due to up-down asymmetry was only about 3 % of the ion thermal speed in the experiments in the TCV tokamak [127]. Also, typically the up-down asymmetry is significant only around the edge.

The slow variation of plasma parameters in the radial direction breaks the symmetry in k_ψ [128, 129, 130]. The effect on the turbulence of the change of temperature gradient and density gradient across the radial dimension of plasma eddies has been investigated in gyrokinetic global codes, but this effect is still not well understood. For a sufficiently small radial correlation length of the turbulence, the effect of the slow radial variation of the gradients is assumed to be too small to break the symmetry significantly.

The higher order correction to the gyrokinetic equation due to the slow poloidal variation of the turbulence can break the symmetry in the poloidal angle θ [131]. The terms in the first line on the right hand side of the higher order gyrokinetic equation in Eq. (F.1) include the slow poloidal variation effect.

In this thesis, I focus on the effect of the diamagnetic flow that introduces a preferential direction in the system [132, 133, 134]. For the marginally unstable turbulence in a tokamak, the size of each symmetry breaking mechanism is estimated in Appendix F, and most mechanisms are smaller than or comparable to the momentum flux due to the diamagnetic flow. The toroidal flow in a tokamak is composed of two different types of flow: the E×B flow and the diamagnetic flow. The toroidal flow depends on the radial electric field through the radial force equation. A radial electric field is generated to balance the Lorentz force due to the toroidal flow and the poloidal flow as well as the radial pressure gradient. In other words, the toroidal flow has a piece of the toroidal E×B drift due to the radial electric field. This will be discussed in Sec 4.3. The diamagnetic flow due to the radial pressure gradient always exists in a tokamak regardless of the size and the sign of the radial electric

field. This implies that there is an inherent preferential direction that breaks the symmetry. These flows are called diamagnetic flows because the flow is the result of particle motion trying to generate a magnetic field whose direction is opposite to the external magnetic field. As shown in Fig. 4-2, the ion diamagnetic flow is due to finite drift orbit size effects. The higher flux for the ions with positive parallel velocity is due to the radial magnetic drift to inner radii where the plasma has a higher temperature and density than at outer radii. Consequently, the amount of diamagnetic flow is determined by the width of the deviation of the poloidal orbit from the flux surface ($\sim \frac{B}{B_\theta}\rho_i$) and the pressure gradient (i.e. $\Omega_{\varphi,d}R \sim \frac{B}{B_\theta}\rho_\star v_{ti}$, where $\Omega_{\varphi,d}$ is the toroidal angular frequency for diamagnetic flow). To take into account the diamagnetic flow in gyrokinetics, one needs to correct the lowest order gyrokinetic equation in Eq (4.2) with the poloidal rhostar higher order terms as will be explained in Sec. 4.2.1.

4.2.1 Higher order gyrokinetic equations

If the toroidal flow is in the high flow level (Mach number ~ 1), the symmetry is broken even to lowest order (i.e. Eq. (4.13) is not valid in the presence of high flow, and $\Pi_1 \neq 0$). In this case, the E×B flow dominates over the diamagnetic flow and the lowest order gyrokinetic equation in Eq. (4.2) should be corrected with the E×B flow. The flow and flow shear can change the main properties of the turbulence (e.g. turbulent eddy size, fluctuation amplitude and frequency), and energy and particle fluxes change significantly as a result. However, this effect is not in the scope of this thesis because the intrinsic toroidal flow or the toroidal flow in the presence of the lower hybrid wave is typically small (Mach number ~ 0.1).

For low flow level, the symmetry is broken by the effect of higher order terms in poloidal rhostar $\rho_{\star,p} \equiv \frac{B}{B_\theta}\rho_\star$. Then, one needs the higher order gyrokinetic equations to evaluate the momentum transport (i.e. $\Pi_1 = 0$ and $\Pi_2 \neq 0$). In this case, the E×B flow is comparable to the diamagnetic flow, and there is only a small effect of the flow on the main properties of the turbulence, except for the momentum transport. The correction to the gyro-Bohm scale turbulence is as small as the ratio of the low flow to the ion thermal speed. For diamagnetic flow, the correction is in the poloidal rhostar $\frac{B}{B_\theta}\rho_\star$ scale which is more or less 10 % of the existing turbulence without the flow.

The higher order gyrokinetic equation is described in Appendix F. The left hand side in Eq. (F.1) is the lowest order gyrokinetic equation, and the right hand side is the correction to $\frac{B}{B_\theta}\rho_\star$ higher order. On the right hand side, besides the terms with f_{1s}^{bg} related to the diamagnetic flow, there are terms related to the higher order corrections due to the slow poloidal variation of the fluctuating potential and distribution function, the parallel nonlinearity, and the neoclassical potential.

There are several regimes in which one term or a group of terms on the right hand side in Eq. (F.1) dominate over the others (see Appendix F). Consequently, the effect of them on the intrinsic rotation can be investigated independently in a self-consistent way. I only focus on the symmetry breaking due to the diamagnetic flow. In the gyrokinetic equations in this section, I only keep the corrections in the third line on the right hand side of Eq. (F.1) related to the diamagnetic flow for simplicity.

Then, the higher order ion gyrokinetic equation with both the diamagnctic flow and the E×B flow in the lab frame is

$$\begin{aligned}&\frac{\partial f_i^{tb}}{\partial t}+\left(v_\parallel\hat{\mathbf{b}}+\mathbf{v}_M-\frac{c}{B}\nabla(\phi_0^{bg}+\langle\phi^{tb}\rangle)\times\hat{\mathbf{b}}\right)\cdot\nabla f_i^{tb}-\frac{Z_ie}{m_i}\mathbf{v}_M\cdot\nabla\phi_0^{bg}\frac{\partial f_i^{tb}}{\partial\mathcal{E}}\\&\quad=\frac{c}{B}\nabla\langle\phi^{tb}\rangle\times\hat{\mathbf{b}}\cdot\nabla f_i^{bg}+\frac{Z_ie}{m_i}[v_\parallel\hat{\mathbf{b}}+\mathbf{v}_M]\cdot\nabla\langle\phi^{tb}\rangle\frac{\partial f_i^{bg}}{\partial\mathcal{E}}+\langle C(f_i)\rangle,\end{aligned}\tag{4.14}$$

where $f_i^{tb}=f_{1,i}^{tb}+f_{2,i}^{tb}$, $f_i^{bg}=f_{0,i}^{bg}+f_{1,i}^{bg,E}+f_{1,i}^{bg,d}$ and $\phi^{tb}=\phi_1^{tb}+\phi_2^{tb}$. Here, $f_{0,i}^{bg}=f_{M,i}$ is the lowest order background piece that is a Maxwellian distribution function as in Eq. (4.2), and $f_{1,i}^{bg,E}$ and $f_{1,i}^{bg,d}$ are the small deviations from the Maxwellian due to the E×B flow and the diamagnetic flow, respectively. I assume that the E×B flow is of the same order as the diamagnetic flow (i.e. $f_{1,i}^{bg,E}\sim f_{1,i}^{bg,d}\sim\frac{B}{B_\theta}\rho_\star f_{0,i}^{bg}$). For the E×B flow, the correction to the background distribution function simply results in a shift of the background Maxwellian by the E×B flow (i.e. $f_{0,i}^{bg}+f_{1,i}^{bg,E}=f_{M,i}(\mathbf{v}-\Omega_{\varphi,E}R\hat{\varphi})$) making $f_{1,i}^{bg,E}\simeq\frac{m_iv_\parallel}{T_i}\frac{I\Omega_{\varphi,E}}{B}f_{M,i}$, where $\Omega_{\varphi,E}$ is the toroidal angular frequency of the E×B flow. The small deviation due to the diamagnetic flow is the neoclassical distribution function [30, 31], which will be explained in the next section.

The long wavelength background potential ϕ_0^{bg} determines the radial electric field and the E×B flow (i.e. $\Omega_{\varphi,E}=-c\frac{\partial\phi_0^{bg}}{\partial\psi}$). Because the radial electric field affects the energy and orbit of the particles, there are two additional terms on the left hand side related to ϕ_0^{bg} (compare to Eq. (4.2)). The term $\left(-\frac{c}{B}\nabla\phi_0^{bg}\times\hat{\mathbf{b}}\right)\cdot\nabla f_i^{tb}$ is the effect of the background

E×B drift and it results in the Doppler shift of the turbulent frequency. The other term, $-\frac{Z_i e}{m_i}\mathbf{v}_M \cdot \nabla\phi_0^{bg}\frac{\partial f_i^{tb}}{\partial \mathcal{E}}$, is the acceleration of the particles in the radial electric field when the particles change their radial positions due to the curvature and ∇B drift. The diamagnetic flow does not have terms like these on the left hand side because it cannot change the orbits and energy of the particles. In Sec. 4.3 I will show that the background E×B drift term and the acceleration term are very important because they make the momentum transport due to the E×B flow and the momentum transport due to the diamagnetic flow different.

From the size of the correction to the background piece, I obtain the size of the corresponding correction to the fluctuating piece $f_{2,i}^{tb} \sim \frac{B}{B_\theta}\rho_\star f_{1,i}^{tb}$ and $\phi_2^{tb} \sim \frac{B}{B_\theta}\rho_\star \phi_1^{tb}$. For the transformations $v_\parallel \to -v_\parallel$, $\theta \to -\theta$ and $k_\psi \to -k_\psi$, all additional higher order terms in the gyrokinetic equation have the parity opposite to the lowest order terms in Eq. (4.2). The parity of the higher order corrections to the distribution function and potential is obtained by linearizing the effect of small corrections in $\frac{B}{B_\theta}\rho_\star$ (compare the following with Eq. (4.8) and (4.9)),

$$\hat{f_{2,i}^{tb}}(\theta, v_\parallel, k_\psi) = \hat{f_{2,i}^{tb}}(-\theta, -v_\parallel, -k_\psi) \tag{4.15}$$

$$\hat{\phi}_2^{tb}(\theta, k_\psi) = \hat{\phi}_2^{tb}(-\theta, -k_\psi). \tag{4.16}$$

The different symmetry of $\hat{f_{2,i}^{tb}}$ and $\hat{\phi}_2^{tb}$ results in non-vanishing higher order momentum transport,

$$\pi_2(\theta, v_\parallel, k_\psi) = \pi_2(-\theta, -v_\parallel, -k_\psi). \tag{4.17}$$

Here, $\pi_2 = \pi_{\parallel,2}+\pi_{\perp,2}$ has parallel and perpendicular contributions, $\pi_{\parallel,2} \propto Re[ik_\alpha(\hat{f_{2,i}^{tb}}\langle\hat{\phi_1^{tb}}\rangle^* + \hat{f_{1,i}^{tb}}\langle\hat{\phi_2^{tb}}\rangle^*)v_\parallel]$ and $\pi_{\perp,2} \propto \sum_{k_\alpha} Re[ik_\alpha(\hat{f_{2,i}^{tb}}\langle\hat{\phi_1^{tb}}\rangle^* + \hat{f_{1,i}^{tb}}\langle\hat{\phi_2^{tb}}\rangle^*)(i(k_\psi|\nabla\psi|^2 + k_\alpha\nabla\psi\cdot\nabla\alpha)v_\perp^2)]$.

4.2.2 Neoclassical correction to Maxwellian equilibria

The correction $f_{1,s}^{bg,d}$ to the Maxwellian distribution function in Eq. (4.14) is derived from the drift kinetic equation for species s [30, 31],

$$v_{\parallel}\hat{\mathbf{b}}\cdot\nabla H_{1,s}+\mathbf{v}_{M,s}\cdot\nabla f_{0,s}^{bg}=C_s[H_{1,s}], \tag{4.18}$$

where $H_{1,s}=f_{1,s}^{bg,d}+\frac{Z_s e\phi_1^{bg}}{T_s}f_{0,s}^{bg}$. Here, the lowest order background potential ϕ_0^{bg} which results in the E×B flow is not included in Eq. (4.18), but the higher order background potential ϕ_1^{bg} due to the neoclassical correction is included. Using $\mathbf{v}_{M,s}\cdot\nabla f_{0,s}^{bg}=Iv_{\parallel}\hat{\mathbf{b}}\cdot\nabla\left(\frac{v_{\parallel}}{\Omega_s}\right)\frac{\partial f_{0,s}^{bg}}{\partial\psi}$, the drift kinetic equation is simplified to

$$v_{\parallel}\hat{\mathbf{b}}\cdot\nabla\left(H_{1,s}-f_{1,s}^{M}\right)=C_s[H_{1s}], \tag{4.19}$$

where $f_{1,s}^{M}=-\frac{Iv_{\parallel}}{\Omega_s}\left[\frac{\partial\ln n_s}{\partial\psi}+\left(\frac{m_s v^2}{2T_s}-\frac{3}{2}\right)\frac{\partial\ln T_s}{\partial\psi}\right]f_{0,s}^{bg}$. Depending on collisionality, different solutions for $H_{1,s}$ are obtained. By employing the quasineutrality condition,

$$\sum_s Z_s\int d^3v\left(H_{1,s}-\frac{Z_s e\phi_1^{bg}}{T_s}f_{0,s}^{bg}\right)=0, \tag{4.20}$$

we can also obtain ϕ_1^{bg}.

To study the symmetry breaking mechanisms in the higher order background distribution function, the solution of the ion drift kinetic equation is decomposed into

$$f_{1,i}^{bg,d}=f_{1,i}^{bg,V_{\parallel}}+f_{1,i}^{bg,q_{\parallel}}+f_{1,i}^{bg,other}\sim\frac{B}{B_\theta}\rho_\star f_{0,i}^{bg}, \tag{4.21}$$

where $f_{1,i}^{bg,V_{\parallel}}$ is the piece resulting in the diamagnetic parallel particle flow, $f_{1,i}^{bg,q_{\parallel}}$ is the piece giving the diamagnetic parallel heat flow, and $f_{1,i}^{bg,other}$ accounts for all other contributions. In other words,

$$f_{1,i}^{bg,V_{\parallel}}=\frac{mv_{\parallel}V_{\parallel,d}}{T_i}f_0^{bg} \tag{4.22}$$

where $V_{\parallel,d}\left(\frac{\partial p_i}{\partial\psi},\frac{\partial T_i}{\partial\psi},\nu_\star...\right)$ is the diamagnetic parallel particle flow that depends on the pressure gradient, temperature gradient and collisionality. Here, the collisionality is the ratio of effective collision frequency for pitch angle scattering to the bounce frequency,

$\nu_\star \equiv \frac{\nu_{ii} q R}{\epsilon^{3/2} v_{ti}}$, where ϵ is the inverse of the aspect ratio and q is the safety factor. To lowest order, the diamagnetic parallel flow is given by

$$V_{\|,d} = -\frac{I(\psi)}{B}\Omega_{\varphi,d}(\psi) + \frac{K(\psi)}{n_i(\psi)}B, \tag{4.23}$$

where $\Omega_{\varphi,d} = -\frac{c}{Z_i e n_i}\frac{\partial p_i}{\partial \psi}$ and $K(\psi) \propto \frac{\partial T_i}{\partial \psi}$. For example, the diamagnetic parallel particle flow in the banana regime $\nu_\star \ll 1$ for concentric circular flux surfaces and large aspect ratio is

$$V_{\|,d} = -\frac{IT_i}{m_i \Omega_{i0}}\left[\frac{1}{h}\frac{\partial \ln p_i}{\partial \psi} - 1.17 f_c h \frac{\partial \ln T_i}{\partial \psi}\right], \tag{4.24}$$

where $h = \frac{B}{B_0}$, B_0 and Ω_{i0} are the magnetic field magnitude and ion gyrofrequency at the magnetic axis, respectively, and f_c is the effective fraction of trapped particles [31].

Combining the parallel diamagnetic flow with the parallel flow due to the radial electric field and the perpendicular flow, the total neoclassical flow in a tokamak is obtained [135],

$$\begin{aligned} \mathbf{V_i} &= (V_{\|,d} + V_{\|,E})\hat{\mathbf{b}} + \mathbf{V}_\perp \\ &= \Omega_\varphi(\psi) R\hat{\varphi} + \frac{K(\psi)}{n_i(\psi)}\mathbf{B}, \end{aligned} \tag{4.25}$$

where $V_{\|,E} = -\frac{cI}{B}\frac{\partial \phi_0^{bg}}{\partial \psi}$ is the parallel flow due to the radial electric field and $\mathbf{V}_\perp = \Omega_\varphi(\psi)\frac{\mathbf{B}\times\nabla\psi}{B^2}$ is the perpendicular flow due to the $E \times B$ and the diamagnetic drift. Here, $\Omega_\varphi = -\frac{c}{Z_i e n_i}\frac{\partial p_i}{\partial \psi} - c\frac{\partial \phi_0^{bg}}{\partial \psi}$, and $\hat{\mathbf{b}} \times \nabla\psi = I\hat{\mathbf{b}} - BR\hat{\varphi}$ is used. Notice that the poloidal flow is determined only by the term proportional to $K(\psi)$, while the toroidal flow is given by both the term related to $\Omega_\varphi(\psi)$ and the term proportional to $K(\psi)$.

The diamagnetic parallel heat flow is due to the terms proportional to $v_\| v^2/2$ in the distribution function, $f_{1,i}^{bg,d}$. The parallel heat flow breaks the symmetry even in the absence of rotation because it corresponds to a distribution function that is odd in $v_\|$,

$$f_{1,i}^{bg,q_\|} = \frac{2}{5}\frac{m v_\| q_\|}{p_i T_i}\left(\frac{mv^2}{2T} - \frac{5}{2}\right) f_0^{bg}, \tag{4.26}$$

where p_i is the ion pressure and the heat flow $q_\| \left(\frac{\partial T_i}{\partial \psi}, \nu_\star ...\right)$ is also a function of the temperature gradient and collisionality. Similarly, the piece $f_{1,i}^{bg,other}$ breaks the symmetry of the turbulence, because it satisfies $f_{1,i}^{bg,other}(\theta, v_\|) = -f_{1,i}^{bg,other}(-\theta, -v_\|)$.

4.2.3 Diffusive and convective momentum transport

There are terms of the gyrokinetic equation in Eq. (4.14) that depend on the toroidal flow and the radial gradient of the toroidal flow. They break the symmetry of the turbulence and thus contribute to the momentum transport. The ion toroidal angular momentum transport can be linearized in the low flow regime, giving an advective term and a diffusive term that are proportional to the flow and the flow shear, respectively,

$$\Pi \equiv \Pi_{\rm int} - P_\varphi n_i m_i \langle R^2 \rangle_s \Omega_\varphi - \chi_\varphi n_i m_i \langle R^2 \rangle_s \frac{\partial \Omega_\varphi}{\partial r}, \tag{4.27}$$

where Ω_φ is the ion toroidal angular frequency, and $r = a(\psi/\psi_0)$ is the radial coordinate that labels flux surfaces. Here, a and ψ_0 are the minor radius and the poloidal flux that label the last closed flux surface, and they are used to normalize ψ. The advective term has the coefficient P_φ which is called momentum pinch coefficient, and the diffusive term is proportional to the momentum diffusivity χ_φ. Here, $\Pi_{\rm int}$ is the intrinsic momentum transport, which is the momentum flux generated even for zero flow and flow shear (i.e. $\Omega_\varphi = 0$ and $\partial\Omega_\varphi/\partial r = 0$). In steady state, the total toroidal angular momentum transport should be zero if there is no external source (i.e. $\Pi = 0$), and the balance between non-zero pieces in Π determines the radial profiles of the toroidal flow, $\Omega_\varphi(r)$.

The momentum diffusion and advection have been theoretically investigated in previous work [136, 137, 138], and the theory has been compared with the experimental observations in NSTX and DIIID of strong E×B flow (Mach number ~ 1) driven by the strong neutral beams [139].

The momentum diffusion is closely related to the ion thermal energy diffusion. The flow shear is diffused out by the same mechanism as the ion thermal energy is diffused out. Consequently, the diffusion rates for the momentum and the ion thermal energy are similar, and the Prandtl number (the ratio of the momentum diffusivity to the ion heat diffusivity) is found to be 0.5-0.8 in many gyrokinetic simulations [136].

The momentum advection is not just due to the momentum carried out by the particle transport, but also due to inherent momentum inward transport (momentum pinch). The momentum pinch is driven by the drift due to the Coriolis force in the rotating frame [137]. The Coriolis drift breaks the symmetry and generates inward momentum transport that is independent of the particle transport. However, in previous work, the difference between

the pinch of the E×B flow and the pinch of the diamagnetic flow explained in Sec. 4.3 was not recognized.

The intrinsic momentum transport for zero flow and flow shear has been also called residual stress, and it accounts for all other momentum transport mechanisms that are not the pinch or diffusion. The intrinsic momentum transport, or residual stress, must be driven by the symmetry breaking mechanisms mentioned in the introduction to Sec. 4.2. This intrinsic momentum transport is important to determine the sign of the intrinsic rotation. Also, many experimental radial profiles of rotation (e.g. the sign change of the rotation at mid-radius in some discharges) cannot be explained by only momentum pinch and diffusion, and so require intrinsic momentum redistribution. A new mechanism for the intrinsic momentum transport is found in Sec. 4.3. It is generated in a non-rotating state in which the diamagnetic flow and the E×B flow cancel each other.

4.3 Intrinsic momentum transport due to different rotation type

In this section, I evaluate the intrinsic momentum transport in a non-rotating state in which the diamagnetic particle flow cancels the E×B flow. For this purpose, I simplify the higher order distribution function in Eq. (4.21) so that it only includes the diamagnetic particle flow piece $f_{1,i}^{bg,d} = f_{1,i}^{bg,V_\parallel}$. Also, I assume that the diamagnetic particle velocity is only due to pressure gradient by neglecting the temperature gradient contribution proportional to $K(\psi)$ in Eq. (4.23), resulting in $f_{1,i}^{bg,d} \simeq \frac{mv_\parallel}{T_i}\frac{I\Omega_{\varphi,d}}{B} f_{M,i}$ in Eq. (4.14) and $\mathbf{V} = \Omega_\varphi(\psi)R\hat{\varphi}$ in Eq. (4.25) . Then, I can directly compare the effect of the E×B flow and the diamagnetic particle flow on the momentum transport. Different momentum pinch coefficients for the different types of flows are obtained with gyrokinetic simulations. The effects due to other pieces of the neoclassical distribution function (e.g. parallel heat flow in Eq. (4.21) and the temperature gradient piece in Eq. (4.23)), which are ignored here, will be included in Chapter 5 to evaluate the intrinsic momentum transport using the experimental plasma parameters in Alcator C-Mod.

4.3.1 Diamagnetic flow and E×B flow

With the assumptions explained above, the toroidal angular frequency of the ion rotation has two pieces,

$$\Omega_\varphi = -\frac{c}{Z_i e n_i}\frac{\partial p_i}{\partial \psi} - c\frac{\partial \phi_0^{bg}}{\partial \psi} \equiv \Omega_{\varphi,d} + \Omega_{\varphi,E}, \tag{4.28}$$

where the piece driven by a pressure gradient $\Omega_{\varphi,d} = -(c/Z_i e n_i)(\partial p_i/\partial\psi)$ corresponds to the diamagnetic particle flow, and the other piece driven by a radial electric field $\Omega_{\varphi,E} = -c(\partial\phi_0^{bg}/\partial\psi)$ corresponds to E×B flow.

The two types of toroidal rotation ($\Omega_{\varphi,d}$ and $\Omega_{\varphi,E}$) have different origins and characteristics. The radial electric field is determined by the Lorentz force due to the toroidal rotation, and as a result the radial electric field changes in the momentum confinement time scale [140]. The electric field changes the energy and orbits of each single particle. Conversely, the pressure gradient is determined by the turbulent anomalous transport of particles and energy, changing on the energy confinement time scale. The pressure cannot change the energy and orbits of individual particles.

Because the pressure driven flow, $\Omega_{\varphi,d}R \sim (B/B_\theta)\rho_\star v_{ti}$, is always subsonic in a tokamak, sonic toroidal flow can only be given by the radial electric field. For example, toroidally oriented neutral beams can result in a sonic flow level of toroidal flow that corresponds to a strong radial electric field, and the pressure driven flow can be neglected. However, the intrinsic toroidal flow without any external momentum input is small, $O(0.1v_{ti} - 0.2v_{ti})$, in many experiments [124]. In this low flow regime, the contributions of the radial pressure gradient and the radial electric field to the toroidal rotation are comparable, and the pressure driven diamagnetic flow should be taken into account. Due to their different characteristics, the effects of the two flows $\Omega_{\varphi,E}$ and $\Omega_{\varphi,d}$ on the turbulent momentum transport are different. Then, in the low flow regime, it is convenient to write the ion toroidal momentum transport as

$$\begin{aligned}\Pi &= \Pi'_{\rm int} - n_i m_i \langle R^2\rangle_s \left[P_{\varphi,d}\Omega_{\varphi,d} + P_{\varphi,E}\Omega_{\varphi,E}\right] \\ &\quad -n_i m_i \langle R^2\rangle_s \left[\chi_{\varphi,d}\frac{\partial \Omega_{\varphi,d}}{\partial r} + \chi_{\varphi,E}\frac{\partial \Omega_{\varphi,E}}{\partial r}\right],\end{aligned} \tag{4.29}$$

where $\Pi'_{\rm int}$ is the intrinsic momentum flux for $\Omega_{\varphi,d} = 0$, $\Omega_{\varphi,E} = 0$, $\partial\Omega_{\varphi,d}/\partial r = 0$ and

$\partial\Omega_{\varphi,E}/\partial r = 0$. By using $\Omega_\varphi = \Omega_{\varphi,d} + \Omega_{\varphi,E}$ and the average of the pinch and diffusion coefficients, the original model in Eq. (4.27) is recovered

$$\begin{aligned}\Pi &= \Pi_{\rm int} - \left[n_i m_i \langle R^2\rangle_s \left(\frac{P_{\varphi,d}+P_{\varphi,E}}{2}\right)(\Omega_{\varphi,d}+\Omega_{\varphi,E})\right] \\ &\quad - \left[n_i m_i \langle R^2\rangle_s \left(\frac{\chi_{\varphi,d}+\chi_{\varphi,E}}{2}\right)\left(\frac{\partial\Omega_{\varphi,d}}{\partial r}+\frac{\partial\Omega_{\varphi,E}}{\partial r}\right)\right].\end{aligned} \tag{4.30}$$

Then, Eq. (4.29) and Eq. (4.30) result in the relation between $\Pi_{\rm int}$ and $\Pi'_{\rm int}$

$$\begin{aligned}\Pi_{\rm int} &= \Pi'_{\rm int} - \frac{1}{2} n_i m_i \langle R^2\rangle_s \Delta P_\varphi (\Omega_{\varphi,d} - \Omega_{\varphi,E}) \\ &\quad - \frac{1}{2} n_i m_i \langle R^2\rangle_s \Delta\chi_\varphi \left(\frac{\partial\Omega_{\varphi,d}}{\partial r} - \frac{\partial\Omega_{\varphi,E}}{\partial r}\right),\end{aligned} \tag{4.31}$$

where $\Delta P_\varphi = P_{\varphi,d} - P_{\varphi,E}$ and $\Delta\chi_\varphi = \chi_{\varphi,d} - \chi_{\varphi,E}$. The relation implies that the difference between the pinch and diffusive coefficients of the two types of rotation can result in intrinsic momentum transport $\Pi_{\rm int}$ in the absence of the total flow and flow shear in Eq. (4.27).

In a non-rotating tokamak, $\Omega_{\varphi,d} = -\Omega_{\varphi,E}$ and Eq. (4.31) can be simplified to

$$\Pi_{\rm int} = \Pi'_{\rm int} - n_i m_i \langle R^2\rangle_s \Delta P_\varphi \Omega_{\varphi,d} - n_i m_i \langle R^2\rangle_s \Delta\chi_\varphi \frac{\partial\Omega_{\varphi,d}}{\partial r}. \tag{4.32}$$

Thus, the intrinsic momentum transport for zero flow and zero flow shear is a function of $\Omega_{\varphi,d}$ and $\frac{\partial\Omega_{\varphi,d}}{\partial r}$. In general, the diamagnetic flow depends on the pressure gradient, the temperature gradient, and collisionality, so the intrinsic momentum transport is

$$\Pi_{\rm int} = \Pi_{\rm int}\left(\frac{\partial p_i}{\partial\psi}, \frac{\partial T_i}{\partial\psi}, \nu_\star, \frac{\partial^2 p_i}{\partial\psi^2}, \frac{\partial^2 T_i}{\partial\psi^2}, \frac{\partial\nu_\star}{\partial\psi}, \Pi'_{\rm int}\right), \tag{4.33}$$

where $\Pi'_{\rm int}$ includes the effect of $f_{1,i}^{bg,q_\parallel}$ and $f_{1,i}^{bg,other}$ in Eq. (4.21). In this chapter, I focus on the effect of the pressure gradient $\frac{\partial p_i}{\partial\psi}$ on $\Pi_{\rm int}$ by evaluating the different momentum pinch coefficients due to the diamagnetic flow and the E×B flow.

4.3.2 A rotating frame transformation

As I explained in Sec. 4.2.3, the mechanism for the momentum pinch for a toroidal flow is clearer in a frame moving with the plasma flow. In particular, the Coriolis drift in the rotating frame is useful to understand the momentum pinch. In this section, I apply the

rotating frame transformation to the gyrokinetic equation in the lab frame, Eq. (4.14), to study the different momentum pinches for the diamagnetic flow and the $E \times B$ flow. To evaluate only the effect of the diamagnetic particle flow, the diamagnetic piece of the background distribution function is approximated by $f_{1,i}^{bg,d} \simeq \frac{mv_\parallel}{T_i}\frac{I\Omega_{\varphi,d}}{B} f_{M,i}$, resulting in $f_i^{bg} = f_{0,i}^{bg} + f_{1,i}^{bg,d} + f_{1,i}^{bg,E} = f_{M,i}\left(\mathbf{v} - \Omega_\varphi R\hat{\varphi}\right) \simeq f_{M,i}(\mathbf{v})\left[1 + (mv_\parallel/T_i)(I\Omega_\varphi/B)\right]$ in Eq. (4.14), where the total toroidal angular frequency is due to both the radial electric field and the pressure gradient (i.e. $\Omega_\varphi = \Omega_{\varphi,d} + \Omega_{\varphi,E}$).

Applying a Lorentz transformation from the lab frame velocity $\mathbf{v}$ to the rotating frame velocity $\mathbf{v}'$ using the relation $\mathbf{v}' = \mathbf{v} - R\Omega_\varphi\hat{\varphi}$, the parallel velocity becomes $v_\parallel' = v_\parallel - I\Omega_\varphi/B$ and the kinetic energy becomes $\mathcal{E}' = \mathcal{E} - I\Omega_\varphi v_\parallel/B$ in the rotating frame [140]. Then, the velocity of the guiding center in the rotating frame is derived for $\rho_\star \ll B_\theta/B \ll 1$ [140],

$$\begin{aligned}\frac{d\mathbf{R}'}{dt} &= v_\parallel'\hat{\mathbf{b}} + \frac{I\Omega_\varphi}{B}\hat{\mathbf{b}} + \mathbf{v}_M' + \mathbf{v}_C' - \frac{c}{B}\nabla\langle\phi\rangle\times\hat{\mathbf{b}} + O\left(\frac{B^2}{B_p^2}\rho_\star^3 v_{ti}\right)\\ &\simeq v_\parallel'\hat{\mathbf{b}} + \Omega_\varphi R\hat{\varphi} - \frac{1}{n_i m_i\Omega_i}\frac{\partial p_i}{\partial\psi}\hat{\mathbf{b}}\times\nabla\psi + \mathbf{v}_M' + \mathbf{v}_C' - \frac{c}{B}\nabla\langle\phi^{tb}\rangle\times\hat{\mathbf{b}}, \quad (4.34)\end{aligned}$$

where $\phi = \phi_0^{bg} + \phi^{tb}$, and $\mathbf{v}_M' = (\mu/\Omega_i)\hat{\mathbf{b}}\times\nabla B + ((v_\parallel')^2/\Omega_i)\hat{\mathbf{b}}\times(\hat{\mathbf{b}}\cdot\nabla b)$ is the ∇B and the curvature drift in the rotating frame. The drift due to the Coriolis force in the rotating frame comes from the curvature drift in the lab frame, $\mathbf{v}_C' = (2v_\parallel'\Omega_\varphi/\Omega_i)\hat{\mathbf{b}}\times[(\nabla R\times\varphi)\times\hat{\mathbf{b}}]$. The time derivative of $\mathcal{E}'$ in terms of the new variables [140] is

$$\begin{aligned}\dot{\mathcal{E}}' &= \dot{\mathcal{E}}\left(1 - \frac{I\Omega_\varphi}{Bv_\parallel'}\right) - \frac{Iv_\parallel'}{B}\frac{\partial\Omega_\varphi}{\partial\psi}\dot{\mathbf{R}}\cdot\nabla\psi - \Omega_\varphi\dot{\mathbf{R}}\cdot\nabla\left(\frac{Iv_\parallel'}{B}\right) \quad (4.35)\\ &\simeq -\frac{Z_i e}{m_i}[v_\parallel'\hat{\mathbf{b}} + \mathbf{v}_M' + \mathbf{v}_C']\cdot\left(-\frac{1}{Z_i e n_i}\frac{\partial p_i}{\partial\psi}\nabla\psi + \nabla\langle\phi^{tb}\rangle\right)\\ &\quad + \frac{Iv_\parallel'}{B}\frac{\partial\Omega_\varphi}{\partial\psi}\left[\mathbf{v}_M' - \frac{c}{B}\nabla\langle\phi^{tb}\rangle\times\hat{\mathbf{b}}\right]\cdot\nabla\psi. \quad (4.36)\end{aligned}$$

Using Eq. (4.34) and (4.36), the ion gyrokinetic equation in the rotation frame is

$$\begin{aligned}&\left(\tfrac{\partial}{\partial t} + \Omega_\varphi R\hat{\varphi}\cdot\nabla\right) f_i^{tb(R)} + \left(v_\parallel'\hat{\mathbf{b}} + \tfrac{1}{B}\Omega_{\varphi,d}\hat{\mathbf{b}}\times\nabla\psi + \mathbf{v}_M' + \mathbf{v}_C' - \tfrac{c}{B}\nabla\langle\phi^{tb}\rangle\times\hat{\mathbf{b}}\right)\cdot\nabla f_i^{tb(R)}\\ &\quad - \tfrac{Z_i e}{m_i c}\Omega_{\varphi,d}\mathbf{v}_M'\cdot\nabla\psi\tfrac{\partial f_i^{tb(R)}}{\partial\mathcal{E}'} = \tfrac{c}{B}\nabla\langle\phi^{tb}\rangle\times\hat{\mathbf{b}}\cdot\left(\nabla f_i^{bg(R)} + \tfrac{Iv_\parallel'}{B}\tfrac{\partial\Omega_\varphi}{\partial\psi} f_i^{bg(R)}\nabla\psi\right)\\ &\quad + \tfrac{Z_i e}{m_i}[v_\parallel'\hat{\mathbf{b}} + \mathbf{v}_M' + \mathbf{v}_C']\cdot\nabla\langle\phi^{tb}\rangle\tfrac{\partial f_i^{bg(R)}}{\partial\mathcal{E}'} + \langle C(f_i)\rangle. \quad (4.37)\end{aligned}$$

Here, the lowest order non-fluctuating piece is related to that in the lab frame by $f_i^{bg(R)}(v'_\parallel) = f_{M,i}(v'_\parallel) = f_i^{bg(L)}(v_\parallel) = f_{M,i}(v_\parallel)\left[1 + (mv_\parallel/T_i)(I\Omega_\varphi/B)\right]$, and the first order fluctuating piece is given by $f_i^{tb(R)}(v'_\parallel) = f_i^{tb(L)}(v_\parallel)$, because the solutions to the equation are not changed after the transformation of variables. The superscript (L) is used to denote the functions in the lab frame in Eq. (4.14). Alternatively, I can also prove that Eq. (4.14) and (4.37) are equivalent by using the linear approximation of the solution, $f_i^{tb(R)}(v'_\parallel) \simeq f_i^{tb(L)}(v'_\parallel) + (I\Omega_\varphi/B)\left(\partial f_i^{tb(L)}/\partial v'_\parallel\right)$ instead of using the time derivative of the variables in real space and velocity space in Eq. (4.34) and (4.36) (see Appendix G).

In the frame of the rotation driven only by the radial electric field ($\Omega_{\varphi,E} \neq 0$ and $\Omega_{\varphi,d} = 0$), the gyrokinetic equation is modified only by the additional Coriolis terms [137], without any energy derivative of the turbulent distribution function. Conversely, the rotation driven by the pressure gradient ($\Omega_{\varphi,E} = 0$ and $\Omega_{\varphi,d} \neq 0$) does not lead to the energy derivative terms in the lab frame, but the energy derivative terms appear in the rotating frame. This additional acceleration term that depends on the type of the rotation, $\frac{Z_i e}{m_i c}\Omega_{\varphi,E}\mathbf{v}_M \cdot \nabla\psi\frac{\partial f_i^{tb(L)}}{\partial\mathcal{E}}$ in Eq. (4.14) or $-\frac{Z_i e}{m_i c}\Omega_{\varphi,d}\mathbf{v}'_M \cdot \nabla\psi\frac{\partial f_i^{tb(R)}}{\partial\mathcal{E}'}$ in Eq. (4.37), results in different momentum pinches for the two rotations either in the lab frame or in the rotating frame. The acceleration term breaks the symmetry of the turbulence because it is odd in the poloidal coordinate (θ). For example, for a circular tokamak, the term is proportional to $\sin\theta$.

The other rotation type dependent term, $\frac{1}{B}\Omega_{\varphi,E}\nabla\psi \times \hat{\mathbf{b}} \cdot \nabla f_i^{tb(L)}$ in Eq. (4.14) or $-\frac{1}{B}\Omega_{\varphi,d}\nabla\psi \times \hat{\mathbf{b}} \cdot \nabla f_i^{tb(R)}$ in Eq. (4.37), can result in the different momentum diffusivities for the diamagnetic flow and the E×B flow. Generally, the radial shear of the rotation reduces the radial correlation length of the turbulent eddies because an eddy radially aligned at an initial time becomes misaligned in time due to the radial gradient of the toroidal flows [11, 63]. The rotation type dependent term contributes to the radial misalignment differently, because the particle orbits are modified not by the pressure gradient but the radial electric field. If there is no rotation shear, the term only gives a Doppler shift of the fluctuations that cannot change the radial transport.

4.3.3 Numerical results

I used the gyrokinetic code GS2 [62] to evaluate the pinch coefficients for the different types of rotation. For numerical reason, the gyrokinetic equation is solved in the frame rotating with $\Omega_{\varphi,E}$, thereby avoiding the energy derivative terms in Eq. (4.14) and Eq. (4.37),

$$\frac{\partial f_i^{tb(R)}}{\partial t'} + \left(v'_\parallel \hat{\mathbf{b}} + \mathbf{v}'_M + \mathbf{v}'_{C\Omega_{\varphi,E}} - \frac{c}{B}\nabla\langle\phi^{tb}\rangle \times \hat{\mathbf{b}}\right) \cdot \nabla f_i^{tb(R)} = \frac{c}{B}\nabla\langle\phi^{tb}\rangle \times \hat{\mathbf{b}} \cdot \nabla f_{i,\Omega_{\varphi,d}}^{bg(R)} + \frac{Z_i e}{m_i}[v'_\parallel \hat{\mathbf{b}} + \mathbf{v}'_M + \mathbf{v}'_{C\Omega_{\varphi,E}}] \cdot \nabla\langle\phi^{tb}\rangle \frac{\partial f_{i,\Omega_{\varphi,d}}^{bg(R)}}{\partial \mathcal{E}'} + \langle C(f_i)\rangle, \tag{4.38}$$

where $\frac{\partial}{\partial t'} = \frac{\partial}{\partial t} + \Omega_{\varphi,E} R\hat{\varphi} \cdot \nabla$ is the time derivative with the doppler shift, $\mathbf{v}_{C\Omega_{\varphi,E}} = \frac{2v'_\parallel \Omega_{\varphi,E}}{\Omega_i}\hat{\mathbf{b}} \times [(\nabla R \times \varphi) \times \hat{\mathbf{b}}]$ is the Coriolis drift due to only the E×B flow, and $f_{i,\Omega_{\varphi,d}}^{bg(R)} = f_{M,i}(v'_\parallel)\left[1 + \frac{m_i v'_\parallel}{T_i}\frac{I\Omega_{\varphi,d}}{B}\right]$ is the perturbed Maxwellian distribution function due to the pressure gradient driven diamagnetic flow. Then, I compare the two momentum pinches in the frame rotating with $\Omega_\varphi = \Omega_{\varphi,d} + \Omega_{\varphi,E}$ by subtracting the convective momentum transport carried by the particles flux using the relation,

$$\Pi^{tb(R)} = \Pi^{tb(L)} - m_i \Omega_{\varphi,d} \langle \Gamma R^2 \rangle_s, \tag{4.39}$$

where Γ is the particle flux. The relation is proven in Appendix G.

For the gyrokinetic simulations in this chapter, I used plasma parameters that model the conditions around the plasma edge with two species (deuteron and kinetic electrons). Accordingly, the temperature gradient, the density gradient, and the safety factor are larger than the parameters of the Cyclone case: $R_0/L_T = 9.0$, $R_0/L_n = 9.0$, $q = 2.5$, $r/a = 0.8$, $R_0/a = 3.0$ and $\hat{s} = 0.8$, where $L_T = -T_i/(dT_i/dr) = -T_e/(dT_e/dr)$ and $L_n = -n/(dn/dr)$ are the characteristic lengths of temperature and density, respectively, $R_0 \simeq \langle R \rangle_s$, q is the safety factor, and $\hat{s}$ is the magnetic shear.

The simulations use 32 grid points in the parallel coordinate θ, 16 grid points in kinetic energy, and 8 grid points in pitch angle. The box size of the simulation in both radial and binomial direction is approximately 125 ρ_i by using 128 and 22 Fourier modes in the radial and binormal coordinates (k_ψ and k_α), respectively.

To study the different effects of the diamagnetic flow and the E×B flow on the momentum transport, I have performed three types of simulations: (i) only with diamagnetic flow ($\Omega_{\varphi,E} = 0$), (ii) only with E×B flow ($\Omega_{\varphi,d} = 0$), and (iii) with both diamagnetic flow and

E×B flow that cancel each other ($\Omega_{\varphi,E} = -\Omega_{\varphi,d}$).

I found that the difference in the momentum diffusivities for the E×B flow and the diamagnetic flow is small for the preceding parameters. The momentum diffusivities, $\chi_{\varphi,E}$ and $\chi_{\varphi,d}$, are estimated by running GS2 in the presence of radial gradients of E×B flow and diamagnetic flow. The radial gradients for both flows result in momentum transport due to the radial gradient of the background distribution function shifted by the parallel flows on the right hand side of Eq. (4.37) (i.e. $\frac{\partial f^{bg(R)}_{i,\Omega_{\varphi,d}}(v'_\parallel)}{\partial\psi} \simeq \left[\frac{m_i v'_\parallel}{T_i}\frac{I}{B}\left(\frac{\partial\Omega_{\varphi,d}}{\partial\psi} + \frac{\partial\Omega_{\varphi,E}}{\partial\psi}\right) + ...\right] f^{bg(R)}_{i,\Omega_{\varphi,d}}$). There is a contribution of the gradient of the perpendicular flow to the time dependent eikonal in GS2 due to the radial shearing rate, but it is included only in the case with a radial gradient of E×B flow. In spite of this difference, the gradients of the two flows give similar Prandtl numbers in the simulations using the above parameters: $\mathrm{Pr}_E \equiv \frac{\chi_{\varphi,E}}{\chi_i} = aR\frac{\Pi}{Q_i}\frac{a}{L_T}\frac{\partial\Omega_{\varphi,E}}{\partial r} = 0.517$ and $\mathrm{Pr}_d \equiv \frac{\chi_{\varphi,d}}{\chi_i} = aR\frac{\Pi}{Q_i}\frac{a}{L_T}\frac{\partial\Omega_{\varphi,d}}{\partial r} = 0.510$, where Q_i is the ion heat flux. Consequently, I assume that the effect of the different momentum diffusivities on the intrinsic momentum transport in Eq. (4.32) is small for this case (i.e. $\chi_{\varphi,d} \simeq \chi_{\varphi,E}$).

On the other hand, I found a significant difference between the momentum pinches for the two types of flows, as shown in Fig. 4-3. The figure shows the normalized momentum transport in terms of the Mach number for the E×B flow (blue curve) and the diamagnetic flow (green curve). The normalization of the momentum transport using the ion heat flux makes the results independent of the turbulence amplitude. The linearity of the graphs confirms that the momentum pinches are proportional to size of the flow, and the slope of the graphs is the pinch coefficient.

The ratio of the pinch coefficient to the momentum diffusivity is important physically because it determines the radial profile of intrinsic toroidal rotation if only pinch and diffusion are considered. The radial slope of the rotation is obtained by balancing the pinch term and the diffusion term in Eq. (4.27) (i.e. $P_\varphi/\chi_\varphi = -\Omega_\varphi{}^{-1}\left(\partial\Omega_\varphi/\partial r\right)$ for $\Pi = 0$ and $\Pi_{\mathrm{int}} = 0$). Instead of calculating momentum diffusivities for every case requiring many extra expensive simulations, I assume the same Prandtl numbers ($\mathrm{Pr} = 0.517$) for the different size and types of flows. This is usually a good assumption [11, 63].

With this assumption, I can obtain the ratio of the pinch coefficient to the momentum diffusivities from the slope of the graphs in Fig. 4-3. It shows that $P_{\varphi,E}/\chi_\varphi \simeq 2.9/R_0$ for the E×B flow, and $P_{\varphi,d}/\chi_\varphi \simeq 3.5/R_0$ for the diamagnetic flow. The difference is about 22% of the pinch. For reference, simple quasilinear estimations of the ratio, in which the

parallel dynamics and the kinetic electrons are neglected, give $P_\varphi/\chi_\varphi = 4/R_0$ for $R_0/L_n = 0$ [138, 141].

Interestingly, the difference in the pinches results in negative momentum flux even for zero rotation ($\Omega_\varphi = \Omega_{\varphi,E} + \Omega_{\varphi,d} = 0$, and $\Omega_{\varphi,d} > 0$ because the pressure decreases with radius), as shown in the red graph in Fig. 4-3. The inward intrinsic momentum flux in the absence of rotation ($\Pi_{\rm int} < 0$) results in peaking of the rotation. The toroidal rotation peaking factor can be defined as,

$$\frac{a}{\Omega_{\varphi,d}}\left(\frac{\partial\Omega_\varphi}{\partial r}\right) = \frac{a}{\Omega_{\varphi,d}}\left(\frac{\Pi_{\rm int}}{\chi_\varphi}\right)\left(\frac{1}{n_i m_i R^2}\right) \tag{4.40}$$

$$= a\frac{P_{\varphi,d} - P_{\varphi,E}}{\chi_\varphi}, \tag{4.41}$$

where the radial slope of the rotation is estimated by balancing the intrinsic momentum transport term and the diffusion term (i.e. $\Pi = 0$ and $\Omega_\varphi = 0$ in Eq. (4.27)). If the linearity between the different pinches holds in Eq. (4.32), the intrinsic momentum transport $\Pi_{\rm int}$ is determined by the difference between the pinch coefficients as given in Eq. (4.41). Based on the simulation results, I found that the linearity holds for low flows with sufficiently small Mach number $\Omega_\varphi R_0/v_{ti} \lesssim 0.1$. However, for the flows with $\Omega_\varphi R_0/v_{ti} \gtrsim 0.1$, the intrinsic momentum transport is more than 50% larger than the difference between the momentum pinches for the two types of flow, due to nonlinearities (note that the slope of the red graph is larger than the difference of the slopes of the green graph and the blue graph in Fig. 4-3). Fig. 4-4 shows the toroidal rotation peaking factor in terms of the different plasma parameters with $\Omega_{\varphi,d}R_0/v_{ti} = 0.3$ and $\Omega_{\varphi,E}R_0/v_{ti} = -0.3$.

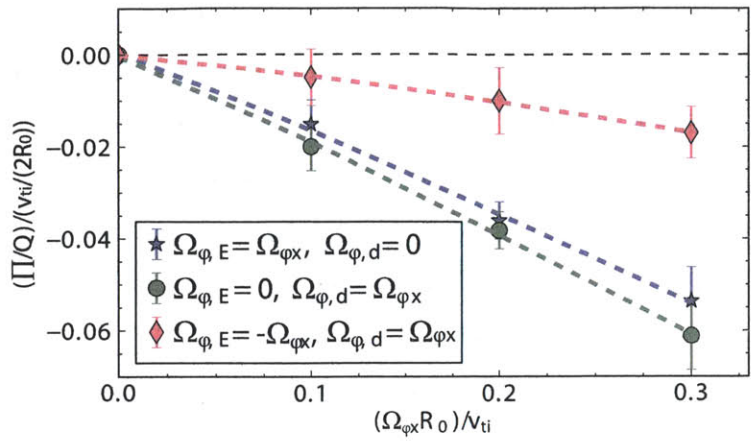

Figure 4-3: Time averaged ratio of ion toroidal angular momentum flux (Π) to ion heat flux (Q_i) as a function of rotation ($\Omega_{\varphi x} R_0/v_{ti}$) for zero rotation shear and the different types of rotation: radial electric field driven rotation (blue-star), pressure gradient driven rotation (green-circle) and opposite rotations of the two types (red-diamond). The error bars show the standard deviation of the fluxes from the time average values due to the typical turbulent fluctuations.

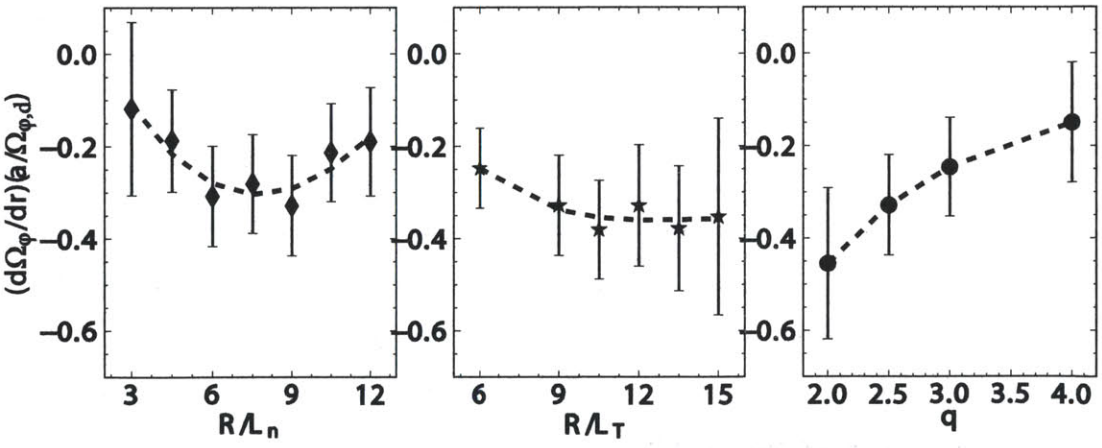

Figure 4-4: The normalized rotation peaking factor generated by the intrinsic momentum flux in terms of (a) the density gradient (R/L_n), (b) the temperature gradient (R/L_T), and (c) the safety factor (q). The parameters, except for the scanned variable, are the same as the default parameters in the text.

4.3.4 Result analysis

The different pinch coefficients evaluated in Sec. 4.3.3 are due to the difference between the terms in the gyrokinetic equation that depend on the E×B flow and those that depend on the diamagnetic flow. For the gyrokinetic equation in the rotating frame with a total flow $\Omega_\varphi = \Omega_{\varphi,d} + \Omega_{\varphi,E}$ in Eq. (4.37), the different parity of the distribution function $\hat{f}^{tb}_{2,i}$ and the potential $\hat{\phi}^{tb}_2$ in Eq. (4.15) and Eq. (4.16) are caused by the Coriolis terms breaking the symmetry in $v'_\parallel$ and the additional acceleration term, $-\frac{Z_i e}{m_i c}\Omega_{\varphi,d}\mathbf{v}'_M \cdot \nabla\psi \frac{\partial f_i^{tb(R)}}{\partial \mathcal{E}'}$ in Eq. (4.37), breaking the symmetry in θ. Notice that the Coriolis term does not depend on the type of flow, while the additional acceleration term depends on the diamagnetic flow in the rotating frame or the E×B flow in the lab frame. It implies that the symmetry breaking due to the Coriolis term is the same for both types of flow, so the acceleration term is the source of the difference between the momentum pinches for the different types of flows.

Consequently, in the non-rotating state in which the diamagnetic flow and the E×B flow cancel each other ($\Omega_{\varphi,d} + \Omega_{\varphi,E} = 0$), the intrinsic momentum transport is due to the acceleration term. Using a balance between the acceleration term, $\frac{Z_i e}{m_i c}\Omega_{\varphi,d}\mathbf{v}'_M \cdot \nabla\psi \frac{\partial f^{tb}_{1,i}}{\partial \mathcal{E}'}$, and the time derivative of $f^{tb}_{2,i}$ ($\partial f^{tb}_{2,i}/\partial t \sim f^{tb}_{2,i}/\tau_{nl}$, where τ_{nl} the nonlinear decorrelation time), I obtain

$$f^{tb}_{2,i} \sim \tau_{nl}\frac{Z_i e}{T_i}(v'^2_\parallel + v'^2_\perp/2)\Omega_{\varphi,d}\frac{B_\theta}{B}\sin\theta\frac{\partial f^{tb}_{1,i}}{\partial \mathcal{E}'}, \tag{4.42}$$

where the magnetic drift of concentric circular flux surfaces is used to make the dependence on θ more transparent. The even parity of the momentum flux π_2 in Eq. (4.17) is due to $\hat{f}^{tb}_{2,i}$ and $\hat{\phi}^{tb}_2$. Accordingly, the intrinsic momentum flux for the same size of diamagnetic flow decreases when the safety factor increases as shown in Fig. 4-4, because $(B_\theta/B) \simeq (r/R)(1/q)$ in Eq. (4.42). The nonlinear decorrelation time is observed to be barely modified by the change of the safety factor in the simulations (the average perpendicular wavelength of the turbulence eddies decreases only 5% and the ion heat flux decreases 10% when the safety factor q is doubled). More analysis is needed to completely understand the dependence on R/L_n and R/L_T in Fig. 4-4.

To study further the effect on the turbulence of the acceleration term, $-\frac{Z_i e}{m_i c}\Omega_{\varphi,d}\mathbf{v}'_M \cdot \nabla\psi \frac{\partial f_i^{tb(R)}}{\partial \mathcal{E}'}$, I use the integrand $\sum_{k_\psi} \pi^{tb}(\theta, v'_\parallel, k_\psi)$ that gives the momentum flux (see Eq. (4.10)). I divide it into a symmetric piece, $\pi^S(\theta, v'_\parallel)$ (i.e. $\pi^S(\theta, v'_\parallel) = \pi^S(-\theta, -v'_\parallel)$)

that gives momentum transport, and an antisymmetric piece, $\pi^A(\theta, v'_{\|})$ (i.e. $\pi^A(\theta, v'_{\|}) = -\pi^A(-\theta, -v'_{\|})$) that does not give momentum transport. I found that $\pi^A \gg \pi^S$ because $\pi^A \simeq \sum_{k_\psi} \pi_1(\theta, v'_{\|}, k_\psi)$ and $\pi^S \simeq \sum_{k_\psi} \pi_2(\theta, v'_{\|}, k_\psi)$ as explained Sec. 4.1 and 4.2.1.

Fig. 4-5 shows $\pi^S(\theta, v'_{\|})$ for two different cases: one with zero rotation in which $\Omega_{\varphi,E}$ and $\Omega_{\varphi,d}$ cancel, and the other with pure E×B rotation in which the only symmetry breaking term is the Coriolis drift. The contours in θ and $v'_{\|}$ for the intrinsic momentum transport in Fig. 4-5 (a) are different from the simple pattern for the Coriolis momentum pinch in Fig. 4-5 (b). Both show the ballooning structure in θ. The difference between Fig. 4-5 (a) and (b) is due to the different symmetry breaking mechanisms.

By integrating the momentum fluxes in Fig. 4-5 in θ and in $v'_{\|}$, respectively, the graphs in Fig. 4-6 (a) and (b) are obtained. The profile in terms of $v'_{\|}$ in Fig. 4-6 (a) shows that the intrinsic momentum transport (red curve) has a larger contribution from particles with large parallel velocity because the particles with large parallel velocity have wider orbits than slow particles and they exchange more energy with the radial electric field, and this energy exchange is the main mechanism behind the intrinsic momentum transport. The asymmetric $\theta-$profile in Fig. 4-6 (b) can be explained by the factor $\sin\theta$ in Eq. (4.42), which is odd in θ.

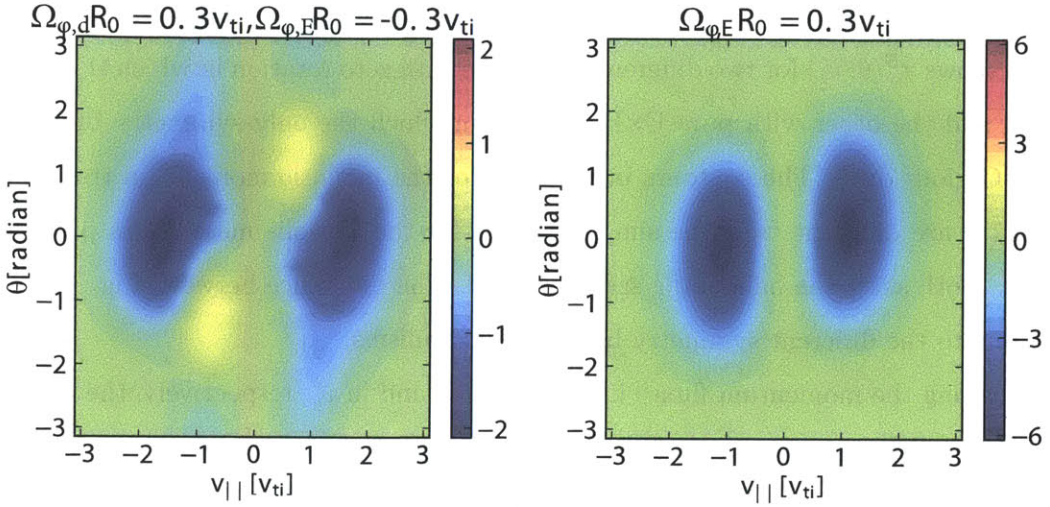

Figure 4-5: The contour plots of the even parity piece of the momentum flux $(\pi^S(\theta, v'_{\|}))$ for (a) $\Omega_{\varphi,d}R_0/v_{ti} = 0.3$ and $\Omega_{\varphi,E}R_0/v_{ti} = -0.3$ and (b) $\Omega_{\varphi,E}R_0/v_{ti} = 0.3$.

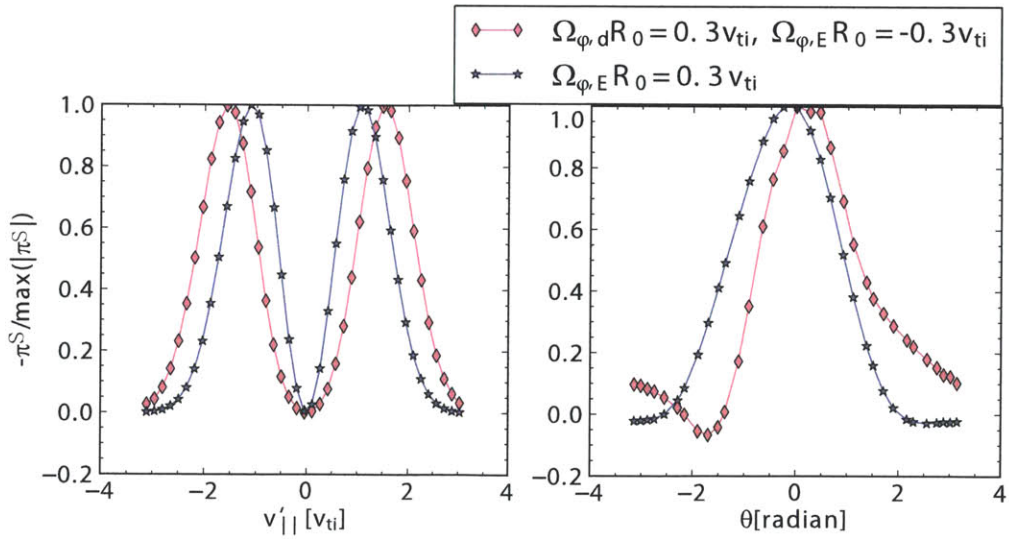

Figure 4-6: The normalized profiles of the even parity momentum flux π^S: (a) $\int_{\theta\min}^{\theta\max} d\theta\pi^S$ in terms of $(v'_{\|}/v_{ti})$, and (b) $\int_0^{\infty} dv'_{\|}\pi^S$ in terms of θ.

4.4 Discussion

When the low confinement mode (L-mode) changes to the high confinement mode (H-mode) in a tokamak, peaking of the intrinsic rotation in the core has been observed [124]. The intrinsic momentum flux due to the different response of the turbulence to the two different types of flows that I found in this chapter can be one of the origins for the rotation peaking in H-mode. In H-mode, a strong radial pressure drop in the pedestal is established, resulting in strong diamagnetic flow, but the measured ion toroidal rotation is not as fast as the diamagnetic flow because a negative radial electric field is generated to balance the diamagnetic flow ($\Omega_{\varphi,E} \sim -\Omega_{\varphi,d} < 0$). In this case, a substantial amount of intrinsic momentum transport occurs because of the different momentum pinches due to the diamagnetic flow and the E×B flow. The main difference is the acceleration of the particles in the radial electric field that breaks the symmetry of the turbulence only for the E×B flow.

The change of the measured rotation in the core at the transition from L-mode to H-mode shows a scaling of $\Delta V_\varphi \simeq C_V \Delta W/I_p$ in many tokamaks, where I_p is the plasma current and ΔW is the stored energy change. The constant for Alcator C-Mod is $C_V \simeq 7 \times 10^5 (m/s)(A/J)$ based on Fig. 1 in [124]. The peaking of the rotation due to the inward intrinsic momentum flux in the pedestal can be estimated using

$$\Delta V_\varphi \sim \Delta r_p \frac{\partial \Omega_\varphi}{\partial r} R_0 \simeq \Delta r_p \frac{\Pi_{\rm int}}{\chi_\varphi n_i m_i R_0} \simeq \frac{(P_{\varphi,d} - P_{\varphi,E})}{\chi_\varphi} \Delta r_p \Omega_{\varphi,d} R_0, \tag{4.43}$$

where Δr_p is the pedestal width and Eq. (4.40) is used. Assuming that the pressure drop at the pedestal is proportional to the stored energy $\Delta W \sim 2\pi^2 a^2 R_0 \Delta p_i$ and using $B_\theta \sim 2I_p/ca$ and $\partial p_i/\partial \psi \sim (1/RB_\theta)(\Delta p_i/\Delta r_p)$, the diamagnetic flow in the pedestal is

$$\Omega_{\varphi,d} R_0 \sim \frac{c^2}{4\pi^2 e n_e a R_0 \Delta r_p} \frac{\Delta W}{I_p}, \tag{4.44}$$

where a low aspect ratio circular tokamak is assumed to estimate the plasma volume and plasma current. Using Eq. (4.43) and Eq. (4.44), the scaling of the rotation change at the top of the pedestal due to the intrinsic momentum flux considered in this chapter is $\Delta V_\varphi (r = a - \Delta r_p) \sim C_{Vd,a} \Delta W/I_p$, where $C_{Vd,a} = \frac{(P_{\varphi,d} - P_{\varphi,E})}{\chi_\varphi} \frac{c^2}{4\pi^2 e n_e a R_0}$. The constant for Alcator C-Mod is $C_{Vd,a} \simeq 2.1 \times 10^5 (m/s)(A/J)$ for $n_e = 10^{20} m^{-3}$, $a = 0.2m$, $R_0 = 0.67m$ and $(P_{\varphi,d} - P_{\varphi,E})/\chi_\varphi = 1.2/R_0$, which is obtained from the red curve in Fig. 4-3. If the inward

momentum pinch in the core is considered, a change in the intrinsic rotation at the pedestal gives a change of the intrinsic rotation in the core that is 2-3 times larger (see the exponential factor $\exp\left(\int_r^{r'} dr'' \frac{P_\varphi}{\chi_\varphi}\right)$ in Eq. (5.3)). This factor makes the change in the rotation at the magnetic axis $\Delta V_\varphi(r=0) \sim C_{Vd,0}\Delta W/I_p$ with $C_{Vd,0} \simeq 4-6\times 10^5 (m/s)(A/J)$. Then, the intrinsic momentum transport mechanism found in this chapter results in rotation that is comparable to observed rotation peaking, and it has the same scaling $\Delta V_\varphi \propto \Delta W/I_p$.

Chapter 5

Rotation change due to lower hybrid waves

The saturation level of the ion toroidal rotation after lower hybrid waves are injected is determined by the balance between the momentum source evaluated in Chapter 3 and the radial transport of momentum by turbulence. The radial momentum transport is determined by the momentum diffusion, the momentum pinch, and the intrinsic momentum transport, as explained in Chapter 4. In this chapter, a preliminary comparison between theory and experiment is performed. I consider two Alcator C-Mod cases: one with high plasma current, 700 kA, and another with low plasma current, 350 kA.

A simple estimation based only on the momentum pinch and the momentum diffusion may explain the rotation observed in the high current case, although the intrinsic momentum flux will probably play a role. The intrinsic momentum transport is definitely needed to explain the change of the rotation observed in the low current plasma discharge, which is in the direction opposite to the wave momentum. In this chapter, the intrinsic momentum transport due to diamagnetic flows is investigated employing the measured plasma parameters in Alcator C-Mod. The change in the plasma current profile due to the lower hybrid waves may partially explain the reversal of the rotation change.

In this chapter, there are three main findings. First, the external momentum injected by the lower hybrid waves is important to explain the rotation saturation in the counter-current direction. Second, the intrinsic momentum transport is required to explain the radial variation of the rotation and the rotation change in the co-current direction. Last,

the diamagnetic effect on the intrinsic momentum transport gives rotation changes of the same order as the changes observed in experiments.

The rest of this chapter is organized as follows. In Sec. 5.1, a formula to reconstruct the steady state ion toroidal rotation is obtained by balancing the momentum source with the turbulent radial transport. In Sec. 5.2, the rotation predicted using only momentum pinch and diffusion is compared with the measured rotation. In Sec. 5.3, the size of the intrinsic momentum transport required to explain the measured intrinsic rotation profile is estimated. As an important source of intrinsic momentum transport, the diamagnetic flow effect is evaluated numerically and the change in the intrinsic momentum transport due to the lower hybrid waves is investigated. I consider the changes in the safety factor profile and the temperature profiles due to lower hybrid wave injection. Finally, I give a summary of possible theoretical explanations for the change in the ion toroidal rotation due to lower hybrid waves in Sec. 5.4.

5.1 Saturation of ion rotation change

To attain steady-state ion toroidal rotation in the presence of lower hybrid waves, the toroidal angular momentum injected by lower hybrid waves should be transported out to the wall. Consequently, the momentum source term and the radial transport term on the right hand side of Eq. (3.33) balance,

$$-\frac{1}{V'}\frac{\partial}{\partial\psi}(V'\Pi)+T_\varphi=0, \tag{5.1}$$

where $T_\varphi=\left\langle\int d^3v m_e R v_\varphi Q(f_e)\right\rangle_s$ is the external torque due to lower hybrid waves.

In Alcator C-Mod, the saturation of the ion rotation is obtained about 100 msec after the lower hybrid wave injection. In Fig. 1-3, for the high plasma current case $I_p=700$kA, the acceleration of the core rotation in the counter-current direction is slowed down and the rotation reaches almost steady state about 400 msec after the wave injection. However, for the low plasma current case, $I_p=350$kA, the initial acceleration of the core rotation is in the counter-current direction, probably due to the external torque, but the acceleration reverses direction after 150 msec, and the rotation change in the co-current direction saturates after 200 msec.

This time scale for the rotation saturation, O(100) msec, is of the order of the turbulent momentum transport time scale, O(10) msec in Alcator C-Mod, and is comparable to the resistive current relaxation time (O(100) msec). The radial current profile is related to the rotation change reversal for the low current case as will be explained in Sec. 5.3.3.

The saturation time is much longer than an ion-ion collision time which is the characteristic time for the perpendicular momentum transfer from the wave to the ions, and much larger than an ion-electron collision time that is the typical time for the parallel momentum transfer from the wave to the ions (see Chapter 3). Hence, the full wave momentum is transferred to the ions, and the external torque in Eq. (5.1) should be the same as the original toroidal angular momentum of the wave injected by the wave launcher.

Because the core rotation change in Fig. 1-3 does not represent the change of the rotation over all radii, the radial profiles of the rotation are given in Fig. 5-1 for the high current case and Fig. 5-2 for the low current case. As shown in Fig. 3-6, the initial acceleration for both discharges is larger at mid-radius, around $\psi/\psi_0 = 0.4$, where the momentum source of lower hybrid waves is more intense (see also the difference between the measured profiles before lower hybrid injection (t=0.75 sec) and after lower hybrid wave injection (t=0.85 sec) in Fig. 5-1 and Fig. 5-2). As a result of the turbulent momentum redistribution, the core rotation starts to accelerate in the counter-current direction for both cases. Interestingly, about 150 msec after the lower hybrid injection, the rotation in the core ($\psi/\psi_0 < 0.3$) has changed significantly, while there is little change in the rotation at mid-radius ($\psi/\psi_0 \gtrsim 0.3$) for both discharges in Fig. 5-1 and Fig. 5-2.

The radial rotation profiles in Fig. 5-1 and 5-2 are estimated using an X-ray spectrometer to measure radiation from impurities [14]. The measurements give line integrated flows and the data needs to be mapped to the reconstructed magnetic field equilibrium. This is done by assuming that the flow is due to a rigid rotation of the flux surface. Due to the weak radiation signal, there are many uncertainties, and the calculation of the radial profiles is not precise enough to believe the spatial oscillation in rotation at outer radii ($\psi/\psi_0 \gtrsim 0.5$).

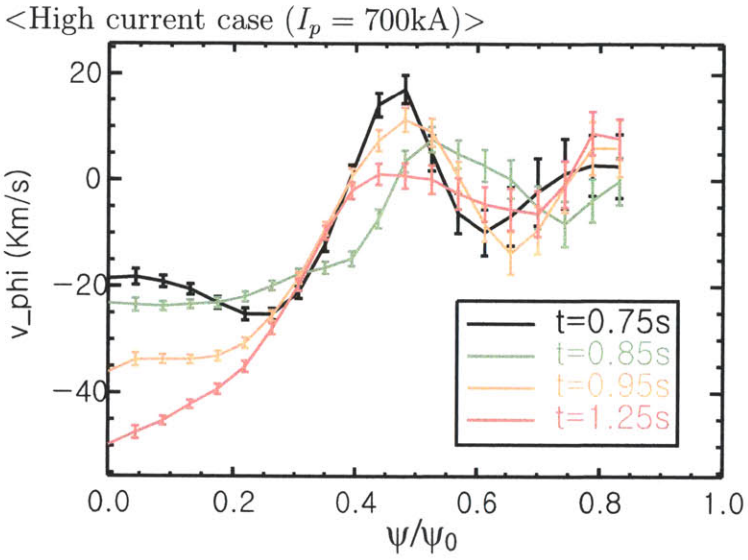

Figure 5-1: Radial profiles of the ion toroidal rotation measured at different times of the high current discharge (I_p = 700kA). The lower hybrid waves are injected at t=0.8 sec. Positive toroidal rotation means co-current, and negative means counter-current.

<Low current case (I_p = 350kA)>
(a) from t=0.75 to t=0.95 sec

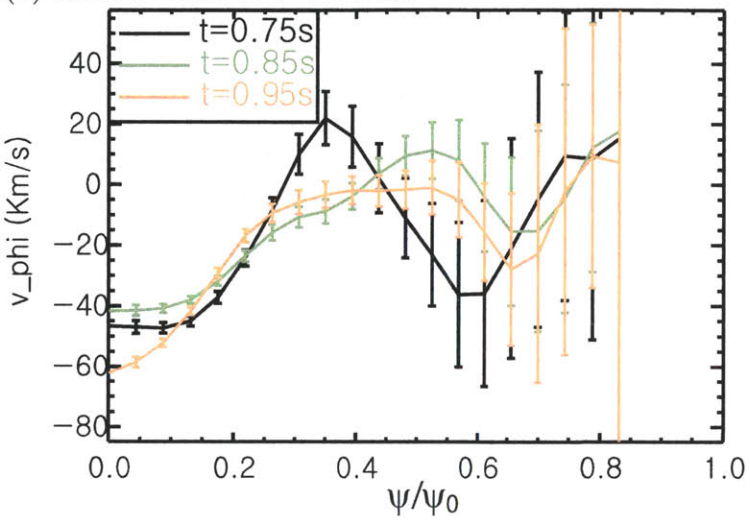

(b) from t=0.95 to t=1.25 sec

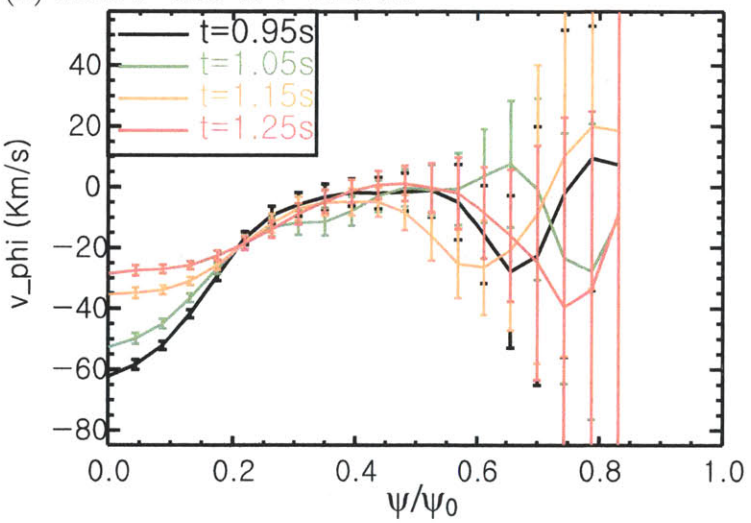

Figure 5-2: Radial profiles of the ion toroidal rotation measured at different times of the low current discharge (I_p = 350kA). The lower hybrid waves are injected at t=0.8 sec. (a) Until t=0.95 sec, the core rotation changes in the same direction as the momentum source (counter-current direction). (b) After t=0.95 sec, the direction of the core rotation change is reversed (in the co-current direction)

Recalling Eq. (4.27) that shows contributions of the intrinsic momentum transport, the momentum diffusion, and the momentum pinch to the radial momentum transport, Eq. (5.1) can be rewritten as

$$\frac{\partial(A\overline{\Pi_{\rm int}})}{\partial r} - m_i \frac{\partial(A\overline{P_\varphi} n_i \langle R^2\rangle_s \Omega_\varphi)}{\partial r} - m_i \frac{\partial}{\partial r}\left(A\overline{\chi_\varphi} n_i \langle R^2\rangle_s \frac{\partial \Omega_\varphi}{\partial r}\right) = (AT_\varphi), \tag{5.2}$$

where $r = a(\psi/\psi_0)$ is the radial coordinate, $A = V'(\psi_0/a)$ is an estimate for the area of the flux surface, and a and ψ_0 are the minor radius and the poloidal flux at the last closed flux surface, respectively. Here, $\overline{\Pi_{\rm int}} = \Pi_{\rm int}/(\psi_0/a)$, $\overline{P_\varphi} = P_\varphi/(\psi_0/a)$, and $\overline{\chi_\varphi} = \chi_\varphi/(\psi_0/a)$ are the rescaled values of the intrinsic momentum flux, the pinch coefficient, and the momentum diffusivity, respectively. The radial rotation profile can be obtained analytically from Eq. (5.2), giving

$$\begin{aligned}
\Omega_\varphi(r) &= \Omega_\varphi(a)\exp\left(\int_r^a dr' \frac{P_\varphi}{\chi_\varphi}\right) \\
&- \int_r^a dr' \left\{ \frac{\Pi_{\rm int}(r')}{\chi_\varphi n_i m_i \langle R^2\rangle_s} \exp\left(\int_r^{r'} dr'' \frac{P_\varphi}{\chi_\varphi}\right)\right\} \\
&+ \int_r^a dr' \left\{ \frac{\int_0^{r'} dr'' A(r'') T_\varphi(r'')}{A\overline{\chi_\varphi} n_i m_i \langle R^2\rangle_s} \exp\left(\int_r^{r'} dr'' \frac{P_\varphi}{\chi_\varphi}\right)\right\},
\end{aligned} \tag{5.3}$$

where the toroidal velocity at the last closed flux surface $\Omega_\varphi(a)$ is given as a boundary condition, and zero momentum flux at the magnetic axis $\Pi(r=0) = 0$ is used as the other boundary condition.

If there is no intrinsic momentum transport and no momentum source ($\Pi_{\rm int} = 0$ and $T_\varphi = 0$), the rotation profile is determined by the first term on the right hand side of Eq. (5.3) due to momentum diffusion and pinch. Then, the sign of the rotation is given by the velocity at the boundary. However, the intrinsic momentum transport (the second term on the right hand side of Eq. (5.3)) can change the sign. Inward intrinsic momentum transport ($\Pi_{\rm int} < 0$) results in a rotation in the co-current direction, and outward intrinsic momentum transport ($\Pi_{\rm int} > 0$) results in a rotation in the counter-current direction. Additionally, notice that $\Pi_{\rm int}$ at outer radii contributes more to the rotation than $\Pi_{\rm int}$ at inner radii because of the exponential factor $\exp\left(\int_r^{r'} dr'' \frac{P_\varphi}{\chi_\varphi}\right)$ in the integral in the second term on the right hand side of Eq. (5.3). The exponential factor arises due to the inward momentum pinch ($P_\varphi/\chi_\varphi > 0$). The last term on the right hand side in Eq. (5.3) is the

contribution of the external torque to the rotation. In the next two sections, I will examine the contribution of each term to the rotation.

5.2 Diffusion and pinch of the momentum injected by lower hybrid waves

In this section, I reconstruct the radial rotation profile using Eq. (5.3) and dropping the intrinsic momentum transport contribution (i.e. $\Pi_{\text{int}} = 0$). For the reconstruction shown in Fig. 5-3, I evaluate the momentum diffusion and pinch coefficients using the gyrokinetic code (GS2) and the experimental parameters in Alcator C-Mod. The pinch and diffusion coefficients at three different radii for the high current case are evaluated and shown in Table 5.1. A transport code, TRANSP [142], is used to prepare the input parameters for the GS2 simulations and analyze the experimental data. The results from GS2 show that P_φ/χ_φ decreases towards the core, which is consistent with the fact that the momentum pinch has to go to zero at the magnetic axis. The Prandtl numbers ($\text{Pr} = \chi_\varphi/\chi_i$) are similar (0.6-0.8) at the three radii, as expected (see Sec. 4.2.3), and the ion heat diffusivities χ_i calculated using GS2 agree well with the estimation in TRANSP based on experimental parameters inside mid-radius. However, there is a non-negligible difference between GS2 and TRANSP for the ion heat flux at outer radii. The difference are not surprising since turbulence is very sensitive to the temperature and density gradients, and the experimental uncertainties on the gradients are large.

In Fig. 5-3, the rotation profiles are estimated using the Prandtl number and the momentum pinch coefficients in Table 5.1. For the ion heat diffusivity, I used the values calculated by TRANSP. The momentum diffusivity is then given by $\overline{\chi_i}_{TRANSP}\text{Pr}_{GS2}$. This calculation is done without the lower hybrid wave momentum source (black dashed curve) and with the lower hybrid wave momentum source (red dashed curve). Fig. 5-3 (a) shows the results for the high plasma current case, and Fig. 5-3 (b) shows the results for the low current case. The toroidal velocity at the boundary is chosen to match the core rotation before the lower hybrid wave injection ($V_\varphi(\psi = \psi_0) = -10\text{km/s}$ in Fig. 5-3 (a) and $V_\varphi(\psi = \psi_0) = -25\text{km/s}$ in Fig. 5-3 (b)).

The measured radial profile change due to the lower hybrid waves in the core agrees

relatively well with the change of the reconstructed profiles near the magnetic axis (see the red solid curve and the red dashed curve in Fig. 5-3 (a) and (b)). For the low current case (b), the reconstructed profile with the momentum source is similar to the the radial profile at t=0.95 sec in which the direction of the rotation change reverses from the counter-current direction to the co-current direction.

The radial profiles obtained with only diffusion and pinch terms (black dashed curve) cannot explain the measured intrinsic rotation (black solid curve) that has rapid spatial oscillations for $\psi/\psi_0 > 0.4$. It requires intrinsic momentum transport to be explained, although some rapid spatial oscillations are probably an artifact of the mapping between the line integrated measurements and the radial profile of the toroidal rotation. The required size of the intrinsic momentum transport will be estimated in Sec. 5.3.1. Previous studies have found that the rotation in the high flow regime (Ma $\sim$ 1) due to the strong neutral beam injection is well described by only diffusion and pinch [139], but the intrinsic momentum contribution is necessary to explain rotation in the low flow regime (Ma $\sim$ 0.1).

There is a more important disagreement between the measurement and the reconstruction only by diffusion, pinch and momentum source in the low plasma current case in Fig. 5-3 (b). The reconstructed profile (red dashed curve) cannot explain the saturated rotation profile (blue solid curve) that shows a change of core rotation in the co-current direction.

Although the saturated radial profile (blue solid curve) may look like the profile before the injection (black solid curve) with stronger diffusion, the time history of the rotation in Fig. 5-2 cannot be explained with an increased momentum diffusivity. There is a significant acceleration due to the wave momentum deposition at $\psi/\psi_0 \sim 0.3$ right after the lower hybrid wave injection as shown in the red solid curve. The difference in $\psi/\psi_0 \sim 0.3$ between the black solid curve and the blue solid curve is probably due to the momentum source rather than stronger momentum diffusion.

The profile change which cannot be understood with only diffusion and pinch is the change after t=0.95 sec in Fig 5-2 (b). In fact, the momentum diffusivity, inferred from the ion heat diffusivity, is unlikely to have changed significantly after the lower hybrid injection, because the ion temperature does not change significantly after. It is more likely due to a change in the intrinsic momentum transport, which will be explored in the next section.

Table 5.1: Evaluation of turbulent momentum diffusions and pinches using GS2 for the high current case shown in Fig. 1-3. The experimental parameters are shown in the upper table and the GS2 results are shown in the lower table. TRANSP is used to obtain the experimental ion heat diffusivity $\overline{\chi_i}$.

	Inputs								
	r/a	q	$\hat{s}$	$\nu_\star$	a/L_{Ti}	a/L_{Te}	a/L_n	ρ_i/a	$v_{ti}/a[10^6 s^{-1}]$
(1) inner radius	0.37	0.88	0.81	0.65	1.58	2.21	0.79	0.0056	1.33
(2) mid-radius	0.54	1.32	1.42	0.93	2.51	3.39	1.21	0.0052	1.18
(3) outer radius	0.79	2.71	2.55	2.31	3.13	4.70	2.20	0.0058	1.16

	GS2				TRANSP
	Pr= χ_φ/χ_i	$(P_\varphi/\chi_\varphi)R_0$	$\overline{\chi_\varphi}[m^2/s]$	$\overline{\chi_i}[m^2/s]$	$\overline{\chi_i}[m^2/s]$
(1) inner radius	0.77	1.15	0.43	0.59	0.46
(2) mid-radius	0.60	2.06	0.57	0.95	0.85
(3) outer radius	0.85	2.73	0.23	0.27	1.68

(a) High current case ($I_p = 700$kA)

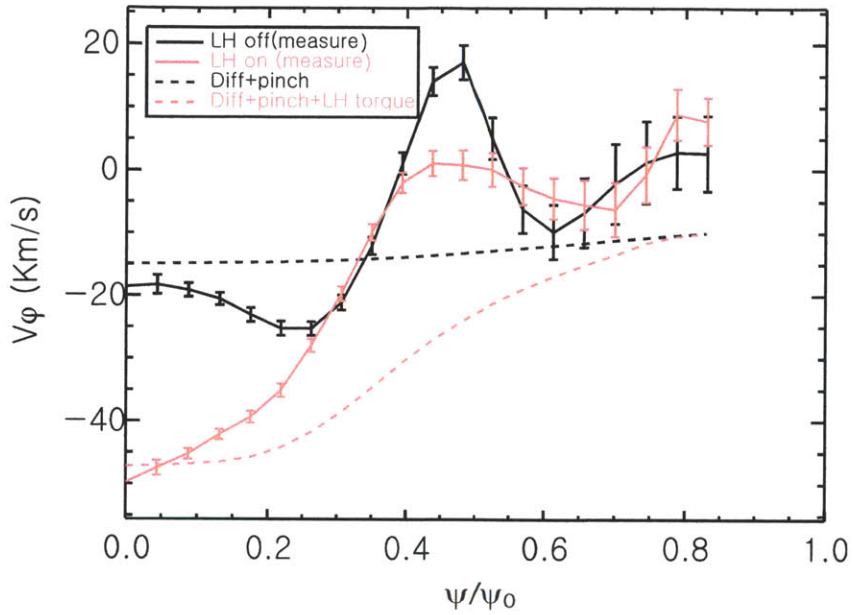

(b) Low current case ($I_p = 350$kA)

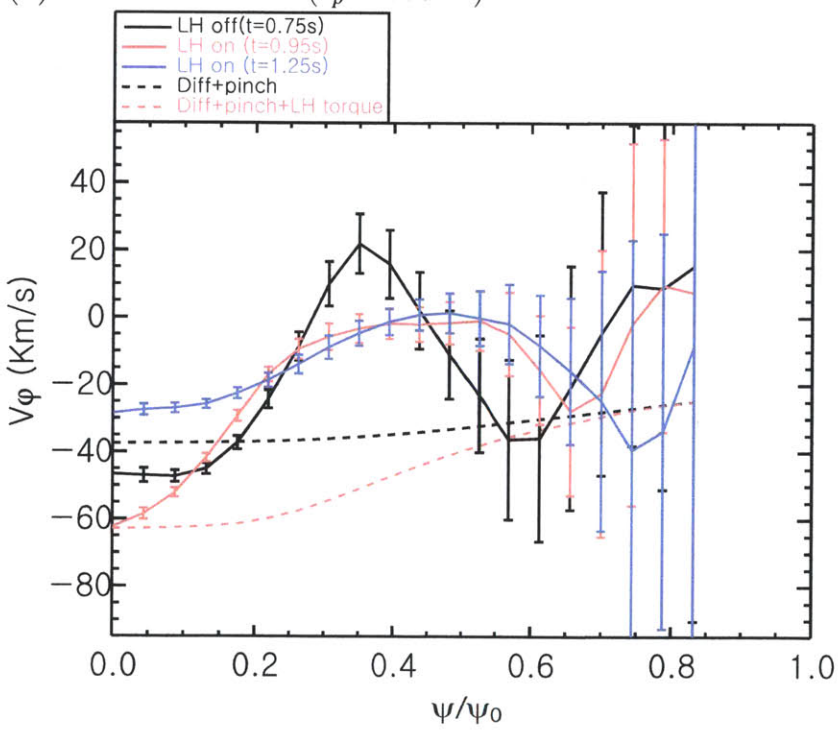

Figure 5-3: Radial profiles of rotation based on measurements (solid lines) and the reconstruction using only the momentum pinch, diffusion and source in Eq. (5.3) (dashed lines). The black curves are the profiles before the lower hybrid wave injection (t=0.75 sec) and the red curves are the profiles after the lower hybrid wave injection (t=1.25 sec for (a) and t=0.95 sec for (b)).

5.3 Change of intrinsic momentum transport due to lower hybrid waves

In this section, the intrinsic momentum transport in the presence of lower hybrid waves is investigated with the experimental parameters of Alcator C-Mod. First, the required amount of the intrinsic momentum transport is estimated using the measured radial profiles of rotation and ion temperature in the absence of lower hybrid waves. Then, the intrinsic momentum transport due to diamagnetic effects is numerically evaluated, and the change of the intrinsic momentum transport due to the lower hybrid waves is estimated.

5.3.1 Required intrinsic momentum transport

Without any external momentum input, the three different contributions to the momentum transport on the right hand side in Eq. (4.27) (diffusion, pinch, and intrinsic momentum transport) must balance (i.e. $\Pi = 0$). Then, the intrinsic momentum flux divided by the ion heat flux is

$$\begin{aligned} \frac{\Pi_{\rm int}}{Q_i} &= \frac{P_\varphi n_i m_i \langle R^2 \rangle_s \Omega_\varphi}{Q_i} + \frac{\chi_\varphi n_i m_i \langle R^2 \rangle_s (\partial \Omega_\varphi / \partial r)}{Q_i} \\ &= -\frac{\Pi_{\rm pinch}}{Q_i} - \frac{\Pi_{\rm diff}}{Q_i}, \end{aligned} \tag{5.4}$$

where the normalized diffusion and pinches are calculated approximately using GS2 and the experimentally measured profiles for rotation and temperature,

$$\frac{\Pi_{\rm diff}}{Q_i} = {\rm Pr} \frac{(\partial \Omega_\varphi / \partial r)}{(\partial T_i / \partial r)} m_i \langle R^2 \rangle_s, \tag{5.5}$$

$$\frac{\Pi_{\rm pinch}}{Q_i} = \frac{\Pi_{\rm diff}}{Q_i} \frac{\Omega_\varphi}{(\partial \Omega_\varphi / \partial r)} \frac{P_\varphi}{\chi_\varphi}. \tag{5.6}$$

Here, I assume that the ion heat flux is mostly caused by the ion temperature gradient and there is no thermal pinch (i.e. $Q_i = -\chi_i n_i \frac{\partial T_i}{\partial r}$). In Fig. 5-4, the intrinsic momentum transport required to explain the experimentally observed intrinsic rotation is obtained using the average Prandtl number and the radially varying values of P_φ / χ_φ given in Table 5.1. Compared to the significant momentum diffusion, the momentum pinch is small for intrinsic rotation in steady state at most radii because the pinch coefficient is small at inner

radii, and the rotation size is small at the outer radii.

The accuracy of the estimated momentum transport is reduced by non-negligible errors in the measurements of the ion temperature and the ion rotation. To estimate more physical intrinsic momentum transport, I need to eliminate the unphysical radial fluctuation in the measured rotation profiles shown in the black curves in Fig. 5-3. Fig. 5-4 (a) and (c) are obtained using the full rotation profiles, while Fig. 5-4 (b) and (d) are obtained using only two rotation values, at the center and the edge, to estimate the value of $\partial\Omega_\varphi/\partial r$. Since most of the intrinsic momentum flux given in Fig. 5-4 is balancing the diffusive flux, the smoother rotation profile with smaller $\partial\Omega_\varphi/\partial r$ gives a much smaller $\Pi_{\rm int}$

The real values of the normalized intrinsic momentum transport for the high current case ($I_p = 700kA$) is between the values obtained using the full rotation profile in Fig. 5-4 (a) and the values obtained using the extremely smoothed rotation profile in Fig. 5-4 (b). Fig. 5-4 (a) gives $-0.2 \lesssim \frac{\Pi_{\rm int}}{Q_i}\frac{v_{ti}}{R_0} \lesssim 0.3$ at most radii, and Fig. 5-4 (b) gives $0.05 \lesssim \frac{\Pi_{\rm int}}{Q_i}\frac{v_{ti}}{R_0} \lesssim 0.1$ at most radii. The overall positive (outward) intrinsic momentum transport results in counter-current rotation in the core.

For the low current case (I_p =350 kA), Fig. 5-4 (c) gives $-0.6 \lesssim \frac{\Pi_{\rm int}}{Q_i}\frac{v_{ti}}{R_0} \lesssim 0.7$, and Fig. 5-4 (d) gives $0.1 \lesssim \frac{\Pi_{\rm int}}{Q_i}\frac{v_{ti}}{R_0} \lesssim 0.2$. The normalized intrinsic momentum transport for the low current case is much larger than that for the high current case. The larger intrinsic momentum transport may be caused by a larger diamagnetic flow, whose size scales with B/B_θ.

Consequently, I can conclude from this analysis that the overall size of the required intrinsic momentum transport in Alcator C-Mod is smaller than $\frac{\Pi_{\rm int}}{Q_i}\frac{v_{ti}}{R_0} = 0.7$ and probably closer to 0.1, since the volume average values and the values from the smoothed profiles are $\frac{\Pi_{\rm int}}{Q_i}\frac{v_{ti}}{R_0} \sim 0.1$, which is comparable to the intrinsic momentum transport due to the diamagnetic flow in gyrokinetic simulations in Sec. 5.3.3.

Among the many symmetry breaking mechanisms described in Sec. 4.2 that can explain the required intrinsic momentum transport, I focus only on the contribution of the diamagnetic effects to the intrinsic momentum transport, as done in Chapter 4.

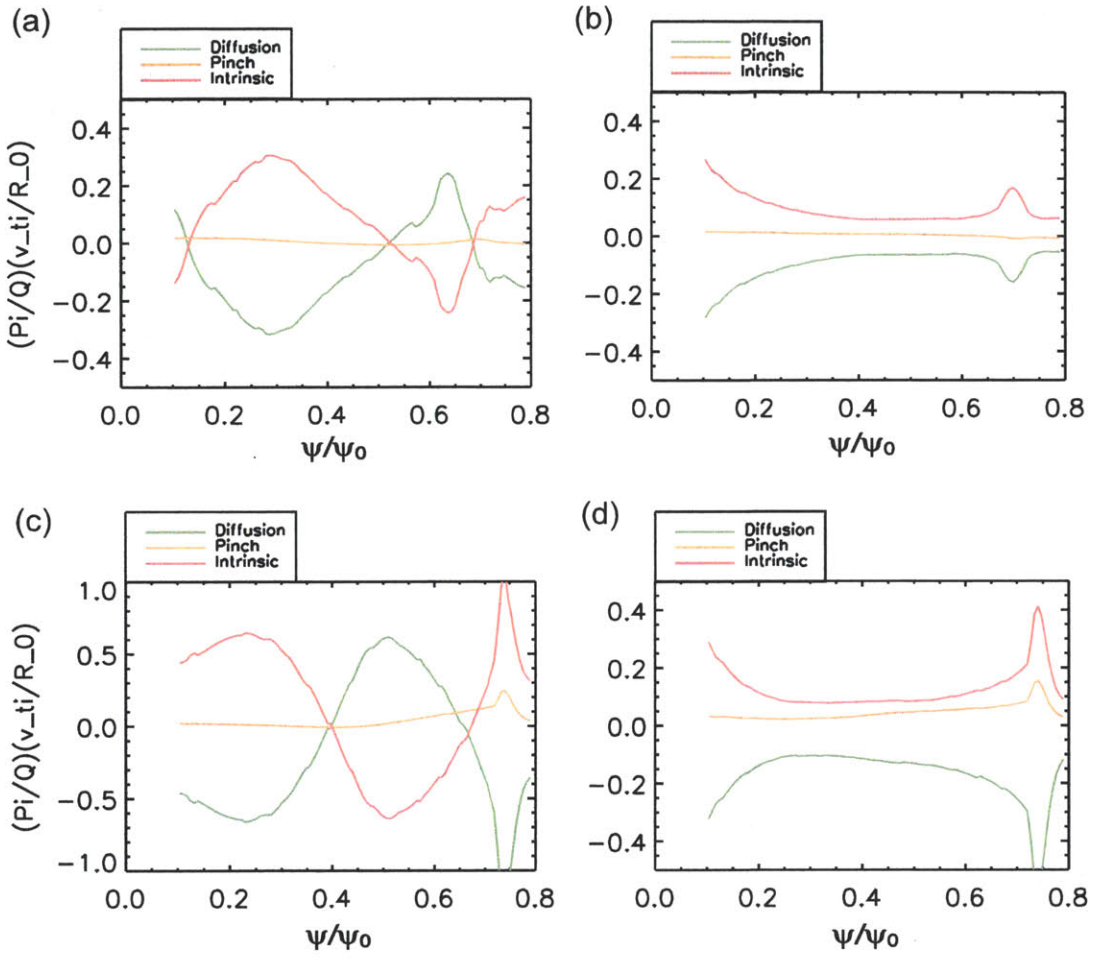

Figure 5-4: Estimation of normalized momentum transport in the absence of any external momentum input using experimental radial profiles of rotation and temperature. Figures (a) and (b) correspond to the high current case (I_p =700 kA), and (c) and (d) to the low current case (I_p =350 kA). The full profiles of measured rotation in Fig. 5-3 (black curves) are used to calculate (a) and (c), while the rotation values at only two radii ($\psi = 0$ and $\psi = \psi_0$) are used to estimate $\partial\Omega_\varphi/\partial r$ for (b) and (d). Momentum diffusion (green), momentum pinch (yellow), and intrinsic momentum transport (red) are obtained using Eq. (5.5), (5.6) and (5.4), and the results in Table 5.1.

5.3.2 Change of the diamagnetic effect due to lower hybrid waves

The diamagnetic effect on the intrinsic momentum transport is significant when the toroidal rotation is in the low flow regime (Ma $\sim$ 0.1), as explained in Sec. 4.2. In Fig. 5-5, the size of the parallel diamagnetic flow is compared with the measured toroidal rotation. The parallel diamagnetic flow is evaluated by solving the drift kinetic equation in Eq. (4.23) using the neoclassical code NEO [143]. Because the parallel diamagnetic flow increases with pressure gradient, the diamagnetic flow increases towards the edge. Consequently, the size of the diamagnetic flow at outer radii ($\psi/\psi_0 > 0.5$) in Fig. 5-5 is comparable to the measured rotation, while the diamagnetic flow in the core is only about 20% of the measured toroidal flow. The gap between the diamagnetic flow size and the measured flow size is compensated by E×B flow due to the radial electric field (i.e. $\Omega_\varphi = \Omega_{\varphi,d} + \Omega_{\varphi,E}$). As I investigated in Sec. 4.3, the different momentum fluxes for the different types of flow (the diamagnetic flow and E×B flow) result in intrinsic momentum transport. The fact that the diamagnetic flow is stronger at outer radii than at inner radii implies that the contribution of the diamagnetic effect to the intrinsic momentum transport at outer radii is more important. Due to the exponential factor of $\exp\left(\int_r^{r'} dr'' \frac{P_\varphi}{\chi_\varphi}\right)$ in Eq. (5.3), we expect Π_{int} at outer radii to be more important for the rotation at the magnetic axis than Π_{int} at inner radii.

In this section, I numerically evaluate the effect of lower hybrid waves on the intrinsic momentum transport due to diamagnetic effects only at a local radius for simplicity. I choose the outermost radius ($\psi/\psi_0 \sim 0.5$) within the range where the lower hybrid waves are strongly damped because the diamagnetic effect is more significant at outer radii and because the intrinsic momentum transport at the outer radii is more important to determine the intrinsic rotation in the core than the intrinsic momentum transport at inner radii.

The intrinsic momentum transport for a non-rotating plasma in which the E×B flow and the diamagnetic flow cancel each other is evaluated by solving the higher order gyrokinetic equation in Eq. (4.14) implemented in GS2, as was done in Chapter 4. However, in this chapter, I include the full neoclassical distribution correction to the background distribution function, $f_{1,i}^{bg,d}$, which is calculated with NEO, to describe the experimental situation more realistically.

In Chapter 4, the correction was just a shift to the Maxwellian due to the diamagnetic particle flow (see Eq. (4.37)). In this chapter, the intrinsic momentum fluxes in Table 5.2 and 5.3 include all contributions to $f_{1,i}^{bg,d}$, that is, all the terms on the right hand side of Eq. (4.31). These contributions to momentum flux include the intrinsic momentum transport (first term) due to the pieces other than the diamagnetic particle flow contribution (i.e. due to $f_{1,i}^{bg,q_\parallel}$ and $f_{1,i}^{bg,other}$ in Eq. (4.21)), the intrinsic momentum transport due to the different momentum pinches for the canceling E×B flow and the diamagnetic particle flow (second term) and the intrinsic momentum transport due to the different momentum diffusivities for the canceling radial gradients of the E×B flow and the diamagnetic particle flow (third term). Here the diamagnetic particle flow retains the additional parallel velocity contribution from $K(\psi)$ in Eq. (4.23), which is proportional to the temperature gradient, whereas the diamagnetic particle flow used in Chapter 4 is only due to the pressure gradient.

The evaluation of the intrinsic momentum transport due to the diamagnetic effect in this chapter follows the procedure in [134], but the measured parameters in Alcator C-Mod are used instead of the Cyclone base plasma parameters used in [134].

The intrinsic momentum fluxes are evaluated in GS2 for four different cases: (a) the high plasma current case before lower hybrid wave injection, (b) the high plasma current case after lower hybrid wave injection, (c) the low plasma current case before lower hybrid wave injection, and (d) the low plasma current case after lower hybrid wave injection (see Table 5.2).

For the high current case, the plasma parameters in Table 5.2 (a) and (b) are almost identical and the effect of the lower hybrid waves on the diamagnetic flow and the intrinsic momentum transport are small. In this case, the radial shear of the diamagnetic flow ($\partial\Omega_{\varphi,d}/\partial r$) at the selected radius is almost zero because the increase in the safety factor $\hat{s} > 0$ and the increase in the temperature gradient $\partial(a/L_{Ti})/\partial r > 0$ toward outer radii compensate for the decrease in the thermal velocity toward outer radii (remember the scaling of the diamagnetic flow, $\Omega_{\varphi,d}R_0 \sim \frac{q}{(r/R)}\frac{\rho_i}{L_T}v_t$).

For the low current case in Table 5.2 (c) and (d), the diamagnetic plasma flows are larger than in the high current case because of the increased safety factor and increased collisionality. Also, the increased gradient of the safety factor and the temperature gradient are not enough to compensate for the decreased gradient in the thermal velocity, giving a negative diamagnetic flow shear. The lower hybrid wave changes the plasma current profiles

and results in a larger safety factor and a decreased magnetic shear at the selected radius (see Fig. 5-6 and Fig. 5-7). As a result, the radial shear of the flow has a larger negative value after the lower hybrid injection than before the injection (compare Table 5.2 (c) and (d)).

As demonstrated by the different ion heat flux Q_i and electron heat flux Q_e in Table 5.2, different turbulence characteristics are observed in each case. For the high plasma current discharge, a strong ITG (ion temperature gradient) instability drives the drift wave turbulence, while trapped electron driven turbulence dominates over the ion temperature gradient driven turbulence for the low plasma current discharge. The different size of the turbulent fluctuations is not critical for the toroidal rotation caused by the intrinsic momentum transport because the rotation term due to the intrinsic momentum transport in Eq. (5.3) is divided by the momentum diffusion that scales with the energy diffusion (i.e. $\frac{\Pi_{\rm int}}{\chi_\varphi n_i m_i \langle R^2 \rangle_s} = \frac{\Pi_{\rm int}}{Q_i} \frac{(\partial T_i/\partial r)}{\rm Pr} \frac{1}{m_i \langle R^2 \rangle_s}$). Consequently, the normalized intrinsic momentum transport ($\frac{\Pi_{\rm int}}{Q_i} \frac{v_{ti}}{R_0}$) in the table is the critical parameter that determines the size and the direction of the ion rotation. The heat fluxes are very sensitive to the gradients of temperature and density, while the normalized intrinsic momentum fluxes are not as sensitive to the gradients as the heat fluxes are, as will be explained in the next section 5.3.3.

As shown in Table 5.2, the normalized intrinsic momentum transport due to diamagnetic effects ($\frac{\Pi_{\rm int}}{Q_i} \frac{v_{ti}}{R_0}$) is substantially affected by the size of the diamagnetic flow ($\frac{\Omega_{\varphi,d} R_0}{v_{ti}}$) and the flow shear ($\frac{\partial \Omega_{\varphi,d}}{\partial r} \frac{R_0 a}{v_{ti}}$), as expected (see Eq. (4.32)). Because the diamagnetic flow for the high current case is smaller than the flow for the low current case, the normalized intrinsic momentum transport for the high current case is also smaller than the flow for the low current case. The fact that the intrinsic momentum transport is larger for the low plasma current case may explain why the reversal of the acceleration direction due to the lower hybrid wave is observed only in the low plasma current discharge. The small intrinsic momentum transport in the high plasma current case does not cause sufficient momentum redistribution to reverse the acceleration direction.

The positive momentum fluxes in Table 5.2 (c) and (d) give total counter current rotation in the core because the plasma tends to expel co-current momentum. However, to explain the reduced counter-current rotation after the lower hybrid wave injection, a significant reduction of the positive momentum flux is necessary. I will show in the next section that a significant reduction of the intrinsic momentum flux can happen for a reduced value of the

magnetic shear.

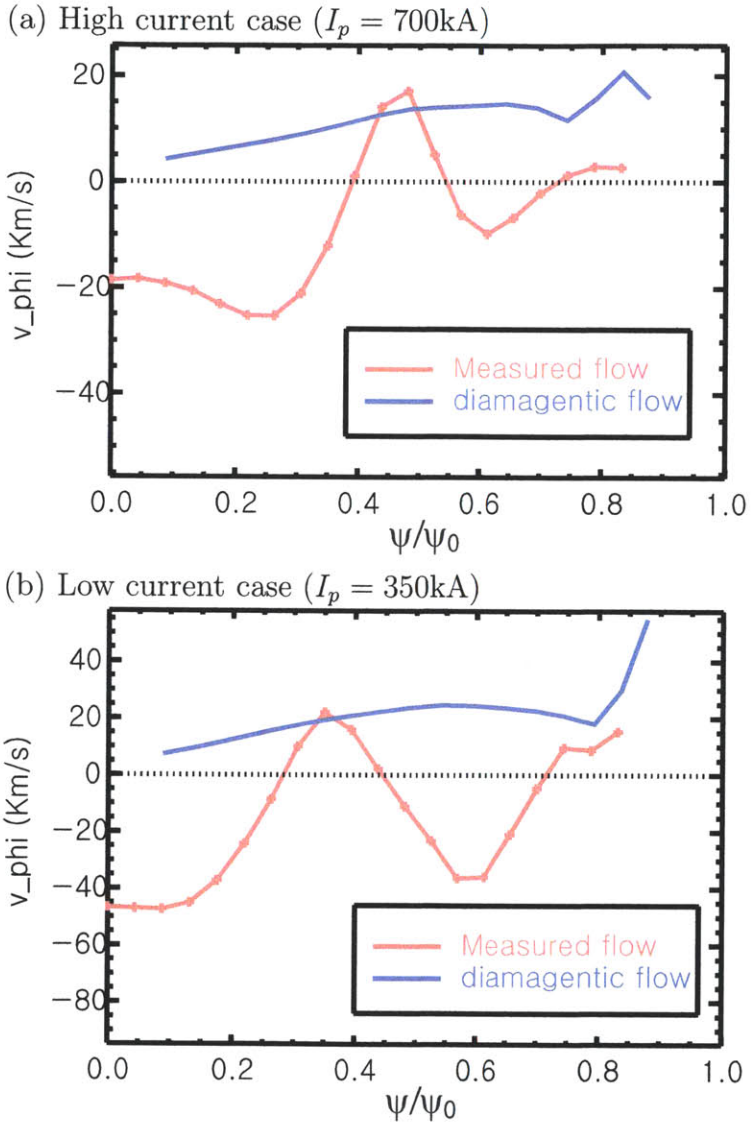

Figure 5-5: Parallel diamagnetic flow in Eq. (4.23) evaluated using NEO (blue) and the measured rotation before the lower hybrid wave injection (t=0.75 sec).

Table 5.2: Simulation results for intrinsic momentum transport in a non-rotating plasma in which E×B flow and diamagnetic flow cancel (i.e. $\Omega_{\varphi,E} = -\Omega_{\varphi,d}$ and $\frac{\partial \Omega_{\varphi,E}}{\partial r} = -\frac{\partial \Omega_{\varphi,d}}{\partial r}$). The measured plasma parameters at r/a=0.54 and R/a=3.0 for the high current discharge (I_p =700 kA) and the low current discharge (I_p =350 kA) in Alcator C-Mod are used. Here, $Q_{GB} = \rho_\star^2 n_i T_i v_{ti}$ is used to normalize the heat fluxes.

	Inputs				
	q	$\hat{s}$	$\nu_\star$	a/L_{Ti}	a/L_{Te}
(a) I_p =700 kA at t=0.75 sec	1.32	1.42	0.93	2.51	3.39
(b) I_p =700 kA at t=1.25 sec	1.32	1.48	0.89	2.45	3.63
(c) I_p =350 kA at t=0.75 sec	2.14	2.34	2.80	2.55	4.93
(d) I_p =350 kA at t=1.25 sec	2.63	2.11	4.40	2.63	4.09

	Inputs			
	$a(\partial(a/L_{Ti})/\partial r)$	a/L_n	ρ_i/a	$v_{ti}/a[10^6 s^{-1}]$
(a) I_p =700 kA at t=0.75 sec	3.44	1.21	0.0037	1.18
(b) I_p =700 kA at t=1.25 sec	3.57	1.42	0.0037	1.13
(c) I_p =350 kA at t=0.75 sec	2.99	1.60	0.0046	1.39
(d) I_p =350 kA at t=1.25 sec	-1.17	1.39	0.0043	1.31

	NEO		GS2		
	$\frac{\Omega_{\varphi,d} R_0}{v_{ti}}$	$\frac{\partial \Omega_{\varphi,d}}{\partial r} \frac{R_0 a}{v_{ti}}$	$\frac{\Pi_{\rm int}}{Q_i} \frac{v_{ti}}{R_0}$	Q_i/Q_{GB}	Q_e/Q_{GB}
(a) I_p =700 kA at t=0.75 sec	0.058	-0.028	0.005	7.48	5.12
(b) I_p =700 kA at t=1.25 sec	0.054	-0.001	0.008	5.18	4.31
(c) I_p =350 kA at t=0.75 sec	0.140	-0.151	0.040	1.11	0.70
(d) I_p =350 kA at t=1.25 sec	0.171	-0.391	0.067	6.04	4.45

5.3.3 Change of the intrinsic momentum transport by modification of plasma parameters

There are many plasma parameters that determine the intrinsic momentum transport due to diamagnetic effects as shown in Eq. (4.33). These parameters can be obtained by experimental measurements as given in Table 5.3. However, there are many sources of errors. In Alcator C-Mod, the safety factor radial profile is inferred from the measurements of the pitch angle of the magnetic field obtained with motional Stark effect (MSE) diagnostics [23, 144]. The radial profiles of temperature and density are measured by Thomson scattering diagnostics [145] and X-ray spectroscopy [65]. The resolution in the diagnostics is not sufficient to give precise radial profiles which are important to evaluate the magnetic shear ($\hat{s} = \frac{r}{q}\frac{\partial q}{\partial r}$) and the first and second radial derivatives of density and temperature. In this subsection, I investigate the effect of the safety factor, the collisionality, the temperature gradient, and their radial derivatives on the momentum transport by modifying the given plasma parameters within the error bars to explain the reversal of the rotation change due to the lower hybrid waves.

First, the uncertainty in the ion temperature gradient is considered. As shown in Table 5.3 (b) and (c), 20% increase or decrease of the ion temperature gradient gives significantly different turbulence characteristics (see the ion heat flux and the electron heat flux). The diamagnetic flow depends on the temperature gradient, and consequently the normalized momentum flux $\frac{\Pi_{\rm int}}{Q_i}\frac{v_{ti}}{R_0}$ depends on the temperature gradient as well. Even though the heat fluxes depend sensitively on the temperature gradient, the normalized momentum flux does not show the same sensitivity. In particular, the sign of the momentum flux, and hence the intrinsic rotation direction, do not seem to depend on the ion temperature gradient.

Second, the second radial derivative of the temperature profile is adjusted in Table 5.3 (d) to see the effect of radial shear of the diamagnetic flow. It does not change the turbulence characteristics as expected. The momentum flux is reduced about 30% by making the radial shear of the diamagnetic flow zero.

Last, I modify the magnetic shear to see the effect of the lower hybrid waves on the momentum transport. The most significant impact of the lower hybrid waves on the plasma parameters is the change in the radial profile of the plasma current, as driving current is the purpose of the lower hybrid wave injection.

In the experiments in Alcator C-Mod, the total current is given by the sum of Ohmic current induced by the central solenoid coils, and the non-inductive current driven by lower hybrid waves. The bootstrap current in Alcator C-Mod is negligible due to the relatively low $\beta_\theta = \frac{8\pi p_e}{B_\theta^2}$ compared to ITER [23]. The total amount of current is controlled to be the same as before the lower hybrid injection. As a result, the increase in LH driven current is compensated by a decrease in the Ohmic current. While the Ohmic current density is peaked in the core due to the high electrical conductivity there, the lower hybrid wave driven current depends on the profile of the lower hybrid wave damping. Thus, the total radial profile is changed after the lower hybrid wave injection. Typically, the total current density is reduced in the core and it is increased where the lower hybrid is strongly damped. Accordingly, the safety factor in the core is increased, while the safety factor at the last closed flux surface is not changed much because there is the same amount of total current inside the last closed flux surface (see Fig. 5-6).

The change in the radial profile of the safety factor is more significant for the low current case than for the high current case if the lower hybrid wave driven current is the same for a given wave power absorption. The efficiency of the lower hybrid current drive in Alcator C-Mod is $\frac{n_e R_0 I_{LH}}{P_{LH}} \simeq 2.3 \times 10^{19} \mathrm{AW}^{-1} m^{-2}$ [23], and it results in about 130 kA LH wave driven current for 850 kW of LH wave power absorption. For the high current case with $I_p = 700kA$, the lower hybrid driven current is only about 18% of the total current. However, for the low current case with $I_p = 350kA$, the lower hybrid driven current is about 36% of the total current, resulting in a significant change in the radial profile of the plasma current.

Fig. 5-6 and Fig. 5-7 show the significant change in the safety factor and the magnetic shear profiles due to the lower hybrid waves for the low current case. The increase in the safety factor due to the LH wave driven current is about 30% at most mid radii and it is reflected in the input parameters in Table 5.2 (d). However, the magnetic shear is more sensitive to the LH driven current profile, and as a result it has a bigger uncertainty.

In Table 5.3 (e), a 50% reduced magnetic shear results in a significant reduction of the intrinsic momentum flux from that in Table 5.3 (a), $(\Delta \left(\frac{\Pi_{\mathrm{int}}}{Q_i} \frac{v_{ti}}{R_0} \right) \sim -0.07)$. This reduced momentum flux would correspond to a decrease of the absolute value of the counter-current rotation, as observed in the low current case.

The amount of the reduction in the momentum flux is large enough to compensate for

the external torque in the counter-current direction. Using Eq. (5.3), the contribution to the rotation of the intrinsic momentum flux is estimated by $\frac{\Pi_{\rm int}(r')}{\chi_\varphi n_i m_i \langle R^2 \rangle_s}$ in the second term on the right hand side, and is compared with the contribution of the external torque estimated by $\frac{\int_0^{r'} dr'' A(r'') T_\varphi(r'')}{A \overline{\chi_\varphi} n_i m_i \langle R^2 \rangle_s}$ in the third term on the right hand side. For the reduced momentum flux $\Delta \left(\frac{\Pi_{\rm int}}{Q_i} \frac{v_{ti}}{R_0} \right) \sim -0.07$ at the radius $r/a = 0.54$, $a \frac{\Delta \Pi_{\rm int}}{\chi_\varphi n_i m_i \langle R^2 \rangle_s} \simeq a \Delta \left(\frac{\Pi_{\rm int}}{Q_i} \frac{v_{ti}}{R_0} \right) \frac{\partial v_{ti}/\partial r}{R_0 {\rm Pr}} = 46{\rm kHz}$ is comparable to the contribution of the external torque $a \frac{\int_0^r dr'' A(r'') T_\varphi(r'')}{A \overline{\chi_\varphi} n_i m_i \langle R^2 \rangle_s} = -52{\rm kHz}$. In fact, a larger amount of reduction in the intrinsic momentum flux is needed to overcome the external torque and explain the observed reduction of the counter-current rotation compared to the rotation before the lower hybrid wave injection shown in Fig. 5-2.

The reduction of the momentum flux is caused by the significant increase in the negative radial shear of the flow due to the reduced magnetic shear. The change of magnetic shear after the LH wave injection is sensitive to the location of the LH wave driven current. If the safety factor profiles in Fig. 5-6 are precise enough to give a reliable magnetic shear profile, Fig. 5-7, the magnetic shear $\hat{s}$ decreases due to the LH wave injection for $\psi/\psi_0 > 0.5$, but it remains almost constant at $\psi/\psi_0 = 0.5$, the reference point that I chose. Outer radii must be considered for a better comparison. The intrinsic momentum flux $\Pi_{\rm int}$ at outer radii is more important than $\Pi_{\rm int}$ at inner radii to determine the rotation according to Eq. (5.3), and at outer radii, the decrease in $\hat{s}$ may mean that $\Pi_{\rm int}$ decreases.

Table 5.3: Simulation results for intrinsic momentum transport in a non-rotating plasma in which the E×B flow and the diamagnetic flow cancel (i.e. $\Omega_{\varphi,E} = -\Omega_{\varphi,d}$ and $\frac{\partial \Omega_{\varphi,E}}{\partial r} = -\frac{\partial \Omega_{\varphi,d}}{\partial r}$). The plasma parameters for the base case in the low current case after the LH wave injection (I_p =350 kA at t=1.25 sec) given in Table 5.2 (d) are modified within error bars.

	Change in inputs	NEO		GS2		
		$\frac{\Omega_{\varphi,d} R_0}{v_{ti}}$	$\frac{\partial \Omega_{\varphi,d}}{\partial r} \frac{R_0 a}{v_{ti}}$	$\frac{\Pi_{\rm int}}{Q_i} \frac{v_{ti}}{R_0}$	Q_i/Q_{GB}	Q_e/Q_{GB}
(a) Base case	same as (4) in Table 5.2	0.171	-0.391	0.067	6.04	4.45
(b) 20% increase in ion temp. gradient	a/L_{Ti} =3.15	0.194	-0.556	0.045	8.29	5.31
(c) 20% decrease in ion temp. gradient	a/L_{Ti} =2.10	0.149	-0.251	0.048	2.59	2.40
(d) A change in second radial derivative of ion temperature	$a(\partial(a/L_{Ti})/\partial r)$ =8.48	0.171	0.039	0.050	7.02	5.13
(e) 50% decrease in magnetic shear	$\hat{s}$=1.05	0.171	-0.614	0.001	5.30	8.58

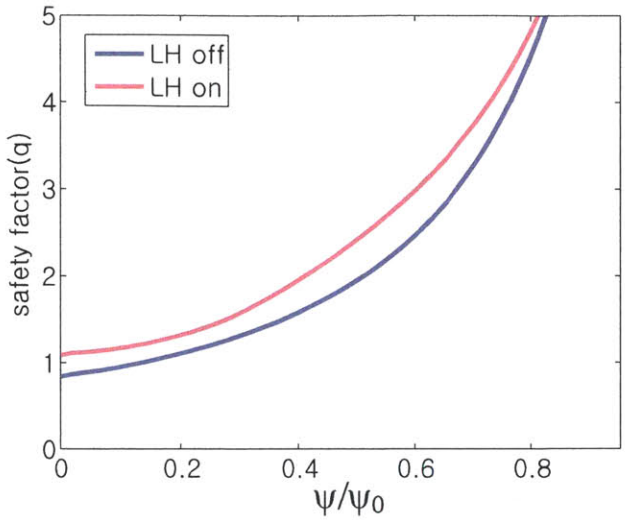

Figure 5-6: Radial profile of the safety factor for the low current case ($I_p = 350$kA) obtained using the equilibrium magnetic field code, EFIT, constrained by MSE measurements. The blue curve is the profile before the lower hybrid wave injection (t=0.75 sec), and the red curve is the profile after the injection (t=1.25 sec).

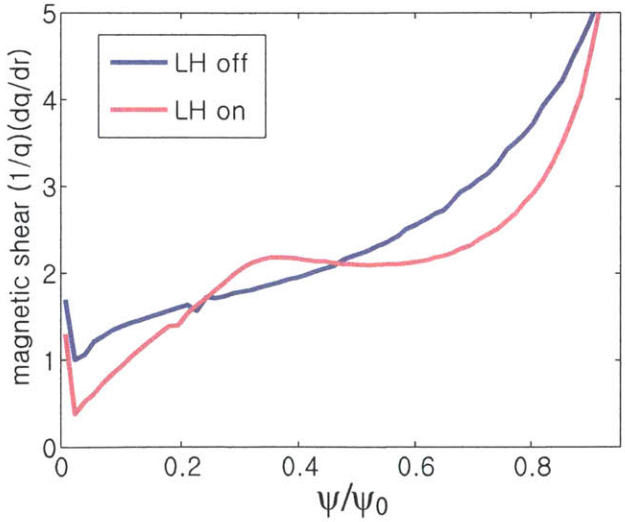

Figure 5-7: Radial profile of magnetic shear $\hat{s} = \frac{r}{q}\frac{\partial q}{\partial r}$ based on the safety factor profile in Fig. 5-6. The blue curve is the profile before the lower hybrid wave injection (t=0.75 sec), and the red curve is the profile after the injection (t=1.25 sec).

5.4 Discussion

In this chapter, the radial transport of the toroidal angular momentum is calculated and used to give a preliminary explanation for the change of the rotation that follows the lower hybrid injection in Alcator C-Mod. Because the wave has toroidal angular momentum in the counter-current direction, it accelerates the ion toroidal rotation in the counter-current direction after the lower hybrid wave is injected as shown in Fig. 5-1 and in Fig. 5-2 (a). However, the change of rotation is saturated after several momentum transport times. The estimated values of the momentum pinch and diffusivity are balanced with the momentum source to reconstruct the rotation radial profile in Fig. 5-3. However, intrinsic momentum transport, which redistributes momentum even for zero rotation and zero rotation shear, is required to explain the measured intrinsic rotation profile, as shown in Fig 5-4. The required size is of the order of $\frac{\Pi_{\rm int}}{Q_i}\frac{v_{ti}}{R_0} = O(0.1)$. For the low plasma current case, at about 150 msec after the lower hybrid wave injection, the change of the rotation is reversed to the direction opposite to the wave momentum direction, which requires a significant change in the intrinsic momentum transport.

To investigate the reasons for the reversal of the rotation change, I evaluate the intrinsic momentum transport due to diamagnetic effects. Because the lower hybrid wave injection changes the diamagnetic flow in a tokamak, it results in a change of the intrinsic momentum transport. Significant changes in the radial profile of the safety factor due to the increased lower hybrid driven current and the decreased Ohmic plasma current can increase the inward momentum transport ($\Delta\left(\frac{\Pi_{\rm int}}{Q_i}\frac{v_{ti}}{R_0}\right) \sim -0.07$), resulting in a co-current direction change of the counter-current rotation (see Table 5.3). The effect of the plasma current on the momentum transport is also consistent with the observed time scale for the reversal of the rotation change. Changes in the safety factor profile take a resistive current relaxation time. In experiments, it takes around a resistive time scale (O(100) msec) for the rotation change to reverse.

The simulations done with the experimental parameters (Table 5.2) could not explain the observations. The magnetic shear obtained using the equilibrium magnetic field code, EFIT, constrained by MSE measurements is not small enough to result in a smaller momentum flux at the reference radius $\psi/\psi_0 \simeq 0.5$ that would explain the reversal of the rotation change. A large reduction of the magnetic shear due to the LH wave injection may occur

at outer radii $\psi/\psi_0 > 0.5$. In addition, not all the intrinsic rotation mechanisms listed in Sec. 4.2 have been studied, and their effects may be important.

The results in this chapter are, however, encouraging. One of the features that the theory can explain well is the dependence of the reversal of the rotation change on the plasma current. The size of the intrinsic momentum transport increases as the diamagnetic flow increases. Because the diamagnetic flow increases with an increase in the safety factor (i.e. with a decrease in the plasma current), the impact of the intrinsic momentum transport on the rotation profiles is more significant for the low plasma current case than for the high plasma current case, and after the lower hybrid wave injection than before the wave injection, as proven by the experimental observations in Alcator C-Mod. Additionally, all the higher order corrections in the gyrokinetic equation (F.1), which result in the intrinsic momentum transport (Π_{int}), scale with the inverse of the plasma current ($1/I_p$). Therefore, if there is a reversal of rotation change in the model, it can only happen at low plasma current.

Chapter 6

Conclusion

In this thesis, the effect of the lower hybrid current drive on ion toroidal rotation is investigated theoretically. The toroidal angular momentum injected by the lower hybrid waves is evaluated in Chapter 2 and Chapter 3. The external torque due to the waves is comparable to the initial change in the ion toroidal rotation observed in Alcator C-Mod. The parallel and perpendicular components of the toroidal angular momentum are transferred from the waves to ions through electrons via two different channels. The perpendicular momentum is transferred to ions through an outward radial electron pinch, while the parallel momentum is transferred through collisions. After several ion collision times, ions obtain the full toroidal angular momentum injected by the lower hybrid waves.

The momentum transferred to the ions is transported out by turbulent radial transport, which is well described by gyrokinetics (see Chapter 4). As an important piece of the turbulent radial transport of toroidal angular momentum, intrinsic momentum redistribution due to the diamagnetic effects is investigated. Finally, in Chapter 5 the change in the steady state rotation due to the lower hybrid waves is estimated theoretically by evaluating the momentum source, the momentum pinch and diffusion, and the intrinsic momentum transport. The estimated rotation is compared with the experimental observations in Alcator C-Mod. The effect on the intrinsic momentum transport of the current profile, which is modified by the lower hybrid wave, may explain the observed reversal of the rotation change from counter-current direction to co-current direction. More theoretical work is needed to confirm this hypothesis. The current theory can explain why discharges with low current display different rotation than discharges with high current, but did not reproduce the

direction of the acceleration in the experimental observations using the measured plasma parameters. For a better comparison between theory and experiment, the precision and the analysis of the experimental radial profiles of several plasma parameters (e.g. ion toroidal rotation, ion temperature, and safety factor), which currently have non-negligible errors in Alcator C-Mod, must also be improved.

In a steady state operation scenario for a reactor size advanced tokamak (e.g. ITER), lower hybrid waves are expected to drive non-inductive off-axis current (e.g. localized at $0.7 < \psi/\psi_0 < 0.8$) to supplement the bootstrap current [146]. To drive 10% of the total current by lower hybrid waves, significant lower hybrid wave power (e.g. ~20-40 MW for ITER) is injected and damped off-axis. Then, a significant amount of the toroidal angular momentum is transferred from the waves to ions through two channels, as explained in Chapter 3. If the absorbed power density in an off-axis flux surface is about 2 MW/m^3, the expected external torque density is about 0.1 N/m^2 for a toroidal refractive index of the wave of $n_\varphi = 2$. The power density, the torque density, and the plasma density in ITER are comparable to the values in Alcator C-Mod as shown in Fig. 2-4, giving similar acceleration of the toroidal angular momentum. However, in ITER the acceleration will be more localized to $0.7 < \psi/\psi_0 < 0.8$ due to strong damping of the wave for high current drive efficiency and accessibility. The change in the plasma current driven by the lower hybrid wave is also localized, which affects the momentum redistribution, as explained in Sec. 5.3.3. Consequently, the localized momentum source and redistribution may result in a stronger toroidal velocity shear.

To predict the toroidal rotation change due to lower hybrid waves when designing a new tokamak, the estimates of the momentum source, the momentum diffusion, the momentum pinch and the intrinsic momentum transport are required. The relation between the lower hybrid waves and the ion toroidal rotation is complex, as shown in Fig. 1-2, and the evaluation must be performed self-consistently.

Appendix A

Energy transfer using the quasilinear diffusion operator

The quasilinear diffusion operator for species s is obtained from

$$Q(f_s) = -\frac{Z_s e}{m_s}\left\langle \nabla_v \cdot \left[\left(\mathbf{E}+\frac{\mathbf{v}\times\mathbf{B}}{c}\right) f_s\right]\right\rangle_W \tag{A.1}$$

$$\simeq -\frac{Z_s e}{m_s}\nabla_v \cdot \left[\sum_{\mathbf{k}}\left\{\overleftrightarrow{I}\left(1-\frac{\mathbf{k}\cdot\mathbf{v}}{\omega}\right)+\frac{\mathbf{kv}}{\omega}\right\}\cdot\mathbf{E}_{-\mathbf{k}} f_{\mathbf{k}}\right], \tag{A.2}$$

where $\langle ... \rangle_W$ in (A.1) indicates the average over a number of wave periods in time and space. Here, m_s and $Z_s e$ are the mass and the charge of the species of interest, respectively, e is the charge of the proton, and $\overleftrightarrow{I}$ is the unit tensor. We have used the Fourier analyzed fluctuating electric field, $\mathbf{E} = \sum_{\mathbf{k}} \mathbf{E}_{\mathbf{k}} \exp(i\mathbf{k}\cdot\mathbf{r} - i\omega_{\mathbf{k}} t)$, the fluctuating magnetic field $\mathbf{B} = \sum_{\mathbf{k}} \mathbf{B}_{\mathbf{k}} \exp(i\mathbf{k}\cdot\mathbf{r} - i\omega_{\mathbf{k}} t)$, and the fluctuating distribution function, $f_s = \sum_{\mathbf{k}} f_{\mathbf{k}} \exp(i\mathbf{k}\cdot\mathbf{r} - i\omega_{\mathbf{k}} t)$. The functions $\mathbf{E}_{\mathbf{k}} \equiv \mathbf{E}(\omega_{\mathbf{k}}, \mathbf{k})$, $\mathbf{B}_{\mathbf{k}} \equiv \mathbf{B}(\omega_{\mathbf{k}}, \mathbf{k})$, and $f_{\mathbf{k}} \equiv f(\omega_{\mathbf{k}}, \mathbf{k})$ satisfy the relation $f_{-\mathbf{k}} \equiv f(\omega_{-\mathbf{k}}, -\mathbf{k}) = f^*(\omega_{\mathbf{k}}, \mathbf{k})$ where $*$ denotes complex conjugate and $\omega_{\mathbf{k}} = -\omega^*_{-\mathbf{k}}$. Faraday's law has been used in going from (A.1) to (A.2) to write $\mathbf{B}_{\mathbf{k}} = (c/\omega)\mathbf{k} \times \mathbf{E}_{\mathbf{k}}$[1].

[1]In typical tokamak geometry, the toroidal and poloidal spectra are discrete due to periodicity, but the radial spectrum is continuous. Although using integrals in Fourier space would be more appropriate, I use the notation $\sum_{\mathbf{k}}$ for simplicity. The summation in the discrete toroidal and poloidal spectrum space is also closer to the numerical evaluation in a code [86, 92].

The quasilinear operator can be written as

$$Q(f_s) \equiv \frac{Z_s e}{m_s}\left[\frac{1}{v_\perp}\frac{\partial}{\partial v_\perp}\left(v_\perp \Gamma_\perp\right) + \frac{1}{v_\perp}\frac{\partial \Gamma_\alpha}{\partial \alpha} + \frac{\partial \Gamma_\parallel}{\partial v_\parallel}\right]. \tag{A.3}$$

The flux in the perpendicular direction is

$$\Gamma_\perp = -\sum_{\mathbf{k}}\left\{E^*_{\mathbf{k},\perp}\left(1 - \frac{k_\parallel v_\parallel}{\omega}\right) + E^*_{\mathbf{k},\parallel}\frac{k_\perp v_\parallel}{\omega}\cos\left(\alpha - \beta\right)\right\} f_{\mathbf{k}}. \tag{A.4}$$

Here, the velocity is defined as $\mathbf{v} = v_\perp \cos\alpha\hat{\mathbf{x}} + v_\perp \sin\alpha\hat{\mathbf{y}} + v_\parallel\hat{\mathbf{b}}$, where α is the gyro phase angle, and x and y are the orthogonal coordinates in the perpendicular plane to the static magnetic field. The wavenumber vector is defined as $\mathbf{k} = k_\perp \cos\beta\hat{\mathbf{x}} + k_\perp \sin\beta\hat{\mathbf{y}} + k_\parallel\hat{\mathbf{b}}$. The flux in the gyro-phase direction is

$$\begin{aligned}\Gamma_\alpha &= -\sum_{\mathbf{k}}\left\{E^*_{\mathbf{k},\alpha}\left(1 - \frac{k_\perp v_\perp}{\omega}\cos\left(\alpha - \beta\right) - \frac{k_\parallel v_\parallel}{\omega}\right)\right. \\ &- \left. E^*_{\mathbf{k},\perp}\frac{k_\perp v_\perp}{\omega}\sin\left(\alpha - \beta\right) - E^*_{\mathbf{k},\parallel}\frac{k_\perp v_\parallel}{\omega}\sin\left(\alpha - \beta\right)\right\} f_{\mathbf{k}},\end{aligned} \tag{A.5}$$

and the flux in the parallel direction is

$$\Gamma_\parallel = -\sum_{\mathbf{k}}\left\{E^*_{\mathbf{k},\parallel}\left(1 - \frac{k_\perp v_\perp}{\omega}\cos\left(\alpha - \beta\right)\right) + E^*_{\mathbf{k},\perp}\frac{k_\parallel v_\perp}{\omega}\right\} f_{\mathbf{k}}. \tag{A.6}$$

Here, the perturbed fluctuating distribution function consistent with a single mode wave is

$$\begin{aligned}f_{\mathbf{k}} &= -\frac{Z_s e}{m_s}\exp(-i\mathbf{k}\cdot\mathbf{r} + i\omega t)\int_{-\infty}^{t} dt' \exp(i\mathbf{k}\cdot\mathbf{r}' - i\omega t') \\ &\times \mathbf{E}_{\mathbf{k}}\cdot\left[\overleftrightarrow{I}\left(1 - \frac{\mathbf{v}'\cdot\mathbf{k}}{\omega}\right) + \frac{\mathbf{v}'\mathbf{k}}{\omega}\right]\cdot\nabla_{v'} f_{0,s},\end{aligned} \tag{A.7}$$

where $(t', \mathbf{r}', \mathbf{v}')$ is a point of phase space along the zero-order particle trajectory. The trajectory end point corresponds to $(t, \mathbf{r}, \mathbf{v})$. The background distribution, $f_{0,s} = f_{0,s}(t, \mathbf{r}, v_\perp, v_\parallel)$, is gyro-phase independent because of the fast gyro-motion. As a result,

$$\begin{aligned}f_{\mathbf{k}} &= -\frac{Z_s e}{m_s}\int_0^\infty d\tau \exp(i\gamma)\left\{\cos\left(\eta + \Omega\tau\right)((E_{\mathbf{k},+} + E_{\mathbf{k},-})U - E_{\mathbf{k},\parallel}V)\right. \\ &\left. -i\sin\left(\eta + \Omega\tau\right)(E_{\mathbf{k},+} - E_{\mathbf{k},-})U + E_{\mathbf{k},\parallel}\frac{\partial f_{0,s}}{\partial v_\parallel}\right\}.\end{aligned} \tag{A.8}$$

Here, $\tau = t - t'$, and $\gamma = (\omega - k_{\|}v_{\|})\tau - \lambda(\sin(\eta + \Omega\tau) - \sin(\eta))$, where $\lambda = \frac{k_{\perp}v_{\perp}}{\Omega}$, $\eta = \alpha - \beta$, $\Omega = Z_s eB_0/mc$ is the gyrofrequency and B_0 is the magnitude of the background magnetic field. Also, $U = \frac{\partial f_{0,s}}{\partial v_{\perp}} + \frac{k_{\|}}{\omega}\left(v_{\perp}\frac{\partial f_{0,s}}{\partial v_{\|}} - v_{\|}\frac{\partial f_{0,s}}{\partial v_{\perp}}\right)$, and $V = \frac{k_{\perp}}{\omega}\left(v_{\perp}\frac{\partial f_{0,s}}{\partial v_{\|}} - v_{\|}\frac{\partial f_{0,s}}{\partial v_{\perp}}\right)$. We follow Stix' notation in [17].

For the energy transfer, the contribution of the flux in the gyro-phase direction vanishes due to the integral over α,

$$\begin{aligned} P_{abs} &= \int_{-\infty}^{\infty} dv_{\|} \int_0^{\infty} dv_{\perp} 2\pi v_{\perp} \left\langle \frac{m_s v^2}{2} Q(f_s) \right\rangle \\ &= \int_{-\infty}^{\infty} dv_{\|} \int_0^{\infty} dv_{\perp} 2\pi v_{\perp} \frac{Z_s e v^2}{2} \left[\frac{1}{v_{\perp}} \frac{\partial}{\partial v_{\perp}} \left(v_{\perp} \langle \Gamma_{\perp} \rangle \right) + \frac{\partial \langle \Gamma_{\|} \rangle}{\partial v_{\|}} \right], \end{aligned} \tag{A.9}$$

with $\langle ... \rangle = \frac{1}{2\pi}\int_0^{2\pi} d\alpha(...)$ the gyroaverage. For this reason, the typical Kennel-Engelmann quasilinear diffusion operator [21], which is gyroaveraged, does not retain the flux in the gyro-phase direction. Then, the power absorption $P_{abs,\mathbf{k}}$ can be evaluated [17, 21] using

$$P_{abs} \equiv \sum_{\mathbf{k}} P_{abs,\mathbf{k}} = \int_{-\infty}^{\infty} dv_{\|} \int_0^{\infty} dv_{\perp} 2\pi v_{\perp} \left\langle \frac{m_s v^2}{2} Q(f_s) \right\rangle, \tag{A.10}$$

with

$$\begin{aligned} P_{abs,\mathbf{k}} &= \frac{\pi Z_s^2 e^2}{m_s^2} \int_{-\infty}^{\infty} dv_{\|} \int_0^{\infty} dv_{\perp} 2\pi v_{\perp} \sum_n \frac{m_s v^2}{2} L\left(v_{\perp}^2 \delta(\omega - k_{\|}v_{\|} - n\Omega) |\chi_{\mathbf{k},n}|^2 L(f_{0,s}) \right) \\ &= -\frac{\pi Z_s^2 e^2}{m_s^2} \int_{-\infty}^{\infty} dv_{\|} \int_0^{\infty} dv_{\perp} 2\pi v_{\perp} \sum_n m_s v_{\perp}^2 \delta(\omega - k_{\|}v_{\|} - n\Omega) |\chi_{\mathbf{k},n}|^2 L(f_{0,s}), \end{aligned} \tag{A.11}$$

where $\chi_{\mathbf{k},n} = E_{\mathbf{k},\|} J_n \frac{v_{\|}}{v_{\perp}} + E_{\mathbf{k},+} J_{n-1} + E_{\mathbf{k},-} J_{n+1}$ is the effective electric field, and the operator $L(f_{0,s}) = \left(1 - \frac{k_{\|}v_{\|}}{\omega}\right)\frac{1}{v_{\perp}}\frac{\partial f_{0,s}}{\partial v_{\perp}} + \frac{k_{\|}v_{\perp}}{\omega}\frac{1}{v_{\perp}}\frac{\partial f_{0,s}}{\partial v_{\|}}$ is introduced in [21, 17]. To evaluate the wave power absorption in Eq. (A.11), we utilize the Bessel function expansion for the sinusoid phase,

$$e^{i\lambda \sin\eta} = \sum_n e^{in\eta} J_n(\lambda), \tag{A.12}$$

$$\sin\eta e^{i\lambda \sin\eta} = -\sum_n i e^{in\eta} J_n'(\lambda), \tag{A.13}$$

$$\cos\eta e^{i\lambda \sin\eta} = \sum_n \frac{n}{\lambda} e^{in\eta} J_n(\lambda), \tag{A.14}$$

and the sifting property of the phase average

$$\int_0^{2\pi} d\eta e^{-i\lambda(\sin(\eta+\Omega\tau)-\sin(\eta))} = \int_0^{2\pi} d\eta \sum_l e^{-il(\eta+\Omega\tau)} J_l(\lambda) \sum_n e^{in\eta} J_n(\lambda) \quad \text{(A.15)}$$

$$= 2\pi \sum_n e^{-in\Omega\tau} J_n^2(\lambda). \quad \text{(A.16)}$$

Appendix B

Bounce average and velocity space integral in a relativistic velocity space

The bounce average is defined as

$$\langle X \rangle_b = \frac{1}{\tau_b} \oint \frac{d\ell\, X}{v_\parallel} = \frac{1}{\tau_b} \oint \frac{d\theta\, X}{v_\parallel \hat{\mathbf{b}} \cdot \nabla\theta}, \tag{B.1}$$

where $\hat{\mathbf{b}}$ is the unit vector in the direction of static magnetic field, $v_\parallel$ is the non-relativistic parallel velocity, θ is the poloidal angle and $\tau_b(\mathcal{E}, \mu) = \oint \frac{dl}{v_\parallel(\mathcal{E},\mu,l)}$ is the bounce time. Here, $\mathcal{E}$ is the relativistic energy and $\mu = u_\perp^2/B$ is the relativistic magnetic moment. Also, the flux surface average is defined as

$$\langle X \rangle_s = \frac{1}{\tau_s} \oint \frac{d\theta\, X}{\mathbf{B} \cdot \nabla\theta} = \frac{1}{\tau_s} \oint \frac{d\ell\, X}{B}, \tag{B.2}$$

where the Jacobian $J = \frac{1}{(\nabla\psi \times \nabla\theta)\cdot\nabla\varphi} = \frac{1}{\mathbf{B}\cdot\nabla\theta}$ is used, and the normalization is $\tau_s = \oint \frac{dl}{B}$. There is a relation between the flux surface average and the bounce average for circulating particles,

$$\langle X \rangle_b \tau_b = \left\langle \frac{B}{v_\parallel} X \right\rangle_s \tau_s. \tag{B.3}$$

For trapped particles, assuming that the flux surface average can be defined only between

the turning points of the orbit, the bounce average is defined as

$$\langle X \rangle_b \equiv \frac{1}{2} \sum_\sigma \frac{\tau_{s\frac{1}{2}}}{\tau_{b\frac{1}{2}}} \left\langle \frac{B}{|v_\parallel|} X \right\rangle_{s\frac{1}{2}}, \tag{B.4}$$

where $\tau_{s\frac{1}{2}}$ and $\tau_{b\frac{1}{2}}$ stand for the integration and the bounce time from one turning point to the other turning point, and $\sigma = v_\parallel/|v_\parallel|$ is the sign of parallel velocity. The symbol $\sum_\sigma$ indicates that we have to sum the contributions with $\sigma = 1$ and $\sigma = -1$. Then the bounce average annihilates the parallel streaming operator $v_\parallel \hat{\mathbf{b}} \cdot \nabla$ for both passing and trapped particles.

The integration of a gyro-averaged function in the relativistic velocity space $(u_\parallel, u_\perp)$ is transformed to the integration in terms of the invariant variables $(\mathcal{E}, \mu)$ or the velocity fixed at a position such as the outer mid plane $(u_{\parallel 0}, u_{\perp 0})$ by the following relation,

$$\begin{aligned} d^3u &= \pi du_\perp^2 du_\parallel = \pi du_{\perp 0}^2 du_{\parallel 0} \left| \frac{\partial u_\perp^2}{\partial u_{\perp 0}^2} \frac{\partial u_\parallel}{\partial u_{\parallel 0}} - \frac{\partial u_\perp^2}{\partial u_{\parallel 0}} \frac{\partial u_\parallel}{\partial u_{\perp 0}^2} \right| \\ &= d^3u_0 \left| \frac{B}{B_0} \frac{u_{\parallel 0}}{u_\parallel} \right|, \end{aligned} \tag{B.5}$$

where $u_\parallel = \sqrt{u^2 - \mu B}$ and the constancy of u and μ along the orbit are applied. Then, a flux surface averaged quantity integrated over the relativistic velocity space is

$$\begin{aligned} \left\langle \int d^3u X \right\rangle_s &= \frac{1}{\tau_s} \left\langle \int d^3u_0 \left| \frac{u_{\parallel 0}}{B_0} \frac{B}{u_\parallel} \right| \frac{v_\parallel}{B} X \right\rangle_b \tau_b = \frac{1}{\tau_s} \int d^3u_0 \frac{u_{\parallel 0}}{\gamma B_0} \langle X \rangle_b \tau_b \\ &= \frac{1}{\tau_s B_0} \int d^3u_0 \lambda \langle X \rangle_b, \end{aligned} \tag{B.6}$$

where $\lambda = v_{\parallel 0} \tau_b$.

Appendix C

Correction of the quasilinear diffusion due to the phase correlation between different resonances

The electron quasilinear diffusion coefficient after bounce averaging and averaging over the toroidal angle is

$$\langle \mathcal{D}_{\mathcal{E},\mathcal{E}} \rangle_b = \frac{e^2}{2m_e^2} \langle I(\mathcal{E},\mu,\ell) \rangle_b. \tag{C.1}$$

The correction to the value of $I(\mathcal{E},\mu,\ell)$ in Eq. (C.1) is evaluated using the phase integral in Eq. (2.19) and (2.23), giving

$$\begin{aligned} \langle I(\mathcal{E},\mu,\ell) \rangle_b \simeq & -\frac{1}{\tau_b} \frac{1}{1-e^{-i\chi_0}} \sum_n \sum_{r_1,r_2} \frac{\langle W(\mathcal{E},\mu,\ell_{r_2}) \rangle_m}{v_\parallel(\ell_{r_1}) v_\parallel(\ell_{r_2})} \int_0^L d\ell_1 e^{i\frac{\kappa'(\ell_{r_1})}{2}\ell_1^2} \\ \times & \int_{\ell_1}^{\ell_1 - L} d\ell_2 e^{-i\frac{\kappa'(\ell_{r_2})}{2}\ell_2^2} \frac{\sin[(s+1/2)dk_\parallel((\ell_2-\ell_1)+(\ell_{r_1}-\ell_{r_2}))]}{dk_\parallel((\ell_2-\ell_1)+(\ell_{r_1}-\ell_{r_2}))/2}, \end{aligned} \tag{C.2}$$

where $\ell_1 = \ell - \ell_{r_1}$, $\ell_2 = \ell' - \ell_{r_2}$, and ℓ_{r_1} and ℓ_{r_2} are the resonance positions in the ℓ and ℓ' integral paths, respectively (see Fig. 18-1 in [17]). Here, $\kappa'(\ell_{r_1})$ and $\kappa'(\ell_{r_2})$ are the function $\kappa'(\ell)$ evaluated at ℓ_{r_1} and ℓ_{r_2}, respectively. By separating the contribution to the summation from $\ell_{r_1} = \ell_{r_2}$ and the piece coming from $\ell_{r_1} \neq \ell_{r_2}$, the bounce averaged value

is

$$\begin{aligned}
&\langle I(\mathcal{E},\mu,\ell)\rangle_b \\
\simeq\ & -\frac{1}{\tau_b}\sum_n\Bigg\{\sum_{r_1=r_2}\frac{\langle W(\mathcal{E},\mu,\ell_{r_2})\rangle_m}{v_\parallel^2(\ell_{r_2})}\frac{1+e^{-i\chi_0}}{2(1-e^{-i\chi_0})}\int_{-\infty}^{\infty}db\int_{-\infty}^{\infty}da\,e^{-i\kappa'(\ell_{r_2})ab}\frac{\sin[(s+1/2)dk_\parallel\sqrt{2}a]}{dk_\parallel\sqrt{2}a/2} \\
&+\sum_{r_1\neq r_2}H_n(\ell_{r_1},\ell_{r_2})\Bigg\},
\end{aligned} \tag{C.3}$$

where $a=\frac{\ell_2-\ell_1}{\sqrt{2}}$, $b=\frac{\ell_2+\ell_1}{\sqrt{2}}$ and $H_n(\ell_{r_1},\ell_{r_2})$ is the contribution to the diffusion coefficient from the phase correlation between different resonances within a period. Here, the integrals in a period $0\le\ell_1<L$ of Eq. (C.2) is not affected by letting $L\to\infty$ for $|\kappa' L^2/2\gg 1|$ except for the the additional phase factor $(1+e^{-i\chi_0})/2$ because half of the distance around the resonance is counted using periodicity between $0\le\ell_1<\epsilon$ and $L\le\ell_1<L+\epsilon$. If the fast decorrelation between the periods makes the contribution of the phase memory $e^{-i\chi_0}$ negligible, Eq (C.3) is

$$\begin{aligned}
&\langle I(\mathcal{E},\mu,\ell)\rangle_b \\
\simeq\ & \frac{1}{\tau_b}\sum_n\left\{\sum_{r_1=r_2}\frac{\langle W(\mathcal{E},\mu,\ell_{r_2})\rangle_m}{2v_\parallel^2(\ell_{r_2})}\int_{-\infty}^{\infty}db\frac{2\pi}{dk_\parallel\sqrt{2}}R\left(\frac{\kappa' b}{\sqrt{2}(2s+1)dk_\parallel}\right)+\sum_{r_1\neq r_2}H_n(\ell_{r_1},\ell_{r_2})\right\} \\
=\ & \frac{1}{\tau_b}\sum_n\left\{\sum_{r_1=r_2}\frac{\pi\langle W(\mathcal{E},\mu,\ell_{r_2})\rangle_m}{|v_\parallel^2(\ell_{r_2})\kappa'(\ell_{r_2})|}(2s+1)+\sum_{r_1\neq r_2}H_n(\ell_{r_1},\ell_{r_2})\right\},
\end{aligned} \tag{C.4}$$

where the Fourier transform of $\frac{\sin(\pi x)}{\pi x}$ results in a function $R(x)$ that is 1 for $-1\le x\le 1$ and otherwise 0. The first term on the right hand side of Eq. (C.4) recovers the original quasilinear diffusion coefficient in Eq. (2.11) because $(2s+1)$ times the average value of $\langle W(\mathcal{E},\mu,\ell_{r_2})\rangle_m$ gives the original summation over the poloidal mode number m.

For $r_1\neq r_2$, the piece for the phase correlation between different resonances in a period is

$$\begin{aligned}
H_n(\ell_{r_1},\ell_{r_2}) =\ & \frac{\langle W(\mathcal{E},\mu,\ell_{r_2})\rangle_m}{v_\parallel(\ell_{r_1})v_\parallel(\ell_{r_2})}\frac{G(\ell_{r_1},\ell_{r_2})}{1-e^{-i\chi_0}}\int_{-\infty}^{\infty}d\ell_1 e^{i\frac{\kappa'(\ell_{r_1})}{2}\ell_1^2}\int_{-\infty}^{\infty}d\ell_2 e^{-i\frac{\kappa'(\ell_{r_2})}{2}\ell_2^2} \\
&\times\frac{\sin[(s+1/2)dk_\parallel((\ell_2-\ell_1)-(\ell_{r_2}-\ell_{r_1}))]}{dk_\parallel((\ell_2-\ell_1)-(\ell_{r_2}-\ell_{r_1}))/2},
\end{aligned} \tag{C.5}$$

where the additional factor $G(\ell_{r_1},\ell_{r_2})$ is due to the phase change between the different

resonances within a period [17], which is defined as

$$\begin{aligned} G(\ell_{r_1},\ell_{r_2}) &= e^{-i\chi(\ell_{r_1},\ell_{r_2})} \quad \text{when} \quad \ell_{r_1} > \ell_{r_2} \\ &= e^{i\chi(\ell_{r_1},\ell_{r_2}-L)} \quad \text{when} \quad \ell_{r_1} < \ell_{r_2}. \end{aligned} \tag{C.6}$$

For the two resonances of a passing particle in an orbit of an up-down symmetric tokamak satisfying $\kappa' = \kappa'(\ell_{r_2}) = -\kappa'(\ell_{r_1})$, $v_\parallel(\ell_{r_1}) = v_\parallel(\ell_{r_2})$ and $\Delta\ell_r = (\ell_{r_2} - \ell_{r_1})$, Eq. (C.5) is

$$\begin{aligned} & H_n(\ell_{r_1},\ell_{r_2}) \\ \simeq\ & \frac{\langle W(\mathcal{E},\mu,\ell_{r_2})\rangle_m}{v_\parallel^2(\ell_{r_2})}\frac{G(\ell_{r_1},\ell_{r_2})}{1-e^{-i\chi_0}}\int_{-\infty}^{\infty} db\, e^{-i\frac{\kappa'}{2}b^2}\int_{-\infty}^{\infty} da\, e^{-i\frac{\kappa'}{2}a^2}\frac{\sin[(s+1/2)dk_\parallel\sqrt{2}(a-\Delta\ell_r/\sqrt{2})]}{dk_\parallel\sqrt{2}(a-\Delta\ell_r/\sqrt{2})/2} \\ =\ & \frac{\langle W(\mathcal{E},\mu,\ell_{r_2})\rangle_m}{v_\parallel^2(\ell_{r_2})}\frac{G(\ell_{r_1},\ell_{r_2})}{1-e^{-i\chi_0}}\sqrt{\frac{2\pi}{i\kappa'}}\int_{-\infty}^{\infty} dp\, e^{-(\frac{2\pi^2}{i\kappa'})p^2-(2\pi i\Delta\ell_r/\sqrt{2})p}\frac{2\pi}{\sqrt{2}dk_\parallel}R\left(\frac{\pi p}{(s+1/2)\sqrt{2}dk_\parallel}\right) \\ =\ & \frac{\langle W(\mathcal{E},\mu,\ell_{r_2})\rangle_m}{v_\parallel^2(\ell_{r_2})}\frac{G(\ell_{r_1},\ell_{r_2})}{1-e^{-i\chi_0}}e^{-i\frac{\kappa'\Delta\ell_r}{4}}\frac{i2\pi}{dk_\parallel\sqrt{\kappa'}}\left[\left\{C\left(\frac{(2s+1)dk_\parallel}{2\sqrt{\kappa'}}-\frac{\Delta\ell_r\sqrt{\kappa'}}{2}\right)\right.\right. \\ & \left.-C\left(-\frac{(2s+1)dk_\parallel}{2\sqrt{\kappa'}}-\frac{\Delta\ell_r\sqrt{\kappa'}}{2}\right)\right\}+i\left\{S\left(\frac{(2s+1)dk_\parallel}{2\sqrt{\kappa'}}-\frac{\Delta\ell_r\sqrt{\kappa'}}{2}\right)\right. \\ & \left.\left.-S\left(-\frac{(2s+1)dk_\parallel}{2\sqrt{\kappa'}}-\frac{\Delta\ell_r\sqrt{\kappa'}}{2}\right)\right\}\right], \end{aligned} \tag{C.7}$$

where I have used $\int_{-\infty}^{\infty} db\, e^{-i\frac{\kappa'}{2}b^2} = \sqrt{2\pi/i\kappa'}$ and the power theorem in Fourier analysis to write $\int_{-\infty}^{\infty} da\, e^{-i\frac{\kappa'}{2}a^2}\frac{\sin[(s+1/2)dk_\parallel\sqrt{2}(a-\Delta\ell_r/\sqrt{2})]}{dk_\parallel\sqrt{2}(a-\Delta\ell_r/\sqrt{2})/2} = \int_{-\infty}^{\infty} dp\, e^{-(\frac{2\pi^2}{i\kappa'})p^2-(2\pi i\Delta\ell_r/\sqrt{2})p}\frac{2\pi}{\sqrt{2}dk_\parallel}R\left(\frac{\pi p}{(s+1/2)\sqrt{2}dk_\parallel}\right)$. Here, $C(x)$ and $S(x)$ are the Fresnel functions.

Appendix D

Bounce averaged quasilinear diffusion operator

For the bounce averaged Fokker-Planck equation in Eq. (2.35), the coefficients are defined by the relation with the coefficients of the original Fokker-Planck equation in Eq. (2.34),

$$\begin{aligned}
\mathsf{A}_0 &= \lambda \langle \mathsf{A} \rangle_b \\
\mathsf{B}_0 &= \lambda \langle \mathsf{B} \rangle_b \\
\mathsf{C}_0 &= \lambda \left\langle \frac{\partial \vartheta_0}{\partial \vartheta} \mathsf{C} \right\rangle_b = \lambda \left\langle \frac{\cos\vartheta}{\sqrt{h}\cos\vartheta_0} \mathsf{C} \right\rangle_b \\
\mathsf{D}_0 &= \lambda \left\langle \frac{\sin\vartheta_0}{\sin\vartheta} \frac{\partial \vartheta_0}{\partial \vartheta} \mathsf{D} \right\rangle_b = \lambda \left\langle \frac{\cos\vartheta}{h\cos\vartheta_0} \mathsf{D} \right\rangle_b \\
\mathsf{E}_0 &= \lambda \left\langle \frac{\sin\vartheta_0}{\sin\vartheta} \frac{\partial \vartheta_0}{\partial \vartheta} \mathsf{E} \right\rangle_b = \lambda \left\langle \frac{\cos\vartheta}{h\cos\vartheta_0} \mathsf{E} \right\rangle_b \\
\mathsf{F}_0 &= \lambda \left\langle \frac{\sin\vartheta_0}{\sin\vartheta} \left(\frac{\partial \vartheta_0}{\partial \vartheta} \right)^2 \mathsf{F} \right\rangle_b = \lambda \left\langle \frac{\cos^2\vartheta}{h^{3/2}\cos^2\vartheta_0} \mathsf{F} \right\rangle_b ,
\end{aligned} \tag{D.1}$$

where $h(\theta) = B(\theta)/B_0$ is the ratio of the local magnetic field to that at the outer-midplane, and $\vartheta = \tan^{-1}(\frac{u_\perp}{u_\parallel})$ is the local pitch angle whereas ϑ_0 is the pitch angle at the outer-midplane. Here, the relation between the flux surface average and the bounce averag in Eq. ($B.6$) is used. For quasilinear diffusion due to the RF wave, $\langle Q(F_{0,e}) \rangle_b$, the convection terms vanish ($\mathsf{A} = 0$ and $\mathsf{D} = 0$), and there are relations between the bounce-averaged

constants due to the resonance condition [85],

$$\mathsf{C}_{0ql} = \mathsf{B}_{0ql}\frac{1}{v\sin\vartheta}\left[\cos\vartheta - \frac{k_\parallel v}{\omega}\right]\frac{\partial\vartheta_0}{\partial\vartheta}\bigg|_{res} \tag{D.2}$$

$$= \mathsf{B}_{0ql}\frac{\sin\vartheta_0}{v_0\cos\vartheta_0}\left[\frac{\cos^2\vartheta}{\sin^2\vartheta} - \frac{\omega - m\Omega}{\omega\sin^2\vartheta}\right]\bigg|_{res} \tag{D.3}$$

$$= \mathsf{B}_{0ql}\frac{(m\Omega_0/\omega) - \sin^2\vartheta_0}{v_0\cos\vartheta_0\sin\vartheta_0}. \tag{D.4}$$

From Eq. (D.2) to (D.3), we use conservation of the magnetic moment ($\frac{\partial\vartheta_0}{\partial\vartheta} = \frac{\cos\vartheta}{\sin\vartheta}\frac{\sin\vartheta_0}{\cos\vartheta_0}$) and the resonance condition ($\omega = kv\cos\vartheta + m\Omega$). In Eq. (D.4), the definition of gyrofrequency in the outer-midplane ($\Omega_0 = \Omega\sin^2\vartheta_0/\sin^2\vartheta$) is used. Notice that the final relation in Eq. (D.4) does not depend on the wavevector $k_\parallel$ and the resonance poloidal location. The remaining coefficients can be written as

$$\mathsf{E}_{0ql} = \mathsf{B}_{0ql}\frac{1}{v\sqrt{h}}\left[\cos\vartheta - \frac{k_\parallel v}{\omega}\right]\frac{\partial\vartheta_0}{\partial\vartheta}\bigg|_{res}$$

$$= \mathsf{B}_{0ql}\frac{(m\Omega_0/\omega) - \sin^2\vartheta_0}{v_0\cos\vartheta_0} = \mathsf{C}_{0ql}\sin\vartheta_0, \tag{D.5}$$

$$\mathsf{F}_{0ql} = \mathsf{B}_{0ql}\frac{1}{v^2\sqrt{h}}\left[\cos\vartheta - \frac{k_\parallel v}{\omega}\right]^2\left(\frac{\partial\vartheta_0}{\partial\vartheta}\right)^2\bigg|_{res} = \mathsf{E}_{0ql}\frac{(m\Omega_0/\omega) - \sin^2\vartheta_0}{v_0\cos\vartheta_0\sin\vartheta_0}. \tag{D.6}$$

Notice that $\mathsf{C}_{0ql}/\mathsf{B}_{0ql} = \mathsf{F}_{0ql}/\mathsf{E}_{0ql}$, and that C_{0ql} and E_{0ql} are odd around the pitch angle $\vartheta_0 = \pi/2$, whereas B_{0ql} and E_{0ql} are even.

Appendix E

Wave momentum transfer by resonance

The toroidal momentum transfer in the parallel direction in Eq. (3.4) can be obtained by inserting the flux $\Gamma_{\|}$ in Eq. (A.6) and the perturbed fluctuating distribution function $f_{\mathbf{k}}$ in Eq. (A.8):

$$\begin{aligned}
T_{\varphi}^{\|} &= -eR\sum_{\mathbf{k}}\int_{-\infty}^{\infty}dv_{\|}\int_{0}^{\infty}dv_{\perp}v_{\perp}\int_{0}^{2\pi}d\alpha(\hat{\mathbf{z}}\cdot\hat{\boldsymbol{\phi}}) \\
&\times \left\{E_{\mathbf{k},\|}^{*}\left(1-\frac{k_{\perp}v_{\perp}}{\omega}\cos(\alpha-\beta)\right)+E_{\mathbf{k},\perp}^{*}\frac{k_{\|}v_{\perp}}{\omega}\right\}f_{\mathbf{k}} \\
&= -\frac{e^{2}R}{m_{e}}\sum_{\mathbf{k}}\int_{-\infty}^{\infty}dv_{\|}\int_{0}^{\infty}dv_{\perp}2\pi v_{\perp}\int_{0}^{\infty}d\tau e^{i(\omega-k_{\|}v_{\|})\tau}\int_{0}^{2\pi}d\eta(\hat{\mathbf{z}}\cdot\hat{\boldsymbol{\phi}}) \\
&\times \sum_{n}e^{in\eta}\left(\left(1-\frac{n\Omega}{\omega}\right)J_{n}E_{\mathbf{k},\|}^{*}+\frac{nJ_{n}}{\lambda}\frac{k_{\|}v_{\perp}}{\omega}(E_{\mathbf{k},+}^{*}+E_{\mathbf{k},-}^{*})+J_{n}'\frac{k_{\|}v_{\perp}}{\omega}(E_{\mathbf{k},+}^{*}-E_{\mathbf{k},-}^{*})\right) \\
&\times \sum_{l}e^{-il(\eta+\Omega\tau)}\left(E_{\mathbf{k},\|}\frac{\partial f_{0}}{\partial v_{\|}}J_{l}+\frac{lJ_{l}}{\lambda}((E_{\mathbf{k},+}+E_{\mathbf{k},-})U-E_{\|}V)+(E_{\mathbf{k},+}-E_{\mathbf{k},-})UJ_{l}'\right).
\end{aligned}$$

The phase $i(\omega-k_{\|}v_{\|}-n\Omega)\tau$ is averaged out in the τ integration except where $\omega-k_{\|}v_{\|}-n\Omega=0$. Using the Dirac-delta function to express this resonance condition, the momentum

transfer becomes

$$
\begin{aligned}
T_{\varphi}^{\parallel} &= -\tfrac{\pi e^2 R}{m_e}\textstyle\sum_{\mathbf{k}}\int_{-\infty}^{\infty}dv_{\parallel}\int_0^{\infty}dv_{\perp}2\pi v_{\perp}\sum_n \delta(\omega-k_{\parallel}v_{\parallel}-n\Omega)(\hat{\mathbf{z}}\cdot\hat{\boldsymbol{\phi}}) \\
&\times\left(\left(1-\tfrac{n\Omega}{\omega}\right)J_n E^*_{\mathbf{k},\parallel}+\tfrac{nJ_n}{\lambda}\tfrac{k_{\parallel}v_{\perp}}{\omega}(E^*_{\mathbf{k},+}+E^*_{\mathbf{k},-})+J_n'\tfrac{k_{\parallel}v_{\perp}}{\omega}(E^*_{\mathbf{k},+}-E^*_{\mathbf{k},-})\right) \\
&\times\left(E_{\mathbf{k},\parallel}\tfrac{\partial f_0}{\partial v_{\parallel}}J_n+\tfrac{nJ_n}{\lambda}((E_{\mathbf{k},+}+E_{\mathbf{k},-})U-E_{\mathbf{k},\parallel}V)+(E_{\mathbf{k},+}-E_{\mathbf{k},-})UJ_n'\right) \qquad \text{(E.1)} \\
&= -\tfrac{\pi e^2 R}{m_e}\textstyle\sum_{\mathbf{k}}\int_{-\infty}^{\infty}dv_{\parallel}\int_0^{\infty}dv_{\perp}2\pi v_{\perp} \\
&\times\textstyle\sum_n \delta(\omega-k_{\parallel}v_{\parallel}-n\Omega)(\hat{\mathbf{z}}\cdot\hat{\boldsymbol{\phi}})\tfrac{k_{\parallel}v_{\perp}^2}{\omega}|\chi_{\mathbf{k},n}|^2 L(f_0) \qquad \text{(E.2)} \\
&= \textstyle\sum_{\mathbf{k}}\tfrac{k_{\parallel}}{\omega}P_{abs,\mathbf{k}}R(\hat{\mathbf{z}}\cdot\hat{\boldsymbol{\phi}})=\sum_{\mathbf{k}}\tfrac{n_{\parallel}}{c}P_{abs,\mathbf{k}}R(\hat{\mathbf{z}}\cdot\hat{\boldsymbol{\phi}}), \qquad \text{(E.3)}
\end{aligned}
$$

where the resonance condition $\omega - k_{\parallel}v_{\parallel} - n\Omega = 0$, the Bessel function identities $nJ_n/\lambda = (J_{n+1}+J_{n-1})/2$ and $J_n' = (J_{n-1}-J_{n+1})/2$, and $\chi_{\mathbf{k},n} = E_{\mathbf{k},\parallel}J_n\frac{v_{\parallel}}{v_{\perp}} + E_{\mathbf{k},+}J_{n-1} + E_{\mathbf{k},-}J_{n+1}$ are used from (E.1) to (E.2).

The rest of the toroidal momentum transfer in Eq. (3.9) can be obtained by inserting the perturbed fluctuating distribution function $f_{\mathbf{k}}$ in Eq. (A.8). Before doing so, I rewrite Eq. (3.9) as

$$
\begin{aligned}
\Delta T_{\varphi}^{\perp}+\Delta T_{\varphi}^{\alpha} &= -eR\textstyle\sum_{\mathbf{k}}\int_{-\infty}^{\infty}dv_{\parallel}\int_0^{\infty}dv_{\perp}2\pi v_{\perp}\int_0^{2\pi}\frac{d\alpha}{2\pi} \\
&\times\Bigg[E^*_{\mathbf{k},\parallel}\tfrac{k_{\perp}v_{\parallel}}{\omega}(\cos\beta(\hat{\mathbf{x}}\cdot\hat{\boldsymbol{\phi}})+\sin\beta(\hat{\mathbf{y}}\cdot\hat{\boldsymbol{\phi}})) \\
&+\left(1-\tfrac{k_{\parallel}v_{\parallel}}{\omega}\right)\Bigg\{\Big((E^*_{\mathbf{k},+}+E^*_{\mathbf{k},-})\cos\beta-i(E^*_{\mathbf{k},+}-E^*_{\mathbf{k},-})\sin\beta\Big)(\hat{\mathbf{x}}\cdot\hat{\boldsymbol{\phi}}) \\
&+\Big((E^*_{\mathbf{k},+}+E^*_{\mathbf{k},-})\sin\beta+i(E^*_{\mathbf{k},+}-E^*_{\mathbf{k},-})\cos\beta\Big)(\hat{\mathbf{y}}\cdot\hat{\boldsymbol{\phi}})\Bigg\}+i\left(\tfrac{k_{\perp}v_{\perp}}{\omega}\right)(E^*_{\mathbf{k},+}-E^*_{\mathbf{k},-}) \\
&\times\Big\{(\sin\eta\cos\beta+\cos\eta\sin\beta)(\hat{\mathbf{x}}\cdot\hat{\boldsymbol{\phi}})-(\cos\eta\cos\beta-\sin\eta\sin\beta)(\hat{\mathbf{y}}\cdot\hat{\boldsymbol{\phi}})\Big\}\Bigg]f_{\mathbf{k}}. \qquad \text{(E.4)}
\end{aligned}
$$

Using Eq. (A.8) for $f_{\mathbf{k}}$ and the Dirac-delta function for the resonance condition gives

$$
\begin{aligned}
& \Delta T_{\varphi}^{\perp} + \Delta T_{\varphi}^{\alpha} \\
= \; & -\tfrac{\pi e^2 R}{m_e} \textstyle\sum_{\mathbf{k}} \int_{-\infty}^{\infty} dv_{\parallel} \int_0^{\infty} dv_{\perp} 2\pi v_{\perp} \delta(\omega - k_{\parallel} v_{\parallel} - n\Omega) \Big[(\cos\beta(\hat{\mathbf{x}} \cdot \hat{\boldsymbol{\phi}}) + \sin\beta(\hat{\mathbf{y}} \cdot \hat{\boldsymbol{\phi}})) \\
& \times \left\{ \tfrac{k_{\perp} v_{\parallel}}{\omega} J_n E_{\mathbf{k},\parallel}^{*} + \left(1 - \tfrac{k_{\parallel} v_{\parallel}}{\omega}\right) J_n (E_{\mathbf{k},+}^{*} + E_{\mathbf{k},-}^{*}) + J_n' \tfrac{k_{\perp} v_{\perp}}{\omega} (E_{\mathbf{k},+}^{*} - E_{\mathbf{k},-}^{*}) \right\} \\
& -i(\sin\beta(\hat{\mathbf{x}} \cdot \hat{\boldsymbol{\phi}}) - \cos\beta(\hat{\mathbf{y}} \cdot \hat{\boldsymbol{\phi}}))) \\
& \times \left\{ \left(1 - \tfrac{k_{\parallel} v_{\parallel}}{\omega} - \tfrac{n\Omega}{\omega}\right) J_n (E_{\mathbf{k},+}^{*} - E_{\mathbf{k},-}^{*}) \right\} \Big] \chi_{\mathbf{k},n} v_{\perp} L(f_0) \qquad \text{(E.5)} \\
= \; & -\tfrac{\pi e^2 R}{m_e} \textstyle\sum_{\mathbf{k}} \int_{-\infty}^{\infty} dv_{\parallel} \int_0^{\infty} dv_{\perp} 2\pi v_{\perp} \sum_n \delta(\omega - k_{\parallel} v_{\parallel} - n\Omega) \\
& \times \left(\cos\beta(\hat{\mathbf{x}} \cdot \hat{\boldsymbol{\phi}}) + \sin\beta(\hat{\mathbf{y}} \cdot \hat{\boldsymbol{\phi}}) \right) \tfrac{k_{\perp} v_{\perp}^2}{\omega} |\chi_{\mathbf{k},n}|^2 L(f_0) \qquad \text{(E.6)} \\
= \; & \textstyle\sum_{\mathbf{k}} \tfrac{\mathbf{k}_{\perp} \cdot \hat{\boldsymbol{\phi}}}{\omega} P_{abs,\mathbf{k}} R = \sum_{\mathbf{k}} \tfrac{n_{\perp}}{c} P_{abs,\mathbf{k}} R \left(\cos\beta(\hat{\mathbf{x}} \cdot \hat{\boldsymbol{\phi}}) + \sin\beta(\hat{\mathbf{y}} \cdot \hat{\boldsymbol{\phi}}) \right). \qquad \text{(E.7)}
\end{aligned}
$$

From Eq. (E.5) to Eq. (E.6), the resonance condition and the Bessel function identities $nJ_n/\lambda = (J_{n+1} + J_{n-1})/2$ and $J_n' = (J_{n-1} - J_{n+1})/2$ are used.

Appendix F

Higher order corrections to the gyrokinetic equations

The gyrokinetic equation with higher order corrections of order $\frac{B}{B_\theta}\rho_\star$ for a species s in a frame rotating with the E×B toroidal flow is

$$\begin{aligned}
&\tfrac{df_s^{tb}}{dt'} + v'_\parallel \hat{\mathbf{b}}\cdot\nabla\theta\tfrac{\partial f_s^{tb}}{\partial\theta} + (\mathbf{v}'_M + \mathbf{v}'_C + \langle\mathbf{v}'_{E1}\rangle)\cdot\nabla_\perp f_s^{tb} \\
&+\langle\mathbf{v}'_{E1}\rangle\cdot\nabla f_{0,s}^{bg} + \tfrac{Z_s e}{T_s}\left(v'_\parallel\hat{\mathbf{b}}\cdot\nabla\theta\tfrac{\partial\langle\phi^{tb}\rangle}{\partial\theta} + (\mathbf{v}'_M+\mathbf{v}'_C)\cdot\nabla_\perp\langle\phi^{tb}\rangle\right) f_{0,s}^{bg} - \langle C\left(f_s\right)\rangle \\
&= -\mathbf{v}'_M\cdot\nabla\theta\tfrac{\partial f_s^{tb}}{\partial\theta} - \langle\mathbf{v}'_{E1}\rangle\cdot\nabla\theta\tfrac{\partial f_s^{tb}}{\partial\theta} - \langle\mathbf{v}'_{E2}\rangle\cdot\nabla_\perp f_s^{tb} - \langle\mathbf{v}'_{E2}\rangle\cdot\nabla f_{0,s}^{bg} \\
&\quad + \tfrac{Z_s e}{m_s}\left(v'_\parallel\hat{\mathbf{b}}\cdot\nabla\theta\tfrac{\partial\langle\phi^{tb}\rangle}{\partial\theta} + \mathbf{v}'_M\cdot\nabla_\perp\langle\phi^{tb}\rangle\right)\tfrac{\partial f_s^{tb}}{\partial\mathcal{E}'} \\
&\quad - \langle\mathbf{v}'_{E1}\rangle\cdot\nabla f_{1,s}^{bg} + \tfrac{Z_s e}{m_s}\left(v'_\parallel\hat{\mathbf{b}}\cdot\nabla\theta\tfrac{\partial\langle\phi^{tb}\rangle}{\partial\theta} + \mathbf{v}'_M\cdot\nabla_\perp\langle\phi^{tb}\rangle\right)\tfrac{\partial f_{1,s}^{bg}}{\partial\mathcal{E}'} \\
&\quad -\mathbf{v}_E^{nc}\cdot\nabla_\perp f_s^{tb} + \tfrac{Z_s e}{m_s}v'_\parallel\hat{\mathbf{b}}\cdot\nabla\phi_1^{bg}\tfrac{\partial f_s^{tb}}{\partial\mathcal{E}'} \\
&\quad +\text{global effect terms,}
\end{aligned} \tag{F.1}$$

where $\frac{d}{dt'} \equiv \frac{\partial}{\partial t} + \Omega_{\varphi,E}R\hat{\varphi}\cdot\nabla$ and $\mathbf{v}_C$ are the time derivative and the Coriolis drift in the rotating frame, respectively, and $\Omega_{\varphi,E} = -c\partial\phi_0^{bg}/\partial\psi$ is the toroidal angular frequency of the background E×B toroidal flow. Here, $\langle\mathbf{v}'_{E1}\rangle = \frac{c}{B}(\hat{\mathbf{b}}\times\nabla_\perp\langle\phi^{tb}\rangle)$ is the dominant piece of the E×B drift due to the fluctuating potential, and $\langle\mathbf{v}'_{E2}\rangle = \frac{c}{B}\left(\frac{\partial\langle\phi^{tb}\rangle}{\partial\theta}\right)(\hat{\mathbf{b}}\times\nabla\theta)$ is the correction to the fluctuating E×B drift due to the slow variation along the magnetic field line of the potential. The gradient in the perpendicular direction (ψ and α) is defined as $\nabla_\perp = \nabla\psi\frac{\partial}{\partial\psi} + \nabla\alpha\frac{\partial}{\partial\alpha}$, and $\mathbf{v}_E^{nc} = \frac{c}{B}(\hat{\mathbf{b}}\times\nabla\phi_1^{bg})$ is E×B drift due to the neoclassical higher

order potential given by Eq. (4.20).

The left hand side of Eq. (F.1) is the lowest order gyrokinetic equation, and the right hand side includes the corrections to order $\frac{B}{B_\theta}\rho_\star$. Besides the terms related to the neoclassical distribution function $f_{1,s}^{bg}$ that contains the diamagnetic flow in the third line on the right hand side of Eq. (F.1), there are correction terms due to the slow poloidal variation of the fluctuating potential and distribution function in the first line, the parallel nonlinearity in the second line, and the neoclassical potential ϕ_1^{bg} in the fourth line.

Assuming low collisionality and marginal instability for ion temperature gradient driven turbulence, some higher order corrections in the ion gyrokinetic equation are dominant over others. Low collisionality results in small neoclassical potentials, so the fourth line on the right hand side of Eq. (F.1) can be neglected.

To estimate the parallel correlation length, needed to estimate the contributions due to the slow poloidal variation and the parallel nonlinearity, the critical balance between the nonlinear decorrelation time (τ_{nl}) and the characteristic time for the particle parallel streaming is used [37] (i.e. $\frac{1}{k_\parallel v_{ti}} \sim \tau_{nl}$, where $k_\parallel$ is the turbulence parallel wavevector and v_{ti} is the ion thermal velocity). At the length scale at which the energy is injected into the turbulence by linear instabilities, the nonlinear correlation time is determined by the time associated with the linear drive due to background temperature and density gradients (i.e. $\frac{1}{\tau_{nl}} \sim k_{\perp,0}\rho_i\frac{v_{ti}}{L_T}$ where $k_{\perp,0}$ is the turbulence perpendicular wavevector). In some cases, the eddies with the largest perpendicular extent reach the longest parallel wavelength in the system (connection length) giving $k_{\parallel,0} \sim \frac{1}{qR}$ where q is the safety factor and R is the major radius. In these cases, the parallel length is related to the perpendicular length by $k_{\parallel,0} \sim \frac{k_{\perp,0}\rho_i}{L_T} \sim \frac{1}{qR}$, resulting the terms in the first and second lines on the right hand sides of Eq. (F.1) being comparable to the terms in the third line.

However, for turbulence near marginal stability, the perpendicular correlation length is limited by the perpendicular wavelength of the marginally stable spectral mode, resulting in turbulence parallel wavelengths that are shorter than the connection length in the system [147],

$$k_{\parallel,0} \sim \frac{k_{\perp,0}\rho_i}{L_T} > \frac{1}{qR}, \tag{F.2}$$

where $k_{\perp,0}$ is the smallest wavelength that is marginally unstable. Then, using the long

wavelength limit of ITG turbulence,

$$\frac{e\langle\phi^{tb}\rangle}{T_e} \sim \frac{f_i^{tb}}{f_{M,i}} \sim \frac{\rho_i}{L_T}\frac{1}{k_{\perp,0}\rho_i} < \frac{\rho_i}{L_T}\frac{qR}{L_T} \sim \frac{B}{B_\theta}\frac{\rho_i}{L_T}. \tag{F.3}$$

Accordingly, the scale of each term on the right hand side of Eq. (F.1) can be estimated. These scalings give $\langle \mathbf{v}_{E1}\rangle \sim \frac{\rho_i}{L_T} v_{ti}$. The term with the diamagnetic flow is

$$\{1\}: \quad \langle \mathbf{v}_{E1}\rangle \cdot \nabla f_{1,i}^{bg} \sim \frac{\rho_i}{L_T}\frac{v_{ti}}{L_T}\frac{B}{B_\theta}\frac{\rho_i}{L_T} f_{M,i}, \tag{F.4}$$

where the characteristic length for the velocity gradient change is assumed to be same as the temperature gradient length scale L_T. The scale of other terms is compared to the diamagnetic flow term in $\{1\}$,

$$\begin{aligned}\{2\}: \quad \frac{Z_i e}{m_i} v_\parallel \hat{\mathbf{b}}\cdot\nabla\theta \frac{\partial\langle\phi^{tb}\rangle}{\partial\theta}\frac{\partial f_i^{tb}}{\partial\mathcal{E}'} &\sim v_{ti}k_\parallel \frac{e\langle\phi^{tb}\rangle}{T}\frac{f_i^{tb}}{f_{M,i}} f_{M,i} \sim k_{\perp,0}\rho_i \frac{v_{ti}}{L_T}\frac{1}{k_{\perp,0}\rho_i}\frac{\rho_i}{L_T} f_{M,i}\frac{\rho_i}{L_T}\frac{1}{k_{\perp,0}\rho_i} \\ &< \frac{\rho_i}{L_T}\frac{v_{ti}}{L_T}\frac{B}{B_\theta}\frac{\rho_i}{L_T} f_{M,i} \sim \{1\},\end{aligned} \tag{F.5}$$

$$\begin{aligned}\{3\}: \quad \mathbf{v}_M\cdot\nabla\theta\frac{\partial f_i^{tb}}{\partial\theta} &\sim v_{ti}\frac{\rho_i}{R}\frac{1}{a}k_\parallel qR\frac{1}{k_{\perp,0}\rho_i}\frac{\rho_i}{L_T} f_{M,i} \sim \frac{\rho_i}{R}\frac{qR}{a}\frac{\rho_i}{L_T}\frac{v_{ti}}{L_T} f_{M,i} \\ &< \frac{\rho_i}{L_T}\frac{v_{ti}}{L_T}\frac{B}{B_\theta}\frac{\rho_i}{L_T} f_{M,i} \sim \{1\},\end{aligned} \tag{F.6}$$

$$\begin{aligned}\{4\}: \quad \langle \mathbf{v}_{E1}\rangle\cdot\nabla\theta\frac{\partial f_i^{tb}}{\partial\theta} &\sim \langle \mathbf{v}_{E2}\rangle\cdot\nabla_\perp f_i^{tb} \sim v_{ti}\frac{\rho_i}{L_T}\frac{1}{a}k_\parallel qR\frac{1}{k_{\perp,0}\rho_i}\frac{\rho_i}{L_T} f_{M,i} \\ &\sim \frac{\rho_i}{L_T}\frac{v_{ti}}{L_T}\frac{B}{B_\theta}\frac{\rho_i}{L_T} f_{M,i} \sim \{1\},\end{aligned} \tag{F.7}$$

$$\begin{aligned}\{5\}: \quad \langle \mathbf{v}_{E2}\rangle\cdot\nabla_\perp f_{0,i}^{bg} &\sim v_{ti}\frac{\rho_i}{L_T}\frac{1}{a}k_\parallel qR\frac{1}{k_{\perp,0}\rho_i}\frac{\rho_i}{L_T} f_{M,i} \\ &\sim \frac{\rho_i}{L_T}\frac{v_{ti}}{L_T}\frac{B}{B_\theta}\frac{\rho_i}{L_T} f_{M,i} \sim \{1\}.\end{aligned} \tag{F.8}$$

Appendix G

Transformation of the gyrokinetic equation to a rotating frame

The distribution function in the lab frame (L) and the rotating frame (R) must describe the same physical state of the plasma. Thus, there are relations between the distribution functions in the two frame,

$$\begin{aligned} f_i^{bg(L)}(v_\parallel) &= f_i^{bg(R)}(v'_\parallel) = f_{M,i}^{(R)}(v'_\parallel) \\ &= \frac{n_i}{\pi^{3/2} v_{ti}^3} \exp\left(-\frac{|\mathbf{v} - R\Omega_\varphi \hat{\varphi}|^2}{v_{ti}^2}\right) \simeq f_{M,i}^{(L)}\left(1 + \frac{m_i v_\parallel}{T_i}\frac{I\Omega_\varphi}{B}\right), \qquad \text{(G.1)} \\ f_i^{tb(L)}(v_\parallel) &= f_i^{tb(R)}(v'_\parallel) \\ &\simeq f_i^{tb(L)}(v'_\parallel) + \frac{I\Omega_\varphi}{B}\frac{\partial f_i^{tb(L)}}{\partial v'_\parallel}, \qquad \text{(G.2)} \end{aligned}$$

where $v_\parallel$ and $v'_\parallel$ are the parallel velocity in the lab frame and the rotating frame, respectively, and $v'_\parallel = v_\parallel - I\Omega_\varphi/B$ is used for the first order approximation of the distribution function in Eq. (G.1) and (G.2). In this Appendix, I transform the gyrokinetic equation in Eq. (4.37) in the frame rotating with the E×B toroidal flow to the lab frame, finding Eq. (4.14). In this Appendix, I proceed differently than in Sec. 4.3.2. For simplicity, I assume that the diamagnetic flow is zero and there is no velocity shear (i.e. $\Omega_\varphi = \Omega_{\varphi,E} = -c(\partial\phi_0^{bg}/\partial\psi)$, $\Omega_{\varphi,d} = 0$ and $\partial\Omega_\varphi/\partial\psi = 0$). With these assumptions, the ion gyrokinetic equation in the

rotating frame is

$$\begin{aligned}
&\frac{\partial f_i^{tb(R)}}{\partial t'} + \left(v'_\parallel \hat{\mathbf{b}} + \mathbf{v}'_M + \mathbf{v}'_C - \frac{c}{B}\nabla\langle\phi^{tb}\rangle \times \hat{\mathbf{b}}\right) \cdot \nabla f_i^{tb(R)} \\
= \;& \frac{c}{B}\nabla\langle\phi^{tb}\rangle \times \hat{\mathbf{b}} \cdot \nabla f_{M,i}^{(R)} + \frac{Z_i e}{m_i}[v'_\parallel \hat{\mathbf{b}} + \mathbf{v}'_M + \mathbf{v}'_C] \cdot \nabla\langle\phi^{tb}\rangle \frac{\partial f_{M,i}^{(R)}}{\partial \mathcal{E}'} + \langle C(f_i)\rangle. \qquad \text{(G.3)}
\end{aligned}$$

Applying the relation between the two turbulent pieces of the distribution function in (G.2),

$$\begin{aligned}
&\frac{\partial\left(f_i^{tb(L)}(v'_\parallel) + \frac{I\Omega_\varphi}{B}\frac{\partial f_i^{tb(L)}}{\partial v'_\parallel}\right)}{\partial t'} + \left(v'_\parallel \hat{\mathbf{b}} + \mathbf{v}'_M + \mathbf{v}'_C - \frac{c}{B}\nabla\langle\phi^{tb}\rangle \times \hat{\mathbf{b}}\right) \cdot \nabla\left(f_i^{tb(L)}(v'_\parallel) + \frac{I\Omega_\varphi}{B}\frac{\partial f_i^{tb(L)}}{\partial v'_\parallel}\right) \\
= \;& \frac{c}{B}\nabla\langle\phi^{tb}\rangle \times \hat{\mathbf{b}} \cdot \nabla f_{M,i}^{(R)} + \frac{Z_i e}{m_i}[v'_\parallel \hat{\mathbf{b}} + \mathbf{v}'_M + \mathbf{v}'_C] \cdot \nabla\langle\phi^{tb}\rangle \frac{\partial f_{M,i}^{(R)}}{\partial \mathcal{E}'} + \langle C(f_i)\rangle. \qquad \text{(G.4)}
\end{aligned}$$

Changing the dummy variable $v'_\parallel$ for $v_\parallel$ and $\mathcal{E}'$ for $\mathcal{E}$, and using the definition of the Doppler shifted time derivative $\frac{\partial}{\partial t'} = \frac{\partial}{\partial t} + R\Omega_\varphi\hat{\varphi}\cdot\nabla$, Eq. (G.4) becomes

$$\begin{aligned}
&\frac{\partial f_i^{tb(L)}}{\partial t}(v_\parallel) + \left(v_\parallel \hat{\mathbf{b}} + \mathbf{v}_M - \frac{c}{B}\nabla(\phi_0^{bg} + \langle\phi^{tb}\rangle) \times \hat{\mathbf{b}}\right) \cdot \nabla f_i^{tb(L)}(v_\parallel) \\
&- \frac{Z_i e}{m_i}\mathbf{v}_M \cdot \nabla\phi_0^{bg}\frac{\partial f_i^{tb(L)}}{\partial \mathcal{E}} - \frac{c}{B}\nabla\langle\phi^{tb}\rangle \times \hat{\mathbf{b}} \cdot \nabla\left[f_{M,i}^{(L)}\left(1 + \frac{m_i v_\parallel}{T_i}\frac{I\Omega_\varphi}{B}\right)\right] \\
&- \frac{Z_i e}{m_i}[v_\parallel \hat{\mathbf{b}} + \mathbf{v}_M] \cdot \nabla\langle\phi^{tb}\rangle \frac{\partial\left[f_{M,i}^{(L)}\left(1 + \frac{m_i v_\parallel}{T_i}\frac{I\Omega_\varphi}{B}\right)\right]}{\partial \mathcal{E}} - \langle C(f_i)\rangle \qquad \text{(G.5)} \\
= \;& \underbrace{-\frac{\partial}{\partial t}\left(\frac{I\Omega_\varphi}{B}\frac{\partial f_i^{tb(L)}}{\partial v_\parallel}\right)}_{\{1\}} \underbrace{- R\Omega_\varphi\hat{\varphi}\cdot\nabla f_i^{tb(L)}}_{\{2\}} \underbrace{- \left(v_\parallel \hat{\mathbf{b}} + \mathbf{v}_M - \frac{c}{B}\nabla\langle\phi^{tb}\rangle \times \hat{\mathbf{b}}\right) \cdot \nabla\left(\frac{I\Omega_\varphi}{B}\frac{\partial f_i^{tb(L)}}{\partial v_\parallel}\right)}_{\{3\}} \\
&\underbrace{- \frac{c}{B}\nabla\phi_0^{bg} \times \hat{\mathbf{b}} \cdot \nabla f_i^{tb(L)}(v_\parallel)}_{\{4\}} \underbrace{- \frac{Z_i e}{m_i}\mathbf{v}_M \cdot \nabla\phi_0^{bg}\frac{\partial f_i^{tb(L)}}{\partial \mathcal{E}}}_{\{5\}} \underbrace{- \mathbf{v}_C \cdot \nabla\left(f_i^{tb(L)}(v_\parallel) + \frac{I\Omega_\varphi}{B}\frac{\partial f_i^{tb(L)}}{\partial v_\parallel}\right)}_{\{6\}} \\
&\underbrace{- \left[\frac{c}{B}\nabla\langle\phi^{tb}\rangle \times \hat{\mathbf{b}} \cdot \nabla\left(\frac{m_i v_\parallel}{T_i}\frac{I\Omega_\varphi}{B}\right) + \frac{Z_i e}{m_i}[v_\parallel \hat{\mathbf{b}} + \mathbf{v}_M] \cdot \nabla\langle\phi^{tb}\rangle \frac{\partial\left(\frac{m_i v_\parallel}{T_i}\frac{I\Omega_\varphi}{B}\right)}{\partial \mathcal{E}}\right] f_{M,i}^{(L)}}_{\{7\}} \\
&\underbrace{- \left[\frac{c}{B}\nabla\langle\phi^{tb}\rangle \times \hat{\mathbf{b}} \cdot \nabla f_{M,i}^{(L)} + \frac{Z_i e}{m_i}[v_\parallel \hat{\mathbf{b}} + \mathbf{v}_M] \cdot \nabla\langle\phi^{tb}\rangle \frac{\partial f_{M,i}^{(L)}}{\partial \mathcal{E}}\right]\left(\frac{m_i v_\parallel}{T_i}\frac{I\Omega_\varphi}{B}\right)}_{\{8\}} \\
&\underbrace{+ \frac{Z_i e}{m_i}\mathbf{v}_C \cdot \nabla\langle\phi^{tb}\rangle \frac{\partial f_{M,i}^{(L)}}{\partial \mathcal{E}}}_{\{9\}}. \qquad \text{(G.6)}
\end{aligned}$$

Here, the left hand side in Eq. (G.6) is the same as the gyro kinetic equation in the lab frame corresponding to Eq. (4.14), but there are additional terms on the right hand side in Eq. (G.6). I will show that all the terms on the right hand side vanish.

For {3} and {5}, a piece of {3} is

$$\begin{aligned} v_\parallel \hat{\mathbf{b}} \cdot \nabla \left(\frac{I v_\parallel}{B} \right) \Omega_\varphi \frac{\partial f_i^{tb(L)}}{\partial \mathcal{E}} &= -\frac{Z_i e}{m_i} \mathbf{v}_M \cdot \nabla \phi_0^{bg} \frac{\partial f_i^{tb(L)}}{\partial \mathcal{E}} = -\{5\} \\ &\gg \mathbf{v}_M \cdot \nabla \left(\frac{I v_\parallel}{B} \right) \Omega_\varphi \frac{\partial f_i^{tb(L)}}{\partial \mathcal{E}}, \end{aligned} \tag{G.7}$$

where I used $\frac{\partial \Omega_\varphi}{\partial \psi} = 0$, $\frac{\partial f_i^{tb(L)}}{\partial v_\parallel}|_\mu = v_\parallel \frac{\partial f_i^{tb(L)}}{\partial \mathcal{E}}|_\mu$, $\nabla v_\parallel = -\frac{\mu \nabla B}{v_\parallel}$ and $v_\parallel \hat{\mathbf{b}} \cdot \nabla \left(\frac{I v_\parallel}{B} \right) = \mathbf{v}_M \cdot \nabla \psi$. The nonlinear acceleration term $\frac{c}{B} \nabla \langle \phi^{tb} \rangle \times \hat{\mathbf{b}} \cdot \nabla \left(\frac{I v_\parallel}{B} \right) \Omega_\varphi \frac{\partial f_i^{tb(L)}}{\partial \mathcal{E}}$ is neglected because it is small. Then,

$$\{3\} + \{5\} = \left(v_\parallel \hat{\mathbf{b}} + \mathbf{v}_M - \frac{c}{B} \nabla \langle \phi^{tb} \rangle \times \hat{\mathbf{b}} \right) \cdot \nabla \left(\frac{\partial f_i^{tb(L)}}{\partial \mathcal{E}} \right) \left(\frac{I v_\parallel}{B} \right) \Omega_\varphi \tag{G.8}$$

For {7}, some pieces are canceled out, because

$$\frac{c}{B} \nabla \langle \phi^{tb} \rangle \times \hat{\mathbf{b}} \cdot \nabla v_\parallel \left(\frac{m_i}{T_i} \frac{I \Omega_\varphi}{B} \right) - \frac{Z_i e}{m_i} \frac{\mu}{\Omega_i} \hat{\mathbf{b}} \times \nabla B \cdot \nabla \langle \phi^{tb} \rangle \frac{\partial \left(\frac{m_i v_\parallel}{T_i} \frac{I \Omega_\varphi}{B} \right)}{\partial \mathcal{E}} = 0 \tag{G.9}$$

$$\frac{c}{B} \nabla \langle \phi^{tb} \rangle \times \hat{\mathbf{b}} \cdot \nabla \left(\frac{I}{B} \right) \left(\frac{m_i v_\parallel}{T_i} \Omega_\varphi \right) - \frac{Z_i e}{m_i} \frac{v_\parallel{}^2}{\Omega_i} \hat{\mathbf{b}} \times (\hat{\mathbf{b}} \cdot \nabla \hat{\mathbf{b}}) \cdot \nabla \langle \phi^{tb} \rangle \frac{\partial \left(\frac{m_i v_\parallel}{T_i} \frac{I \Omega_\varphi}{B} \right)}{\partial \mathcal{E}} \simeq 0. \tag{G.10}$$

Using $\frac{\partial v_\parallel}{\partial \mathcal{E}} = \frac{1}{v_\parallel}$, $\nabla (I/B)/(I/B) = -\hat{\mathbf{b}} \cdot \nabla \hat{\mathbf{b}} + O(\frac{B_p}{BR})$ and Eq. (G.10), the term {7} is

$$\begin{aligned} \{7\} &= \left(\frac{c}{B} \nabla \langle \phi^{tb} \rangle \times \hat{\mathbf{b}} \cdot \nabla \psi \right) \frac{m_i v_\parallel}{T_i} \frac{I \Omega_\varphi}{B} \left(-\frac{\partial \ln T_i}{\partial \psi} \right) f_{M,i}^{(L)} + \frac{Z_i e}{m_i} v_\parallel \hat{\mathbf{b}} \cdot \nabla \langle \phi^{tb} \rangle \frac{\partial \left(\frac{m_i v_\parallel}{T_i} \frac{I \Omega_\varphi}{B} \right)}{\partial \mathcal{E}} f_{M,i}^{(L)} \\ &= \left(\frac{c}{B} \nabla \langle \phi^{tb} \rangle \times \hat{\mathbf{b}} \cdot \nabla \psi \right) \frac{m_i v_\parallel}{T_i} \frac{I \Omega_\varphi}{B} \left(-\frac{\partial \ln T_i}{\partial \psi} \right) f_{M,i}^{(L)} + \frac{Z_i e}{m_i} (\hat{\mathbf{b}} \cdot \nabla \langle \phi^{tb} \rangle) \left(\frac{m}{T_i} \frac{I \Omega_\varphi}{B} \right) f_{M,i}^{(L)} \end{aligned}$$

Finally, the term {8} is

$$
\begin{aligned}
\{8\} &= \left[\frac{c}{B}\nabla\langle\phi^{tb}\rangle\times\hat{\mathbf{b}}\cdot\nabla f_{M,i}^{(L)}+\frac{Z_i e}{m_i}[v_\parallel\hat{\mathbf{b}}+\mathbf{v}_M]\cdot\nabla\langle\phi^{tb}\rangle\frac{\partial f_{M,i}^{(L)}}{\partial\mathcal{E}}\right]\left(\frac{m_i v_\parallel}{T_i}\frac{I\Omega_\varphi}{B}\right)\\
&= -\frac{\partial}{\partial\mathcal{E}}\left[\frac{c}{B}\nabla\langle\phi^{tb}\rangle\times\hat{\mathbf{b}}\cdot\nabla f_{M,i}^{(L)}+\frac{Z_i e}{m_i}[v_\parallel\hat{\mathbf{b}}+\mathbf{v}_M]\cdot\nabla\langle\phi^{tb}\rangle\frac{\partial f_{M,i}^{(L)}}{\partial\mathcal{E}}\right]\left(v_\parallel\frac{I\Omega_\varphi}{B}\right)\\
&\quad+\left(\frac{c}{B}\nabla\langle\phi^{tb}\rangle\times\hat{\mathbf{b}}\cdot\nabla\psi\right)\frac{m_i v_\parallel}{T_i}\frac{I\Omega_\varphi}{B}\frac{\partial\ln T_i}{\partial\psi}f_{M,i}^{(L)}\\
&\quad+\frac{Z_i e}{m_i}\frac{\partial[v_\parallel\hat{\mathbf{b}}+\mathbf{v}_M]}{\partial\mathcal{E}}\cdot\nabla\langle\phi^{tb}\rangle\frac{\partial f_{M,i}^{(L)}}{\partial\mathcal{E}}\left(v_\parallel\frac{I\Omega_\varphi}{B}\right) \qquad \text{(G.11)}\\
&\simeq -\frac{\partial}{\partial\mathcal{E}}\left[\frac{\partial f_i^{tb(L)}}{\partial t}+\left(v_\parallel\hat{\mathbf{b}}+\mathbf{v}_M-\frac{c}{B}\nabla\langle\phi^{tb}\rangle\times\hat{\mathbf{b}}\right)\cdot\nabla f_i^{tb(L)}\right]\left(v_\parallel\frac{I\Omega_\varphi}{B}\right)\\
&\quad+\left(\frac{c}{B}\nabla\langle\phi^{tb}\rangle\times\hat{\mathbf{b}}\cdot\nabla\psi\right)\frac{m_i v_\parallel}{T_i}\frac{I\Omega_\varphi}{B}\frac{\partial\ln T_i}{\partial\psi}f_{M,i}^{(L)}\\
&\quad+\frac{Z_i e}{m_i}\left[\frac{1}{v_\parallel}\hat{\mathbf{b}}+\frac{2}{\Omega_i}\hat{\mathbf{b}}\times(\hat{\mathbf{b}}\cdot\nabla\hat{\mathbf{b}})\right]\cdot\nabla\langle\phi^{tb}\rangle\frac{\partial f_{M,i}^{(L)}}{\partial\mathcal{E}}\left(v_\parallel\frac{I\Omega_\varphi}{B}\right) \qquad \text{(G.12)}\\
&\simeq -(\{1\}+\{3\}+\{5\})+\frac{Z_i e}{m_i}\frac{\partial\left(v_\parallel\hat{\mathbf{b}}+\mathbf{v}_M\right)}{\partial\mathcal{E}}\cdot\nabla f_i^{tb(L)}\left(v_\parallel\frac{I\Omega_\varphi}{B}\right)\\
&\quad+\left(\frac{c}{B}\nabla\langle\phi^{tb}\rangle\times\hat{\mathbf{b}}\cdot\nabla\psi\right)\frac{m_i v_\parallel}{T_i}\frac{I\Omega_\varphi}{B}\frac{\partial\ln T_i}{\partial\psi}f_{M,i}^{(L)}\\
&\quad-\frac{Z_i e}{m_i}\left(\hat{\mathbf{b}}\cdot\nabla\langle\phi^{tb}\rangle\right)\frac{m_i}{T_i}\frac{I\Omega_\varphi}{B}f_{M,i}^{(L)}+\frac{Z_i e}{m_i}\mathbf{v}_C\cdot\nabla\langle\phi^{tb}\rangle\frac{\partial f_{M,i}^{(L)}}{\partial\mathcal{E}} \qquad \text{(G.13)}\\
&\simeq -(\{1\}+\{3\}+\{5\})+\hat{\mathbf{b}}\cdot\nabla f_i^{tb(L)}\frac{I\Omega_\varphi}{B}+\mathbf{v}_C\cdot\nabla f_i^{tb(L)}-(\{7\}+\{9\}) \qquad \text{(G.14)}\\
&\simeq -(\{1\}+\{2\}+\{3\}+\{4\}+\{5\}+\{6\}+\{7\}+\{9\}). \qquad \text{(G.15)}
\end{aligned}
$$

From Eq. (G.11) to Eq. (G.12), the gyrokinetic equation in Eq. (G.3) is used and the second order terms proportional to $(\Omega_\varphi R/v_{ti})^2$ are ignored. From Eq. (G.12) to Eq. (G.13), the approximation $\mathbf{v}_C = \frac{2v_\parallel\Omega_\varphi}{\Omega_i}\frac{I}{B}\hat{\mathbf{b}}\times(\hat{\mathbf{b}}\cdot\nabla\hat{\mathbf{b}})) \simeq \frac{2v_\parallel\Omega_\varphi}{\Omega_i}\hat{\mathbf{b}}\times[(\nabla R\times\hat{\varphi})\times\hat{\mathbf{b}}]$ is applied and the terms small in (B_θ/B) are neglected. From Eq. (G.14) to Eq. (G.15), I used $\{2\}+\{4\} = -\hat{\mathbf{b}}\cdot\nabla f_i^{tb(L)}\frac{I\Omega_\varphi}{B}$.

Thus, all the terms on the right hand side of Eq. (G.6) vanish and the gyrokinetic equation in the lab frame on the left hand side remains. In other words, the relation between the two turbulent functions in Eq. (G.2) holds for the solutions of the gyrokinetic equations in the two frames given in Eq. (4.14) and Eq. (4.37)

The transformation of the parallel contribution to the radial flux of toroidal angular

momentum in Eq. (4.11) to the rotating frame is

$$\begin{aligned}\Pi_{\parallel}^{(R)} &= \left\langle \left(\frac{c}{B}\nabla\langle\phi^{tb}\rangle \times \hat{\mathbf{b}}\cdot\nabla\psi\right)\int dv'^3 \frac{Im_i v'_{\parallel}}{B} f_i^{tb(R)}(v'_{\parallel})\right\rangle_{\psi} \\ &= \left\langle \left(\frac{c}{B}\nabla\langle\phi^{tb}\rangle \times \hat{\mathbf{b}}\cdot\nabla\psi\right)\int dv'^3 \left(\frac{Im_i v_{\parallel}}{B} - \frac{I^2 m_i}{B^2}\Omega_{\varphi}\right) f_i^{tb(L)}(v_{\parallel})\right\rangle_{\psi} \\ &= \Pi_{\parallel}^{(L)} - I^2 m_i \Omega_{\varphi}\left\langle \frac{\Gamma^{(L)}}{B^2}\right\rangle_{\psi}, \end{aligned} \tag{G.16}$$

where $\Gamma^{(L)}$ is the turbulent particle flux in the lab frame, and the relation $v'_{\parallel} = v_{\parallel} - \frac{I}{B}\Omega_{\varphi}$ is applied. Alternatively, Eq. (G.16) can be obtained from the relation in Eq. (G.2)

$$\begin{aligned}\Pi_{\parallel}^{(R)} &= \left\langle \left(\tfrac{c}{B}\nabla\langle\phi^{tb}\rangle \times \hat{\mathbf{b}}\cdot\nabla\psi\right)\int dv'^3 \tfrac{Im_i v'_{\parallel}}{B} f_i^{tb(R)}(v'_{\parallel})\right\rangle_{\psi} \\ &= \left\langle \left(\tfrac{c}{B}\nabla\langle\phi^{tb}\rangle \times \hat{\mathbf{b}}\cdot\nabla\psi\right)\int dv'^3 \left(\tfrac{Im_i v'_{\parallel}}{B}\right)\left(f_i^{tb(L)}(v'_{\parallel}) + \tfrac{I\Omega_{\varphi}}{B}\tfrac{\partial f_i^{tb(L)}}{\partial v'_{\parallel}}\right)\right\rangle_{\psi} \\ &= \left\langle \left(\tfrac{c}{B}\nabla\langle\phi^{tb}\rangle \times \hat{\mathbf{b}}\cdot\nabla\psi\right)\int dv^3 \left(\tfrac{Im_i v_{\parallel}}{B}\right)\left(f_i^{tb(L)}(v_{\parallel}) + \tfrac{I\Omega_{\varphi}}{B}\tfrac{\partial f_i^{tb(L)}}{\partial v_{\parallel}}\right)\right\rangle_{\psi} \\ &= \Pi_{\parallel}^{(L)} - I^2 m_i \Omega_{\varphi}\left\langle \tfrac{\Gamma^{(L)}}{B^2}\right\rangle_{\psi}, \end{aligned} \tag{G.17}$$

where integration by parts is used.

The transformation of the perpendicular contribution to the radial flux of toroidal angular momentum in Eq. (4.12) to the rotating frame is

$$\begin{aligned}\Pi_{\perp}^{(R)} &= \left\langle \left(\frac{m_i c}{B^2}\nabla\langle\phi^{tb}\rangle \times \hat{\mathbf{b}}\cdot\nabla\psi\right)\int dv'^3 f_i^{tb(R)}(\mathbf{v}'\times\hat{\mathbf{b}})\cdot\nabla\psi\right\rangle_{\psi} \\ &= \left\langle \left(\frac{m_i c}{B^2}\nabla\langle\phi^{tb}\rangle \times \hat{\mathbf{b}}\cdot\nabla\psi\right)\int dv'^3 f_i^{tb(L)}(\mathbf{v}\times\hat{\mathbf{b}}\cdot\nabla\psi - \Omega_{\varphi}|\nabla\psi|^2)\right\rangle_{\psi} \\ &= \Pi_{\perp}^{(L)} - m_i\Omega_{\varphi}\left\langle \frac{\Gamma^{(L)}}{B^2}|\nabla\psi|^2\right\rangle_{\psi}, \end{aligned} \tag{G.18}$$

where $\mathbf{v}' = \mathbf{v} - \Omega_{\varphi} R\hat{\varphi}$ and $R\hat{\varphi} = \frac{I}{B}\hat{\mathbf{b}} - \frac{1}{B}\hat{\mathbf{b}}\times\nabla\psi$ are used.

By summing the contributions in Eq. (G.16) and (G.18), the transformation of the radial flux of toroidal angular momentum is

$$\begin{aligned}\Pi^{(R)} &= \Pi_{\parallel}^{(R)} + \Pi_{\perp}^{(R)} \\ &= \Pi^{(L)} - m_i\Omega_{\varphi}\left\langle \Gamma^{(L)} R^2\right\rangle_{\psi}, \end{aligned} \tag{G.19}$$

where $B^2R^2 = I^2 + |\nabla\psi|^2$ is used.

Bibliography

[1] M. Kikuchi. Steady state tokamak reactor based on the bootstrap current. *Nuclear fusion*, 30(2):265, 1990.

[2] Y. Koide et al. Progress in confinement and stability with plasma shape and profile control for steady-state operation in the japan atomic energy research institute tokamak-60 upgrade. *Physics of Plasmas*, 4:1623, 1997.

[3] X. Litaudon, A. Bécoulet, F. Crisanti, et al. Progress towards steady-state operation and real-time control of internal transport barriers in jet. *Nuclear fusion*, 43(7):565, 2003.

[4] A. Boozer. Theory of tokamak disruptions. *Physics of Plasmas*, 19:058101, 2012.

[5] R. Fitzpatrick and A. Y. Aydemir. Stabilization of the resistive shell mode in tokamaks. *Nuclear fusion*, 36(1):11, 1996.

[6] K. H. Burrell. Effects of e× b velocity shear and magnetic shear on turbulence and transport in magnetic confinement devices. *Physics of Plasmas*, 4:1499, 1997.

[7] N. J. Fisch. Theory of current drive in plasmas. *Reviews of Modern Physics*, 59(1):175, 1987.

[8] G. T. Hoang, C. Gil, E. Joffrin, et al. Improved confinement in high li lower hybrid driven steady state plasmas in tore supra. *Nuclear fusion*, 34(1):75, 1994.

[9] A. Bondeson and D. J. Ward. *Physical Review Letters*, 72:2709, 1994.

[10] E. J. Strait, T. S. Taylor, A. D. Turnbull, J. R. Ferron, L. L. Lao, B. Rice, O. Sauter, S. J. Thompson, and D. Wrblewski. *Physical Review Letters*, 74:2483, 1995.

[11] M. Barnes, F. I. Parra, E. G. Highcock, A. A. Schekochihin, S. C. Cowley, and C. M. Roach. *Physical Review Letters*, 106:175004, 2011.

[12] F. I. Parra, M. Barnes, E. G. Highcock, A. A. Schekochihin, and S. C. Cowley. *Physical Review Letters*, 106:115004, 2011.

[13] C. L. Fiore, D. R. Ernst, Y. A. Podpaly, et al. Production of internal transport barriers via self-generated mean flows in alcator c-mod. *Physics of Plasmas*, 19:056113, 2012.

[14] A. Ince-Cushman and et.al. *Physical Review Letters*, 102:035002, 2009.

[15] M. Porkolab. Survey of lower hybrid experiments. *Plasma Science, IEEE Transactions on*, 12(2):107–117, 1984.

[16] Y. Takase and M. Porkolab. Parametric excitation of ion-sound quasimodes during lower-hybrid heating experiments in tokamaks. *Physics of Fluids*, 26(10):2992–3003, 1983.

[17] T. H. Stix. *Waves in Plasmas.* AIP Press, 1992.

[18] P. T. Bonoli and E. Ott. Toroidal and scattering effects on lower-hybrid wave propagation. *Physics of Fluids*, 25(2):359–375, 1982.

[19] P. T. Bonoli. Linear theory of lower hybrid heating. *Plasma Science, IEEE Transactions on*, 12(2):95–107, 1984.

[20] L. Landau. *J. Phys. USSR*, 10:25, 1946.

[21] C. F. Kennel and F. Engelmann. *Phys. Fluids*, 9:2377–2388, 1966.

[22] V_E Golant. Plasma penetration near the lower hybrid frequency. Technical report, Ioffe Inst. of Physics and Tech., Leningrad, 1972.

[23] P. T. Bonoli, J. Ko, R. Parker, et al. Lower hybrid current drive experiments on alcator c-mod: Comparison with theory and simulation. *Physics of Plasmas*, 15(5):056117–056117, 2008.

[24] J. C. Wright, P. T. Bonoli, and A. E. Schmidt. *Physics of Plasmas*, 16:072502, 2009.

[25] O. Meneghini, S. Shiraiwa, and R. R. Parker. *Physics of Plasmas*, 16:090701, 2009.

[26] G. M. Wallace, R. R. Parker, P. T. Bonoli, A. E. Hubbard, J. W. Hughes, and et.al. *Physics of Plasmas*, 17:082508, 2010.

[27] R. Cesario, L. Amicucci, A. Cardinali, et al. Current drive at plasma densities required for thermonuclear reactors. *Nature Communications*, 1:55, 2010.

[28] R. Cesario, L. Amicucci, C. Castaldo, M. Kempenaars, and et. al. *Plasma Physics of Controlled Fusion*, 53:085011, 2011.

[29] R. W. Harvey and M. G. McCoy. *Proc. IAEA TCM on Advances in Sim. and Modeling of Thermonuclear Plasmas, available through USDOC/NTIS No. DE93002962.*

[30] F. L. Hinton and R. D. Hazeltine. Theory of plasma transport in toroidal confinement systems. *Reviews of Modern Physics*, 48(2):239, 1976.

[31] P. Helander and D. J. Sigmar. *Collisional Transport in Magnetized Plasmas.* Cambridge University Press, 2002.

[32] M. Kotschenreuther, W. Dorland, M. A. Beer, and G. W. Hammett. Quantitative predictions of tokamak energy confinement from first-principles simulations with kinetic effects. *Physics of Plasmas*, 2:2381, 1995.

[33] A. M. Dimits, G. Bateman, M. A. Beer, et al. Comparisons and physics basis of tokamak transport models and turbulence simulations. *Physics of Plasmas*, 7:969, 2000.

[34] W. M. Tang. Microinstability theory in tokamaks. *Nuclear Fusion*, 18(8):1089, 1978.

[35] W. Horton. Drift waves and transport. *Reviews of Modern Physics*, 71(3):735, 1999.

[36] A. N. Kolmogorov. *C. R. Acad. Sci. URSS*, 30, 1941.

[37] M. Barnes, F. I. Parra, and A. A. Schekochihin. *Physical Review Letters*, 107:115003, 2011.

[38] B. Coppi, M. N. Rosenbluth, and R. Z. Sagdeev. Instabilities due to temperature gradients in complex magnetic field configurations. *Physics of Fluids*, 10:582, 1967.

[39] H. Biglari, P. H. Diamond, and M. N. Rosenbluth. Toroidal ion-pressure-gradient-driven drift instabilities and transport revisited. *Physics of Fluids B: Plasma Physics*, 1:109, 1989.

[40] F. Romanelli and S. Briguglio. Toroidal semicollisional microinstabilities and anomalous electron and ion transport. *Physics of Fluids B: Plasma Physics*, 2:754, 1990.

[41] D. R. Ernst, b J. Lang, W. M. Nevins, M. Hoffman, Y. Chen, W. Dorland, and S. Parker. *Physics of Plasmas*, 16:055906, 2009.

[42] W. Dorland, F. Jenko, M. Kotschenreuther, and B. N. Rogers. Electron temperature gradient turbulence. *Physical Review Letters*, 85(26):5579–5582, 2000.

[43] F. Jenko, W. Dorland, M. Kotschenreuther, and B. N. Rogers. Electron temperature gradient driven turbulence. *Physics of Plasmas*, 7:1904, 2000.

[44] E. A. Frieman and L. Chen. Nonlinear gyrokinetic equations for low-frequency electromagnetic waves in general plasma equilibria. *Physics of fluids*, 25:502, 1982.

[45] F. Jenko and W. Dorland. Nonlinear electromagnetic gyrokinetic simulations of tokamak plasmas. *Plasma physics and controlled fusion*, 43(12A):A141, 2001.

[46] F. Romanelli. Ion temperature-gradient-driven modes and anomalous ion transport in tokamaks. *Physics of Fluids B: Plasma Physics*, 1:1018, 1989.

[47] S. C. Cowley, R. M. Kulsrud, and R. Sudan. Considerations of ion-temperature-gradient-driven turbulence. *Physics of Fluids B: Plasma Physics*, 3:2767, 1991.

[48] F. Romanelli and F. Zonca. The radial structure of the ion-temperature-gradient-driven mode. *Physics of Fluids B: Plasma Physics*, 5:4081, 1993.

[49] G. W. Hammett and F. W. Perkins. Fluid moment models for landau damping with application to the ion-temperature-gradient instability. *Physical review letters*, 64(25):3019–3022, 1990.

[50] S. E. Parker, W. W. Lee, and R. A. Santoro. Gyrokinetic simulation of ion temperature gradient driven turbulence in 3d toroidal geometry. *Physical review letters*, 71(13):2042–2045, 1993.

[51] A. M. Dimits, T. J. Williams, J. A. Byers, and B. I. Cohen. Scalings of ion-temperature-gradient-driven anomalous transport in tokamaks. *Physical review letters*, 77(1):71–74, 1996.

[52] R. E. Waltz and R. L. Miller. Ion temperature gradient turbulence simulations and plasma flux surface shape. *Physics of Plasmas*, 6:4265, 1999.

[53] B. N. Rogers, W. Dorland, and M. Kotschenreuther. Generation and stability of zonal flows in ion-temperature-gradient mode turbulence. *Physical review letters*, 85(25):5336–5339, 2000.

[54] M. N. Rosenbluth and F. L. Hinton. *Physical Review Letters*, 80:724, 1998.

[55] F. L. Hinton and M. N. Rosenbluth. *Plasma Physics of Controlled Fusion*, 41:A653, 1999.

[56] T. S. Hahm, M. A. Beer, Z. Lin, G. W. Hammett, W. W. Lee, and W. M. Tang. Shearing rate of time-dependent e× b flow. *Physics of Plasmas*, 6:922, 1999.

[57] J. W. Connor and H. R. Wilson. A review of theories of the lh transition. *Plasma physics and controlled fusion*, 42(1):R1, 2000.

[58] P. H. Diamond, S. I. Itoh, K. Itoh, and T. S. Hahm. Zonal flows in plasmaa review. *Plasma Physics and Controlled Fusion*, 47(5):R35, 2005.

[59] K. Itoh, S. I. Itoh, P. H. Diamond, T. S. Hahm, A. Fujisawa, et al. Physics of zonal flows. *Physics of plasmas*, 13:055502, 2006.

[60] P. J. Catto. *Plasma Physics*, 20:719, 1978.

[61] P. J. Catto, W. M. Tang, and D. E. Baldwin. Generalized gyrokinetics. *Plasma Physics*, 23(7):639, 1981.

[62] W. Dorland, F. Jenko, M. Kotschenreuther, and B.N. Rogers. *Physics Reveiw Letters*, 85:5579, 2000.

[63] E. G. Highcock, M. Barnes, A. A. Schekochihin, F. I. Parra, C. M. Roach, and S. C. Cowley. *Physical Review Letters*, 105:215003, 2010.

[64] F. I. Parra and P. J. Catto. *Plasma Physics of Controlled Fusion*, 52:045004, 2010.

[65] Y. A. Podpaly. *Rotation Generation and Transport in Tokamak Plasmas*. PhD thesis, Massachusetts Institute of Technology, 2012.

[66] J. E. Rice, Y. A. Podpaly, M. L. Reinke, C. Gao, S. Shiraiwa, and et. al. *Nuclear Fusion*, page to be submitted, 2013.

[67] J. P. Lee, P. T. Bonoli, and J. C. Wright. *Physics of Plasmas*, 18:012503, 2011.

[68] J. H. Malmberg and C. B. Wharton. *Physical Review Letters*, 13:184, 1964.

[69] H. Derfler and T. C. Simonen. *Physical Review Letters*, 17:172, 1966.

[70] D. A. Hartmann, C. F. Driscoll, T. M. O'Neil, and V. D. Shapiro. *Physics of Plasmas*, 2:654, 1995.

[71] F. Doveil, A.Macor, and K. Auhmani. *Plasma Physics of Controlled Fusion*, 47:A261, 2005.

[72] F. Doveil, A.Macor, and A. Aissi. *Plasma Physics of Controlled Fusion*, 49:B125, 20057.

[73] T. M. O'Neil. *Phys. Fluids*, 8:2255, 1965.

[74] B. V. Chirikov. *Phys.Rep.*, 52:263, 1979.

[75] J.C.Adam, G.Laval, and D.Pesme. *Physical Review Letters*, 43:1671, 1979.

[76] J. R. Cary, D. F. Escande, and A. D. Verga. *Physical Review Letters*, 65:3132, 1990.

[77] V. D. Shapiro and R. Z. Sagdeev. *Physics Reports*, 283:49–71, 1997.

[78] G. Laval and D. Pesme. *Plasma Phys. Control. Fusion*, 41:239–246, 1999.

[79] M-C.Firpo, F.Doveil, Y.Elskens, P.Bertand, M.Poleni, and D.Guyomarc'h. *Physical Review E*, 64:026407, 2001.

[80] M-C.Firpo, F.Leyvraz, and G.Attuel. *Physics of Plasmas*, 13:122302, 2006.

[81] Y. Kominis. *Physical Review E*, 77:016404, 2008.

[82] A. B. Rechester. *Physical Review A*, 52:2664–2672, 1981.

[83] I. Doxas and J. R. Cary. *Physics of Plasmas*, 4:7, 1997.

[84] I. Bernstein and D. Baxter. *Phys. Fluids*, 24:1, 1981.

[85] G. D. Kerbel and M. G. McCoy. *Phys. Fluids*, 28:12, 1985.

[86] M. Brambilla. *Nucl.Fusion*, 47:175–180, 2007.

[87] G. V. Pereverzev. Use of the multidimensional wkb method to describe propagation of lower hybrid waves in tokamak plasma. *Nuclear fusion*, 32(7):1091, 1992.

[88] J. C. Wright, E. J. Valeo, C. K. Phillips, et al. Full wave simulations of lower hybrid waves in toroidal geometry with non-maxwellian electrons. *Communications in Computer Physics*, 2008.

[89] M. Brambilla. Numerical simulation of ion cyclotron waves in tokamak plasmas. *Plasma Physics and Controlled Fusion*, 41(1):1, 1999.

[90] M Brambilla. Finite larmor radius wave equations in tokamak plasmas in the ion cyclotron frequency range. *Plasma physics and controlled fusion*, 31(5):723, 1989.

[91] D. G. Swanson. Derivation of the mode conversion-tunneling equation from the vlasov equation. *Physics of Fluids*, 24(11):2035–2038, 1981.

[92] J. C. Wright, J. P. Lee, E. Valeo, P. T. Bonoli, et al. *IEEE Transactions on Plasma Science*, 38:2136, 2010.

[93] E. F. Jaeger, R. W. Harvey, and et. al. *Nuclear Fusion*, 46:S397, 2006.

[94] J. P. Lee and J. C. wright. *Computer Physics Communications*, Submitted, 2013.

[95] J. Killen, G. D. Kerbel, M. G. McCoy, and A. A. Mirin. *Computational Methods for Kinetic Models of Magnetically Confined Plasmas.*

[96] B. J. Braams and Charles F. F. Karney. *Physics of Fluids B*, 1:1355, 1989.

[97] N. J. Fisch and A. H. Boozer. Creating an asymmetric plasma resistivity with waves. *Physical Review Letters*, 45(9):720–722, 1980.

[98] A. Bers. *Linear Waves and Instabilities.* Les Houches, 1972.

[99] J. P. Lee, J. C. wright, , P. T. Bonoli, R. R. Parker, P. J. Catto, Y. A. Podpaly, J. E. Rice, and M. L. Reinke. *19th Topical Conference on Radio Frequency Power in Plasmas*, 1406:459, 2011.

[100] T. Hellsten. *Plasma Physics of Controlled Fusion*, 53:054007, 2011.

[101] S. Wang. *Physics of Plasmas*, 18:102502, 2011.

[102] J. P. Lee, F. I. Parra, R. R. Parker, and P. T. Bonoli. *Plasma Physics of Controlled Fusion*, 54:125005, 2012.

[103] N. J. Fisch and C. F. F. Karney. *Physics of Fluids*, 24:27, 1981.

[104] Z. Gao, N. J. Fisch, and H. Qin. Radial electric field generated by resonant trapped electron pinch with radio frequency injection in a tokamak plasma. *Physics of Plasmas*, 18:082507, 2011.

[105] P. Helander, M. Valovic R. J. Akers, the MAST team, and Y Peysson. *Plasma Physics of Controlled Fusion*, 47:B151–B163, 2005.

[106] P. T. Bonoli and R. Englade. *Physics of Fluids*, 29:2937, 1986.

[107] R. Klima. *Czechoslovak Journal of Physics*, B30:874, 1980.

[108] N. C. Lee and G. K. Parks. *Physics of Fluids*, 26:724, 1983.

[109] L. A. Berry, E. F. Jaeger, and D. B. Batchelor. *Physics of Plasmas*, 82:1871, 1999.

[110] J. R. Myra and D. A. D'Ippolito. *Physics of Plasmas*, 7:3600, 2000.

[111] E. F. Jaeger, L. A. Berry, and D. B. Batchelor. *Physics of Plasmas*, 7:3319, 2000.

[112] J. R. Myra, L. A. Berry, D. A. D'Ippolito, and E. F. Jaeger. *Physics of Plasmas*, 11:1786, 2004.

[113] Z. Gao, N. J. Fisch, H. Qin, and J. R. Myra. *Physics of Plasmas*, 14:084502, 2007.

[114] S. P. Hirshman and D. J. Sigmar. *Nuclear Fusion*, 21:1079, 1981.

[115] A. G. Elfimov, V. Petrzilka, and J. A. Tataronis. *Physics of Plasmas*, 1:2882, 1994.

[116] V. S. Chan and S. C. Chiu. *Physics of Fluids B*, 5:3590, 1993.

[117] E. F. Jaeger, L. A. Berry, and D. B. Batchelor. *Physics of Plasmas*, 7:641, 2000.

[118] Z. Gao, N. J. Fisch, and H. Qin. *Physics of Plasmas*, 13:112307, 2006.

[119] A. A. Ware. *Physics Reveiw Letters*, 25:15, 1970.

[120] K. C. Shaing and S. P. Hirshman. *Physics of Fluids B*, 1:705, 1989.

[121] Y. Xiao, P. J. Catto, and K. Molvig. Collisional damping for ion temperature gradient mode driven zonal flow. *Physics of plasmas*, 14:032302, 2007.

[122] N. Winsor, J. L. Johnson, and J. M. Dawson. *Physics of Fluids*, 11:2448, 1968.

[123] H. Sugama and T.-H. Watanabe. *J. Plasma Physics*, 72:825, 2006.

[124] J. E. Rice, A. Ince-Cushman, L.-G. Eriksson, Y. Sakamoto, and et. al. *Nuclear Fusion*, 47:11, 2007.

[125] H. Sugama, T. H. Watanabe, M. Nunami, and S. Nishimura. *Plasma Physics of Controlled Fusion*, 53:024004, 2011.

[126] F. I. Parra, M. Barnes, and A. G. Peeters. Up-down symmetry of the turbulent transport of toroidal angular momentum in tokamaks. *Physics of Plasmas*, 18:062501, 2011.

[127] Y. Camenen, A. Bortolon, B. P. Duval, and Others. Experimental evidence of momentum transport induced by an up-down asymmetric magnetic equilibrium in toroidal plasmas. *Phys. Rev. Lett.*, 105:135003, Sep 2010.

[128] Y. Camenen, Y. Idomura, S. Jolliet, and A. G. Peeters. Consequences of profile shearing on toroidal momentum transport. *Nuclear Fusion*, 51(7):073039, 2011.

[129] O. E. Gürcan, P. H. Diamond, P. Hennequin, et al. Residual parallel reynolds stress due to turbulence intensity gradient in tokamak plasmas. *Physics of Plasmas*, 17:112309, 2010.

[130] R. E. Waltz, G. M. Staebler, and W. M. Solomon. Gyrokinetic simulation of momentum transport with residual stress from diamagnetic level velocity shears. *Physics of Plasmas*, 18:042504, 2011.

[131] T. Sung, R. Buchholz, F. Casson, E. Fable, et al. Toroidal momentum transport in a tokamak caused by symmetry breaking parallel derivatives. *arXiv preprint arXiv:1302.6453*, 2013.

[132] F. I. Parra, M. F. F. Nave, A. A. Schekochihin, and et. al. *Physical Review Letters*, 108:095001, 2012.

[133] J. P. Lee, F. I. Parra, and M. Barnes. Turbulent momentum pinch of diamagnetic flows in a tokamak. *arXiv preprint arXiv:1301.4260*, 2013.

[134] M. Barnes, F. I. Parra, J. P. Lee, E. A. Belli, M. F. F. Nave, and A. E. White. *arXiv:1304.3633*, 2013.

[135] M. N. Rosenbluth and F. L. Hinton. *Nuclear Fusion*, 36:55, 1996.

[136] A.G. Peeters, C. Angioni, A. Bortolon, and Others. *Nuclear Fusion*, 51:094027, 2011.

[137] A. G. Peeters, D. Strintzi, Y. Camenen, C. Angioni, F. J. Casson, and W. A. Hornsby. *Physics of Plasmas*, 16:042310–1, 2009.

[138] T. S. Hahm, P. H. Diamond, . D. Grcan, and R. Singh. *Physics of Plasmas*, 14:072302, 2007.

[139] W. M. Solomon, S. M. Kaye, R. E. Bell, et al. Momentum-transport studies in high e× b shear plasmas in the national spherical torus experiment. *Physical review letters*, 101(6):065004, 2008.

[140] F. I. Parra, M. Barnes, and P. J. Catto. *Nuclear Fusion*, 51:113001, 2011.

[141] A. G. Peeters, C. Angioni, and D. Strintzi. *Physical Review Letters*, 98:265003, 2007.

[142] R. J. Hawryluk et al. An empirical approach to tokamak transport. *Physics of Plasmas Close to Thermonuclear Conditions*, 1:19, 1980.

[143] E. A. Belli and J. Candy. Kinetic calculation of neoclassical transport including self-consistent electron and impurity dynamics. *Plasma Physics and Controlled Fusion*, 50(9):095010, 2008.

[144] J. Ko, S. Scott, S. Shiraiwa, M. Greenwald, et al. Intrashot motional stark effect calibration technique for lower hybrid current drive experiments. *Review of Scientific Instruments*, 81(3):033505–033505, 2010.

[145] J. W. Hughes, D. A. Mossessian, A. E. Hubbard, E. S. Marmar, D. Johnson, et al. High-resolution edge thomson scattering measurements on the alcator c-mod tokamak. *Review of Scientific Instruments*, 72(1):1107–1110, 2001.

[146] G. T. Hoang, A. Bécoulet, J. Jacquinot, et al. A lower hybrid current drive system for iter. *Nuclear Fusion*, 49(7):075001, 2009.

[147] F. I. Parra, C. Yoo, M. Barnes, and J. P. Lee. Critical balanced itg turbulence near marginal stability. In *Proceedings of 2013 International Sherwood Fusion Theory Conference*, Santa Fe, New Mexico, USA, April 2013.